DAA/LANGLEY

IN-38

69627-CR

P.274

V1610109

# COLLEGE OF ENGINEERING

# VIRGINIA POLYTECHNIC INSTITUTE AND STATE UNIVERSITY

BLACKSBURG, VIRGINIA

# FINAL REPORT

# OPTICAL FIBER SENSORS FOR THE NON-DESTRUCTIVE EVALUATION OF MATERIALS

January-December 1986

Prepared for
NASA Langley Research Center
Hampton, VA
NAG-1-679

Prepared by
Fiber and Electrooptics Research Center
Dept. of Electrical Engineering
Virginia Tech, Blacksburg VA
February 1987

# Table of Contents

**Introduction** . . . . . 1

**Current Research Areas** . . . . . 2
The Modal Domain Sensor . . . . . 2
The Modal Domain Sensor in Vibration Analysis . . . . . 3
The Modal Domain Sensor in Acoustic Emission Detection . . . . . 4
Effects of DC Strain on MDS . . . . . 5
Additional Areas of Fiber Sensing . . . . . 6
Acoustic Fiber Waveguides . . . . . 7

**Fiber Fabrication Facility** . . . . . 8

**Appendix A. Fiber Optic Modal Domain Sensing of Structural Vibrations** . . . . . 9

**Appendix B. Detection of Acoustic Emission in Plywood** . . . . . 10

**Appendix C. Optical Fiber Modal Domain Sensing of Stress Waves** . . . . . 11

**Appendix D. Axial Strain Effects on Optical Fiber Mode Patterns** . . . . . 12

**Appendix E. Single Mode Optical Fiber Vibration Sensor** . . . . . 13

**Appendix F. Imbedded Optical Fiber Sensor of Differential Strain and Temperature in Composites** . . . . . 14

**Appendix G. Damage Monitor System Using Imbedded Fibers** . . . . . 15

**Appendix H. Acoustic Fiber Waveguide Devices** . . . . . 16

**Appendix I. BASIC Program for Processing of Digitized Waveforms** . . . . . 17

# Introduction

This report will provide a survey of recent research efforts in fiber optics at the Fiber and Electrooptics Research Center at Virginia Tech. With support during 1986, work has continued toward the development of fiber optic sensors with major focus on the technique of modal domain sensing (MDS) and its application to vibration and acoustic emission analysis. New work aimed at understanding some of the mechanisms of MDS is also underway. In addition, imbedded interferometric fiber sensors capable of detecting temperature, strain and differential temperature levels in graphite epoxy composites have been studied along with imbedded fiber arrays for the detection of impact damage. A related new program dedicated to the development of acoustic fiber waveguides has been started with the addition of a new faculty member, Dr. Ahmad Safaai-Jazi. Each of these areas will be addressed individually with references to recent thesis topics, thechnical papers and conference proceedings. Since MDS represents the major research thrust at this time, a brief theoretical background of single fiber interferometric or modal domain sensors will be given to provide a foundation for the technical survey of work being done in this area. Readers will be referenced to the appendices for the specific articles and publications reviewed in this report.

# Current Research Areas

## *The Modal Domain Sensor*

Presently, modal domain sensing represents the largest area of our fiber sensor research. Modal domain sensing is a term which may be considered synonomous with single fiber interferometric sensing. Traditional fiber optic sensors employing an interferometric technique have taken the form of standard Mach-Zehnder type systems with single mode fibers comprising the two arms of the interferometer. By exposing one arm of the system to external stimuli (temperature or strain) induced phase changes in the light signal propagating in this arm may be detected at the interferometer output and related to the applied temperature or strain. Modal domain sensor systems seek to exploit a similar interferometric effect between the modes of a low moded multimode fiber.

We first select a fiber which is designed to operate as single mode at a particular wavelength. If we instead operate the fiber at a slightly shorter wavelength we effectively increase the $V$ number of the fiber and several low order modes are excited. Each of these modes may be described by their specific propagation constant (wave number) $\beta_i$. For a fiber of length $L$, the phase $\varphi$ of the $i$ th mode at the fiber end may be written as

$$\varphi_i = \beta_i L \tag{1}$$

If an optical fiber is exposed to some level of strain, it is known that a phase change will be induced in the propagating light. The change in phase of the $i$ th mode, $\Delta\varphi_i$, can be described as

$$\Delta\varphi_i = \beta_i \Delta L + L\Delta\beta_i \tag{2}$$

Just as the two arms of the Mach-Zehnder interferometer transmit signals of different relative phase, the low order modes of the MDS propagate with different phase, this phase difference being related to the applied strain. The fact that *each mode* experiences a *distinct* phase change suggests the existence of a potential interference mechanism between these different modes analagous to the interference mechanism in the two fiber interferometer. This is indeed the case and has been demonstrated both theoretically and experimentally. As the single, low-moded fiber is exposed to some time varying stress, the subsequent phase changes in the various modes result in a phase modulation of the light at the fiber output. The far field output pattern of the optical fiber consists of a collection of several blobs or lobes; an interference pattern generated by the different modes of the fiber. The phase modulation induced through the perturbation of the fiber manifests itself as a movement and intensity variation of this lobe pattern. Spatially filtering the pattern (placing a small aperture in the far field of the fiber output) gives a sensor signal which is amplitude modulated at the frequency of the time dependent strain applied to the fiber. Detecting the fiber output with a photodiode allows one to demodulate the AM sensor signal thus detecting the applied strain. Earlier investigators of this technique perturbed the fiber by coupling it to a piezoelectric (PZT) device. In this way a sinusoidaly time dependent strain could be excited in the fiber and subsequently detected in the photodiode signal. Though this system has proved to be considerably less sensitive than the traditional single mode interferometer it represents a much simpler sensor.

## The Modal Domain Sensor in Vibration Analysis

Our work in MDS has concentrated on applying this sensor to somewhat more complex systems. Specifically, we wish to demonstrate the use of this sensor in the monitoring of structural vibration and acoustic emissions. This first application was the subject of a recent masters thesis which may be referred to in Appendix A. Where previous workers relied on PZT devices to initiate strain in the fiber, we coupled the fiber to some simple laboratory

vibrational systems with the hope of inducing strain, These included a vibrating string, a clamped-free or cantileverd beam and finally a large free-free beam structure. The purpose of this work was to investigate the sensors abilty to respond to the various harmonic frequencies generated by a vibrating structure. By coupling the fiber to the structure's surface, time dependent strains, introduced into the fiber through the vibration, should occur at these same frequencies and subsequently modulate the light signal. If so, then the predicted component frequencies of the vibrating structure should appear in the frequency spectrum of the demodulated fiber output. By performing fast Fourier transforms on digitized sensor signals we were able to compare frequency spectra obtained from each structure with the structure's calculated harmonic frequencies. In each case, the fundamental component and sometimes several higher order harmonics, depending on the structure, were available in the signal spectrums. However, in addition to the expected structural frequencies the spectra also contained several anomolous components not indicative of the structures' motion. Often these anomolies could be attributed to known effects within the sensor itself. Detailed studies of this application are available in Appendix A.

## The Modal Domain Sensor in Acoustic Emission Detection

In a second application of modal domain sensing, low-moded fiber was imbedded in symmetric cross-ply graphite epoxy specimens. Failure of graphite fibers and matrix material under tensile loads results in the release of acoustic energy. This phenomena, known as acoustic emission, results in the propagation of a stress wave throughout the sample. Failures were generated by loading the composite specimen on an automated tension frame. As a reference, PZT transducers were coupled to the sample's surface. PZT and fiber sensor responses were monitored simultaneously. Excellent time correlation between the two sensors was observed during the occurance of acoustic emissions. Where the PZT response was characterized by very short, sharp pulses the fiber response was characterized by a rapid reaction to the emission followed by a relatively long, damped response. This is due to the fact that the acoustic stress wave propagates throughout the specimen and its influence is distributed over the fiber length. A similar experiment was performed on a balsa wood lami-

nate sample. Four rectangular balsa wood plys were bonded in an alternating 0° – 90° orientation with a single optical fiber imbedded in the 0° direction. The specimen was set up as a cantilevered beam and failures were initiated by loading the beam's free end at its center. Sensor response was similar to that seen during graphite composite failure monitoring: rapid, sharp responses with long decay times. Details of these two studies are available in the conference proceedings shown in Appendices B and C.

## Effects of DC Strain on MDS

Although this technique has seen a range of applications in the laboratory with a fair amount of success, there seems to be an inherent problem of reproducibilty with this sensor. Sensor response seems to be a strong function of the state of the lobe pattern. Placement of the aperture, shape of the lobe pattern and launching of light into the fiber all affect sensor behaviour. It is known that the interference or lobe pattern which characterizes the fiber output is related to the induced strain in the fiber. These strains cause rotation, redistribution and intensity variations of these lobes. Precisely how strain and these observed reactions in the speckle pattern are related is not understood. Work aimed at better defining the correlation between applied strain, speckle pattern behaviour and subsequent sensor response is currently underway. The effects of axial strain on speckle pattern and MDS behaviour was the subject of recently completed masters thesis. The optical fiber was mounted in an automated load frame capable of providing precisely controlled strain rates. As fiber axial load was continually increased speckle pattern behaviour and sensor response were observed. The slow, continuous stress caused a noticeable rotation of the output pattern. Spatial filtering and detection of the fiber output during the continuous strain process yielded a sinusoidal sensor signal. This type of behaviour would tend to indicate that there are ideal levels of applied DC strain, strain biasing if you like, which could maximize the fiber's sensitivity. Perturbations around this constant strain level, induced through vibrations or acoustic emissions, could be sensed more effectively due to the presence of this DC strain. This was observed experimentally when the "DC strained" fiber was also coupled to a vibrating clamped-free beam under constant, controlled strain. By adjusting the strain level via the load

frame the sensor's respones to the beam's vibration could be maximized; the small strains induced by the beam were augmented at particular levels of DC strain. A complete description of this work is given in Appendix D.

## *Additional Areas of Fiber Sensing*

In addition to research utilizing modal domain methods we are also exploring techniques which exploit the polarizing effects of single mode fibers under applied stress (vibration, pressure). Strain induced birefringence in a single mode fiber causes modulation in the polarization states of the modes orthogonal polarization components. By analyzing the polarization state of the fiber otput we may detect this modulation. Moderate success has been achieved in these early investigations while trying to detect simple structural vibrations such as those encountered in a cantileverd beam. This work will be presented at an upcoming IEEE conference and is referenced in Appendix E. Future work in this area will include application of polarization preserving fiber as the sensor medium and systems which launch other polarization schemes into the fiber.

A traditional Mach-Zehnder fiber optic interferometer sensor system has recently been studied for use in monitoring stress, temperature and differential temperature gradients in graphite epoxy laminate specimens. A potential application of this sensor could be accurate and precise monitoring of cure level within the composite during the actual cure cycle. Using single mode fiber, one arm of the interferometer is incorporated within the laminae. Exposing the specimen to temperature or pressure results in a phase shift within the fiber sensing arm. This produces a movement of the characteristic fringe pattern at the interferometer output. Fringe movements are then counted and can be related to the temperature or pressure change in the sample. Sensitivity of this system is extremely high, about 20 dB above that of the modal domain sensor discussed earlier. The obvious disadvantages of this sensor are allignment requirements and the need to observe interference fringe movements. See Appendix F for details on this research.

Fiber sensor arrays have been imbedded in graphite epoxy samples with the intention of detecting inpact damage within the specimen. Light is coupled into the multimode fiber array using two fused biconical taper couplers manufactured in our laboratory. Output intensity of each fiber in the array is monitored, over controlled levels of impact, for any drop in light transmission caused by impact damage to the optical fibers. Preliminary results show promise for the location and characterization of impact and impact damage. This work is referenced in Appendix G.

## *Acoustic Fiber Waveguides*

Our newest area of research, acoustic fiber technology, began in September of 1986. Acoustic fibers have strong promise in the area of sensors due to the reduced signal velocities in the fiber. Acoustic fibers differ from their optical counterparts in that they transmit a mechanical stress wave rather than an electromagnetic wave. They are however very similar in construction: Two concentric cylinders of glass drawn from an initial fiber preform. Boundary conditions determining the propagation of confined modes are a function of the sound velocities in, and densities of, the glasses which are used.

Preliminary work here at VPI has been concerned with simple attempts at drawing glass rods into fibers. Simple systems for holding and heating the fiber as it is manually drawn have been configured in the lab. Several attempts at producing rough acoustic fiber preforms have been made with limited success. Air pockets between the concentric glass rods and incompatibility of the glasses were the sources of the difficulties. The ITT Corporation in Roanoke, Virginia recently manufactured for us a fairly simple acoustic fiber preform from glass cylinders supplied by our laboratory. This preform will be used in the new fiber draw facility currently under construction here at VPI to produce a first run of acoustic fiber waveguide. We are now in the process of gathering sufficient transducers for the launching of acoustic energy into the fiber itself. Appendix H gives the details of this work.

# Fiber Fabrication Facility

The beginning of January '87 was to mark the groundbreaking for the new fiber manufacturing facility at VPI. Initial projections had the draw tower containment structure completed by mid January with delivery of the tower to follow immediately. Minor design disagreements followed by major weather setbacks have forced delay in the construction of the structure's foundation. Recent fair weather may allow this construction to get underway though over one month behind schedule. Delivery of the tower is now contingent only upon the completion of the draw tower building. Following the completion of the structure it will be necessary to erect a scafolding around the draw tower itself to allow access to the different system components. Several manufacturers have agreed to donate fiber preforms which will be used in the first runs of the system and should be available immediately. Actual fiber manufacture then should be underway as soon as construction is completed.

# Appendix A. Fiber Optic Modal Domain Sensing of Structural Vibrations

# Fiber Optic Modal Domain Sensing of Structural Vibrations

by

Paul A. Ehrenfeuchter

Thesis submitted to the Faculty of the

Virginia Polytechnic Institute and State University

in partial fulfillment of the requirements for the degree of

Master of Science

in

Electrical Engineering

APPROVED:

Richard O. Claus, Chairman

Ronald J. Pieper

Ahmad Safaai-Jazi

December, 1986

Blacksburg, Virginia

**Fiber Optic Modal Domain Sensing of Structural Vibrations**

by

Paul A. Ehrenfeuchter

Richard O. Claus, Chairman

Electrical Engineering

(ABSTRACT)

This paper investigates the application of single, low-moded, fiber optic sensors to the detection of structural vibration. Several laboratory vibration systems which demonstrate a range of component frequencies and dynamic range are analyzed in an effort to characterize the sensor's behaviour. We compare frequency spectra of the sensor output with calculated frequency components of the structures to determine if the sensor is responding to the various structural harmonics. Specifically, we wish to demonstrate the dynamic range and frequency response of the sensing technique. Experimental results and observations are preceeded by a brief review of sensor mechanisms in optical fibers and presentation of a theory describing the operation of the modal domain sensor.

# Acknowledgements

I should like to express my gratitude to Dr. R.O. Claus, my graduate advisor, for his guidance, assistance and patience. Thanks goes to Dr. A. Safaai-Jazi and Dr. R. Pieper for serving on my graduate committee. A very strong pledge of thanks to Dr. W. Hallauer, Dept. of Aerospace Engineering at Virginia Tech for his endless help and advice concerning structural vibration analysis and experimentation.

Many thanks to my fellow graduate students K.T. Srinivas and N.K. Shankarananayn for their advice and consultation and Ms. Robin Rogers and Anne Goette for their assistance in organization and providing helpful sustenance. And finally to my family and very dear friend Ms. Karen Lund for their unending support and encouragement.

# Table of Contents


**1.0 Introduction** ..... **1**

**2.0 Fiber Optic Sensors** ..... **3**

2.1 Waveguide Modes ..... 3

2.2 Sensor Mechanisms ..... 7

**3.0 Single Fiber Sensors** ..... **12**

**4.0 The Modal Domain Sensor** ..... **19**

**5.0 Experiments** ..... **25**

5.1 The Vibrating String ..... 28

5.2 The Clamped-Free Beam ..... 31

5.3 The Free-Free Beam ..... 32

**6.0 Observations and Analysis** ..... **35**

6.1 The Vibrating String ..... 37

6.2 The Clamped-Free Beam ..... 40

6.3 The Free-Free Beam ..... 41

**7.0 Conclusions** ..... **44**

**Bibliography** ..... **71**

**Appendix A. The Vibrating String** ..... **73**

A.1 The Plucked String ..... 77

**Appendix B. Simple Vibrating Beams** ..... **80**

B.1 Clamped-Free Boundary Conditions ..... 83

B.2 Free-Free Boundary Conditions ..... 86

**Appendix C. Experimental Measurement of Young's Modulus** ..... **88**

Vita ..... 90

# List of Illustrations


Figure 1. Step-index optical fiber with reflected ray path. . . . . 47

Figure 2. V number vs. normalized propagation constant. . . . . 48

Figure 3. E field distribution due to fiber bending for the $HE_{11}$ mode . . . . . 49

Figure 4. Calculated $HE_{11}$ and $TM_{01}$ mode intensities and phase at fiber endface . . . . . 50

Figure 5. Differential phase model of two-mode optical fiber . . . . . 51

Figure 6. Modal Domain Sensor system. . . . . 52

Figure 7. Output interference pattern of 850 nm fiber with 633 nm laser . . . . . 53

Figure 8. Vibrating string experimental setup. . . . . 54

Figure 9. Inital displacement measurement device used in string and CF beam experiments. 55

Figure 10. Clamped-free beam experimental setup showing coupling of fiber to structure. . . 56

Figure 11. Free-free beam experiment . . . . . 57

Figure 12. Time domain response of modal domain sensor. . . . . 58

Figure 13. Frequency spectrum of string excitation at 196 Hz . . . . . 59

Figure 14. Frequency spectrum of string excitation at 196 Hz . . . . . 60

Figure 15. Frequency spectrum of string excitation at 294 Hz . . . . . 61

Figure 16. Frequency spectrum of string excitation at 294 Hz . . . . . 62

Figure 17. Frequency spectrum of string excitation at 392 Hz . . . . . 63

Figure 18. Frequency spectrum of string excitation at 392 Hz . . . . . 64

Figure 19. Frequency spectrum of sensor output for clamped free beam excitation . . . . . 65

Figure 20. Frequency spectrum of sensor output for clamped-free beam excitation . . . . . 66

Figure 21. Frequency spectrum of sensor output for clamped-free beam excitation showing effects of carrier phase and endface reflection . . . . . 67

Figure 22. Frequency spectrum of sensor output for first free-free beam excitation . . . . . 68

Figure 23. Frequency spectrum of sensor output for second free-free beam excitation . . . . . 69

Figure 24. Frequency spectrum of sensor output for third free-free beam excitation . . . . . 70

Figure 25. Differential string element [25]. . . . . 79

Figure 26. Differential beam element showing neutral surface and bending radius. . . . . 87

# 1.0 Introduction

Sensors and communications exist as the two major thrusts in current fiber optic technology. The past ten to fifteen years have given rise to many fiber optic sensor systems capable of detecting temperature, pressure, acoustic stress waves and strain. The principle mechanism employed in the majority of sensor systems is a strain induced change of refractive index resulting in phase shifts of the propagating fiber modes. Mach-Zehnder interferometer systems which employ this effect have been developed for the detection of acoustic stress waves in solids and ambient water mediums. This type of sensor utilizes single mode fibers in each arm of the interferometer. The strain induced photo-elastic effect in one arm results in a detectable shift of the interference fringes which can be related to pressure and frequency.

Single fiber sensors have also been studied. These systems, known as modal domain sensors, utilize fibers which propagate a small number of modes at the given operating wavelength. Strain induced changes in refractive index affect the phase of each propagating mode differently giving rise to an effective phase and amplitude modulation of the detected light. Experiments investigating these sensors have focused primarily on high frequency piezoelctrically induced strain. This paper investigates the application of these low moded, single fiber sensors to the detection of low frequency structural vibration. Ultimately, we would like the ability to detect the component vibration frequencies which describe the structure's motion. We begin with a treatment of guided

wave propagation in optical fibers and develop the concept of waveguide modes in cylindrical step index dielectric waveguides. This is necessary background for chapter three which develops a simple theoretical model for the operation of the single fiber sensor. An analysis of fiber modes in the presence of strain and how these modes interact to develop an effective amplitude modulation of the light is given. Here the term modal domain sensing is coined to define this type of sensor.

With an understanding of single fiber or modal domain sensor operation we proceed to chapter four which discusses the application of this sensor in monitoring the vibrations of structures. The mechanisms of induced strain developed in the previous chapter are related to the fiber-structure system in describing how vibrations may actually be detected in the fiber. The actual sensor system is also defined. Chapter five describes the actual experiments and vibrational systems which were studied: the vibrating string, the clamped-free beam and the free-free beam. The final chapter addresses overall observations gleaned from the experiments along with results specific to each individual system. Comparisons of these results to the predicted behaviour and to the results of other workers who have investigated single fiber sensors are made. In this way the performance of the modal domain sensor as a low frequency structural vibration monitor is evaluated.

# 2.0 Fiber Optic Sensors

Two primary mechanisms may be considered responsible for fiber optic sensor operation: induced strain and fiber bending [1]. Generally one of these mechanisms, through its respective effects upon the propagating light, is isolated in the sensor detection scheme. To understand how strain and bending may combine to affect guided light transmission we must first look at the operation of a dielectric waveguide.

## *2.1 Waveguide Modes*

In addressing this problem we will restrict our arguments to step index fibers as shown in Fig. 1. This fiber consists of a central core of refractive index $n_1$ surrounded by a concentric cladding of index $n_2$ with $n_1 > n_2$. Consider a light ray travelling in the core, incident on the $n_1 - n_2$ boundary. Since $n_1 > n_2$, at some critical angle, $\theta_c$, all light will be reflected back into the core. In this way the ray may propagate along the fiber core due to consecutive total internal reflections. This is known as the geometric or ray optic approach and is the most basic description of optical fiber operation.

If there exists a particular critical angle within the fiber which supports ray propagation then there must be some external input condition describing which rays will meet the critical angle criteria. This defines the numerical apperture or $NA$ of the fiber. The $NA$ is a function of the fiber parameters and is given by [2]

$$NA = \sqrt{n_1^2 - n_2^2} \ . \tag{2.1}$$

The final constraint which the ray optics technique predicts relates to the phase of the rays. Referring again to Fig. 1, if one considers the phase change of the ray due to propagation through $n_1$ (path ABC) and the reflection at the core-cladding boundary we see that only those rays with a phase shift of $2\pi n$ will propagate, all others will detructively interfere and damp out. This indicates that only discrete ray paths corresponding to particular internal reflection angles at the boundary are allowed [2].

Although the ray optics approach gives an intuitive understanding of light transmission it does not provide the information needed to develop a theory of fiber sensor behaviour. We require a more quantitative description of the effects discussed above. This is derived from the more realistic electromagnetic approach [3,4]. We start by charachterizing the light as a set of guided electromagnetic waves within the fiber which repeat at intervals of $\lambda$, the wavelength of the light. As will be seen these guided waves exist as discrete modes within the fiber. Only specific modes can propagate and a specific finite number exist as determined by the fiber properties and light wavelength. We begin with the wave equation for the $\overline{E}$ and $\overline{H}$ fields within the fiber as derived from Maxwell's equations

$$\nabla^2 \begin{bmatrix} \overline{E} \\ \overline{H} \end{bmatrix} = \frac{1}{c^2} \frac{\partial^2}{\partial t^2} \begin{bmatrix} \overline{E} \\ \overline{H} \end{bmatrix} . \tag{2.2}$$

Here $\nabla^2$ is the Laplacian operator in cylindrical coordinates, the assumed coordinate system within the fiber. Only the $E_z$ and $H_z$ components of the vector fields will assume a simple form since the $\hat{\theta}$ and $\hat{r}$ component vectors are not constant. Assuming an $e^{-i\omega t}$ dependence we obtain

$$(\nabla^2 + k^2)\begin{bmatrix} E_z(r, 0,z) \\ H_z(r, 0,z) \end{bmatrix} = 0 \tag{2.3}$$

$$k^2 = \omega^2\varepsilon\mu = \omega^2 n^2/c^2 .$$

where $n$ is the index of refraction of the propagating medium (core or cladding). Since we are considering the electromagnetic waves to be travelling along the fiber axis we assume a periodic field dependence along the $z$ direction

By applying Maxwell's equations

$$\nabla \times \overline{E} = -\frac{1}{c}\frac{\partial \overline{B}}{\partial t} \qquad \nabla \times \overline{H} = \frac{1}{c}\frac{\partial \overline{D}}{\partial t} \tag{2.5}$$

to equation (2.4) we may express the radial and azimuthal field components in terms of $E_z$ and $H_z$. Thus our goal is to solve for the $\overline{E}$ and $\overline{H}$ components in the $z$ direction. This will render a complete discription of the electromagnetic field within the fiber. We substitute the assumed solution for $E_z$ and $H_z$ into the wave equation. This results in the partial differential equation

$$\left[\frac{\partial^2}{\partial r^2} + \frac{1}{r}\frac{\partial}{\partial r} + \frac{1}{r^2}\frac{\partial^2}{\partial \theta^2} + (k^2 - \beta^2)\right]\begin{bmatrix} E_z \\ H_z \end{bmatrix} = 0 . \tag{2.6}$$

The separable solution to this equation may be written as

$$\begin{bmatrix} E_z \\ H_z \end{bmatrix} = \psi(r)\exp^{\pm i\theta} ,$$

and gives Bessel's equation

$$\frac{\partial^2\psi}{\partial r^2} + \frac{1}{r}\frac{\partial\psi}{\partial r} + \left[(k^2 - \beta^2) - \frac{l^2}{r^2}\right]\psi(r) = 0 \tag{2.7}$$

for the radial solution $\psi(r)$. Bessel's equation has specific sets of solutions which depend upon the sign of the quantity $(k^2 - \beta^2)$. For $(k^2 - \beta^2) > 0$ the set of solutions to Bessel's equation are Bessel functions $J_l$ and $Y_l$. For $(k^2 - \beta^2) < 0$ the solutions are modified Bessel functions $I_l$ and $K_l$. The actual solutions are determined from the boundary conditions. Specifically, these boundary conditions require evanescent (decaying) fields in the region $r > a$ and boundedness as $r$ approaches zero. These considerations give the Bessel function solutions $J_l$ (corresponding to $k_1^2 - \beta^2 > 0$) in the region $r < a$ and modified Bessel function solutions $K_l$ (corresponding to $k_2^2 - \beta^2 < 0$) for $r > a$. Here $k_1$ and $k_2$ are wave numbers in the core and cladding respectively and are defined as

$$k_1 = \omega n_1/c \quad , \quad k_2 = \omega n_2/c .$$

This results in a range of allowable values for the $z$-component of the actual propagation constant $\beta$ for which guided core modes and evanescent clad modes exist:

$$n_2 k_o < \beta < n_1 k_o . \tag{2.8}$$

$$k_o = \omega\sqrt{\mu_o \varepsilon_o}$$

This condition correlates with the ray optics prediction of a critical cutoff angle $\theta_c$.

Finally, the boundary conditions must be met at the boundary $r = a$, i.e. the tangential field components must be continuous. These conditions lead to a homogeneous linear system for the field components. In order to obtain a non-trivial solution the determinant of this system must be zero. This generates a characteristic equation whose solution gives unique values for the propagation constant $\beta$. Stated more exactly: the system yields the eigenvalues $\beta_i$. Only discrete values of $\beta$ exist which will satisfy the $n_1 - n_2$ interface boundary condition. This correlates with the ray optics prediction of distinct guided rays. In the electromagnetic approach we refer to the distinct electromagnetic field solutions charachterized by the $\beta_i$ eigenvalues as modes.

The number of modes in the waveguide is related to a quantity known as the $V$ number [2]:

$$V = k_o a\sqrt{n_1^2 - n_2^2} \tag{2.9}$$

The $V$ number determines which specific modes may propagate in the waveguide. Fig. 2 shows the $V$ number as a function of the normalized propagation constant $\beta/k$ for several waveguide modes. Through equation (2.8) the quantity $\beta/k$ has definite limits which allow guided mode propagation. Fig. 2 demonstrates the fact that below particular $V$ numbers certain modes will not propagate since their propagation constant does not satisfy equation (2.8).

## 2.2 *Sensor Mechanisms*

Strain and bending, as discussed earlier, are the primary mechanisms of fiber sensor operation. The two may of course be considered related since bending-induced tension and compression result in some form of strain within the fiber. However, we generally consider strain and bending seperately when describing their effect upon the transmitted light. The simplest type of fiber optic sensor employs the effects of bending exclusively. The overall result of bending an optical fiber is a drop in transmitted light intensity at the fiber output. This is due to an effect known as bend loss whose causes will now be discussed.

To understand the properties of bend loss we must return to the electromagnetic analysis. In general, bend loss results from the radiation of higher order modes out of the core and cladding due to the physical bending of the fiber [5,6,7]. This can be witnessed as a glowing of the optical fiber in a region local to the bending. The cause of this mode radiation is related to the electromagnetic field distribution within the fiber core. Each wave or mode will have its own unique distribution of $\overline{E}$ and $\overline{H}$ field magnitudes across the fiber cross section. These can be determined by solving for the various field components at a particular coordinate location. Fig. 3 shows the $\overline{E}$ field distribution across the core for the $HE_{11}$ mode of a multimode fiber with V = 12.6. The central solid curve represents the theoretical magnitude for a straight, unperturbed fiber. Bending will result in a perturbation of this curve. Marcuse has predicted the behaviour of the electromagnetic field within the fiber as the fiber is bent through a circular arc of radius $R$. He has shown that fiber bending results

in three distinct perturbations of the field intensity having distinct influences upon the bend loss. Firstly, the peak intensity, located at at $r/a = 0$ in Fig. 3, tends to shift from its unperturbed position towards the core-cladding interface as bending radius is decreased. This causes some of the power initially confined to the core to radiate into the cladding increasing the radiative loss of the fiber. Secondly, the width of the intensity distribution may either widen or narrow as the bending radius is varied (narrowing in the case of Fig. 3). A narrowing of the distribution decreases radiative bend loss while a widening serves to increase loss. Hence, this effect may tend to either augment or diminish that of the peak intensity shift. The third consideration is the slope of the intensity distribution function at the boundary $r = a$. Steeper slopes indicate higher bend loss. Marcuse's theory, in accounting for the effects of distribution widening and slope, predicts an increased low mode loss and a decreased higher mode loss in comparison with previous theories. Bend loss is a simple mechanism to apply since it requires only the monitoring of output light intensity. It has been applied predominately to the sensing of applied pressure [1].

The second and most dominant mechanism employed in optical fiber sensing is that of induced strain [8]. Strain may be introduced through various stimuli: temperature, acoustic stress waves, pressure. The influence of strain on the refractive index $n$ of the fiber material is responsible for the perturbations of the transmitted light. Specifically, the variation in refractive index will introduce a phase shift. If we define $L$ as the length of the fiber and recall that $\beta$ is the $z$-component of the propagation constant, the phase of an electromagnetic field in the waveguide can be written as

$$\varphi = \beta L . \tag{2.10}$$

The phase *change*, $\Delta\varphi$, is related to an induced change in $L$ and $\beta$

$$\Delta\varphi = L\Delta\beta + \beta\Delta L . \tag{2.11}$$

The second term represents the strain induced change in length of the fiber. For a fiber under isotropic stress due to pressure $P$ we can write the stress components $\sigma_i$ as a vector

$$\bar{\sigma} = \begin{bmatrix} -P \\ -P \\ -P \end{bmatrix}.$$

The resulting strain $\bar{\varepsilon}$ is related to $\bar{\sigma}$ via the elastic constants

$$\bar{\varepsilon} = \begin{bmatrix} (1-2\mu)/E \\ (1-2\mu)/E \\ (1-2\mu)/E \end{bmatrix} \bar{\sigma},$$

where $\mu$ is Poisson's ratio and $E$ Young's modulus. The second term of equation (2.11) can now be defined

$$\beta\Delta L = \beta\varepsilon L = -\beta(1-2\mu)LP/E. \tag{2.12}$$

The first term represents the change in phase $\varphi$ due to a change in $\beta$ and has two origins: a strain-optic effect which causes a change in refractive index and a mode dispersion effect due to a change in fiber diameter. This may be expressed as

$$L\Delta\beta = L\frac{\partial\beta}{\partial n}\Delta n + L\frac{\partial\beta}{\partial D}\Delta D. \tag{2.13}$$

The diameter change defined by the second component of equation (2.12) can be shown to be negligible relative to the other effects and will not be considered. The propagation constant $\beta$ can be written as $\beta = n_{eff}k_o$ for small differences in $n_1$ and $n_2$ which gives

$$\frac{\partial\beta}{\partial n} \cong k_o. \tag{2.14}$$

We now need to define $\Delta n$. The change in index of refraction is related to induced strain through the photo-elastic constants $p_{ij}$. In general $p_{ij}$ is a tensor and appears as a change in the components of the optical index ellipsoid

$$\Delta\left(\frac{1}{n^2}\right)_i = \sum_{j=1}^{6} p_{ij}\varepsilon_i . \tag{2.15}$$

We calculate $\Delta n_i$ from

$$\Delta n_i = \left[\frac{\partial}{\partial n}\frac{1}{n^2}\right]^{-1} \Delta\left(\frac{1}{n^2}\right)_i .$$

Then the general expression for the change in index of refraction is given by

$$\Delta n_i = -\frac{1}{2}n^3 \sum_{j=1}^{6} p_{ij}\,\varepsilon_j \quad , i = 1,6 . \tag{2.16}$$

For the case of isotropic strain, no shear ($\varepsilon_4 = \varepsilon_5 = \varepsilon_6 = 0$) and an isotropic medium $i, j = 1,2,3$ this reduces to

$$\begin{aligned} \Delta n_{1,2} &= -\frac{1}{2}n^3 \Delta\left(\frac{1}{n^2}\right)_{1,2} \\ &= \frac{1}{2}n^3\left(\frac{P}{E}\right)(1-2\mu)\left[\,2p_{12} + p_{11}\,\right] \end{aligned} \tag{2.17}$$

This equation, and its more general form equation (2.12), relate the applied stress, or induced strain $\bar{\varepsilon}$ , to the shift in refractive index. In conjunction with equations (10) through (12) the total phase shift in the fiber may be predicted.

The usual technique is to subject one arm of a single mode fiber optic interferometer to some strain-inducing stimulus. The subsequent changes in $\varphi$ due to the photoelastic effect result in a shifting of the characteristic intereference fringes when the output of the two arms are mixed. The sensor is calibrated in terms of fringe displacements per unit of stress.

Although this effect is normally exploited in single mode fibers, modal phase changes also occur in multimode fiber. In this circumstance each propagation constant eigenvalue, $\beta_i$ , will be influenced differently by the photoelastic strain mechanism, equation (2.12). Hence each mode, which is characterized by its respective $\beta_i$ , will experience a different phase shift. It is this phenomena which forms the basis for single fiber interferometers and defines the operation of the

modal domain sensor. In the following chapter single fiber systems are expanded and a simple model for their operation is presented.

# 3.0 Single Fiber Sensors

In the previous chapter, operation of the step index fiber was described in terms of the simple ray optics approach and more quantitatively through an electromagnetic analysis employing Maxwell's equations to describe the electromagnetic fields in the fiber. The common result of the two analyses was the existence of discrete waveguide modes defined by the $z$-component of of their propagation constant, $\beta$. Next, fiber optic sensors were analyzed by defining the response of these waveguide modes to induced strain and bending. In closing, the possibility of utilizing a single multi-mode fiber as a phase dependent sensor was suggested. This sensor would employ phase differences between modes to produce strain-dependent intramodal interference; similar to the interference of the shifted and unshifted single modes in the two arms of a Mach-Zehnder interferometer. Several authors [9,10] have investigated the response of low-moded multi-mode fibers to pressure-induced strain demonstrating interference between the phase shifted modes. This chapter will review these investigations since it is this same effect which defines the operation of the modal domain sensor in the detection of vibration.

The systems in which previous authors have applied this technique have typically isolated the effect of induced strain and discounted that of bending. In exposing the fiber to acoustic stress waves in water for example or wrapping the fiber around a piezo-electric device, the effects of bending can be neglected. The fiber is exposed exclusively to high frequency (40-50 KHz), low

amplitude stress. Ultimately, the reaction of the fiber is the same as that discussed in chapter two and defined by equation (2.11)

$$\Delta\varphi = L\Delta\beta + \beta\Delta L . \tag{3.1}$$

In the former case only one mode was considered to be present, hence only one $\beta$. However in a multimode fiber the various modes must be defined by their individual propagation constants, $\beta_i$, thus modifying equation (3.1) [9].

$$\begin{aligned} \varphi_i(t) &= \left[ \left( \frac{\partial \beta_i}{\partial P} \right) L + \beta_i \left( \frac{\partial L}{\partial P} \right) \right] P_o \sin \omega_m t \\ &= \varphi_i \sin \omega_m t \end{aligned} , \tag{3.2}$$

where $P_o$ is the applied pressure and $\omega_m$ is the vibration frequency. Here the individual modes are defined by $\beta_i$ and the phase change of each mode by $\varphi_i$. Since $\beta_i$ will vary among different modes so will the respective phase shifts $\varphi_i$. It is the *difference* between the phase shifts of seperate modes, $(\varphi_i - \varphi_j)$, which initiates the desired interference behaviour. Consider two modes propagating in the fiber

$$\begin{aligned} E_1 &= E_1(r, \theta) \exp[i(\beta_1 z - \omega t) + i\psi_1] \\ E_2 &= E_2(r, \theta) \exp[i(\beta_2 z - \omega t) + i\psi_2] \end{aligned} , \tag{3.3}$$

with similar equations for the $H$ components. Here $\omega$ is the optical angular frequency, $\beta_1$ and $\beta_2$ the propagation constants of each mode and $\psi_1$ and $\psi_2$ the initial phase components of the modes. Exposing the fiber to a time-dependent stress induces the phase shift of equation (3.2) in each mode. We may write for a generalized phase shifted field component

$$A_i(r, \theta, t) = A(r, \theta) \exp i [\, \beta_i z - \omega t + \psi_i + \varphi_i \sin \omega_m t \,] . \tag{3.4}$$

We wish to determine the intensity at $z = L$ of the two modes, $i = 1, 2$, defined in equation (3.3). This is given by the time average of the real part of the complex Poynting vector obtained from the sum of the two modes

$$\overline{S} = (\overline{E}_1 + \overline{E}_2) \times (\overline{H}_1 + \overline{H}_2).$$

For small phase differences

$$\Delta\varphi = \varphi_1 - \varphi_2 < < 1,$$

the intensity at $z = L$ can be reduced to an equation resembling

$$I(r, \theta, t) = I_o(r, \theta) + I_1(r, \theta)[\cos(\Delta\psi + L\Delta\beta) - \Delta\varphi \sin(\Delta\psi + L\Delta\beta) \sin \omega_m t], \tag{3.5}$$

where $\Delta\psi = \psi_1 - \psi_2$ and $\Delta\beta = \beta_1 - \beta_2$. Hence the intensity is effectively modulated at the frequency of $P$ with an amplitude modulation index of $\Delta\varphi$ (the cos and sin terms can be forced to zero and one respectively) defined through equation (3.2) as

$$\Delta\varphi = \left[ (\beta_1 - \beta_2) \left(\frac{\partial L}{\partial P}\right) + L \frac{\partial}{\partial P}(\beta_1 - \beta_2) \right] P_o \sin \omega_m t. \tag{3.6}$$

To maximize sensor sensitivity $\Delta\varphi$ must be maximized, the maximum phase difference, $\Delta\varphi_{max}$, being limited by the range of $\beta$

$$n_2 k_o < \beta < n_1 k_o.$$

Then $\Delta\varphi_{max}$ is given by

$$\Delta\varphi_{max} = k_o \left[ (n_1 - n_2) \left(\frac{\partial L}{\partial P}\right) + L \frac{\partial}{\partial P}(n_1 - n_2) \right] P_o \sin \omega_m t. \tag{3.7}$$

In referring to Fig. 2 we see that choosing values of $\beta_1$ and $\beta_2$ to maximize $\Delta\varphi$ is tantamount to selecting modes in the fiber which have a large difference in $\beta$. In addition we would like a simple dependence of $I_o$ and $I_1$ in equation (3.5) on $r$ and $\theta$ and the phase of these terms invariant with respect to $\theta$. This limits the choice of waveguide modes to the family of $HE_{1m}$ modes or the $HE_{11}$ and $TM_{01}$ mode combinations in calculating the resulting intensities at the fiber end face. The intensity and phase relations are shown in Fig. 4 for the interference between the $HE_{11}$ and $TM_{01}$

modes. Curve *a* of Fig. 4a shows the resultant intensity due to the combination of the constituent modes. Also shown is the phase of the intensity as a function of position across the face of the fiber. To detect the modulated intensity an equiphase portion of the intensity pattern (the side lobe in Fig. 4a for example) would be spatially filtered and monitored. Experiments have shown this technique to be about 30 dB lower [9] in sensitivity than the single mode Mach-Zehnder technique. This is due to the limited amount of phase difference achievable between lower order modes.

A second approach has been developed by Kingsley [10] to describe the two mode single fiber sensor. Though Kingsley's method arrives at a result similar to that of Bucaro it also predicts several other effects which have a definite impact upon the sensor's performance. Consider the simple model of the two mode sensor shown in Fig. 5. The amplitude modulation effects of bending are again disregarded, a reasonable assumption considering the application of this sensor (acoustic wave and low amplitude stress detection). Assume an equal excitation of the two modes in the fiber represented by the two paths of Fig. 5. As in the former analysis, each mode will experience different phase shifts defined as $\varphi_1$ and $\varphi_2$. In addition consider a group delay $\tau$ in one mode of the fiber due to dispersion and a phase term $\psi$ introduced by the carrier (laser). Now, if the fiber is again perturbed by a sinusoidal isotropic pressure field $\sin \omega_m t$ a phase modulation is introduced into the carrier signal. The phase-modulated fields in each mode may be written [10]

$$\begin{aligned} &\frac{1}{2}E_c \sin[\, \omega_c t + \varphi_1 \sin \omega_m t \,] \\ &\frac{1}{2}E_c \sin[\, \omega_c t + \varphi_2 \sin \omega_m (t - \tau) + \psi \,] \end{aligned} \tag{3.8}$$

These two fields combine to give the composite electric field in the fiber. Assuming negligible dispersion ($\tau \cong 0$) this field may be written as

$$E_c \sin\left\{ \omega_c t + \frac{1}{2}[(\varphi_1 + \varphi_2) \sin \omega_m t + \psi \,]\right\} \cos \frac{1}{2}[\, (\varphi_1 - \varphi_2) \sin \omega_m t - \psi \,]. \tag{3.9}$$

The first term is a phase modulated carrier with a modulation index $\frac{1}{2}(\varphi_1 + \varphi_2)$ while the second term represents an amplitude modulation. Square-law detection of the signal at the photodetector will result in demodulation of the AM component and is given by

$$i(t) = \cos^2\frac{1}{2}[\,(\varphi_1 - \varphi_2)\sin\omega_m t - \psi\,]\,. \tag{3.10}$$

Expanding the $\cos^2$ term this equation can be written as

$$i(t) = \frac{1}{2}\{\,1 + \cos[\,(\varphi_1 - \varphi_2)\sin\omega_m t\,]\cos\varphi + \sin[\,(\varphi_1 - \varphi_2)\sin\omega_m t\,]\sin\varphi\,\}\,.$$

This equation may now be expanded in terms of Bessel functions to give the result

$$\begin{aligned} i(t) = \frac{1}{2}[\,1 &+ J_o(\varphi_1 - \varphi_2)\cos\psi \\ &+ 2J_1(\varphi_1 - \varphi_2)\sin\psi\sin\omega_m t \\ &+ 2J_2(\varphi_1 - \varphi_2)\cos\psi\cos 2\omega_m t + \cdots\,] \end{aligned} \tag{3.11}$$

The second term of this equation is proportional to the modulation signal $\sin\omega_m t$. To recover an undistorted version of this signal we require $\cos\psi = 0$ and $(\varphi_1 - \varphi_2) << 1$. If one considers the very special case of carrier phase $\psi = \pm\,\pi/2$ and small $(\varphi_1 - \varphi_2)$ then

$$i(t) = \pm\,\frac{1}{2}(\varphi_1 - \varphi_2)\sin\omega_m t \tag{3.12}$$

a result similar to that of Bucaro's. The sign ambiguity accounts for the phase ambiguity in $\psi$.

Unlike the previous analysis however, equation (3.11) predicts several additional effects. 1) Higher order harmonics of the modulating frequency $\omega_m$ now become possible. The random carrier phase ,$\psi$, of the laser cause these higher harmonics to surface in $i(t)$. 2) The effect of dispersion, assumed zero when deriving equation (3.9), tends to introduce a second phase to amplitude modulation conversion mechanism which could interfere with the primary differential phase mechanism of equation (3.12). 3) Random polarizations of the different modes caused by the strain induced birefringence in the fiber may result in destructive interference between the modes. 4) The detection scheme assumed that radiation patterns of the two modes mixed and interfered at the detector. This may or may not be the case and is dependent upon various factors such as the launching of the light into the fiber and the transmission properties of the fiber endface.

Finally, phase to amplitude modulation may occur in the fiber endface reflections which have made multiple transits of the fiber [10,11]. These modes, which have already experienced phase modulation on their first pass through the fiber, will undergo additional phase changes on their multiple transits and interfere with the single pass signal. Kingsley refers to this phenomenon as optical homodyning and has observed its effects experimentally. We can write the field equations for the multiple transit signal by accounting for the additional phase change and the reflections at the fiber endfaces. The first echo will experience a phase change of $3\varphi_1$ and two reflections, one at each end, characterized by the amplitude reflection coefficients $r_1$ and $r_2$

$$\frac{1}{2}E_c\sqrt{r_1 r_2 10^{-2\alpha L}}\ \sin[\ \omega_c t + 3\varphi_1 \sin \omega_m t + \psi\ ]\,. \tag{3.13}$$

Here the attenuation of the additional passes has been included. Assuming the propagation time is much smaller than the modulation period, $2\pi/\omega_m$, we can ignore any phase difference between the single and triple transit signals. Treating this signal similar to that of equation (3.9) the expansion in terms of Bessel functions yields

$$\begin{aligned} i(t) = \frac{1}{2}\sqrt{r_1 r_2 10^{-2\alpha L}}\,[\ 1 &+ J_o(2\varphi_1)\cos\psi \\ &+ 2J_1(2\varphi_1)\sin\psi\sin\omega_m t \\ &+ 2J_2(2\varphi_1)\cos\psi\sin 2\omega_m t + \cdots\ ]\,. \end{aligned} \tag{3.14}$$

This equation is similar to equation (3.11) except for its amplitude terms. However, where equation (3.11) represented the sensor signal, equation (3.14) represents an undesirable interference term. In its multiple transitions over the fiber this signal interferes or homodynes with the phase modulated field described by equation (3.9) disturbing the baseband signal $i(t)$. Circumstances may arise where this interference mechanism combines with other detrimental effects to severely disrupt the sensor performance. Typically this problem is resolved by using an index matching fluid between the fiber and detector.

This approach demonstrates several key elements relating to the performance of the single fiber sensor. The appearance of harmonics in the detected signal caused by the random source phase $\psi$

added a degree of ambiguity to the frequency spectrum of the detected modulating signal. Dispersion of the modes adds a second phase to amplitude modulation conversion mechanism which may interfere with that of the differential phase mechanism. This model considered only two modes in the fiber. Realistically this cannot occur since each mode may have two possible polarizations. Strain will effect each polarization through the change in refractive index disturbing the predicted amplitude modulation. We also assumed the modes would mix at the detector generating the modulation, a condition which cannot be guaranteed. And finally the generation of multiple transit signals in the fiber by end face reflections added another source of potential interference with the desired signal.

Several workers have investigated this sensor experimentally and have observed behaviour indicative of these anomolous effects. The majority of these experiments have focused on the detection of very small amplitude, high frequency stress. The remainder of this paper will deal with the application of this technique to the detection of structural vibrations; excitations large in amplitude and much lower in frequency relative to these previous applications. Experimental results will be compared to determine if similar effects are present in the two applications. This method will hereinafter be referred to as modal domain sensing.

# 4.0 The Modal Domain Sensor

With the operation of the single fiber modal domain sensor outlined its use in vibration sensing can now be discussed. The applications considered in this paper concern the detection of vibrations induced in straight beams and beam-like structures (strings) excited through some initial displacement. Excitations and boundary conditions were selected which would generate simple periodic vibrations easily described in terms of their frequency components and structural equations of motion. The theoretical treatment of the actual structures is considered in the appendices. The previous section showed that a fiber subjected to stress experiences a refractive index change and a subsequent phase shift of the fiber modes. This phase difference between the modes was found to be responsible for the detected amplitude modulation of the light. Demonstrations of this effect have primarily focused on exposing the fiber to very small amplitude, high frequency strains; those that can be induced either through an acoustic interaction or through directly coupling the fiber to a source of time varying stress - a piezoelectric (PZT) cylinder for example [12,13]. The impetus for subjecting the fiber to these limited sources of stress is of course their inherent controlability. Time-varying acoustic pressure waves and PZT responses are very consistent and model the theoretical assumption of sinusoidal stress fairly closely. The types of excitations studied in these investigations, however, are not typical of those experienced in structural vibrations. Structural vibration, although often very periodic, is characterized by frequencies much lower (1-300 Hz) and

by displacements much greater than those generated piezoelectrically. In addition, complex structural vibrations are composed of several constituent frequencies whereas PZT excitations can be tuned to a dominant resonant frequency. Nevertheless, the structure still has the ability to induce strain in the fiber giving rise to the same reactions as those considered in chapters 2 and 3. Referring to the appendices we see that beam vibrations are described in terms of a superposition of specific mode shapes, determined from the boundary conditions at the beam ends, and vibrational frequencies whose magnitudes depend upon the initial excitation. If we expect the structure to initiate strain in the fiber we may also expect that the resultant time-dependent strain is a superposition of the frequency components of the structure itself. In other words, the vibrational frequencies which combine to describe the structure's motion induce a time-dependent strain which is a superposition of those same frequencies. Referring to equation (3.2), this sinusoidal stress now becomes a superposition of stresses whose frequencies are those of the vibrating structure. Through the mechanisms described in the previous chapter this will result in a modulation of the sensor signal which can be demodulated to give the vibrational frequency components of the structure itself. This defines the workings of the modal domain sensor in vibration detection.

A principle difference between structural and PZT excitation arises due to the increased presence of fiber bending. Where previously, the bending stress amplitude was small enough to ignore, structural vibrations may involve large flexural amplitudes which couple to the fiber creating mode loss. This periodic fiber bending results in an amplitude modulation of the light signal which coexists with that produced by strain induced phase modulation. In chapter two it was shown that bend loss is a strong function of the fiber bend radius: small radii result in a large loss. It is then a question of the structural dimensions and the type of vibration which determines the amount of bend loss present. For example, a very long beam with few higher order frequency components, would inflict little small radius bending in a fiber. Thus bend loss would have a negligible effect on the sensor in this case. A small structure, however, or a structure with substantial higher frequency components would induce small bending radii causing bend loss modulation. Bending-induced amplitude modulation has been observed in low-moded multi-mode fibers [14]. Fibers with small radius bends (4 cm) were mechanically vibrated in a region local to the bending at amplitudes small

(0.39D) compared to the fiber diameter D. Vibrations ranging from 150 Hz to 1500 Hz were excited at the bend and amplitude modulation of the light at the resonant frequencies of the fiber section was observed. A modulation index on the order of five percent was measured. However the conditions under which bend loss was observed were made ideal through small bending radius and preferred excitation of higher order waveguide modes at the fiber input. Increased bend radius and enhanced excitation of the $HE_{11}$ mode reduced bend loss modulation significantly. Losses on the order of the fiber attenuation were observed in single mode fibers at a bending radius of about ten centimeters [15]. The degree then, to which bend loss has an effect upon the sensor's behaviour will be determined by the characteristics of the particular vibration system. Smaller structures with large vibration amplitude or large structures with appreciable higher mode content could initiate bending of small enough radius to result in bend loss modulation.

Fig. 6 shows the modal domain sensing system. Each section of the system will be discussed with the exception of the signal processing which will be addressed in the next chapter. The most vital component is of course the optical fiber itself. The fiber chosen for these experiments was single mode at a wavelength of 850 nm. The source was a linearly polarized helium-neon laser (633 nm wavelength). From the manufacturers specifications of core radius ($a$ = 4 μm) we may compute the $V$ number from equations (2.1) and (2.9) and a measured value of the $NA$. The $NA$ was found to be approximately 0.097 for this fiber giving a $V$ of 3.88. This gives a total of seven modes propagating in the fiber [16], each with two possible polarization states. This is only an approximate calculation based on nominal values of the fiber pararmeters and should not be used to establish a theoretical prediction of the sensor behaviour. However it does give an indication that we are dealing with a low-moded fiber as required by the theory of chapter three. Light was launched into the fiber using a 0.1 $NA$ microscope objective which provided good matching to the fiber $NA$. The distance from the lens to the fiber end was adjusted to give a maximum fiber output intensity. This distance was found to be about 3.5 cm. The fiber was positioned using a standard adjustable fiber mount to again give maximum DC output intensity. No consideration was given to what possible modes were being excited in the fiber; output intensity was the only criterion.

The output pattern of this fiber is illustrated in Fig. 7. This pattern results from the interference of the phase shifted propagating modes in the fiber diffracted at the fiber endface. This three lobe structure with variations on the shapes and positions of the three lobes was typical of the fiber output throughout the experiment and is indicative of a low moded fiber output. As the fiber is perturbed this diffraction pattern exhibits two effects: 1) a change in intensity of the lobes and 2) a physical movement of the observed pattern. The first effect is caused by bend loss modulation and more predominately by phase-to-amplitude modulation conversion. The second effect is the result of the phase changes in the modes causing an effective rotational movement of the intensity pattern in the far field of the fiber. In chapter three the intensity pattern at the fiber end face was calculated. It was suggested [9] that a single phase modulated intensity lobe could be spatially filtered and demodulated to obtain the perturbation signal. However the effects of diffraction at the fiber end face for a fiber propagating seven modes will most likely distort this intensity pattern giving a *transmitted* pattern which is entirely different in the far field. Even if one could reasonably predict a field intensity distribution at the fiber end due to several fiber modes the effects of diffraction at the boundary must be described to predict the projected fiber output. Stated differently, which of the projected lobes are carrying the desired amplitude modulation? This question was resolved somewhat arbitrarily by selecting a lobe which when demodulated gave a strong amplitude modulation in the detector signal. As will be seen, this method faired reasonably well if only for the lack of a better method. The selected lobe was spatially filtered using a small square aperture, approximately 2 mm by 2 mm in dimension, placed a distance from the fiber such that the aperture was completely covered by the selected lobe. The detector (refer to Fig. 6) was placed a distance beyond the filter such that the square illuminated image of the aperture covered the detector surface area. Aperture distance from the fiber had little relation to the sensor signal other than a decreased amplitude due to a diminished DC level. The detector was a standard PIN photodiode with suitable speed and bandwidth for these measurements. Diode signals were amplified 10 dB using a simple 741 op-amp based inverting amplifier. Processing of the sensor output will be discussed in the following chapter.

Finally, the perturbation region of the sensor will be addressed. This is the segment of the sensor system in which the actual detection of the vibration takes place. The fiber must first be

coupled by some means to the structure in a manner which will not perturb its motion but at the same time will allow the sensor to faithfully follow the structure's movement. Ultimately we are trying to convert the motion of the structure into a resultant strain and bending of the fiber. As the fiber experiences the flexural bending movement of the structure, like the structure itself, the fiber will experience tension and compression along its length. This tension and compression will work to impart a strain in the fiber. A second mechanism of strain coupling can be realized if the fiber is adhesively bonded to the structure's surface. The local tension and compression at the surface are then coupled to the fiber as a direct longitudinal strain component. In each of these mechanisms the amplitude of the vibration and bending curvature will determine the level of induced strain. Previous experiments [12,13] have demonstrated that very small stress amplitudes (on the order of what can be generated piezoelectrically) are detectable using this single fiber modal domain technique. Hence we would expect very good dynamic range in the detection of structural vibrations if strong strain coupling can be achieved. This is demonstrated in the following experiments where varying amplitudes are excited in an effort to determine minimum sensor responses. The sensor's frequency response will also be addressed. There is some question as to whether the low frequency oscillations inherent in structures can be monitored with fidelity in the presence of noise sources, temperature for example. The following experiments show, for the cases considered, the sensor responds well at all frequency ranges. It is also important that movement in the fiber be isolated to the area of the perturbation region. Any fiber movement outside of this region will be responsible for unwanted perturbations which are not relavent to the actual structural vibration. This poses a problem in cases where one end of the beam is not secured preventing excess fiber movement. In the study of the free-free beam for example, since the beam ends were not constrained, the fiber had to be connected to the beam in a way that would prohibit excess fiber movement. This will be considered in the next chapter where the coupling of the fiber to the structures is considered.

The following chapter will describe the application of this sensor to several simple vibrational systems. Since each system required a slight modification of the sensor application (how the fiber was coupled to the structure, the recording of the sensor signal) the individual configuration of each

experiment will also be addressed. After discussing these procedures, chapter six will present an analysis of the results and observations.

# 5.0 Experiments

The modal domain sensor will be applied to three simple mechanical vibration systems: the linear stretched string, the clamped-free (CF) beam and the free-free (FF) beam. The theoretical analyses of each of these structures can be found in the appendices. We saw in the previous chapter how the single fiber sensor analysis of chapter three could be addressed in speculating the sensor's reaction to structural vibration. These speculations will now be investigated through the above mechanical systems.

We wish to demonstrate the sensors ability to respond to structural frequency components and evaluate its actual frequency response and dynamic range. This will be done by exposing the sensor to a range of vibrational frequencies and amplitudes and by comparing the frequency spectra of the demodulated sensor signal with the calculated frequency components of the structure. The system described in chapter four represents what may be considered the vibration sensor. The output of this sensor "unit" is the modulated photodetector signal which carries the actual vibration information. Although the application of this unit to a particular structure differs with the structure's geometry, the processing of the output is the same regardless. The general procedure used in investigating structural behaviour with this sensor and a description of its application to the proposed vibrational systems will be the subject of this chapter.

The coupling of the fiber to the structure, again, depended largely on the geometry and will be discussed individualy for each structure considered. For now it is only necessary to keep in mind the ideas of in chapter four (strong strain coupling). With the fiber coupled to the beam, light was launched into the fiber and adjusted to give a maximum DC output intensity. Now the output pattern of the fiber was observed in the far field simply by holding a screen (an index card) at some distance from the fiber end. The lobe pattern referred to in chapter four was identified and a lobe selected for spatial filtering. It was sometimes necessary to physically bend or somehow stress the fiber in order to achieve a desireable lobe structure which had strong amplitude modulation. Experiments showed the more distinct and symmetric the interference pattern the cleaner the time domain signal. To be more precise, the signal seemed to show better periodicity with less high frequency. The interference pattern was filtered and detected as described in chapter four. Lobes other than the strongest of the pattern were also investigated. Responses generated from these different interference patterns will be addressed later.

The sensor was now ready for operation. Controlled excitations of the structures were performed to initiate the vibrations. These excitations consisted of measured initial displacements which could be described theoretically to determine the structure's expected response. These excitations will also be discussed with the individual structures. Dynamic range information was obtained by measuring the physical displacements of the excitations and the subsequent sensor response. For each excitation the interference pattern and DC level of the filtered and detected lobe were recorded to determine if there was any correlation with the sensor signal. The lobe pattern would often undergo changes in its shape with the different structural excitations and it sometimes became necessary to realign the filter and detector or perturb the fiber in some way to maintain consistent detections of the lobe pattern.

The sensor signals were recorded on a Nicolet model 204-A digital oscilloscope. This device digitized the analog detector outputs for later digital signal processing. All waveforms were recorded using 2048 (2K) sampling points, this was the limit specified by the PC program which reads the digitized waveforms from the scope Since numerical fast Fourier transforms (FFT) were to be performed on the time domain waveforms the Nyquist sampling frequency of the digitizer had to

be considered. This was determined by the time per point setting of the oscilloscope. Sampling rates which gave Nyquist frequencies high enough to include the component frequencies of the structure had to be used. Thus a knowledge of the vibrational frequencies was required a priori to insure proper FFT bandwidths which offered sufficient resolution at lower frequencies where the majority of the vibration spectrum resided yet still included the higher structural modes. Generally a sampling rate was selected which would give an FFT bandwidth capable of including three to seven vibration modes depending on the structure and its predicted frequency spectrum, i.e. its excitation. If higher order modes were expected to be highly attenuated then fewer modes could be considered.

Triggering of the oscilloscope could usually be performed internally in the normal triggering mode. The level was simply set such that the scope triggered as the structure was released from its initial displacement. This worked well for the string and CF beam cases however an external trigger became necessary in the FF case and will be described along with that experiment. This oscilloscope also had a pretrigger option. The trigger could be delayed a preselected amount so that signal prior to the trigger could be observed. In this way the noise level could be directly compared with the signal level. Waveforms were recorded with a pretrigger of about 15 to 20 percent of the total sweep length. The vertical sensitivity was usually determined by the vibration amplitude or the detector signal level generated by the given lobe pattern. Signal levels ranged anywhere from 20 mV to 1 V throughout the experiments.

Once waveforms were recorded they were passed to an IBM PC for formatted disk storage. This was accomplished using a specialized IEEE 488 interface between the PC and oscilloscope. This interface was a hardware addition to the PC, programmable through BASIC to control data transfers with peripherals on the communications bus. The program transferred the 2K digitized waveform points from oscilloscope to PC memory and reproduced the waveform on the PC screen. It could also store the waveform points and additional waveform documentation on disk for eventual FFT analysis.

The final step of the procedure was to perform a frequency component analysis on the time domain sensor signals. This was accomplished using an FFT algorithm on the university's VM

computer system [17]. As described in chapter four, the frequency components of the analyzed structure should induce modulations in the sensor signal. These same frequencies should be present in the spectrum of the demodulated signal generated by the FFT routine. Digital waveform data stored on disk at the PC was uploaded to the VM system for signal processing and the generated frequency data plotted to give the frequency spectrums of the demodulated sensor signals. Again, the bandwidth of the FFT was determined by the sampling rate selected at the time the waveform was recorded. The FFT algorithm was modified to allow windowing of the time domain data. That part of the waveform which included the pretriggered signal (signal existing earlier than the actual vibration signal due to selected pretriggering) was discarded by setting these points to zero before performing the FFT. Also, the segment of the waveform just after excitation representing transients induced by the excitation itself, the plucking of the string for example, was removed. In this way only the steady state vibrations of the structure influenced the frequency spectrum of the demodulated sensor response. Generally either the first 512 or 1024 points of the (2K) point waveform were set to zero. Since it was still a 2K point FFT no resolution in the FFT was lost, only the unwanted frequency information. Windowing of course has no effect on the bandwidth of the FFT. It was also necessary to low pass filter the resulting FFT waveform. The high DC component of the signal reduced the vertical resolution of the FFT plots. This was rectified by filtering (setting to zero) the first few points of the FFT which carried the DC component.

This describes the general procedures used in the experiments for analyzing the sensors response to vibration. These methods were common to each vibration system studied. The specifics of each system will now be addressed individually.

## *5.1 The Vibrating String*

The first vibration system considered was the linear stretched string. This is the easiest vibrational system to describe, in its linear first order case, and its analysis is given in Appendix A.

String vibrations will account for frequencies ranging from 165 Hz to 390 Hz. Fig. 8 shows the laboratory system used in studying the vibrating string. An aluminum base mounted with grooved string supports, a tension scale calibrated in pounds and a tuning machine identical to that used on a guitar. The distance between mounts was set at 63.5 cm - a distance typical of the string length found on guitars. The string was a standard steel wound guitar string. The mass per unit length was measured as 0.004 g/cm with a diameter of 0.08 cm. The string was tuned to its prescribed frequency of 220 Hz corresponding to the note of A three half steps below middle C. The required tension was attained by comparing the audible tone of the string to a tuning fork oscillating at 220 Hz - much the same way a guitar would be tuned.

As discussed in chapter four the bonding of the fiber to the structure is critical in determining the level of induced strain. Since adhesively bonding the fiber would further perturb the string's natural motion, the fiber was simply wrapped around the string in a helical fashion fourteen to fifteen times and secured at the string's supports with tape. This also increased the length of the fiber (the sensor area) over the structure which should serve to increase sensitivity. It was necessary to keep the fiber tightly wrapped around the string as it vibrated since any slack in the fiber caused excess movement; the fiber would tend to loosely flap on the string if not held taut at each end. This could be seen in the sensor signal as a reduction in the periodicity and an increase in the higher frequency components. As the fiber was pulled tighter around the string the signal became much cleaner with a distinct periodic structure.

With the fiber satisfactorily coupled the string was now ready to be excited. There are two string excitations which are easily described theorotically: the plucked string and the struck string. The plucked string represents an initial displacement while the struck string represents an initial velocity imparted on the string. Since displacement is much simpler to characterize than initial velocity the plucked string was selected. Fig. 9 shows the device which was used to measure the string's initial displacement. The thin horizontal bar was placed under the string at some specific location along the string's length, its distance below the string adjusted with the micrometer. The string would simply be pressed down to the bar, usually with my fingernail, and released. There was enough damping in the string to prevent it from double striking the bar as it vibrated. The

trigger level of the oscilloscope was adjusted such that triggering was initiated as the string was released; no external triggering was necessary. When triggering occured the device would initiate one full sweep then capture the next. This option is referred to as the Hold Next storage mode. This also allowed some of the transient signal, introduced when the string was first released, to subside. Sampling rates of 100 μs or 50 μs per point were used to digitize the waveforms depending upon the fundamental frequency of the vibration. At 2K data points this gave a total sweep length of 200 ms (100 ms).

Several excitations were performed in order to generate a range of vibrating frequencies and amplitudes. As mentioned earlier, fundamental frequencies ranging from 165 Hz to 390 Hz were obtained by adjusting the string tension and length to achieve the desired frequency. String tension was adjusted with the tuning mechanism. Length was varied by placing a third grooved support under the string at a position calculated to give the desired frequency. The actual frequencies were then tuned by comparing the tones to those of a tuned guitar. A total of five frequencies were excited: 164.8, 196, 220, 293.6, and 392 Hz. At each of these frequencies the string was excited at two positions: a point mid-length on the string and a point close to the end (a distance of 5/6 of the total string length). In this way vibrations with different modal contents could be achieved; the end excitation induces more high order frequency components in the strings vibration. We could then determine if the sensor was responsive to an increase in higher modes by comparing the resopnses at the two excitations. Each of these frequencies were excited at only one initial displacement: 0.1 in (0.254 cm). To characterize the dynamic range, displacements ranging from 0.05 in to 0.5 cm were initiated. These were performed at mid-length and at two fundamental frequencies (164.8 and 220 Hz) to determine if the dynamic range varied with frequency.

## 5.2 *The Clamped-Free Beam*

The experimental considerations described for the string will now be applied to the second vibration system, the clamped-free (CF) or cantilever beam. This structure represents fundamental frequencies more than an order of magnitude below those seen in the string ( $\cong$ 6Hz) for the length and material considered. The theoretical description of the CF beam is given in Appendix B. Unlike the ideal string the CF beam does not possess harmonics which are integer multiples of the fundamental. Beam harmonics occur at non-linear multiples due to the nature of the characteristic eigenvalue equation describing the beam modes. Fig. 10 shows the CF beam used in the experiment. The actual beam was simply a steel hack saw blade measuring approximatly 30.5 x 1.3 x 0.064 cm. One end of the beam, about a 2.5 cm length, was clamped between aluminum blocks as shown in Fig. 10. This gave an active beam length of 28 cm. The fiber was ran onto the beam at its clamped end, ran up and back the top side of the beam and adhesively bonded with rubber cement to insure strong strain coupling.

The beam was excited in much the same way as the string, through an initial displacement. The beam end was displaced through some initial distance by pressing the beam tip downward, measured with the device used in the string experiment. Only one beam length was considered, hence only one beam frequency. However, this experiment now investigated the effect of the interference pattern on the sensor signal. The lobe pattern was varied by randomly bending and moving a section of the fiber which was not bonded to the structure. A short coil of excess fiber was left between the laser and the beam for this purpose. It was observed that by filtering different parts of various interference patterns, different time domain waveforms were obtained. This was somewhat disheartening since this implied an inate inconsistency with the sensor. This however was to be expected from the discussions of chapter four where it was concluded that an inherent ambiguity existed in the detection of the fiber output. Several signals were recorded for the various interference patterns and filter positions all performed at the same beam excitation of 0.635 cm displacement at the beam tip.

Dynamic range measurements were also performed on this structure. Displacements in the range of 0.005 cm to 2.50 cm were performed to demonstrate the sensors sensitivity. Response at amplitudes as low as 0.015 cm displacement were observed. The oscilloscope was again configured to trigger at the release of the structure in the Hold Next storage mode. A sampling period of either 5 ms or 1 ms per point was used in sampling the waveforms. These left sufficient bandwidth for the processing of several higher order modes.

## 5.3 *The Free-Free Beam*

The free-free (FF) beam is a beam structure which has no constraints at its ends, they are free to move. Appendix B considers the analysis of this structure also. How one may go about actually obtaining this structure is difficult to imagine, however in certain limits models may be assumed which give a reasonable approximation to a FF structure. A very long beam, suspended by thin wire like supports from above and connected at only a few points along the beams length can be considered to model a FF beam fairly closely [18]. The beam was to be excited by physically pulling it at its center in a pendulum fashion and then releasing. This would result in two motions of the beam: 1) the desired flexural vibration and 2) a pendulum motion. In order to insure that the flexural vibration and pendulum motion were uncoupled one final constraint had to be met: The pendulum frequency of the beam as it swings from the overhead support should be lower than the fundamental flexural vibration frequency of the beam itself. An order of magnitude difference is more than sufficient. Fig. 11 shows the model used in the experiment. The beam itself was a 610 cm length of cylindrical PVC drainpipe with an outer-diameter of 2.857 cm and an inner-diameter of 2.54 cm. The beam was suspended by three 150 cm lengths of thin nylon string spaced along the beam as shown. The pendulum frequency is given by

$$\frac{1}{2\pi}\sqrt{\frac{g}{l}} \ ,$$

where $l$ is the support length and $g$ the acceleration due to gravity giving a pendulum frequency of 0.4 Hz. From Appendix B the fundamental frequency of the beam is found to be 1.5 Hz. The factor of four between the two frequencies should be enough to insure isolation of the two motions. Since the plane of motion for the flexural vibrations was normal to the support strings the fiber was run up and back the length of the beam bonded to its *side*. This would assure maximum strain in the fiber as the beam was bending. Unlike the previous structures the FF beam had no supports at either end hence no way of connecting the fiber to the beam without allowing the excess fiber movement discussed in chapter four. This was overcome by running the fiber up and down the support string at one end of the beam, overhead and finally down to the laser and detector. An independent experiment showed that pendulum motion initiated little or no strain in the fiber sufficient to produce sensor output. Thus any signal produced should have been due exclusively to the flexural vibration. This turned out not to be entirely true since the beam movement induced a time varying longitudinal strain in the support strings which coupled to the fiber.

As described above, the beam was excited by pulling it back from its center in a pendulum fashion then releasing it to induce a flexural vibration. A small string was tied at the beams midpoint which was drawn and clamped as shown in Fig. 11. As the clamp was released the scope was externally triggered and the signal waveform captured. External triggering was much simpler since setting of the trigger level was difficult in this experiment. Two initial amplitudes were imparted corresponding to displacements of 13 and 25 cm from the equilibrium position.

Strong air currents in the room vibrated sections of the fiber not connected to the beam giving excessive higher frequency noise (relative to the beam frequencies). A low pass filter with a cutoff frequency of 30 Hz was placed at the detector output to reduce the noise component of the sensor signal. This cutoff is about 10 Hz above the sixth order frequency component of the beam vibration. Very little signal is expected above the fourth order mode (7.86 Hz) so the filter did not attenuate any meaningful signal. Dynamic range measurements were not done on this structure however the effects of varying interference patterns were studied. In fact, changing of the interference pattern between excitations became somewhat of a problem. Due to the longitudinal strain induced in the fiber at the support string and the eratic fiber movement caused by the gale force

winds in our laboratory the output lobe pattern changed regularly. This had a noticeable effect on the time domain waveforms between excitations and it was often necessary to perturb the fiber to generate a clean, distiguishable lobe pattern which would give a reasonable signal. Sampling periods of 5 ms per point were used for each waveform giving an FFT bandwidth of 100 Hz, well above the fourth and fifth order modes of the beam.

This describes the experiments which were performed in analyzing the sensor's response to vibrations. Observations and analyses were withheld until the following chapter where they will be presented for each structure. These independent observations will then be considered on a whole and conclusions concerning the sensors performance will be developed.

# 6.0 Observations and Analysis

The results of the preceeding experiments will be outlined and discussed. General observations common throughout the experiments will first be reviewed followed by results of the individual experiments. We will begin however with a brief review of previous work done by other investigators who have also studied the modal domain sensor. Results may then be compared for similarities in sensor behaviour between the different applications.

As mentioned earlier, previous investigators have traditionally subjected the sensor to either acoustic or PZT excitations. Kingsley wrapped the fiber around a cylindrical PZT device [12,10] operating at a resonance of 45 kHz while Bucaro [9] insonified a circular loop of fiber approximately 26 m in length and 5 cm in diameter with acoustic energy at 23.3 kHz in an ambient water medium. In each experiment the frequency structures of the photodetector signals were analyzed on a spectrum analyzer. The predicted phenomena of chapter three were observed in each case and will be reviewed here. The transducer frequency initiating the stress field was able to be demodualted and detected in the fiber signal. In addition, the multiple harmonics predicted by equation (3.11) were also visible in the spectrum of the demodulated sensor output. Sometimes odd fundamental harmonics would be augmented while even harmonics attenuated, or vice versa. This was due to the random carrier phase $\psi$ acting to cancell harmonics generated by the differential phase modulation of chapter three. At other times all harmonics were observable indicating a carrier phase of $\pi/4$ .

These effects were witnessed in the real time frequency spectrum as a slow fading of the harmonic components. The effects of the interference with the phase modulated triple transit reflection signal were also apparent. For cases where all of the harmonic components were attenuated a strong interference between differential and reflection phase modulation was assumed. Higher components in the frequency spectrum could be attributed to the demodulated reflection signals. The fading of these components was also caused by random carrier phase but was much more rapid due to the increased transit length of the reflection signal.

In studying the results of the vibration experiments we will be looking for much these same kinds of behaviour. Before addressing each vibration system individually, observations which were common to each experiment will first be discussed. Fig. 12 shows a time domain sensor response for the vibrating string. The type of periodic behaviour shown here was typical in practically all of the vibration measurements. The transient portion at the start of the waveform was caused by the initial release of the structure. This segment of the waveform was not included in the frequency analysis since only the steady state portion of the signal was of interest. The lobe structure shown in Fig. 7 was not constant throughout each experiment but rather varied with temperature, fiber movement and structural excitations. It was possible to achieve different lobe patterns by stressing or moving a portion of the fiber not on the structure. This was sometimes necessary to maintain consistency in the interference pattern over a series of measurements. This brings up the point made earlier that different lobe patterns tend to give varying sensor signals Even different areas of the same pattern would give differing responses. (We could compare signals generated from different patterns by displaying different portions of the oscilloscope memory.) However by returning to a particular lobe in a given pattern the original signal could be recovered within some phase variation. This observation indicates that each lobe is carrying a unique phase modulation; which lobe is correct, if any, is indeterminable. However an FFT analysis of the time domain signals from different lobes indicates that common frequency components exist throughout their signal spectrums. Only the magnitudes of these common frequencies vary. Figs. 22 and 23 for example show frequency spectrums of the FF vibrating beam obtained from lobe patterns that gave different time domain responses. We see that their spectrums exhibit similar frequency peaks but with dif-

ferent component magnitudes. This same behaviour was also observed in the other structures studied. Therefore, although the resulting interference patterns at the fiber output may carry differing amplitude modulations for a given vibration, the phase modulation responsible for the AM seems to be initiated by unique frequency components.

The DC level of the detector output from *different* interfernce lobes showed no correlation with the signal amplitude between the respective lobes. Higher output intensity was not necessarily indicative of strong amplitude modulation. High intensity lobes often gave modulation signals with much smaller amplitudes than lower intensity lobes. Light intensity *within a particular lobe* however did affect the signal amplitude. Diminishing the intensity, by moving the apperture further from the fiber output for example, reduced the modulation amplitude of the sensor output. Intuitively these observations seem reasonable since in comparing DC intensity we are really only comparing the relative carrier levels, not the degree of modulation in the different lobes. These observations will now be carried over and related to those made on the individual structures which will provide a more detailed characterization of the sensor's behaviour.

## *6.1 The Vibrating String*

Three of the five string excitations studied will be discussed in terms of their individual sensor responses. Discussing each of the six trials individualy would be redundant since similar behaviour was observed throughout the experiments. Therefore the results of these other excitations will simply be incorporated in the present discussions. The six excitations were performed at both mid-string and end-string locations and correspond to fundamental frequencies of 196, 294 and 392 Hz. Figs. 13 through 18 show the FFT frequency components for these six excitations respectively. Also listed are the theoretical Fourier series components as derived in Appendix A. The peaks of the spectrum marked by the circles represent expected frequency components while those marked by the boxes represent anomolous components. This convention will be adopted throughout all

of the discussions. Frequencies were determined by identifying the peaks in the actual FFT numerical data. The minimum and maximum resolution of all FFT's is 2.5 Hz and 0.05 Hz respectively and is given simply by the FFT bandwidth divided by 2000, the number of sample points. Figs. 13,15 and 17 represent spectrums of mid-string excitations for the corresponding fundamental frequency. Theory predicts that only odd harmonics of the fundamental should occur for this excitation. Although the expected odd harmonics are visible there are many anomolous components also produced. In Fig. 13 for example the fundamental 196 Hz and fifth order 587 Hz peaks can be seen but are accompanied by several other evenly spaced peaks as well. Inspection shows that the first visible peak of the spectrum is at a frequency equal to one half of the fundamental (97.6 Hz). The remaining anomolous components are located at odd multiples of this subharmonic (292 Hz, 483 Hz and 683 Hz). This same behaviour can also be seen in the other spectrums with the exception of Fig. 17 which does not contain a subharmonic. In Fig. 15 the subharmonic component is actually greater than the fundamental. For excitations near the string end (5/6 L) Figs. 14 and 18 show the expected increase in the higher frequency components characteristic of end excitation with harmonics occuring at the predicted integer multiples of the fundamental. Fig. 14 shows this very clearly but again the multiples of the fundamental subharmonic ($f_1/2$) are apparent. In Figs. 16 and 18 this subharmonic is again greater than the fundamental. So although these spectrums show the expected increase in higher order components they are still plagued by the existence of a $f_1/2$ subharmonic and its related multiples. The theoretical amplitudes of the harmonics are normalized to the experimental and theoretical fundamental components. We also see then that there is no absolute agreement between experimental and predicted amplitudes of the frequency commponents.

Some possible explanations for the observed sensor performance will now be discussed. To begin, we may consider the nature of the structure itself. We are assuming a first order, linear model of the strings behaviour. This is indeed an oversimplification since we are dealing with a massy bass string which in addition is loaded with the optical fiber. More than likely this is a nonlinear vibrational system. Nonlinear string analysis predicts the existence of additional vibrational frequencies not predicted by the ideal string model [19,20,21]. Other investigators have in fact detected

frequencies in vibrating strings microphonically at multiples of one half the expected fundamental [22]. The $f_1/2$ subharmonic however was not detected. The non-ideal end supports and the presence of the tension scale at the string end also contribute to non-linear perturabtions [23].

Though these deviations from ideal string behaviour are likely to have some effect upon the sensor response a good part of the anomolous behaviour must be attributed to the sensor itself. The same mechanisms described by other authors and discussed earlier can be applied here to account for these anomolies. Multiples of low order fundamental frequencies were predicted in chapter three and reported by these other investigators [12,13]. Random carrier phase is responsible for the variations in harmonic amplitudes hence their lack of agreement with predicted amplitude values as can be seen in Figs. 13-18. Coupling of phase modulated reflection signals to the $f_1/2$ harmonics could reenforce these components. The existence of the actual $f_1/2$ subharmonic is difficult to explain. The fact that more than two fiber modes exist may be responsible but this subharmonic was not observed in the other vibration systems. Thus it could be related to the fiber coupling or the higher frequencies of the string. It may be that the sensor is not responding at all to the fundamental frequencies but only to this subharmonic and higher modes are merely a result of carrier phase and reflection effects. However the increase in higher harmonics at the end string excitation shows the sensor is responsive to higher frequency vibration modes. Also, Fig. 17 shows no existence of this subharmonic at 392 Hz, the highest frequency studied. These observations lead us to believe that this subharmonic is an artifact of the sensors operation peculiar to this experiment; that the sensor is in fact detecting the expected frequencies but at the same time manufacturing these related anomolous components. The type of strain induced by the string simply seems to support this mechanism moreso than the other systems.

Response up to almost 400 Hz was demonstrated by the string without any modification of the sensor itself. The sensor showed good response at displacements as low as 0.05 cm however these very small displacements were accompanied by a strong increase in the subharmonic magnitude.

## 6.2 *The Clamped-Free Beam*

The clamped-free (CF) beam structure represented the simplest and most consistent of the three structures studied. Only one beam length was considered hence only one fundamental vibration frequency. Figs. 19 through 21 show the frequency spectrums for several beam excitations. Figs. 19 and 20 show spectrums resulting from two beam excititions of different initial displacements. The spectrum of Fig. 19 was generated by a 0.076 cm displacement while that of Fig. 20 by a 0.50 cm displacement. Both spectrums show frequencies at 6.8 Hz and 41 Hz with no other major peaks visible. These values are almost exactly equal to the predicted fundamental and second mode frequencies derived in Appendix B. Since the beam modes do not reside at integer multiples of the fundamental this second peak cannot be due to random carrier phase or modulation of reflected signals. These spectrums were also obtained from waveforms taken at two different times but with very similar lobe structures. Fig. 21 shows another spectrum generated by the same 0.5 cm displacement. The graph clearly shows the effects of reflected signal interference and carrier phase randomness. Each peak occurs at a multiple of the fundamental 6.8 Hz component. The increased amplitudes in the higher harmonics is problably due to strong constructive interference in the reflection signals. It is interesting to note that this waveform was obtained directly after that of Fig. 19, the only difference being the sampling period of the scope. This then clearly shows the influence of random interference between the modulated reflection signal and the differential phase modulated single transit signal with random carrier phase. Vibrations measured in other trials from different interference patterns and filtered lobes showed very similar behaviour. In these other cases the higher order harmonics were often attenuated but the lower second and third order harmonics of the fundamental at 13.2 Hz and 20 Hz were stronger, with the peak at 41 Hz still present. Thus the different interference patterns seem to contain the same frequency information but differing component magnitudes. Note that none of these spectrums exhibit the $f_1/2$ subharmonic seen previously as was the case in all of the CF frequency spectrums generated. Reasons for this are not clear but examining the differences between experiments may provide some insight. Perhaps the

different fiber coupling had some effect. The coupling in the CF beam experiment provided an ideal longitudinal stress in the fiber whereas the helical winding of the fiber around the string resulted in a more complicated stress field. The increased length of the fiber over the string may have been responsible however the subharmonic was not detected in the FF beam experiments. The exact sources of the anomolous subharmonic are difficult to determine from these broad studies. However, this experiment demonstrated the potential ability of the sensor to detect extremely small mechanical vibrations with excellent fidelity as indicated by the results shown in Figs. 19 and 20.

## 6.3 *The Free-Free Beam*

The final analysis to be considered is that of the free-free (FF) beam. The single excitation mechanism described in chapter five is responsible for the frequency spectrums of Figs. 22 through 24. These spectrums were generated from different displacement amplitudes and interference patterns. Maintaining a constant interference pattern was very difficult due to the strain induced in the fiber at the support string. Interference patterns with more symmetric three lobe structures seemed to give cleaner more periodic time domain waveforms. However FFTs again indicated the existence of common frequency components between the varying patterns despite their different time domain signals with only the magnitudes of the harmonics varying. Figs. 22 and 23 for example show similar frequency components but with differing relative magnitudes.

The predicted vibrational frequencies of this structure are at 1.5, 4.0, 7.86, and 13.05 Hz from Appendix B. Figs. 22, 23 and 24 all show strong fundamentals at 1.66 Hz just slightly greater than the predicted 1.5 Hz fundamental. There are several possible reasons for this slight discrepancy. The pendulum motion may not be totally isolated from the flexural motion resulting in a distortion of the frequency components of an ideal FF beam. The presence of damping in a structure acts to distort the expected undamped frequency components [24]. The apparent frequency differences may be due in part to the high degree of damping in this material. The third possibilty is the sus-

pected reliabilty of the nominal elastic constant and density values used in calculating the theoritical frequency modes.

Fig. 24 shows the presence of several fundamental harmonics at 3.3 Hz and 5.02 Hz. Like the CF beam, the FF beam posseses no frequency components at integer multiples of the fundamental. The components at 3.3 and 5.02 Hz represent second and third order multiples of the 1.66 Hz fundamental. The frequencies of 13.2 Hz and 15 Hz correspond to the eighth and ninth harmonics, all within the resolution of the FFT (0.05 Hz). The 8.8 Hz peak is at approximately the fifth harmonic. Other spectrums showed peaks at 10 Hz, the sixth harmonic, and 8.4 Hz the fifth harmonic. These harmonics are due to demodulation of the triple transit reflection signals. The increased magnitude at the higher orders, compared to the other experiments, is due to the increased fiber sensor length. Equation (3.14) tells us that the demodulated detector current contains harmonic multiples of the modulating frequency $\omega_m$ which are weighted by the Bessel functions $J_k(2\varphi_1)$, where $\varphi_1$ is the phase change in the reflected triple transit echo mode. Equation (3.2) then shows that an increase in fiber length serves to increase $\varphi_1$. This, coupled with the factor of 2, tends to increase the argument of $J_k$. By increasing the argument it may be that the weighting of the lower order Bessel functions is diminished while that of the higher order functions is increased due to the behaviour of the Bessel functions themselves. Hence higher order harmonics (5 throgh 9) can be of greater magnitude than the lower order harmonics (2 through 4). It appears that none of the predicted higher order modes of the actual beam vibration are present in the spectrums. All frequency structure above the 1.66 Hz fundamental is due to reflected mode demodulation. This is not all that surprising considering the structures material and the induced vibration. Higher order vibration modes will most likely be severely attenuated in this material and for the applied excitation. The subharmonics below 1.66 Hz do not exist at 0.83 Hz, one half of the fundamental, but rather at 0.488 Hz, close to the pendulum frequency of the swinging beam which problably accounts for this subharmonic.

The frequency spectrums shown for each of the structural systems studied have been discussed. In most circumstances the theoretical models together with the observations of other investigators could be applied to explain the behaviour of each system. The effects of random carrier phase and

triple transit reflection signals, described in (3.11) and (3.14), worked well to account for unexpected spectral components not indicative of the structures vibration. The observed behaviour was in fact very similar to that of the other investigators. The effects of amplitude modulation due to bend loss or polarization have not been addressed. It is believed that bend loss had a negligible effect due to the nature of the structures studied and the excitation of low order frequency modes. Polarization modulation was most likely present and responsible for some of the observed anomolous response. The major anomoly which could not be explained was the existence of the one half fundamental subharmonic. The fact that this anomally was peculiar to only the string structure leads to two possible conclusions: 1) the sensor is simply not capable of detecting structural vibrations at these frequencies or 2) the subharmonic and its resulting harmonic multiples are an artifact of the string-fiber coupling; the fiber is sensitized to a frequency exactly one half the fundamental frequency. Since the fiber responded favorably to end string excitations and the subharmonic is not always present (Fig. 17) we are led to believe that the sensor is in fact capable of responding to these high frequency vibrations.

The dynamic range and frequency response of the sensor have then been demonstrated. Responses to frequencies ranging from 1.6 to 392 Hz have been shown with no modification of the sensor itself. Beam vibrations at amplitudes as low as 0.015 cm have been analyzed in terms of their first and second vibrational modes. There still exists however this inate inconsistency with the sensor brought about by the predicted effects of carrier phase and mode reflection.

# 7.0 Conclusions

The operation of the modal domain vibration sensor has been demonstrated in several simple vibrational systems. Two apparent advantages are the sensors bandwidth and sensitivity. An inherent drawback of standard vibration detection devices is their rapid cost increase with high frequency bandwidth. This sensor showed consistent response in the frequency range of 1.5 to 400 Hz. By imparting very small but measurable excitations in the structures we were able to establish the sensors ability to respond to very low order vibration induced strain. Dynamic ranges on the order of 18 to 22 dB for the CF beam and string systems respectively were observed. The sensor itself represents a very simple system: a coherent source, a single fiber and a low bandwidth detector. The inherent advantages of ruggedness and immunity to external radiation can also be added. Finally, the sensor minimally impairs structural motion through loading, an advantage in monitoring small vibrations or lightweight structures.

Of course the sensor was not without its own drawbacks. It is true we were able to detect structural frequencies however the sensor introduced its own anomolous frequency information as well. The primary sources of these inherent anomolies were thought to be the effects of random carrier phase and multiple transit endface reflections. Endface reflections have been reduced by index matching the fiber to the source and detector, however the effect of carrier phase has no immediate solution. Additional problems may have been encountered with strain induced

polarization and potential bending induced amplitude modulation. Polarizations of the individual modes are changed due to strain induced birefringence. This will result in some level of amplitude modulation at the detector. Phase differences between the various amplitude modulations will provide a source of interference.

The sensor was exposed to vibrations with only one degree of freedom in order to provide simple, defineable vibration systems. However normal structural vibrations may consist of oscillations with multiple degrees of freedom. This will impart a much more complicated stress on the fiber with dimensional components that behave differently in time. The strain induced phase modulation will then be caused by the resultant of these complicated stress components. Resolving the frequency components of the resulting amplitude modulation into the $x,y,z$ component vibrational modes would problably prove to be impossible. A fiber sensitized specifically to strain in one direction would be a possible solution (polarization preserving fiber). This very problem may have been exhibited in the study of the vibrating string. The non-linearity of the string causes vibration to occur in not just one but two dimensions [19]. The string actually precesses in a circular fashion as it vibrates, with a precessional frequency much lower than the strings fundamental. Hence the string has equations of motion in *two* dimensions which are coupled in such a way as to produce the precessional motion. The movement of the string in two dimensions may be the source of the subharmonic and its multiples observed in the vibration spectrums.

The investigations performed here certainly established the potential of the modal domain sensor however further experimentation is necessary to genuinely quantify its behaviour. For example, the dynamic range of the sensor was demonstrated through various excitation amplitudes. Essentially what this qualifies is the strain in the fiber necessary to generate a recognizable response. A more quantitative approach to dynamic range would be to specify this actual strain. It may be that the sensor has a limited range of linearity. Perhaps large non-linear strains are induced in structural vibrations and the assumed linear model [8] is not valid. Response at large frequencies was demonstrated but in a structure with questionable characteristics (the string). Structures with better experimental integrity (beams) could be forced to vibrate at higher frequencies helping to establish the sensors ability to detect higher order modes. The behaviour of the fiber modes could

also be further addressed. A fiber with fewer modes or preferred excitation of different modes in the fiber studied here may prove useful. Polarization modulation in single mode fibers has been studied by several others in acoustic stress wave detection [31]. This may provide an entirely different approach to vibration sensing. I believe the performance of the modal domain sensor demonstrated in these experiments warrants these further investigations.

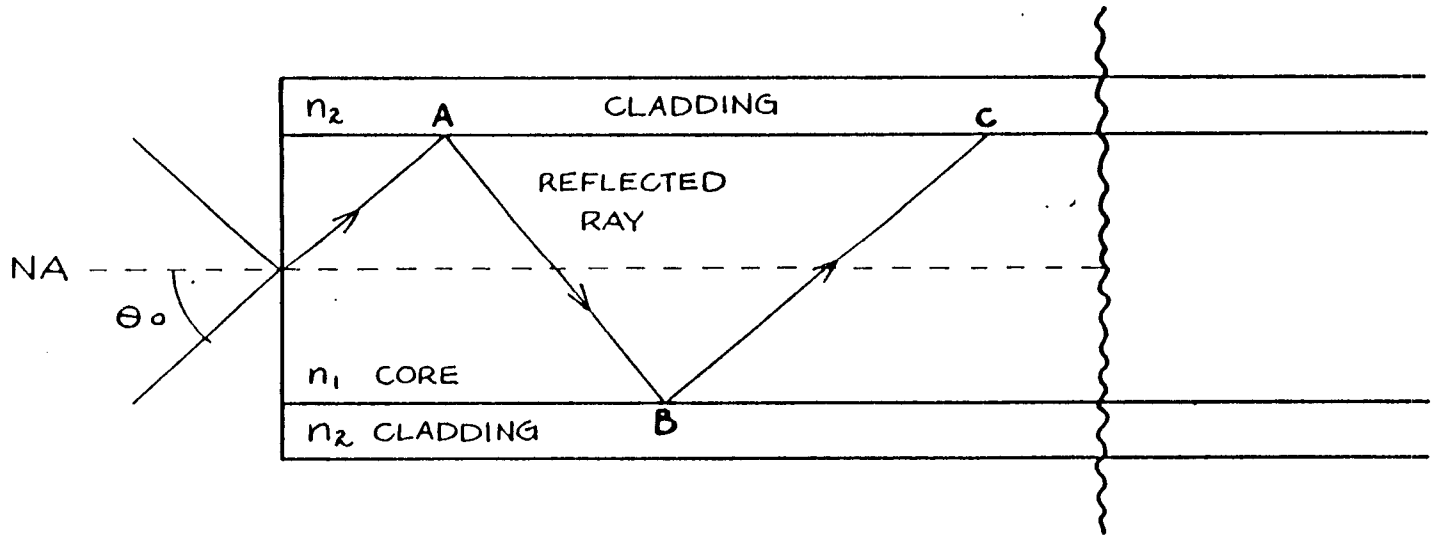


Figure 1. Step-index optical fiber with reflected ray path.

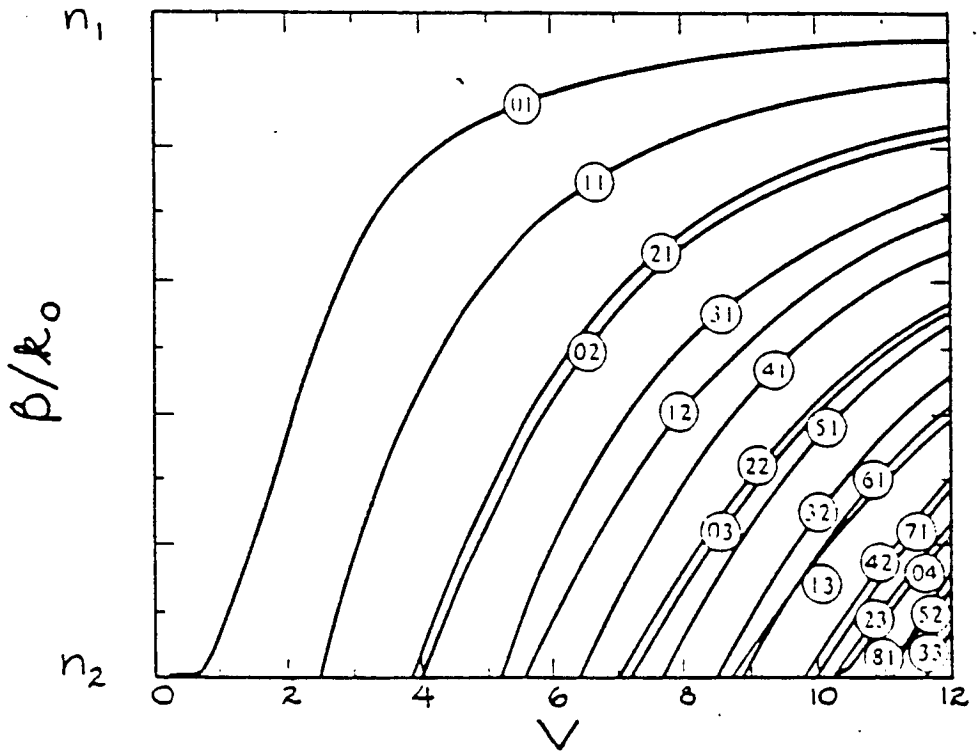


Figure 2. V number vs. normalized propagation constant.: [2]

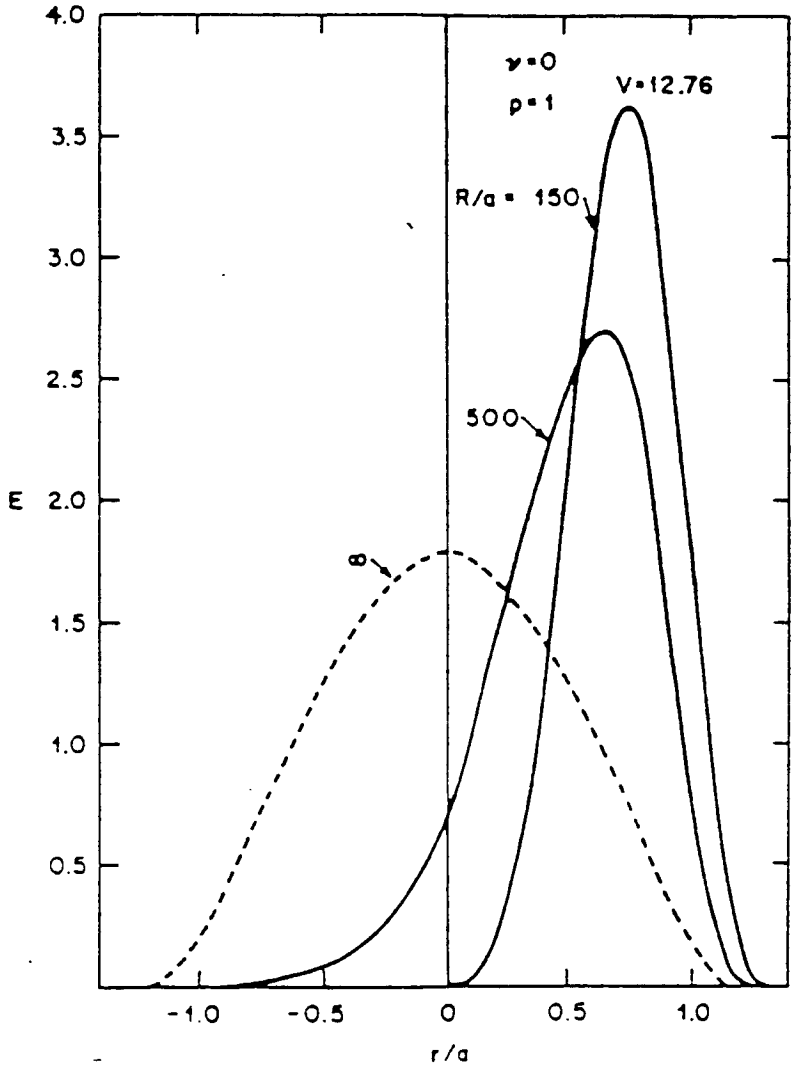


Figure 3. E field distribution due to fiber bending for the $HE_{11}$ mode: [5]

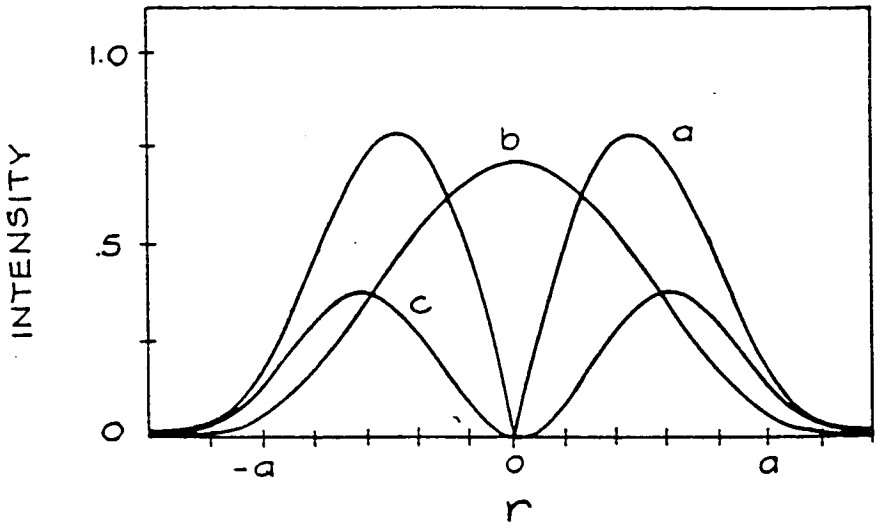


a.

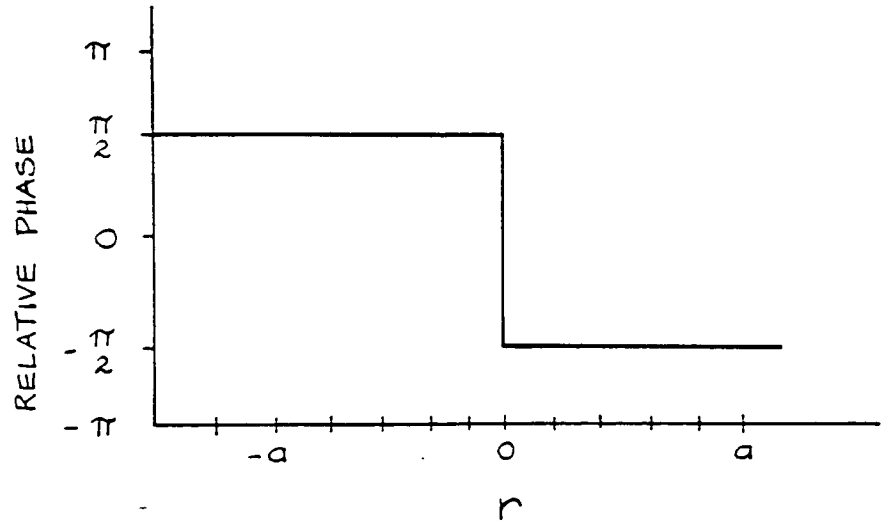


b.

Figure 4. Calculated $HE_{11}$ and $TM_{01}$ mode intensities and phase at fiber endface: (a) magnitude of interference term; (b) $HE_{11}$ mode intensity; (c) $TM_{01}$ mode intensity [9]

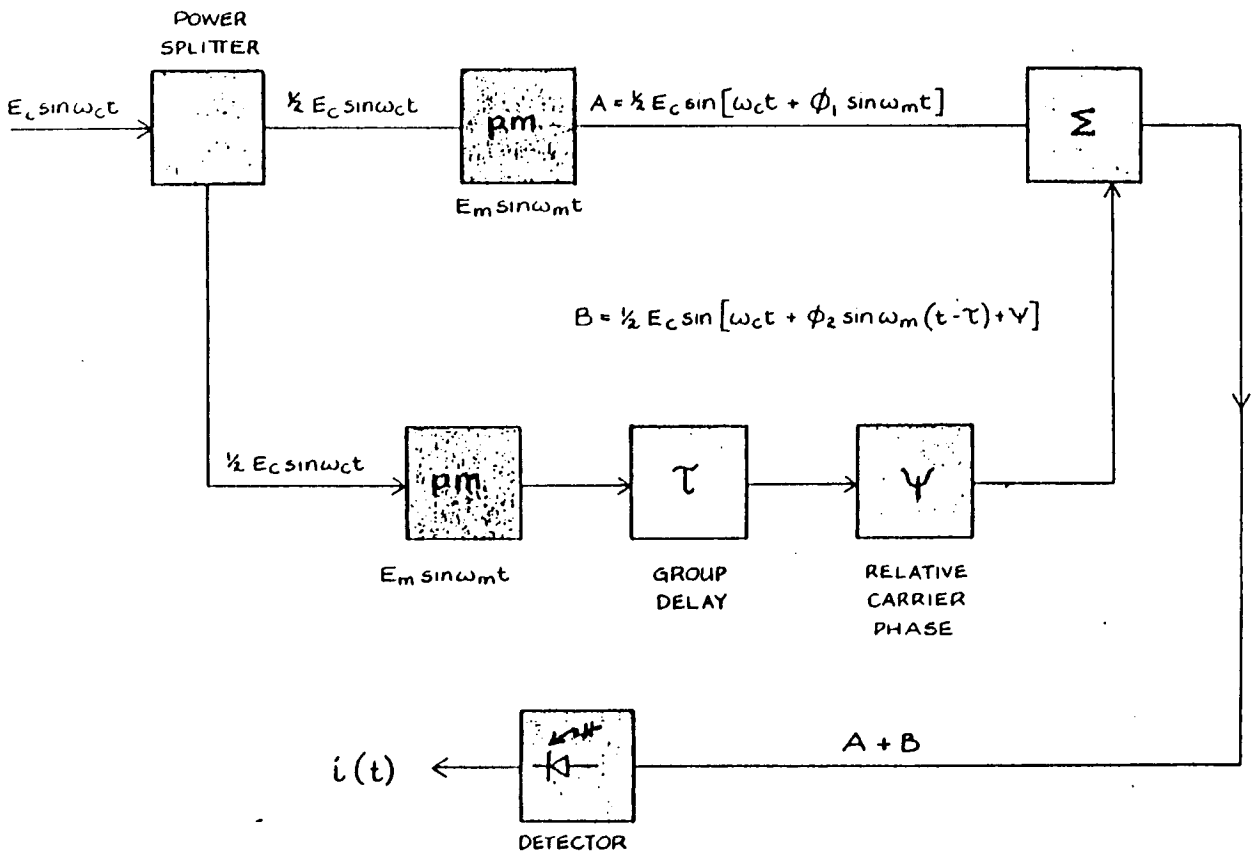


Figure 5. Differential phase model of two-mode optical fiber: [10]

ORIGINAL PAGE IS
OF POOR QUALITY

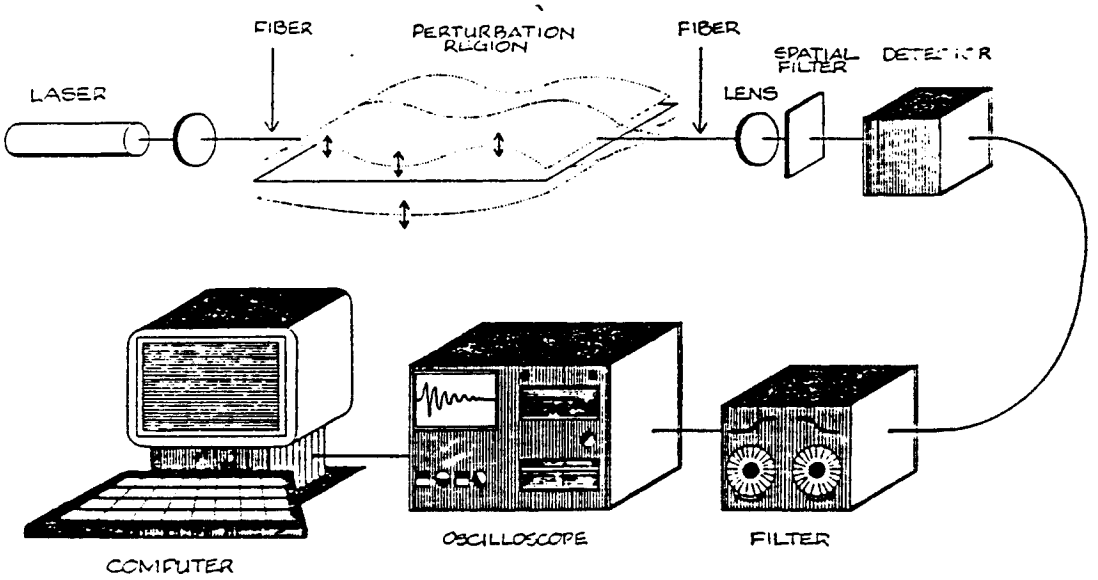


Figure 6. Modal Domain Sensor system.

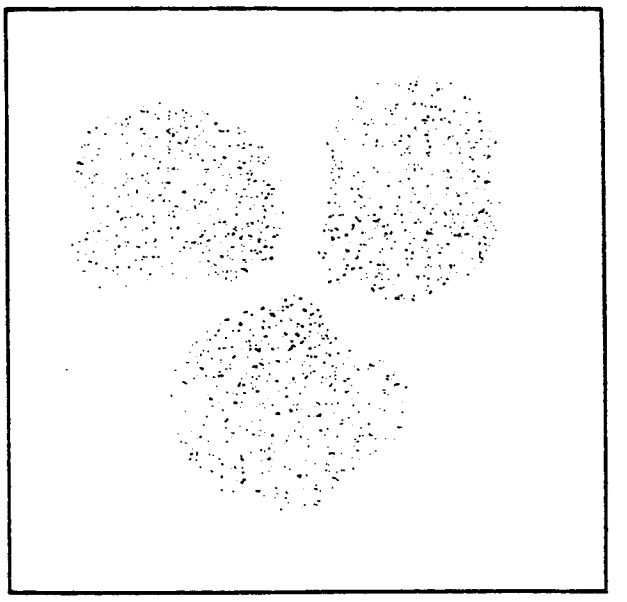

Figure 7. Output interference pattern of 850 nm fiber with 633 nm laser

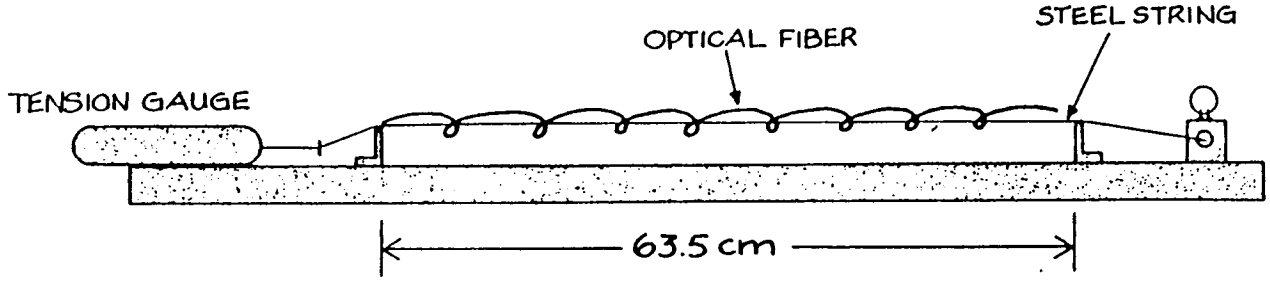


Figure 8. Vibrating string experimental setup.

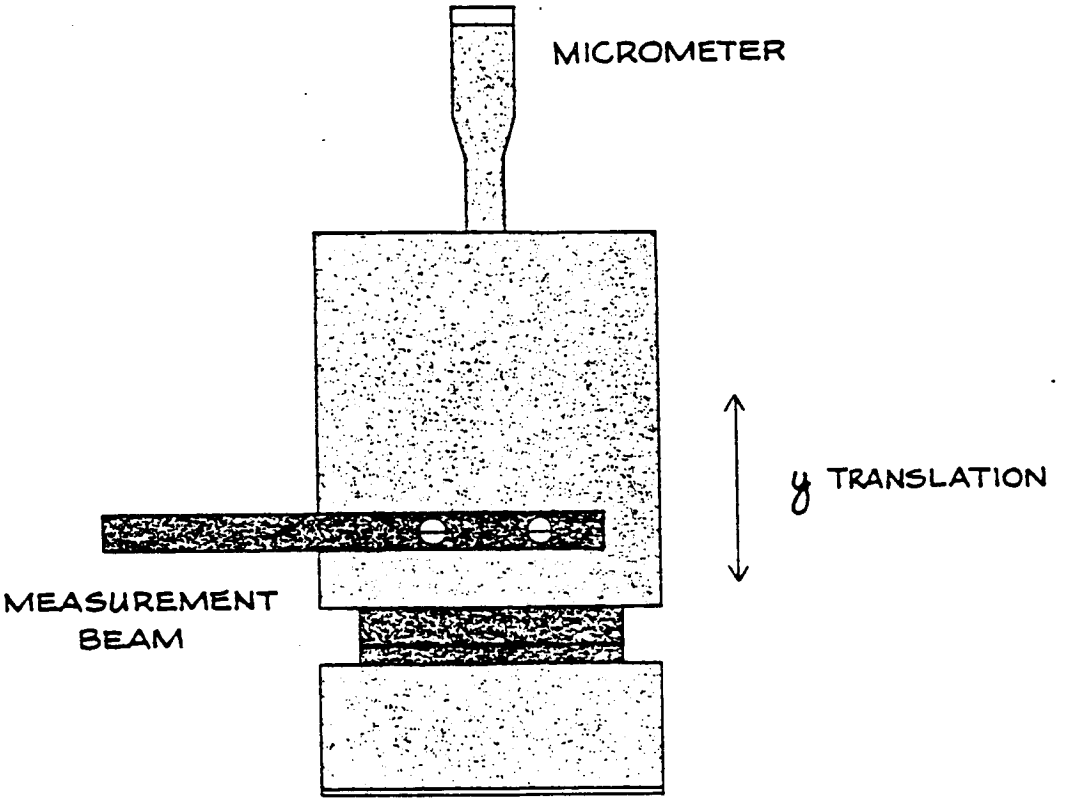


Figure 9. Inital displacement measurement device used in string and CF beam experiments.

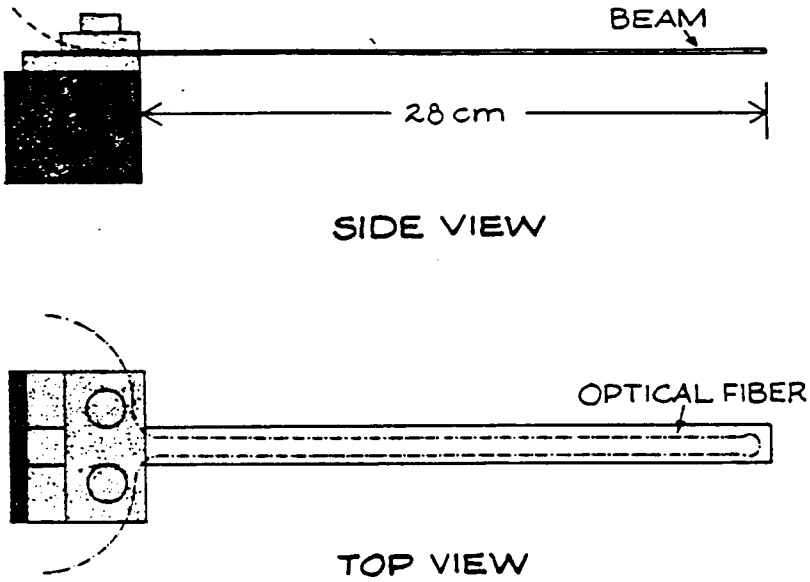


Figure 10. Clamped-free beam experimental setup showing coupling of fiber to structure.

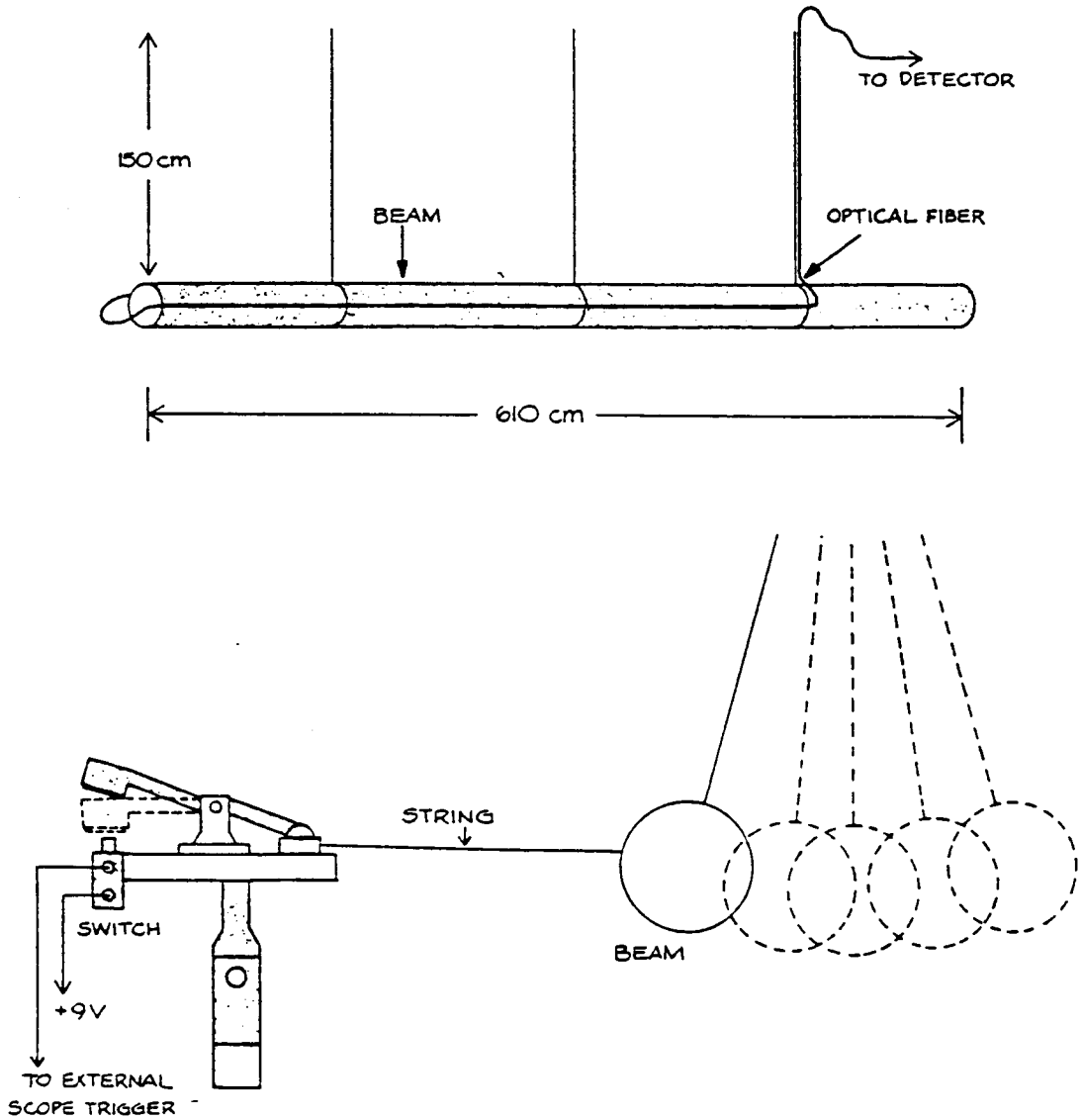


Figure 11. Free-free beam experiment: (a) laboratory beam model; (b) pendulum displacement of beam showing scope triggering system.

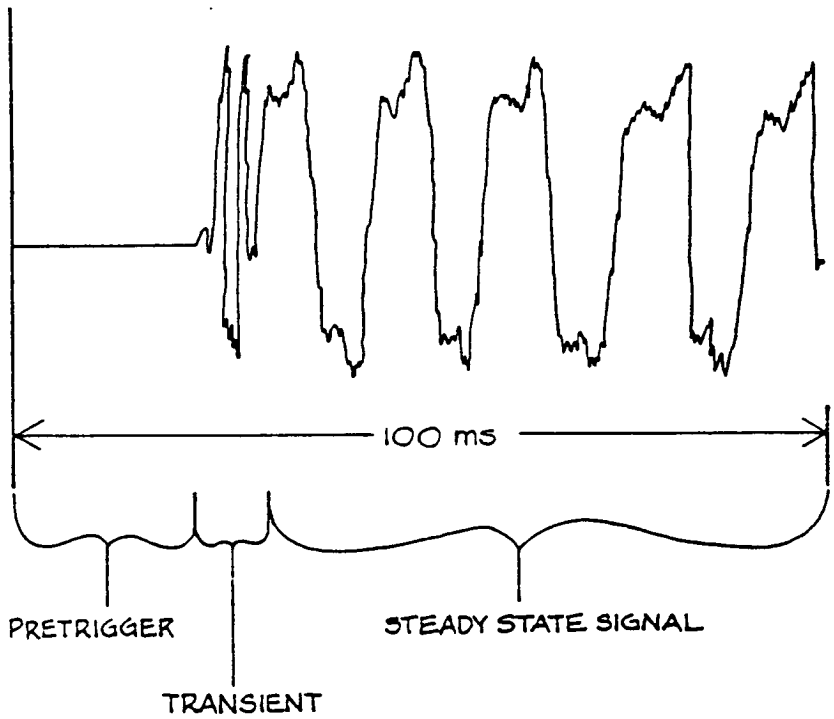


Figure 12. Time domain response of modal domain sensor.

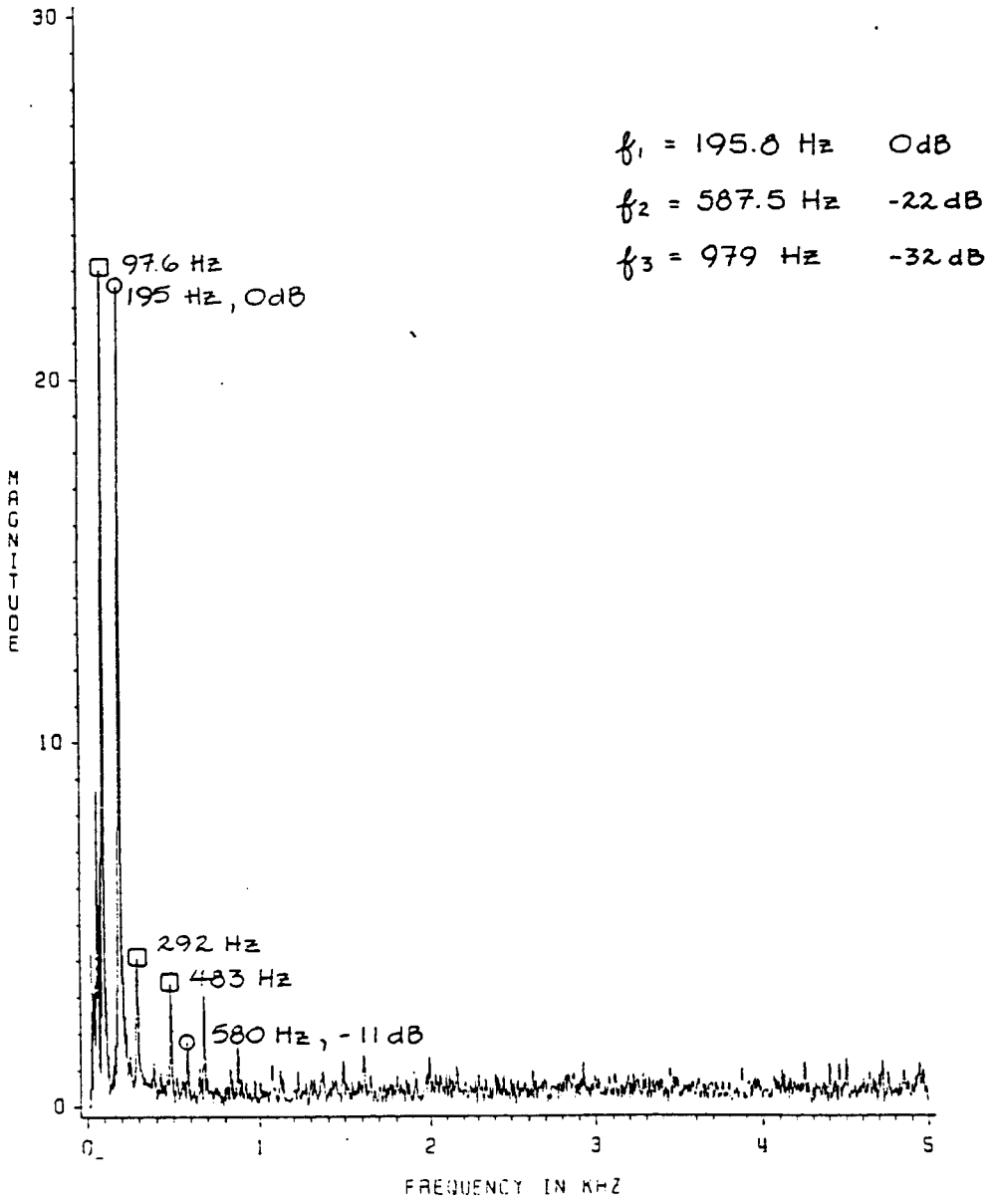


Figure 13. Frequency spectrum of string excitation at 196 Hz: displacement at 1/2 L; table shows calculated frequencies and amplitudes.

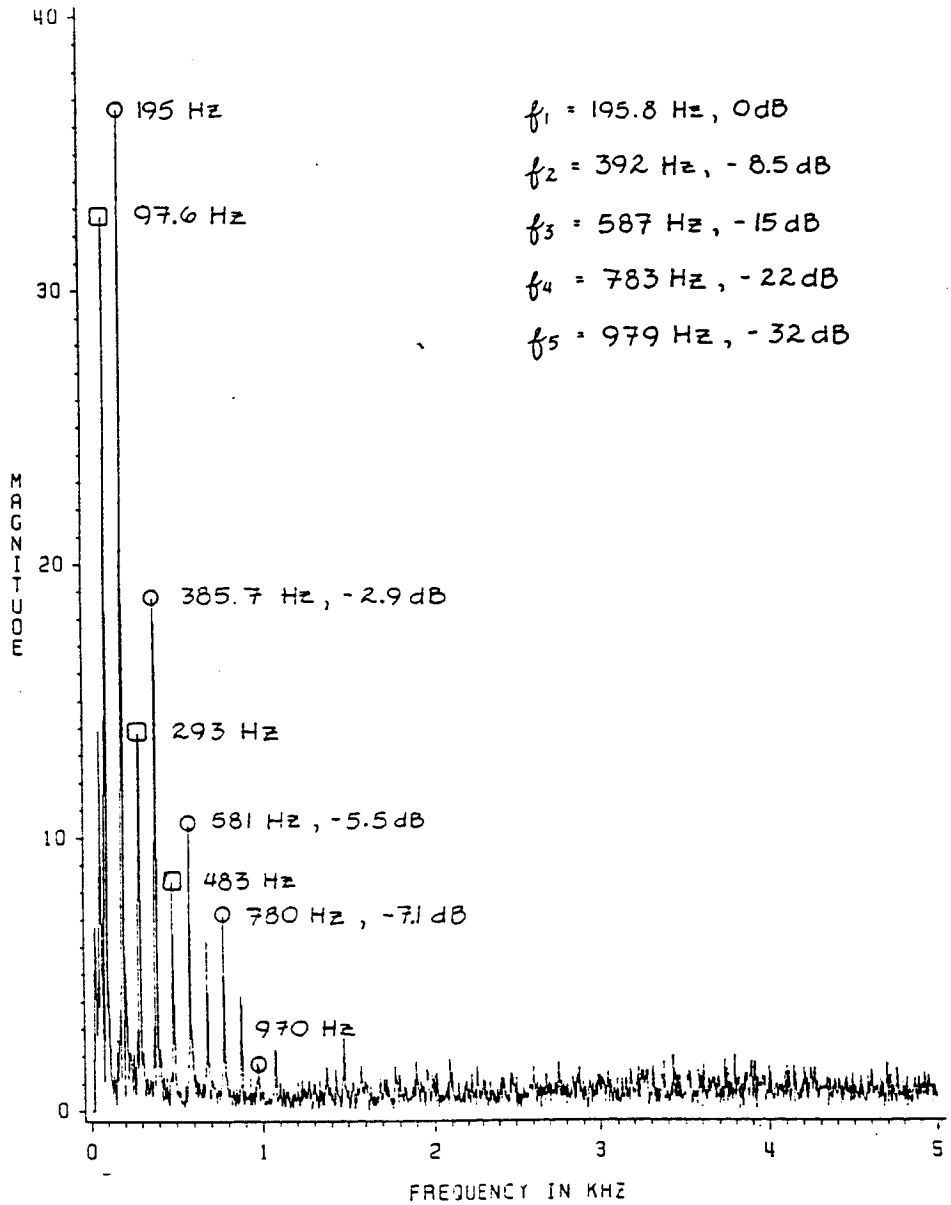


Figure 14. Frequency spectrum of string excitation at 196 Hz: displacement at 5/6 L; table shows calculated frequencies and amplitudes

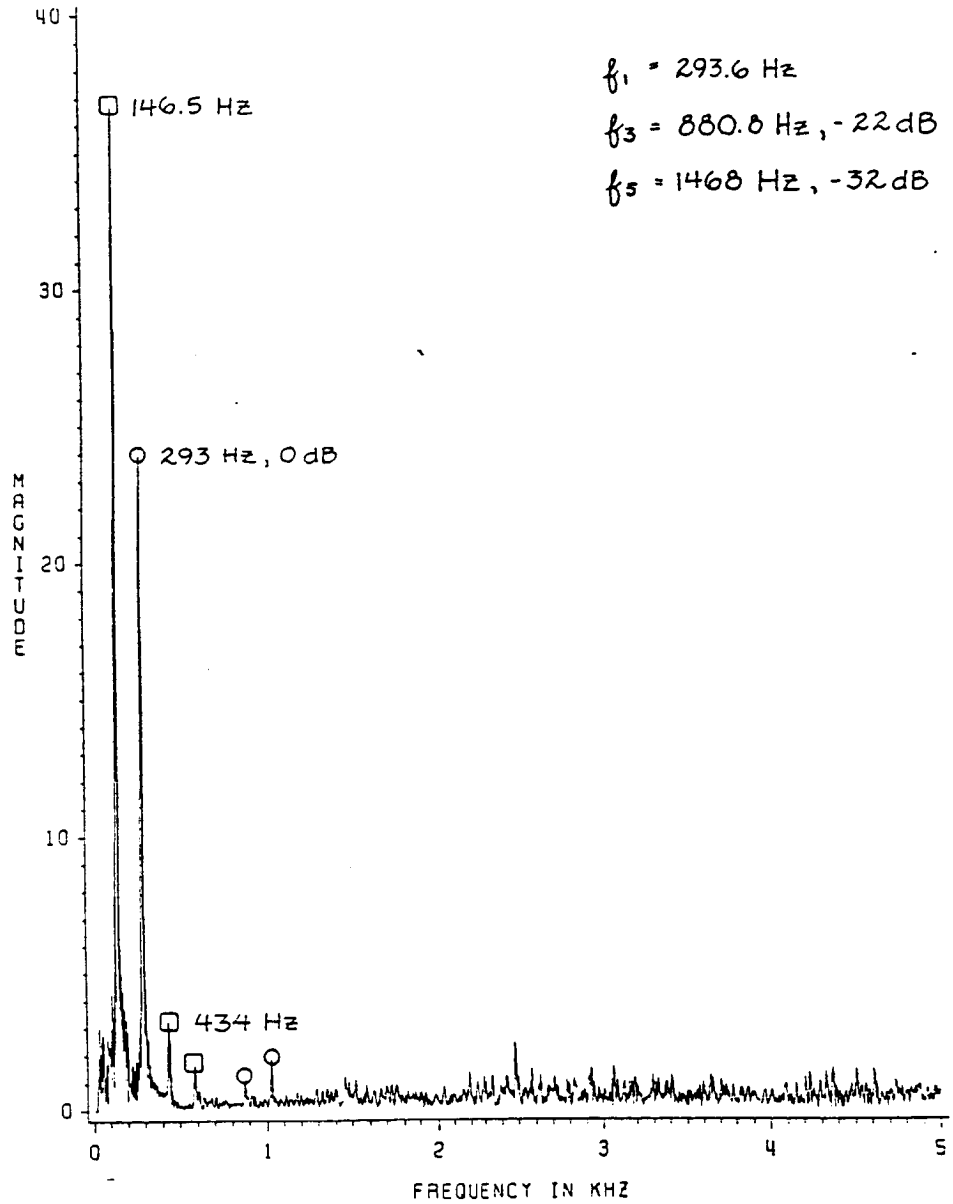


Figure 15. Frequency spectrum of string excitation at 294 Hz: displacement at 1/2 L: table shows calculated frequencies and amplitudes.

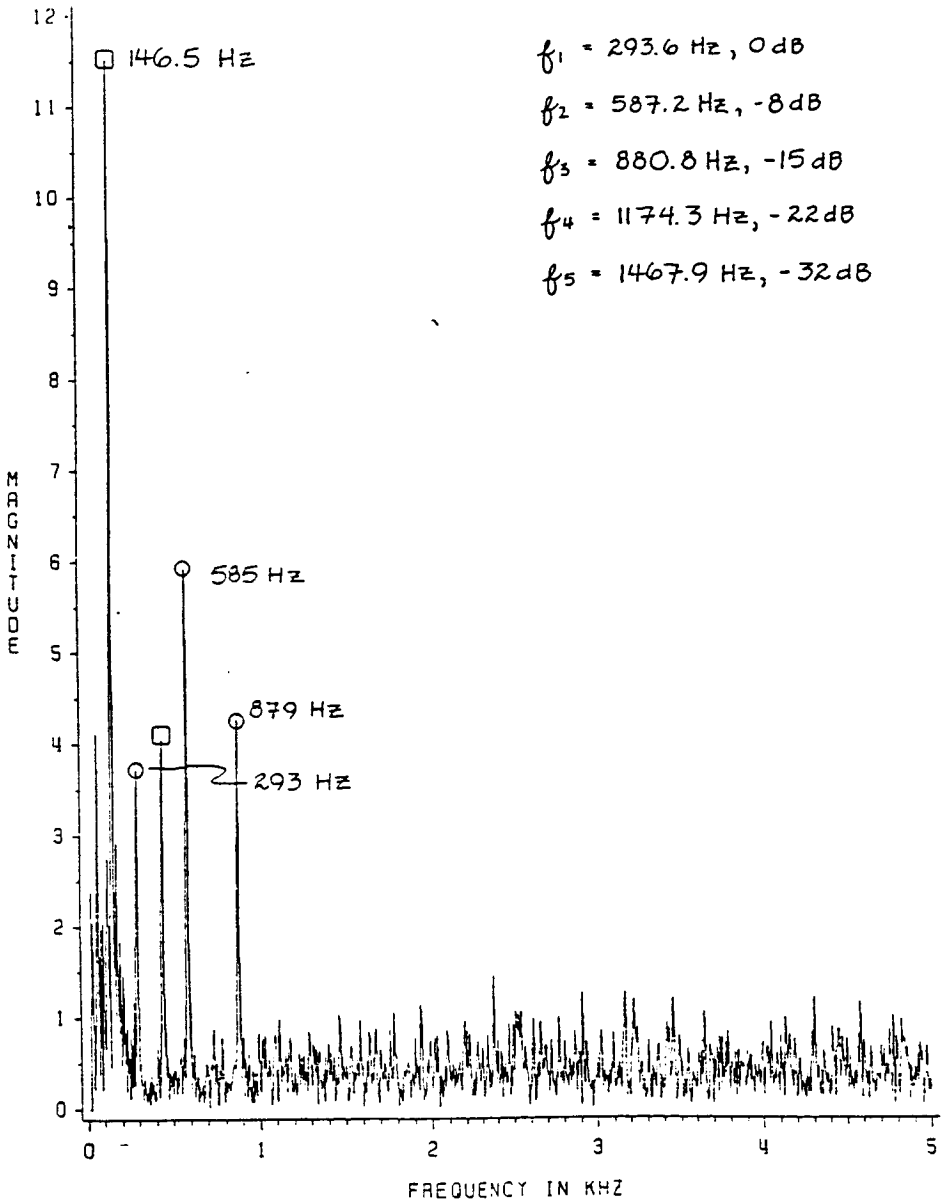


Figure 16. Frequency spectrum of string excitation at 294 Hz: displacement at 5/6 L; table shows calculated frequencies and amplitudes.

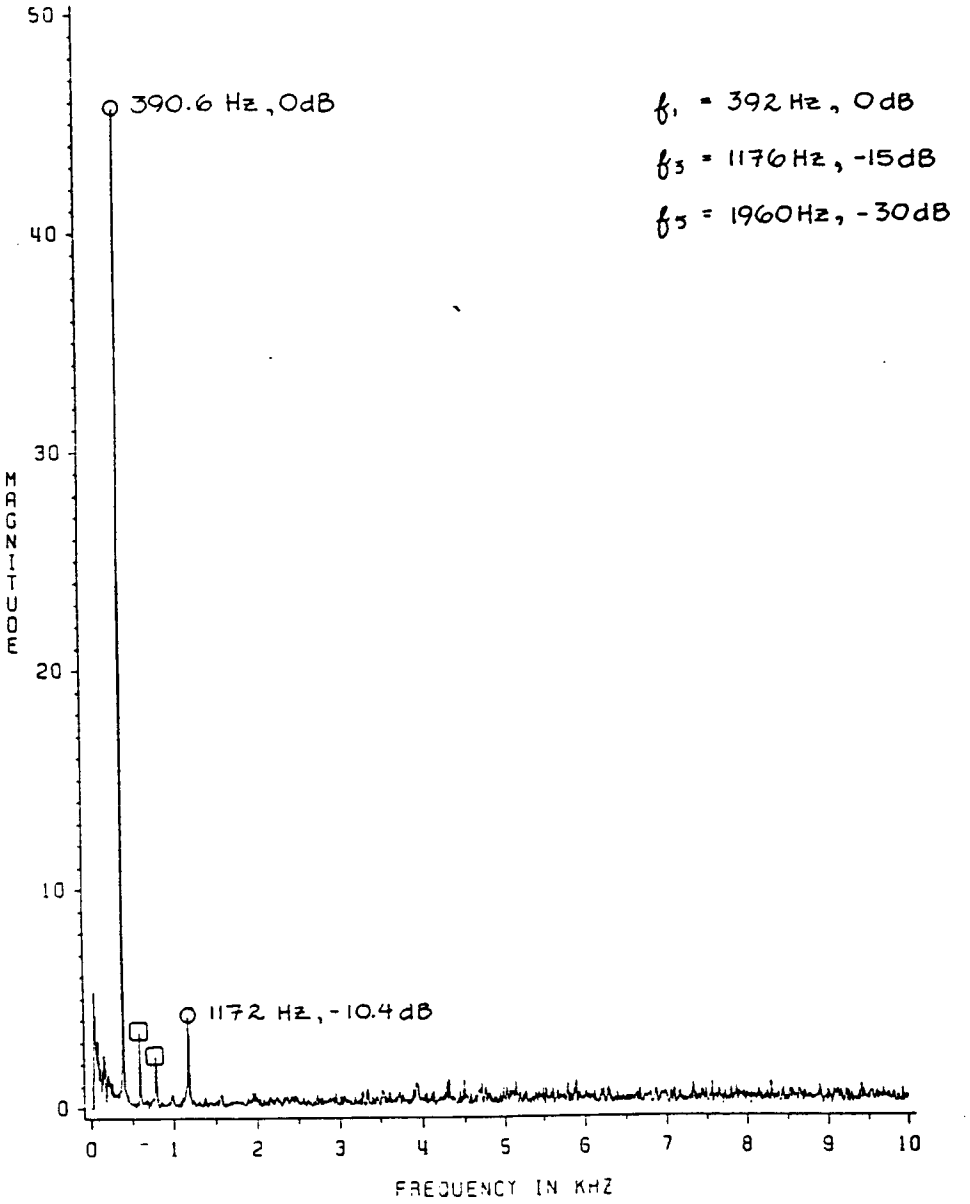


Figure 17. Frequency spectrum of string excitation at 392 Hz: displacement at 1/2 L; table shows calculated frequencies and amplitudes.

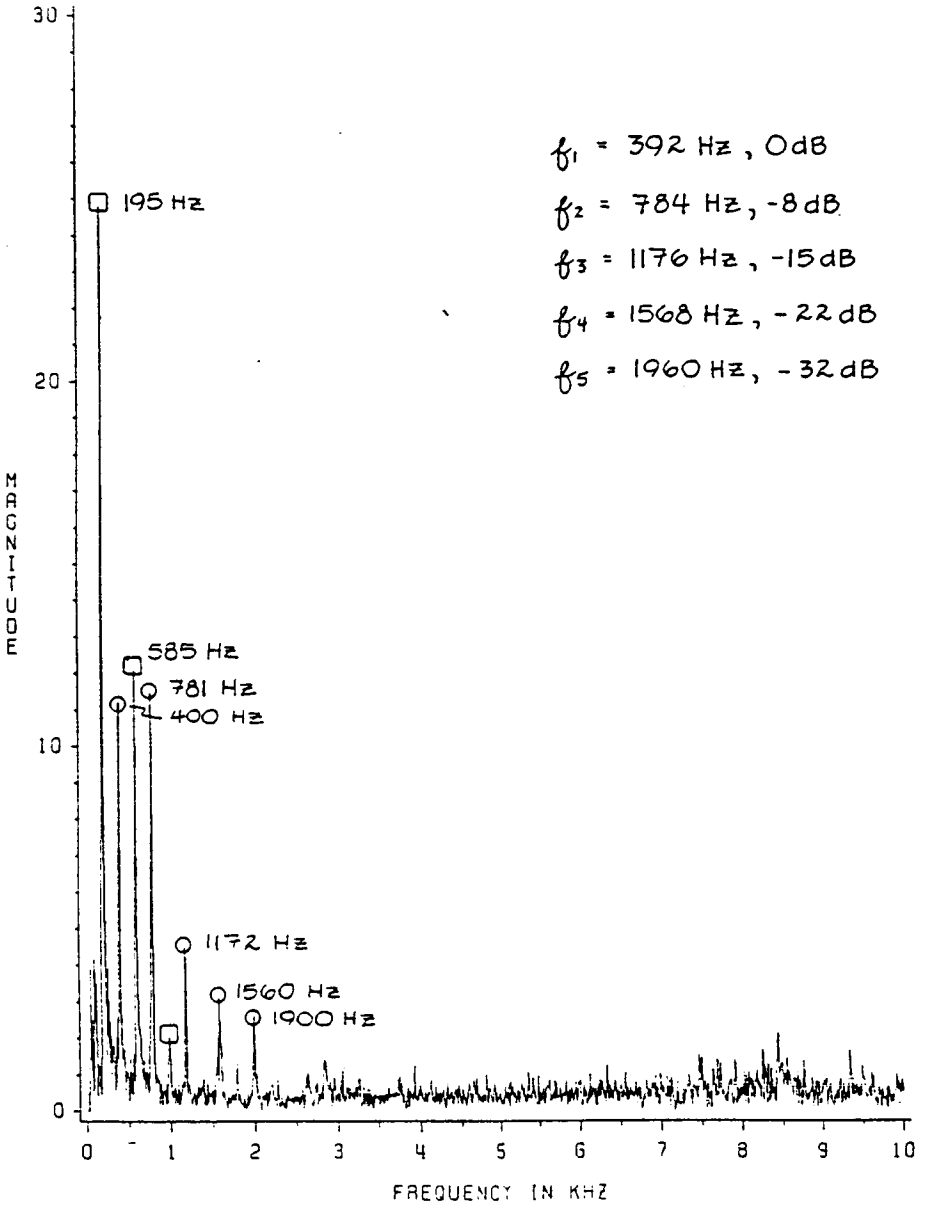


Figure 18. Frequency spectrum of string excitation at 392 Hz: displacement at 5/6 L; table shows calculated frequencies and amplitudes.

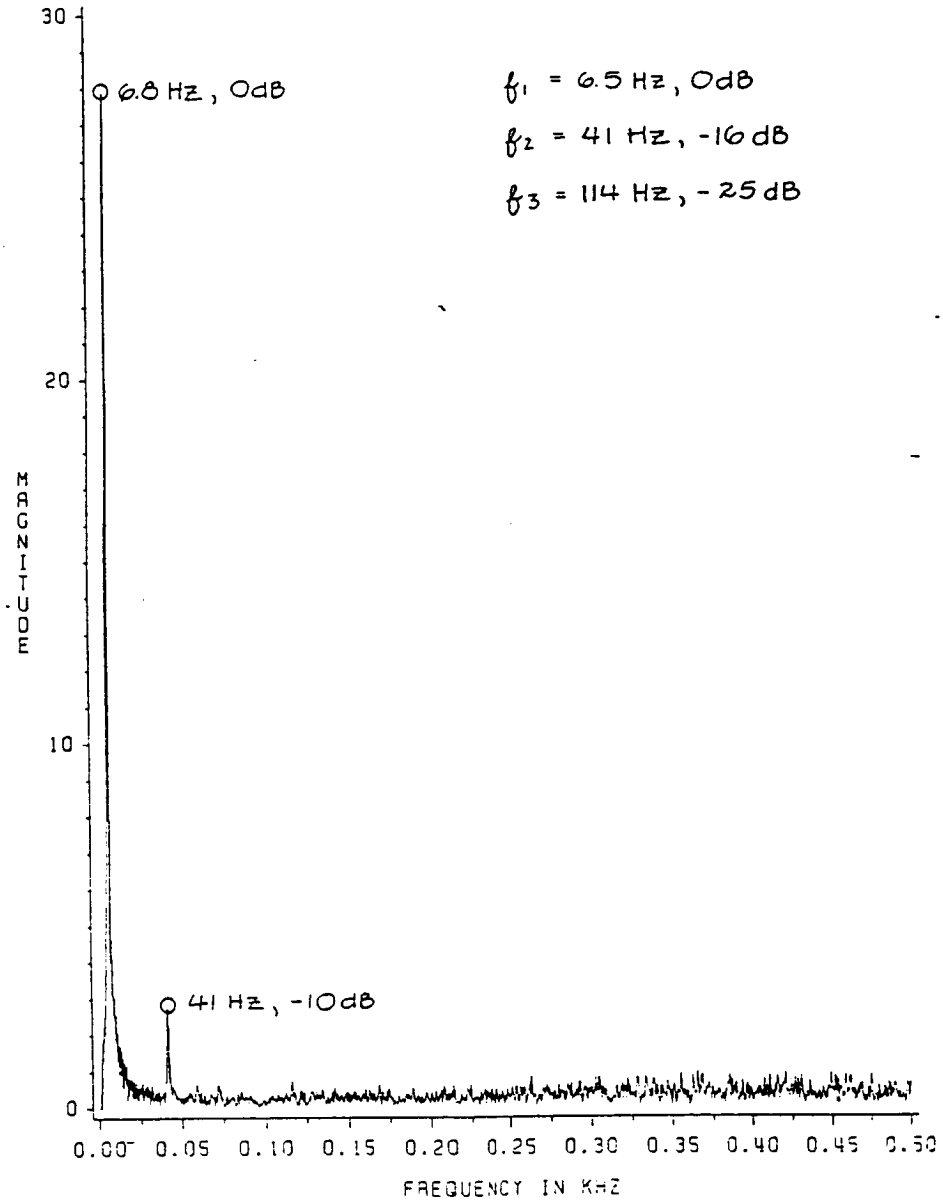


Figure 19. Frequency spectrum of sensor output for clamped free beam excitation: initial displacement of 0.08 cm; table shows calculated frequencies and amplitudes.

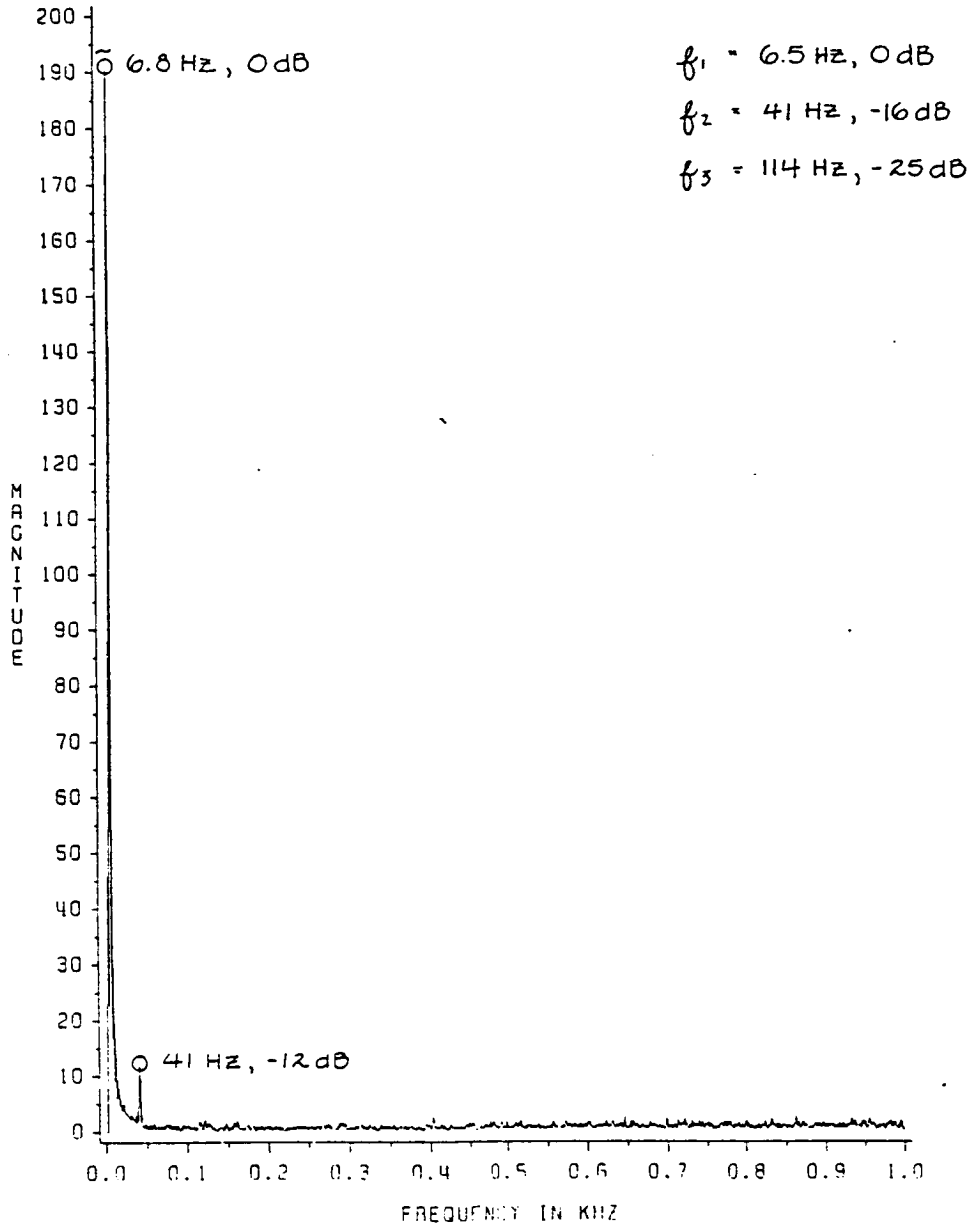


Figure 20. Frequency spectrum of sensor output for clamped-free beam excitation: initial displacement of 0.5 cm.

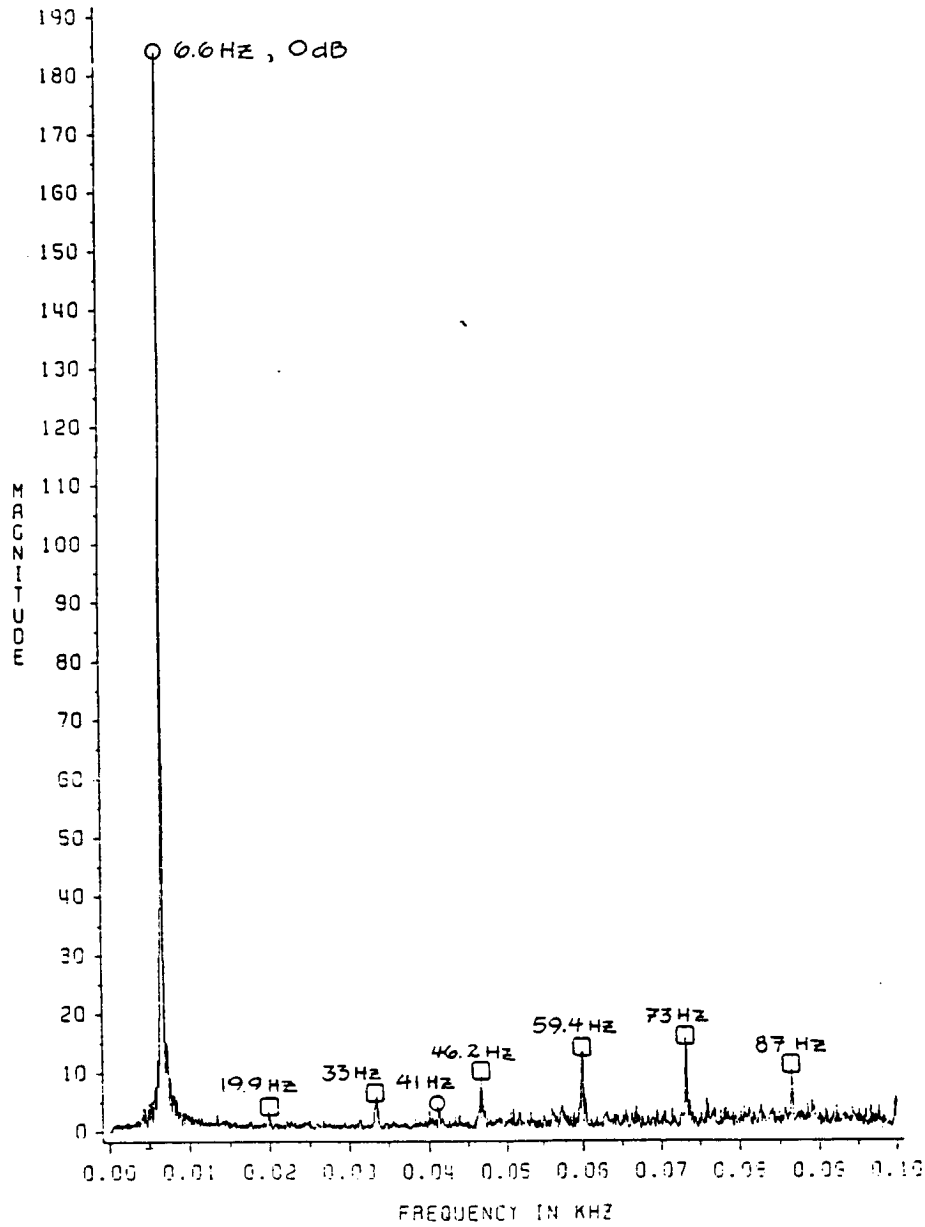


Figure 21. Frequency spectrum of sensor output for clamped-free beam excitation showing effects of carrier phase and endface reflection

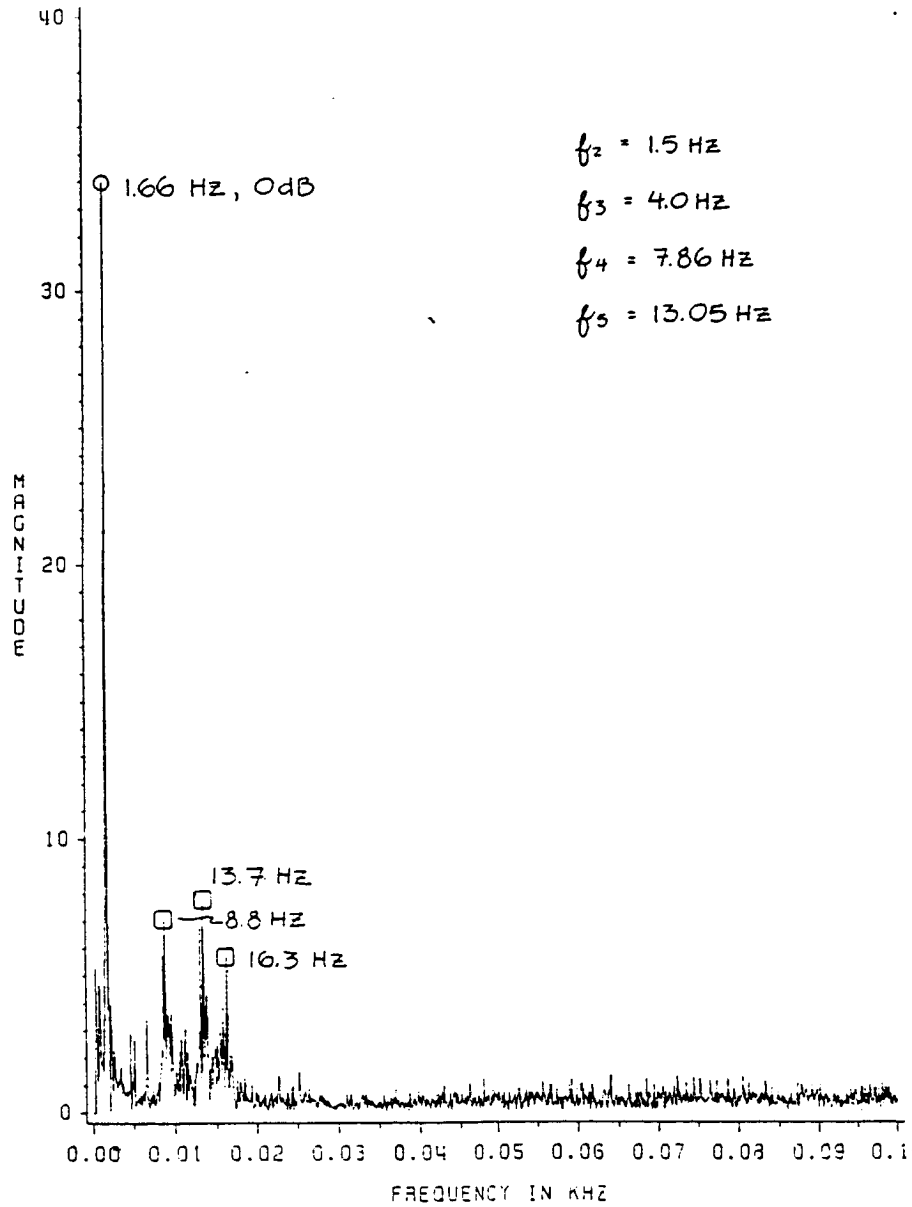


Figure 22. Frequency spectrum of sensor output for first free-free beam excitation: differing interference pattern; table shows calculated frequencies

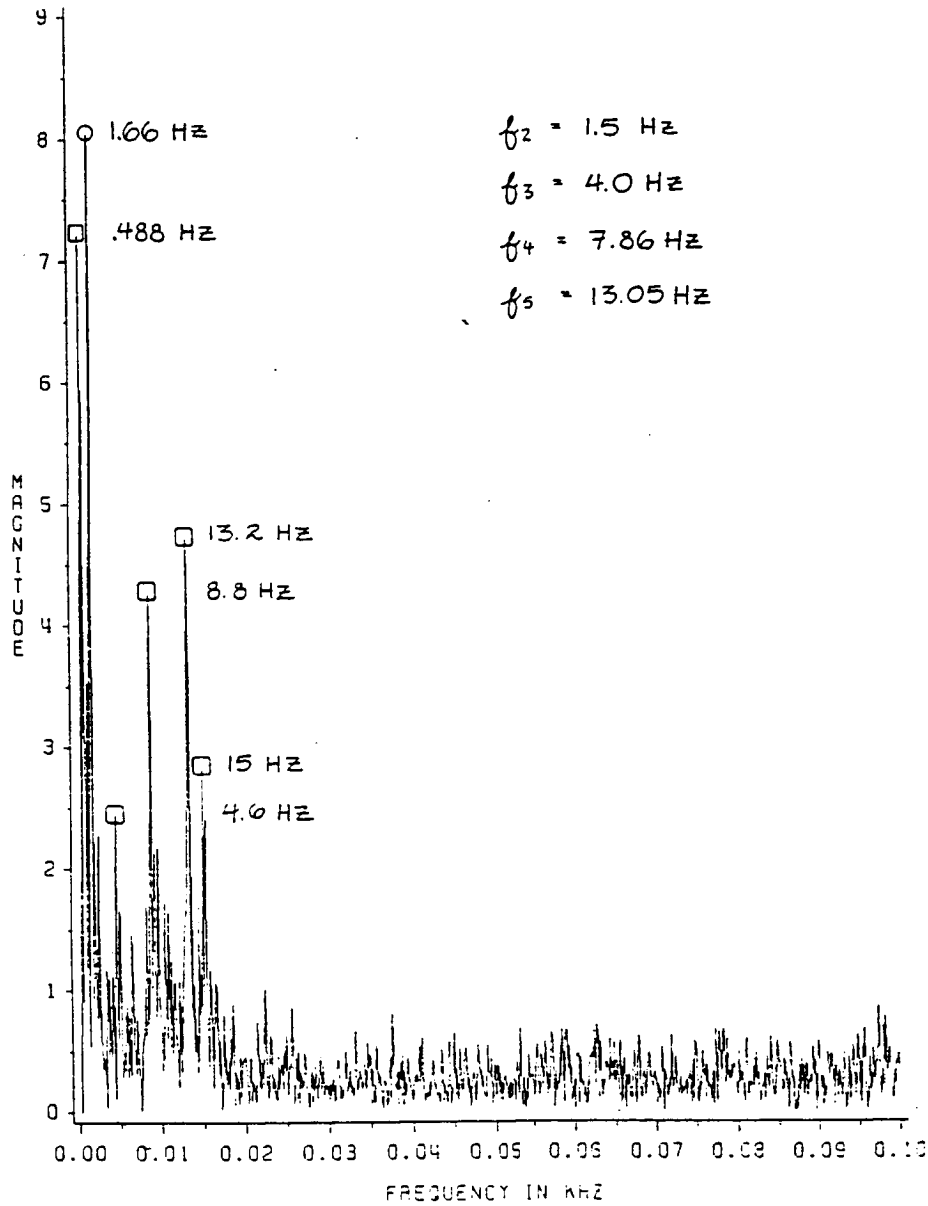


Figure 23. Frequency spectrum of sensor output for second free-free beam excitation: differing interference pattern: table shows calculated frequencies

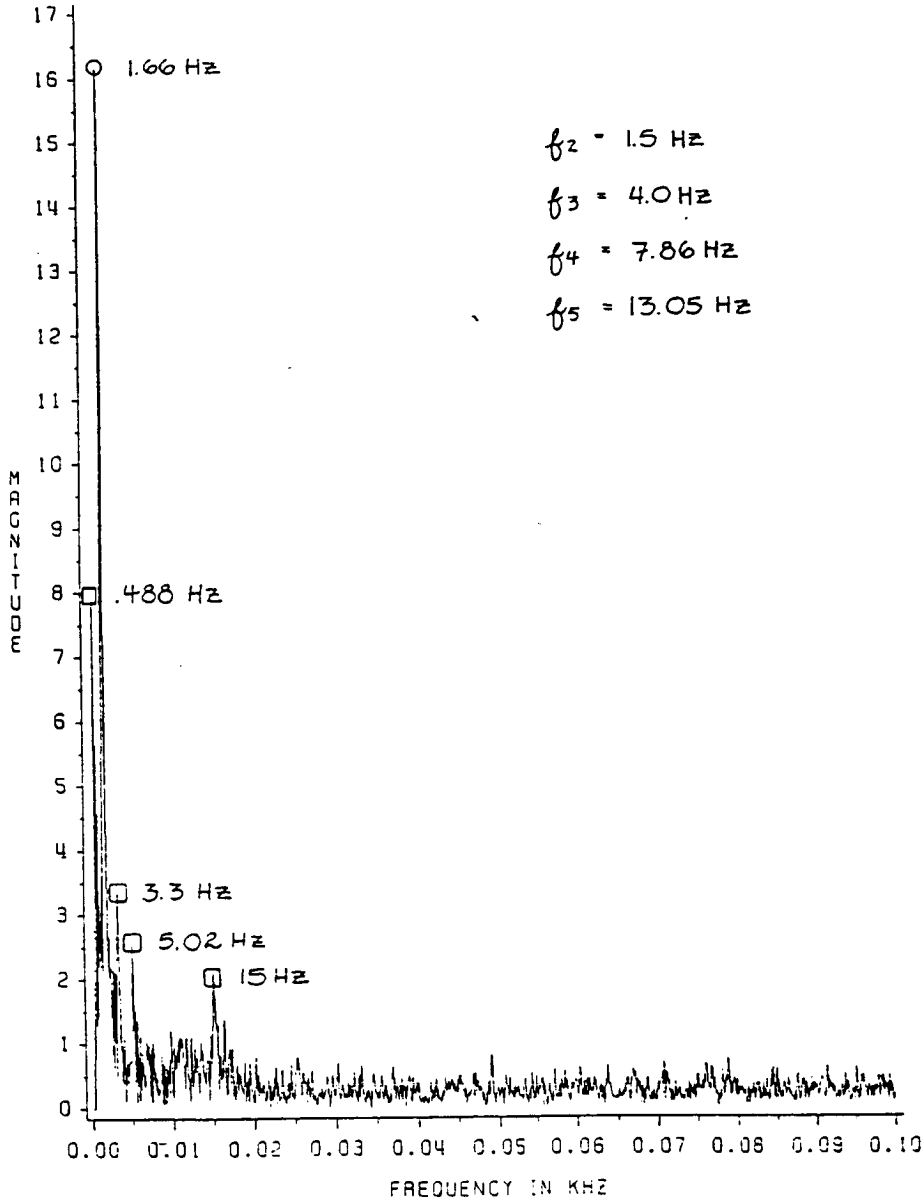


Figure 24. Frequency spectrum of sensor output for third free-free beam excitation: differing interference pattern; table shows calculated frequencies.

# Bibliography


1. Davis, C. M., "Fiber Optic Sensors: an Overview," *Optical Engineering* **24**, 347, Mar. 1985.

2. Keiser, G., "Optical Fibers: Structures and Fundamentals," in *Optical Fiber Communications*, McGraw Hill, New York, 1983.

3. Yariv, A., "Propagation of Optical Beams in Fibers," in *Optical Electronics 3rd Edition*, Holt, Rinehart and Winston, New York, 1985.

4. Snitzer, E., "Cylindrical Dielectric Waveguide Modes," *J. Opt. Soc. Amer.* **51**, 491, May, 1961.

5. Marcuse, D., "Field Deformation and Loss Caused by Curvature in Optical Fibers," *J. Opt. Soc. Amer.* **66**, 311, April, 1976.

6. Taylor, H.,"Bending Effects in Optical Fibers," *J. of Lightwave Tech.* **LT-2**, 617, Oct., 1984.

7. Sakai, J., "Simplified Bending Loss Formula for Single Mode Optical Fibers," *Applied Optics* **18**, 951, Apr., 1979.

8. Hocker, G., "Fiber Optic Sensing of Pressure and Temperature," *Appl. Opt.* **18**, 1445, May, 1979.

9. Layton, M.R., Bucaro, J.A., "Optical Fiber Acoustic Sensor Utilizing Mode-Mode Interference," *Appl. Opt.* **18**, 666, Mar., 1979

10. Kingsley, S.A., Davies, D.E., "Multimode Optical Fiber Phase Modulators and Discriminators," *Electron. Lett.* **14**, 322, May, 1978.

11. Bucaro, J.A., Carome, E.F., "Single Fiber Interferometric Acoustic Sensor," *Appl. Opt.* **17**, 330, Feb., 1978.

12. Kingsley, S.A., "Fiberdyne Systems for Passive or Semipassive Fiber Optic Sensors," *Electron. Lett.* **14**, May, 1978

ORIGINAL PAGE IS
OF POOR QUALITY


13. Kingsley, S.A., "Multimode Optical Fiber Phase Modulators," *Electron. Lett.* **14**, 335, May, 1978.

14. Nelson, D.F., Kleinman D.A., Wecht K.W., "Vibration Induced Modulation of Fiberguide Transmission," *Appl. Phys. Lett.* **30**, 94, 15 Jan., 1977.

15. Kapron, F.P., Keck, D.B., Marer R.D., *Appl. Phys. Lett.* **17**, 423, 1970.

16. Cherin, A.H., *An Introduction to Optical Fibers*, McGraw-Hill, New York, 1983

17. Virginia Tech Computing Center, IMSL Program Library, Program no. FFTRC

18. Roy, A.K., Plunkett R., "Dispersive Bending Waves in Uniform Bars," *Experimental Mechanics* **25**, 308, Sept., 1985

19. Gough, C., "The Non-Linear Free Vibration of a Damped Elastic String," *J. Acous. Soc. Amer.* **75**, 1770, Jun., 1984.

20. Elliot, J., "Non-Linear Resonance in Vibrating Strings," *Amer. J. of Phys.* **50**, 1148, Dec., 1982.

21. Elliot, J., "Intrinsic Non-Linear Effects in Vibrating Strings," *Amer. J. of Phys.* **48**, 478, Jun., 1980.

22. deDayan, H.G., Behan A., "The Quality of Strings for Guitars- an Experimental Study," *J. of Sound and Vibration* **64**, 421, Jun., 1979.

23. Josephs, J., "Stringed Instruments," in *The Physics of Musical Sound*, D. Van Nostrand Co., Princeton, NJ, 1967.

24. Skudrzyk, E., "Continuous Systems," in *Simple and Complex Vibration Systems*, The Pennsylvania State University Press, University Park, PA, 1968.

25. Myint-U, T., "Mathematical Models," in *Partial Differential Equations of Mathematical Physics*, North Holland, New York, 1980.

26. Elmore, W., Heald, M., *Physics of Waves*, McGraw-Hill, New York, 1969.

27. Gorman, D.J., *Free Vibration Analysis of Beams and Shafts*, John Wiley and Sons, New York, 1975.

28. Srinivasan, P., "Vibrations of Beams, Plates, Rings and Shells," in *Mechanical Vibration Analysis*, Tata McGraw-Hill, New Delhi, 1982.

29. Vernon. J.B., "Continuous Systems-Classical Methods," in *Linear Vibration Theory*, John Wiley and Sons, New York, 1967.

30. Beer, F., Johnston, E.R., *Mechanics of Materials*, McGraw-Hill, New York, 1981.

31. DePaula, R., Flax, L., Cole, J., Bucaro, J., "Single Mode Fiber Ultrasonic Sensor," *IEEE J. of Quantum Electron.* QE-18, 680, April, 1982

# Appendix A. The Vibrating String

One of the simplest and most fundamental problems in the study of vibration is that of the stretched string. This problem provides insight to the solution of more complicated vibration systems as well as many similar problems in mathematical physics. Consider first a stretched string of length $L$ fixed at its endpoints. Our goal is to determine an equation of motion for the string, $u(x,t)$, which characterizes the position of each point $x$ on the string at time $t$ after some given initial disturbance. Several assumptions must first be made about the system in order to obtain a simple equation [26]:

1. The magnitude of the tension $\tau$ in the string is constant and always in a direction tangent to the existing string profile.

2. The angle which the string makes with respect to the $x$ axis is small.

3. Only movement of the string in a single transverse direction is allowed.

With these assumptions we may now consider the differential string element of Fig. 25. Let $\tau$ be the magnitude of the tension at either end of the element. The forces on the string in the vertical direction are [25]

$$\tau \sin \beta - \tau \sin \alpha \ ,$$

which must be equal to the acceleration of the element times its mass. If $\Delta s$ represents the arc length of the element and $\rho$ its mass per unit length we may write a differential equation of motion as

$$u_{tt}(x,t)\, \rho \Delta s = \tau \sin \beta - \tau \sin \alpha \ , \tag{A.1}$$

where $u_{tt}$ denotes a second derivative with respect to time. This equation may be simplified by considering the previous assumptions. Since the slope of the string is small, from assumption 2 we may consider

$$\Delta s \cong \Delta x \ ,$$

and also

$$\sin \alpha \cong \tan \alpha \quad , \quad \sin \beta \cong \tan \beta \ .$$

Then equation (A.1) becomes

$$\tan \beta - \tan \alpha = \frac{\rho \Delta x}{\tau} u_{tt}(x,t) \ . \tag{A.2}$$

However the tangents of the angles $\alpha$ and $\beta$ at points $x$ and $x + \Delta x$ respectively can simply be defined as

$$\tan \alpha = u_{tt}(x,t)_{x,t} \quad , \quad \tan \beta = u_{tt}(x,t)_{x+\Delta x,\, t} \ .$$

Rewriting equation (A.2) we get

$$\frac{1}{\Delta x}\left[ u_x|_x - u_x|_{x-\Delta x} \right] = \frac{\rho}{\tau} u_{tt} \ .$$

In the limit as $\Delta x$ goes to zero the term on the left is simply the definition of second derivative. This equation becomes

$$\frac{\partial^2}{\partial t^2} u(x,t) = c^2 \frac{\partial^2}{\partial x^2} u(x,t) \ . \tag{A.3}$$

where $c^2 = \tau/\rho$. This equation has the form of the one dimensional wave equation which defines the motion of a string.

To completely describe the system we require initial and boundary conditions on the wave equation (A.3). For the described string these may be written as

$$\begin{aligned} u(x,0) &= f(x) \quad , \quad 0 \le x \le l \ , \ t > 0 \\ u_t(x,0) &= g(x) \quad , \quad 0 \le x \le l \\ u(0,t) &= 0 \quad , \quad t \ge 0 \\ u(L,t) &= 0 \quad , \quad t \ge 0 \ , \end{aligned} \tag{A.4}$$

where $f(x)$ and $g(x)$ represent the initial displacement and velocity respectively. By the method of seperation of variables we assume a solution to equation (A.3) of the form

$$u(x,t) = X(x)\, T(t) \ . \tag{A.5}$$

This gives the two ordinary differential equations

$$\begin{aligned} X'' - \lambda^2 X &= 0 \\ T'' - \lambda^2 c^2 T &= 0 \ , \end{aligned} \tag{A.6}$$

where $\lambda$ is the seperation constant. Applying the boundary conditions to equation (A.5) leads to the eigenvalue problem

$$\begin{aligned} X'' + \lambda^2 &= 0 \\ X(0) &= 0 \\ X(L) &= 0 \ . \end{aligned} \tag{A.7}$$

The only non-trivial solution to this equation is of the form

$$X(x) = A \cos \lambda x + B \sin \lambda x \ .$$

The condition $X(0) = 0$ implies $A = 0$. Applying the second boundary condition $X(L) = 0$ gives

$$B \sin \lambda L = 0 \ .$$

For non-trivial solutions ($B \neq 0$) we require solutions to the equation $\sin \lambda L = 0$. These solutions are the eigenvalues of the problem and are given by

$$\lambda_n = n\pi/L \ .$$

Then the solutions to equation (A.7) are

$$X_n(x) = B_n \sin n\pi x/L \ . \tag{A.8}$$

We now consider the equation

$$T'' - \lambda^2 c^2 T = 0 \ .$$

This equation takes the general solution, assuming the discrete values for $\lambda$ derived above,

$$T_n(t) = C_n \cos \frac{n\pi c}{L} t + D_n \sin \frac{n\pi c}{L} t \ . \tag{A.9}$$

The general solution for the string's equation of motion is a superposition of these seperable solutions, equations (A.8) and (A.9). Combining this fact with the product solution of equation (A.5) we get

$$u(x,t) = \sum_{n=1}^{\infty} \left[ a_n \cos \frac{n\pi c}{L} t + b_n \sin \frac{n\pi c}{L} t \right] \sin \frac{n\pi x}{L} \ . \tag{A.10}$$

This equation represents the Fourier series solution to the partial differential equation. Hence the series components represent orthogonal functions from which we can derive the constants $a_n$ and $b_n$. Given the initial conditions of equations (A.4) the orthogonality relation gives

$$\begin{aligned} a_n &= \frac{2}{L}\int_o^L f(x)\sin\frac{n\pi x}{L}dx \\ b_n &= \frac{2}{n\pi c}\int_o^L g(x)\sin\frac{n\pi x}{L}dx \ . \end{aligned} \tag{A.11}$$

The two components of the solution represented by $X(x)$ and $T(t)$ are the spatial and temporal descriptions of the string's motion respectively. The $X(x)$ solution tells us the possible *mode shapes* of the string while the $T(t)$ solution gives the harmonic behaviour of each mode shape in time. Hence $T(t)$, through the frequency eigenvalue $\omega_n = n\pi c/L$, defines the actual frequencies of oscillation of the string; each mode shape oscillating with a respective frequency. The possible frequencies are a function of the initial conditions which impart the actual motion.

## *A.1 The Plucked String*

The case of initial displacement with no initial velocity will be considered. Referring to equations (A.4) this will give $g(x) = 0$ . Now $f(x)$, the initial position of each point on the plucked string, must be defined. These initial conditions can be written as [25]

$$f(x) = u(x,0) = \begin{cases} hx/a \ , & 0 \le x \le a \\ h\dfrac{(L-x)}{(L-a)} \ , & a \le x \le L \end{cases} , \tag{A.12}$$

where $h$ and $a$ define the initial displacement height of the string and distance from the end $x=0$ respectively. These initial conditions are substituted into equations (A.11) to give the constants $a_n$ and $b_n$ from which we get

$$b_n = 0$$
$$a_n = \frac{2hL^2}{\pi^2 a(L-a)} \frac{1}{n^2} \sin \frac{n\pi a}{L} \ . \tag{A.13}$$

The final solution for the plucked string then becomes

$$u(x,t) = \frac{2hL^2}{\pi^2 a(L-a)} \sum_{n=1}^{\infty} \frac{1}{n^2} \sin \frac{n\pi a}{L} \sin \frac{n\pi x}{L} \cos \frac{n\pi c}{L} t \ . \tag{A.14}$$

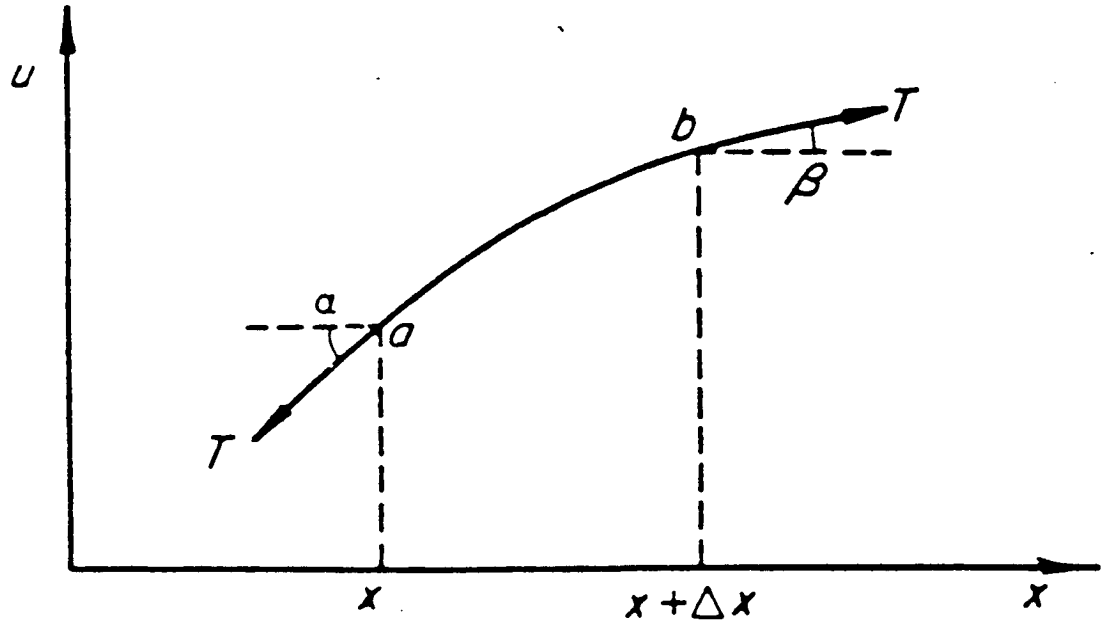


Figure 25. Differential string element: [25]

C-2

# Appendix B. Simple Vibrating Beams

The transversely vibrating beam represents a slightly more complicated vibration system. In the case of a vibrating string, the string's stiffness is ignored and only the tension gives rise to the restoring force. For a beam however, it is the stiffness itself which provides this restoring force. The analysis will consider only *transverse* motion of a slender beam ignoring the effect of gravity and the action of the beam supports. Consider a beam of cross sectional area $A$ to be loaded with a continuous, static load per unit length $w(x)$ across the length of the beam. The bending moment $M(x)$ acting on the beam can be related to the distributed load by [26]

$$\frac{d^2M(x)}{dx^2} = w(x) \ . \tag{B.1}$$

If there exists a bending moment $M(x)$ initiating a bend of curvature $R(x)$ (Fig. 26), the two can be related through the equation

$$M(x) = \frac{EI}{R(x)} \ . \tag{B.2}$$

where $E$ is the materials Young's modulus and $I$ is the section moment. This is defined as the second moment of the area about a transverse axis through the beam's neutral surface (Fig. 26)

$$I = \int y^2 dA \ . \tag{B.3}$$

However, we would like to relate the *displacement* of a point on the beam to $M(x)$. If we designate $u(x)$ as a point on the beam's neutral surface then for small displacements, $u(x)$ can be related to the beam's radius of curvature due to bending, $R(x)$, as

$$\frac{d^2u(x)}{dx^2} = \frac{1}{R(x)} \ . \tag{B.4}$$

Then equation (B.2) can be used to obtain

$$M(x) = EI\frac{d^2u(x)}{dx^2} \ . \tag{B.5}$$

This equation relates an applied bending moment to the actual beam displacement. By solving this equation for an applied $M(x)$ the resulting shape of the bent beam could be determined.

We may also relate $u(x)$ to an applied load $w(x)$ through equation (B.1). This gives

$$EI\frac{d^4u(x)}{dx^4} = w(x) \ . \tag{B.6}$$

It is from this equation that we may approach the subject of beam vibration. As a beam vibrates due to the pressence of a transverse wave, the applied load $w(x)$ can be considered a *kinetic reaction* of the beam in opposing the acceleration imparted by the wave [26]. This acceleration is responsible for the transverse motion of the beam, hence a force $w_t(x,t)$ exists due to the wave acceleration and the beam mass. Defining $\rho$ as the beam's density and $A$ as the cross sectional area we can write this force as

$$w_t(x,t) = \rho A\frac{\partial^2 u}{\partial t^2} \ . \tag{B.7}$$

Now we may consider the *opposing* force of (B.6) equivalent to the accelerating force of equation (B.7) along the beam. However, since these forces oppose one another a sign difference must be introduced. Equating (B.6) and (B.7) accordingly we get

$$\frac{\partial^4}{\partial x^4} u(x,t) = -\frac{\rho A}{EI} \frac{\partial^2}{\partial t^2} u(x,t) \ . \tag{B.8}$$

This is the differential equation which describes beam vibration. In deriving this equation we have disregarded the fact that each element of the beam, $\Delta x$, has an associated moment of inertia. As the beam vibrates a torque is required to generate a rotary acceleration of this moment through some small angle. This effect, known as rotary inertia, is usually negligible in the treatment of low order beam vibrations.

Solutions to the differential equation (B.8) are required. Applying the technique of seperation of variables a solution of the form

$$u(x,t) = X(x)\, T(t) \ , \tag{B.9}$$

is assumed. Substitution into equation (B.8) and defining the seperation constant $\omega^2$ gives two ordinary differential equations of the form

$$\frac{d^2T}{dt^2} + \omega^2 T = 0 \tag{B.10}$$

$$\frac{d^4X}{dx^4} - k^4 X = 0 \ . \tag{B.11}$$

where $k^4 = \omega^2(\rho A/EI)$. We first consider solutions of the fourth order equation (B.11) since it is these solutions which provide the necessary eigenvalues describing the vibration system. The general solution to this equation is of the form [27]

$$X(x) = A \sin kx + B \sin kx + C \sinh kx + D \cosh kx \ . \tag{B.12}$$

We must now apply the necessary boundary conditions. There are three possible classical boundary conditions which describe the state of the beam ends: free, hinged and clamped, and any combination of these three conditions may appear. The two which will be discussed here are the clamped-free and free-free combinations.

## *B.1 Clamped-Free Boundary Conditions*

Each end of the beam is considered independently. At the clamped end ($x = 0$) securing the beam causes the displacement and slope of the beam to be zero [26]

$$u(x,t)\,|_{x=0} = 0 \qquad \frac{\partial}{\partial x}u(x,t)\,|_{x=0} = 0 \tag{B.13}$$

At the free end of the beam ($x = L$) the bending moment and shearing force both vanish. This is described by

$$\frac{\partial^2}{\partial x^2}u(x,t)\,|_{x=L} = 0 \qquad \frac{\partial^3}{\partial x^3}u(x,t)\,|_{x=L} = 0\ . \tag{B.14}$$

Substituting these boundary conditions into equation (B.12) will yield the characteristic equation [28]

$$\begin{gathered}\cosh\beta\ \cos\beta + 1 = 0 \\ \beta = kL\ .\end{gathered} \tag{B.15}$$

The solutions of this equation are the eigenvalues, $\beta_n$. The first three eigenvalues are found to be [27]

$$\beta_{1,2,3} = 1.875,\ 4.694,\ 7.855\ .$$

From this the beam's frequencies are given by

$$f_n = \frac{\omega_n}{2\pi} = \frac{\beta_n^2}{2\pi L^2}\sqrt{\frac{EI}{\rho A}} \ . \tag{B.16}$$

Equation (B.16) is applicable to any beam system for which the eigenvalues, $\beta_n$, are known. Hence to determine the modal frequencies of a beam we need only to solve for these eigenvalues by applying the particular boundary conditions to equation (B.12).

However, this does not tell us the contribution of each frequency mode to the actual vibration. In other words, we do not yet know the magnitudes of the individual frequency components. This is a function of the beam's initial conditions which may be expressed as

$$\begin{aligned} u(x,0) &= f(x) \quad , \quad 0 \le x \le L \\ \frac{\partial}{\partial t}u(x,0) &= g(x) \ . \end{aligned} \tag{B.17}$$

The general solution to the vibrating beam is given by equation (B.9). Since there are an infinite number of solutions this product becomes a superposition, hence

$$u(x,t) = \sum_{n=1}^{\infty} [A_n \cos \omega_n t + B_n \sin \omega_n t] X_n(x) \ .$$

The mode shapes $X_n(x)$ are derived from the boundary conditions and equation (B.12)., given the eigenvalues $\beta_n$. For the clamped-free beam $X_n(x)$ is given by [27]

$$\begin{aligned} X_n(x) &= C_n\{ \sin k_n x - \sinh k_n x - \gamma[\cos k_n x - \cosh k_n x]\} \\ \gamma &= \frac{\sin \beta_n + \sinh \beta_n}{\cos \beta_n + \cosh \beta_n} \\ k_n &= \beta_n / L \ , \end{aligned} \tag{B.18}$$

where $C_n$ is a constant. Absorbing this constant in $A_n$ and $B_n$ we solve for these constants by orthogonality of the series functions as

$$A_n = \frac{\int_0^L f(x) X_n \, dx}{\int_0^L X_n^2 \, dx} \tag{B.19}$$

$$B_n = \frac{\int_0^L g(x) X_n \, dx}{\int_0^L X_n^2 \, dx} ,$$

where $f(x)$ and $g(x)$ are the initial conditions of equation (B.17). We now need to characterize these initial conditions. For our purposes we will consider the specific case of a downward displacement by a force $P$ at the beam tip. This will make $g(x) = 0$. To determine $f(x)$ we must solve equation (B.5) for $u(x) = f(x)$ with the applied moment $M(x)$. By summing the moments around the beam and setting them equal to zero (static case) we obtain

$$M(x) = P(x - L) .$$

Substituting this in equation (B.5) and integrating with the initial conditions

$$u(x) = \frac{\partial}{\partial x} u(x) \big|_{x=0} = 0 ,$$

we get for $f(x)$, the displacement of the beam at $t = 0$ ,

$$f(x) = u(x,0) = \frac{P}{EI} \left[ \frac{x^3}{6} - \frac{Lx^2}{2} \right] . \tag{B.20}$$

Substitution of equations (B.18) and (B.20) into (B.19) will give the expansion coefficient $A_n$ ($B_n = 0$) for the corresponding eigenmode $X_n(x)$. The first three coefficients are found to be [29]

$$A_1 = .32356 P \frac{L^3}{EI}$$
$$A_2 = .00824 P \frac{L^3}{EI}$$
$$A_3 = .00105 P \frac{L^3}{EI} .$$

Since the pressure $P$ could not be readily measured, equation (B.20) was utilized to solve for $P$. The displacement at the beam tip, $x = L$, was measured and $P$ derived accordingly.

## *B.2 Free-Free Boundary Conditions*

Determination of the free-free beam modal frequencies is identical to that of the clamped-free beam. To begin, the boundary conditions must be defined. We have already seen the interpretation of the free end boundary condition and need now only to apply it to both ends of the beam. The free-free boundary conditions are written as

$$\frac{d^2u(x)}{dx^2} = \frac{d^3u(x)}{dx^3}\Big|_{x=0,L} = 0 \ . \qquad (B.21)$$

Application of these conditions to equation (B.12) yields the eigenvalue equation [28]

$$\begin{aligned} \cosh\beta \ \cos\beta &= 1 \\ \beta &= kL \ . \end{aligned} \qquad (B.22)$$

Solving this equation for $\beta$ gives the free-free beam eigenvalues. This equation has a double root at $\beta = 0$. These two eigenvalues correspond to the lowest order pendulum modes of the free-free beam; the first to the transverse motion of the beam and the second to a rigid rotation about its center

its center of mass [27]. The first non-zero roots are at

$$\beta_{2,3,4} = 4.73, \ 7.853, \ 10.996 \ .$$

With the use of equation (B.16) the actual beam frequencies may be calculated.

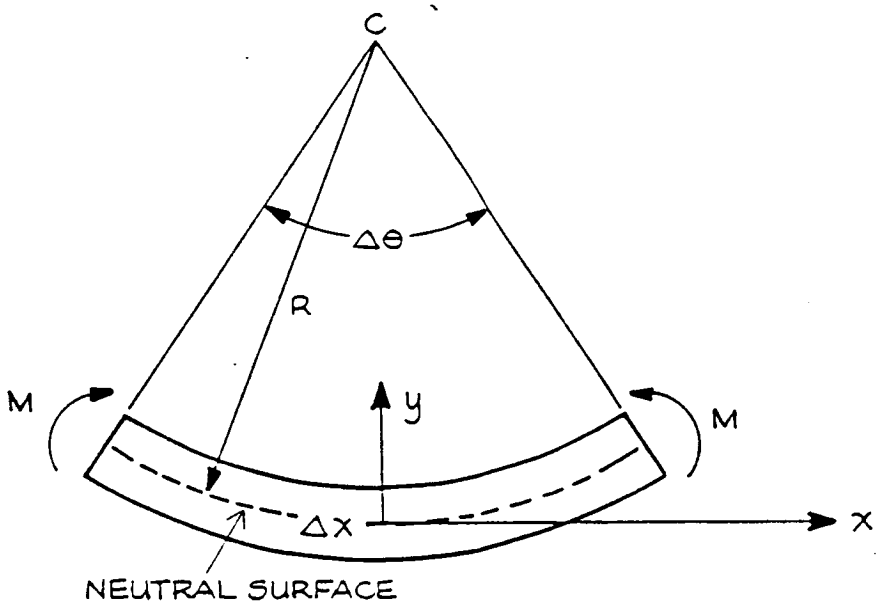


Figure 26. Differential beam element showing bending radius and neutral surface

# Appendix C. Experimental Measurement of Young's Modulus

The use of equation (B.16) to calculate beam eigenfrequencies is precluded by a knowledge of $E$, the Young's modulus. Rather than use reported nominal values for the modulus of the beam materials, steel and PVC, an independent experiment was performed to determine $E$. This experiment measures the fundamental frequency of a cantilever beam then uses the computed first order eigenvalue (Appendix B) to solve for the product $EI$ knowing $\rho$ and $A$. In the case of the steel hack saw blade used in the clamped-free beam vibration studies it was only necessary to perform the experiment on the existing beam to calculate $EI$. In the case of the PVC cylindrical beam however a second sample of PVC was obtained for the experiment: a rectangular slab measuring 41 x 5.64 x 0.33 cm. This specimen could be set up as a cantilever beam in order to measure its $EI$ value. From this, and a knowledge of $I$ for the rectangular and cylindrical PVC beams, the $EI$ product of the cylindrical free-free beam could be determined.

The experiment used the cantilever beam system of Fig. 10. A laser was focused on the long edge of the beam such that the laser light was blocked. A detector was then placed in line with the laser light on the beam's opposite side. As the beam vibrated the laser was periodically blocked giving a series of spikes in the inverted detector output. The period of these spikes was then half

the fundamental beam period. Thus, by measuring the period of this signal we had an independent method of measuring fundamental clamped-free beam frequencies. This experiment was performed on both the steel and PVC rectangular beams.

In the case of the steel beam it was not necessary to calculate $I$ since the same beam was to be used in the modal domain sensor experiments. Hence the product $EI$ derived from equation (B.16) using the measured fundamental was sufficient. However the actual value of $E$ was needed in the case of the PVC rectangular beam for use in the cylindrical free-free beam calculations. It was therefore necessary to compute the section moments of both the PVC rectangular and cylindrical beams. These are designated by $I_R$ and $I_C$ respectively and are given by [30]

$$\begin{aligned} I_R &= \frac{bh^3}{12} \\ I_C &= \frac{\pi}{4}[b^4 - a^4] \ . \end{aligned} \tag{C.1}$$

In the first equation $b$ and $h$ represent the rectangular beam's base and height respectively while in the second equation $a$ and $b$ are the inner and outer radii of the cylindrical beam, respectively. From beam dimensions $I_R$ was found to be $3.97\text{x}10^{-4}$ and $I_c$, $4.95\text{x}10^{-2}$. The resulting value of Young's modulus for PVC obtained from the experiment was $3.65\text{x}10^{5}$ giving an $EI_C$ product of $1.8\text{x}10^{4}$. The measured $EI$ product for the steel beam was found to be 19.49. These values were employed in equation (B.16) in the determination of theoretical beam frequencies.

# Vita

Paul A. Ehrenfeuchter was born on June 22, 1960 and attended Neshaminy Langhorne High School in Langhorne Pennsylvania. He graduated from Drexel University in 1983 earning a B.S. in Physics and continued working in the non-destructive testing laboratory at the Naval Air Development Center as a research physicist. He returned for graduate study in 1984 and completed his degree requirements in 1986 earning a Master of Science in Electrical Engineering from Virginia Polytechnic Institute and State University.

# Appendix B. Detection of Acoustic Emission in Plywood

# DETECTION OF ACOUSTIC EMISSION IN PLYWOOD USING IMBEDDED OPTICAL FIBER SENSORS

## OBJECTIVE

The objective of the research presented in this report is to determine whether or not acoustic emission in plywood can be detected using imbedded optical fiber sensors.

## INTRODUCTION

The monitoring of acoustic emission is an important technique in the nondestructive characterization of strained materials because time and frequency domain analyses of AE events yield information about the type, geometry and location of defects,as well as how a material may fail. The quantative interpretation of AE event signatures is critically dependant upon the faithfullness of the acoustic transduction and signal processing system in reproducing localized stress wave amplitude as a function of time. Although the usual sensor for acoustic emission is the piezoelectric transducer, several investigators have considered the application of interferometric optical sensing techniques which offer good spatial resolution and frequency response [1,2]. These techniques typically focus one beam of a modified Michelson interferometer to a small spot on the surface of a specimen and measure the time-dependant normal component of surface displacement at the location of that spot.

This report describes the self-referenced interferometric optical detection of acoustic emission in plywood using an optical fiber waveguide imbedded directly within the composite matrix.

## EXPERIMENT

Multimode optical fiber was imbedded between the two center plys in a four-ply symmetric cross-ply balsa wood composite. Common wood glue was used to bond the laminae together, and the overall dimensions of the laminate were 15.24cm x 15.24cm x 1.27cm.

As seen in Figure 1, the plywood specimen was clamped to an optical table in a cantilever beam comfiguration. The plywood was then loaded in the center of the free end, and using modal domain sensing techniques, the output of the imbedded fiber

sensor was monitored [3]. The output waveforms were then recorded on a self-triggerable digital storage oscilloscope. This detection system recorded burst events at the same time as audible acoustic events were noted.

## RESULTS & OBSERVATIONS

Typical events recorded for the specimen at different times during loading are shown in Figures 2, 3 and 4. These event signatures show remarkable similarity to the signatures of acoustic emission due to composite fiber breakage found by Bennett [3] in a similar experiment using graphite-epoxy composites. Note that in Figures 3 and 4 two separate events were recorded.

Additional interesting observations were made prior to loading the plywood as described above. After initially setting up the experiment, the free end of the clamped plywood was impacted with the eraser end of an ordinary pencil. The output corresponding to this impact is shown in Figure 5. The damped oscillation is approximately 195.0 Hz with a 16.3 Hz envelope superimposed upon it. The 195 Hz oscillation is suspected to be at a frequency corresponding to a plate mode vibration of the plywood specimen. To check this, a speaker from a transistor radio was mounted on the free end of the plywood beam and connected to a signal generator. The signal generator was then swept in frequency from 180 Hz to 210 Hz. A sharp rise in output amplitude was seen when the speaker was driven at 195 Hz. The output of the imbedded optical fiber sensor when the plywood beam was forced to vibrate at 195 Hz is shown in Figure 6. We were unable to cause a forced vibration of large enough amplitude at 16.3 Hz to be detected. Further investigation will be required to determine the cause of this lower frequency vibration.

## CONCLUSION

The results presented in this report show that acoustic emission in plywood can be observed using imbedded optical fibers employed in a modal domain sensing system which is simple and inexpensive. Extensions of this method include the location of the emission source in the two planar dimensions of the composite by triangulation and improvement in the spatial resolution of the sensor by selectively coating sections of the fiber. Also, it has been shown that imbedded optical fiber sensors can be used to collect information on the plate mode vibrations of plywood.

| PLY ORIENTATION | |
|---|---|
| 1 | 90° |
| 2 | 0° |
| FIBERS | 0° |
| 3 | 0° |
| 4 | 90° |
| | |

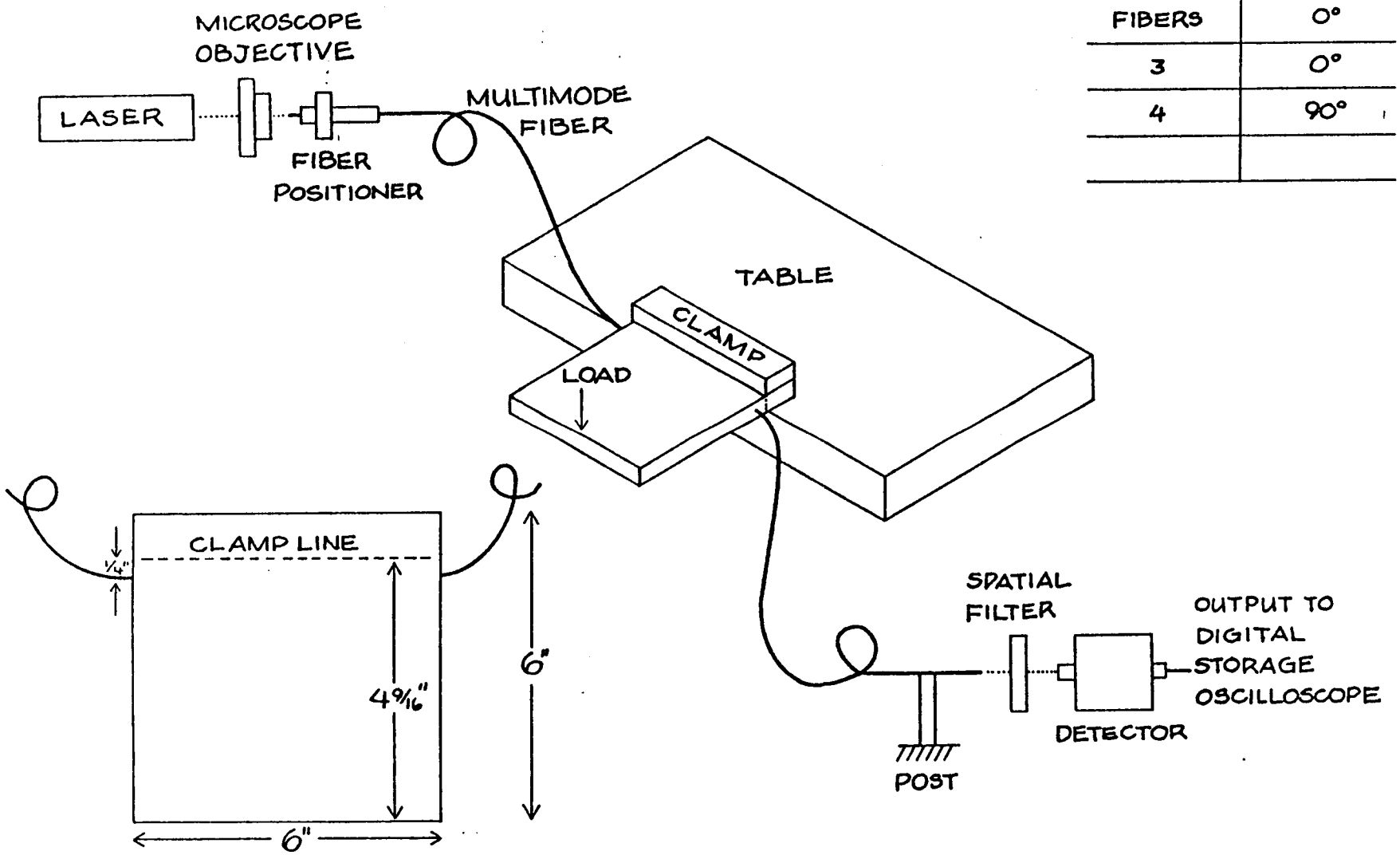


FIGURE 1. EXPERIMENTAL SET-UP

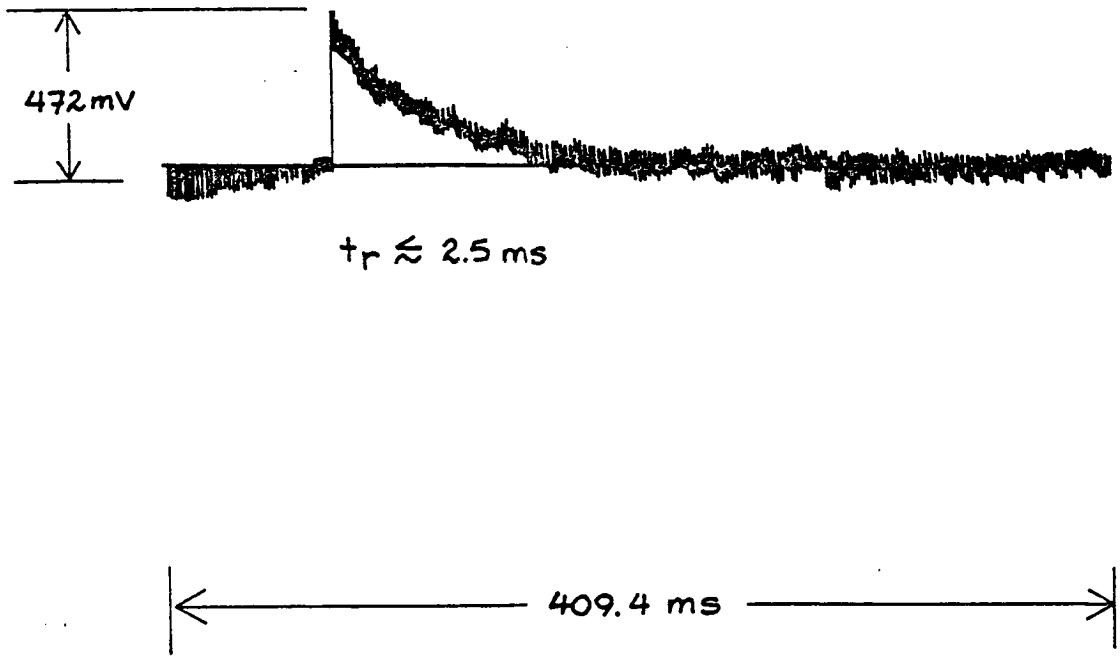


FIGURE 2

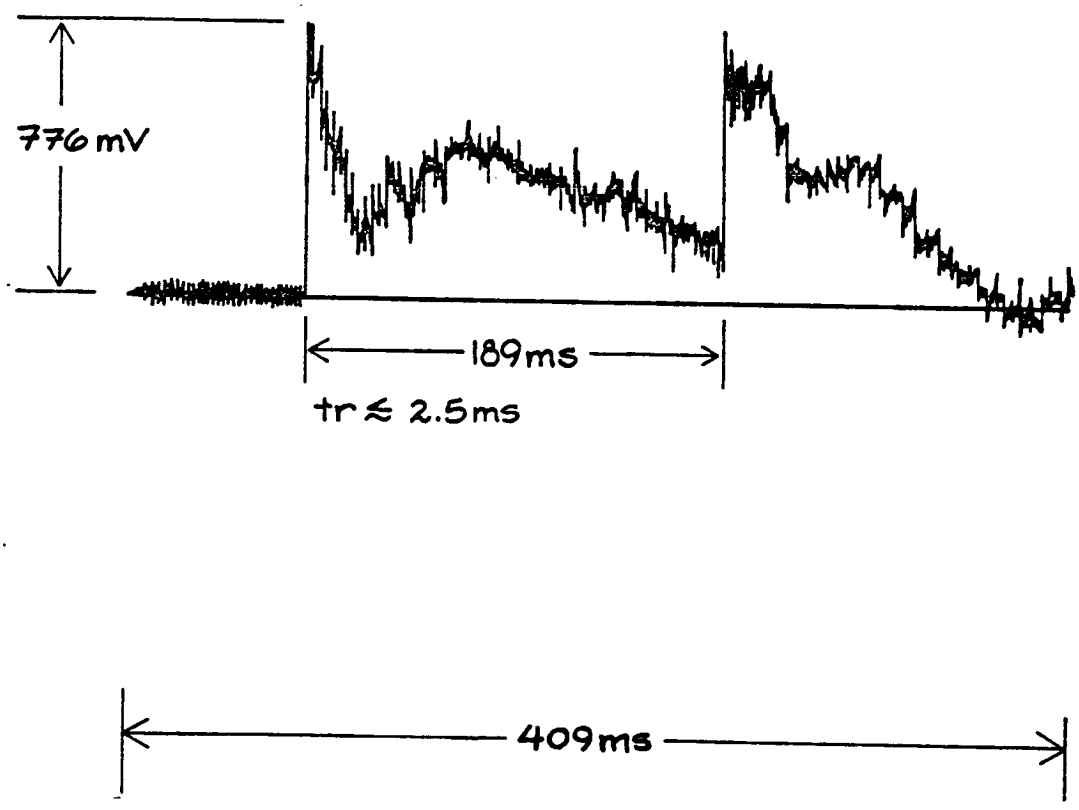


FIGURE 3.

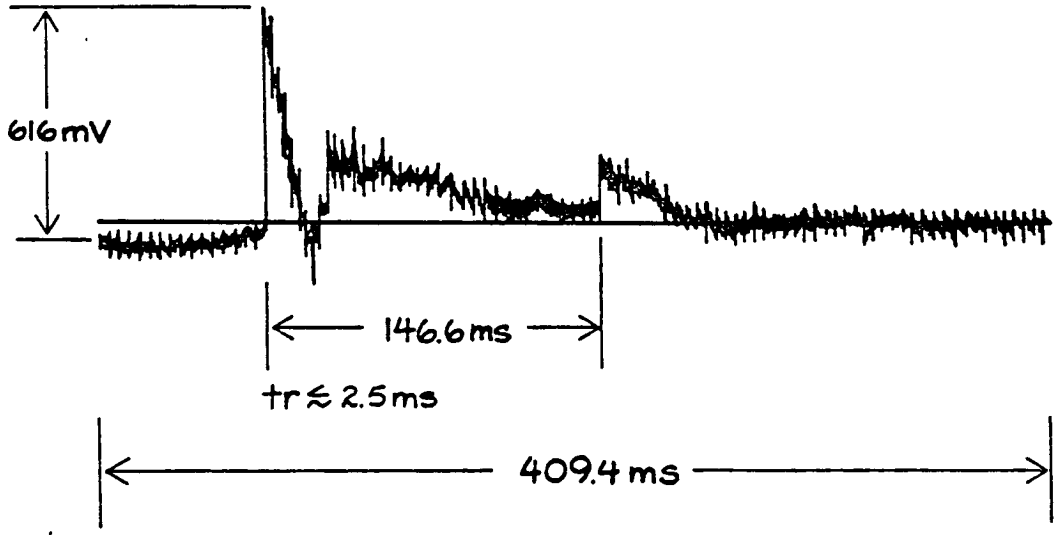


FIGURE 4.

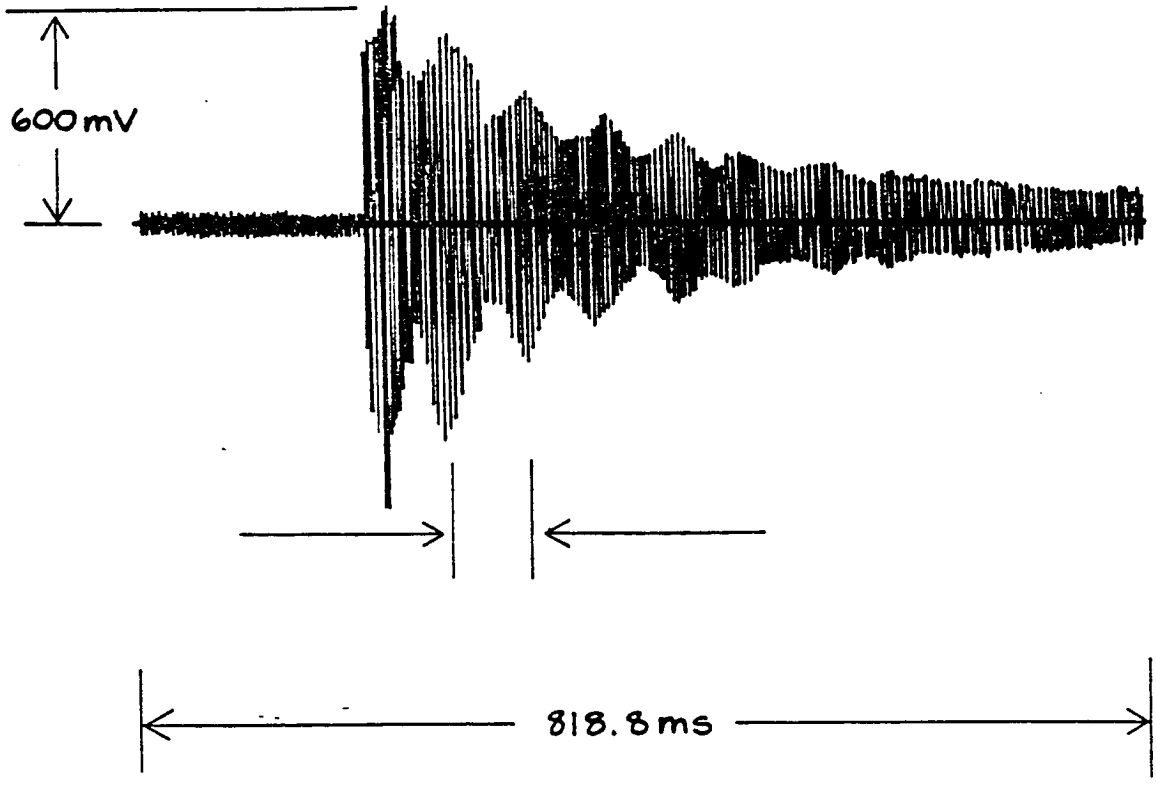


FIGURE 5.

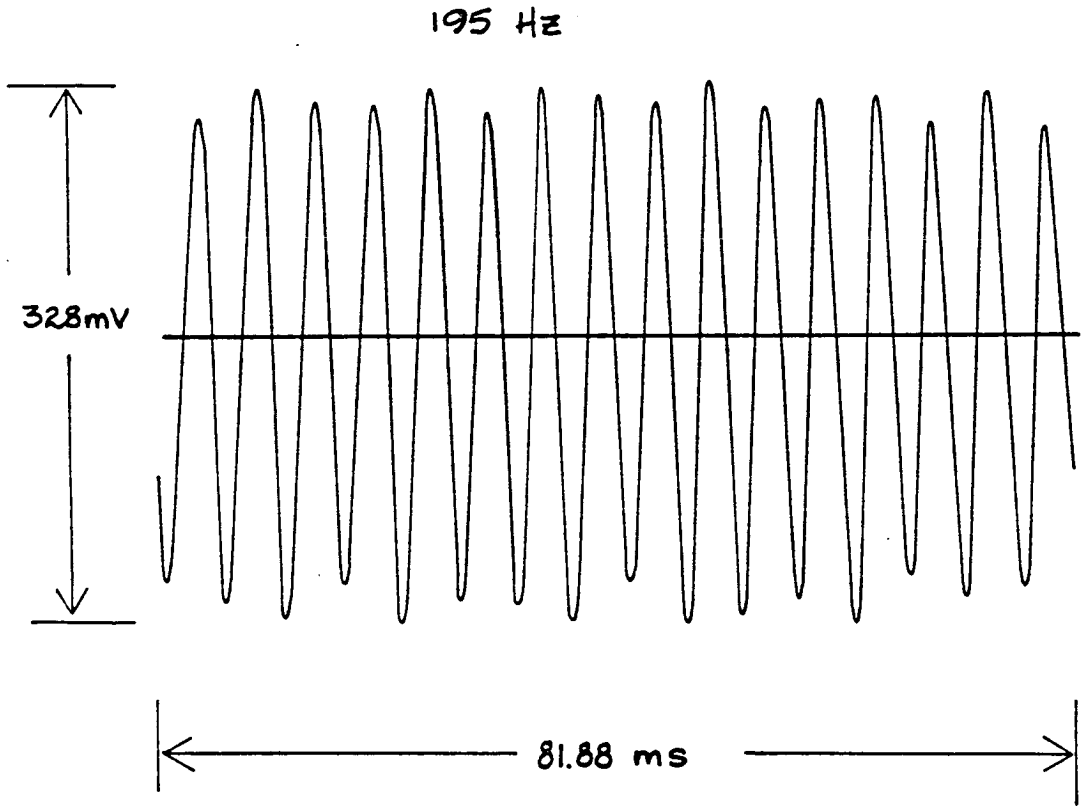


FIGURE 6.

## REFERENCES


1. C. H. Palmer and R. E. Green, Appl. Opt. 16, 2333 (1977).

2. R. A. Kline, R. E. Green and C. H. Palmer, J. Acoustic. Soc. Am. 64, 1633 (1978).

3. K. D. Bennett, R. O. Claus and M. J. Pindera, Proc. Review of Progress in Quantitative NDE Conference (San Diego, CA), August 1986.

ORIGINAL PAGE IS
OF POOR QUALITY

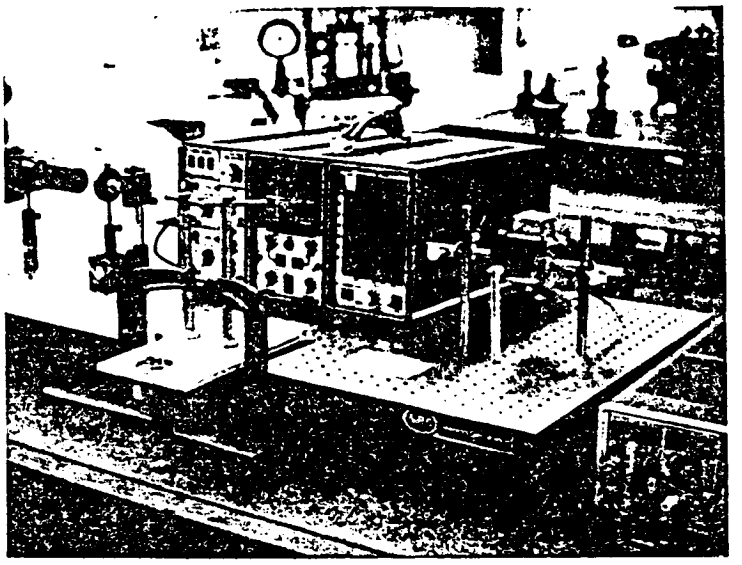

EXPERIMENTAL SET-UP FOR THE DETECTION
OF ACOUSTIC EMISSION IN PLYWOOD

# Appendix C. Optical Fiber Modal Domain Sensing of Stress Waves

ORIGINAL PAGE IS
OF POOR QUALITY

# OPTICAL FIBER MODAL DOMAIN DETECTION OF STRESS WAVES

N.K.Shankaranarayanan, K.D.Bennett, and R.O.Claus

Fiber and Electro-Optics Research Center
Virginia Tech
Blacksburg, VA 24061

## ABSTRACT

Modal domain methods utilizing mode-mode interference have been used to detect acoustic emission, stress waves and vibration in composite specimens. Experiments have been conducted to investigate the modal domain method using few-mode fibers as well as multi-mode fibers. These results and a generalized theory of modal sensing phenomena are presented. Observations about modal domain techniques are also discussed.

## INTRODUCTION

Fiber optic acoustic and strain sensors based on interferometric methods have been reported in the literature [1,2]. Aside from analysis of conventional dual-beam interferometers, interference between different modes in the same fiber has also been studied by various authors. "Modal domain" modulation mechanisms have been used to detect acoustic waves [3,4], vibration in structures [5,6] and acoustic emissions from graphite-epoxy composite laminae [7].

Modal domain techniques are based on the interference between modes in an optical fiber, primarily due to phase modulation effects. Unlike dual-beam interferometric sensors, modal domain sensors are very simple to implement because all of the participating modes are in the same fiber. Complex methods of stabilizing the reference arm are not neccessary and such sensors are amenable to rugged sensor designs. Their sensitivity to strain is about 20 dB lower than conventional interferometers [3].

This paper reports the detection of acoustic emission and related stress waves in composites using modal domain methods and includes results from the sensing of vibrational components of simple beam structures. A generalized analysis and model based on phase modulation due to strain is also presented.

## MODAL DOMAIN SENSING: THEORY AND TECHNIQUES

If we consider the operation of dual-beam interferometry in terms of interference between two differentially modulated light waves, it is reasonable to expect similar effects from the interference between modes in the same fiber.

We shall first review the mechanism of phase modulation in optical fibers. The phase of a mode is given by $\varphi = \beta L$ . A phase modulating effect such as strain in the axial direction will change the phase and this is described by

$$\Delta\varphi = \beta\Delta L + L\Delta\beta.$$

Note that the changes in L and β could arise from many different effects. Such phase modulations have been analysed by others [2,10]. We reproduce from the latter the following expression giving the change in phase due to longitudinal strain $\varepsilon_l$ and radial strain $\varepsilon_r$. Thus

$$\Delta\varphi = 2\pi\frac{L}{\lambda}\left[\varepsilon_l - \frac{n^2}{2}(P_{11} + P_{12})\varepsilon_r + P_{12}\varepsilon_l\right],$$

where L is the length of interaction, n is the index of the core, and $P_{11}$ and $P_{12}$ are photoelastic constants for the optical fiber material.

To see how this phase modulation due to strain results in a modal domain sensing signal, we focus our attention on two modes propagating in the fiber. We have for modes m and n,

$$E_m(\rho,\theta,z) = E_{mo}(\rho,\theta)\exp(i\beta_m z + i\varphi_m), \text{ and}$$
$$E_n(\rho,\theta,z) = E_{no}(\rho,\theta)\exp(i\beta_n z + i\varphi_n).$$

After phase modulation we have

$$E_m(\rho,\theta,z) = E_{mo}(\rho,\theta)\exp(i\beta_m z + i\varphi_m + i\psi_m), \text{ and}$$
$$E_n(\rho,\theta,z) = E_{no}(\rho,\theta)\exp(i\beta_n z + i\varphi_n + i\psi_n).$$

The above expressions illustrate the fact that different modes have different β, phases, and phase changes. Different modulation schemes can be considered to represent the different mechanisms involved in mode-mode interference [4] . The three primary factors are differential phase modulation, group delay demodulation due to different group delay times and a triple transit echo due to multiply reflected waves. This analysis predicts the occurrence of harmonic multiples in the modulation and also indicates optimimum conditions for greater change in the intensity distribution.

Another approach is to consider the field intensity distribution at the endface by calculating the real part of the z component of the complex Poynting vector [3] . Here, all possible inter-

Prprint, Proceedings, IEEE Ultrasonics Symposium (Williamsburg, VA), Nov. 1986

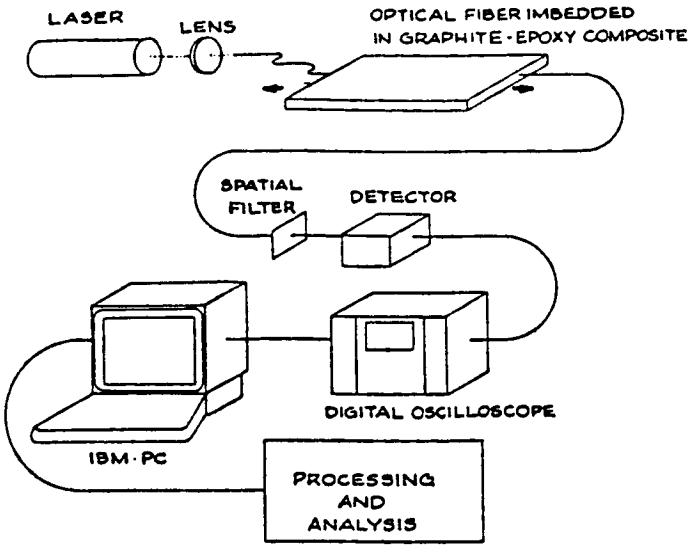


Fig. 1. Optical fiber modal domain sensing: Modal domain sensing itilizes the mode-mode interference in optical fibers due to perturbations. The far-field output pattern is spatially filtered and local intensity responses are detected by an optical detector.

actions must be considered and this approach is impractical beyond a few modes. This approach reveals specific optimum conditions. Ideal combinations are modes having large differences in $\beta$ and modulation. $HE_{11}, HE_{12}$ are good candidates and so are $HE_{11}, TM_{01}$.

The technique used by us at Virginia Tech for modal domain sensing is spatial filtering of the (far-field) output pattern to obtain a region that reproduces mode-mode interference effects. We have used few-mode fibers as well as multi-mode fibers to observe these mode-mode interference effects. In both cases, we have observed a redistribution of the far-field pattern due to perturbations. The few-mode fiber ($V \simeq 4$) of course has fewer speckles in the output pattern. Far-field diffraction patterns of particular mode combinations have been analysed before [9].

Our hypothesis is that the re-distribution of the speckle pattern is due to the phase changes in the components of the fields at the fiber endface. A speckle pattern (with either a few large speckles or numerous small speckles) is the far-field diffraction pattern of the field distribution at the fiber endface and specifically, speckles arise from mode-mode interference effects analagous to the fringe patterns from dual beam single-mode interferometers. The speckle pattern redistribution is much like a two-dimensional fringe shift and can be related directly to phase modulation in the fiber. The intrinsic amplitude modulation effect due to bend loss and other mechanisms are negligible when considering the more sensitive phase modulation.

Because the mode components are in the same fiber, there is a reduction of absolute sensitivity since the modes are affected by marginal differential phase modulation. Moreover, the optimum mode combinations referred to above cannot always be launched. This is a more important problem in the few mode fiber because the placement of the detector and spatial filter becomes difficult. For patterns with numerous small speckles, this is not so critical because of the random effects in the phases of the many carriers.

## EXPERIMENT

Several experimental systems were used for verification of the modal domain stress wave and strain mechanisms. First, optical fibers of core/clad diameters 8/125 μ with $V \simeq 4$ were imbedded in 25.4 x 2.54 cm, symmetric cross-ply graphite-epoxy composite specimens. The specimens had eight 1.02 mm plies and were laid up by hand using

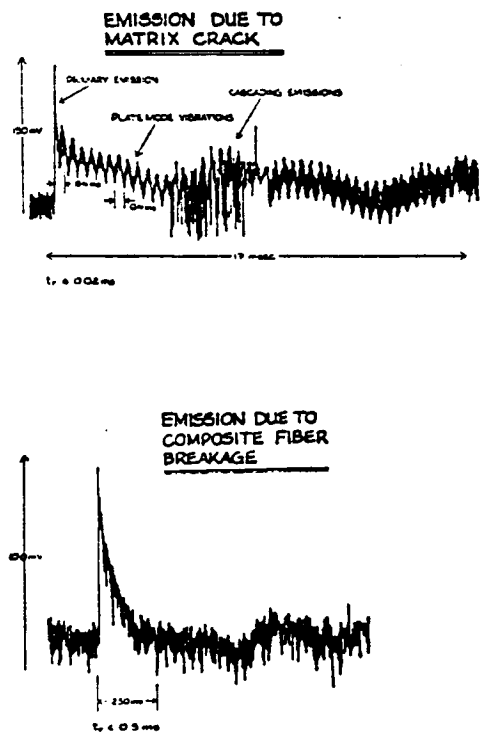


Fig. 2. Optical fiber response to acoustic emission: The sharp rise in the first emission is characteristic of matrix failure. The slow decay in the second is characteristic of graphite fiber failure.

ORIGINAL PAGE IS
OF POOR QUALITY

prepreg tapes. This provided a convenient way of bonding optical fibers inside a medium.

It is well known that failure of the matrix material as well as the graphite fibers occurs in graphite-epoxy composites under tensile loads. This releases acoustic energy as acoustic emissions. An acoustic emission is a release of a burst of bonding energy which propagates as a stress wave in the sample. For our applications, it is a convenient stress wave generator.

Coherent light of 633 nm wavelength was injected into the fiber and a speckle pattern monitored at the output. To observe mode-mode interference, the speckle pattern was spatially filtered such that a small part of the pattern fell on the detector. It was found by experience that it was best to select a small region on the edge of one of the large speckles for such detection. This positioning turned out to be quite critical as expected. The composite specimen was loaded slowly on an automated tension frame and audible acoustic emissions were generated during the process.

Fiber detected acoustic emission signals are shown in Fig. 2. The sharp peak in the first signal is characteristic of matrix failure whereas the second signal is characterisitc of graphite fiber failure because of the slow decay. Just after an acoustic emission, the point on the fiber nearest to the failure is first affected by the stress wave resulting in phase modulation. An AET piezoelectric transducer on the surface was used as a reference in some of the tests and excellent correlation in time between the AET and fiber sensor signals is evident in Fig. 3. These events also occurred at times when the events were noted as audible acoustic emissions. Note the damped nature of the optical fiber response. This is due

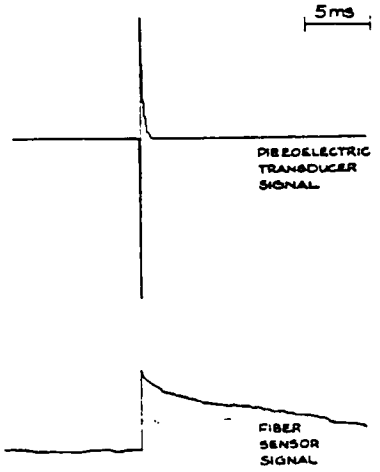


ACOUSTIC EMISSION
IN GRAPHITE-EPOXY COMPOSITES

Fig. 3. Acoustic transducer and optical fiber responses to acoustic emission: The acoustic transducer was placed on the surface of the specimen whereas the fiber was imbedded in the center.

to the fact that as the stress wave propagates through the specimen, it influences the optical fiber over its length and we see a cumulative effect. This effect could be advantageous in developing a distributed sensor.

After the initial burst of energy, we expect vibrations as dictated by the mechanics of the structure. Optical fibers imbedded in a structure experience strain when the structure vibrates. To study strain and vibration in beams, further experiments were done.

A cantilever (clamped-free) beam as well as a clamped-clamped beam were set-up with optical fibers imbedded in them. These specimens were 4-ply, symmetric cross-ply, 25.4 x 10.16 cm composites. To study the modal domain mechanisms with multimode fibers, we imbedded 50/125 μ, 0.2 NA multimode fibers between the center two plies. As expected, the speckle pattern had numerous small speckles and the placement of the detector was not as critical as the few-mode fiber and coupling efficiency was higher because of the larger core and NA. We feel that it would be more practical to use multi-mode fiber to develop sensors for ease of design and production.

We obtained vibration signals for the cantilever beam with an initial lateral displacement as well as the clamped-clamped beam with an initial impact. The frequency spectra for the two cases are shown in Fig. 4.

The average strain in a cantilever beam is [2]

$$\varepsilon = \frac{3da}{2L^2},$$

where a is the distance from the axis, L is the length and d the initial displacement. To observe this strain effect better a cantilever was set up with an optical fiber imbedded in the center with a return path on the top surface. Thus, in the second case, there was a cumulative influence from the two layers. The frequency spectrum is shown in Fig. 5. We note a perfect correlation with theory for the frequency of the second harmonic. It is very interesting that the fiber displays faithfully the second harmonic of vibration in the beam. The reponse from the fiber in the center only is probably due to non-idealities in the system. The response from the surface is however more faithful to the vibrational characteristics of the beam. The observed multiples of the fundamental frequency are predicted from the phase modulation analysis and are components arising from carrier modulation phenomena. These results reveal the fidelity of the modal domain sensing mechanism to strain and vibration.

## CONCLUSION

We have used the modal domain sensing mechanism to detect acoustic emission, stress waves, and vibration in composites. A general analysis of the problem has been presented. Current and future work include additional quantitative tests and mathematical analyses. The sensitivity of such sensors is about two orders lower than MZI sensors [3]. Dynamic range is limited because only a 2π

ORIGINAL PAGE IS
OF POOR QUALITY

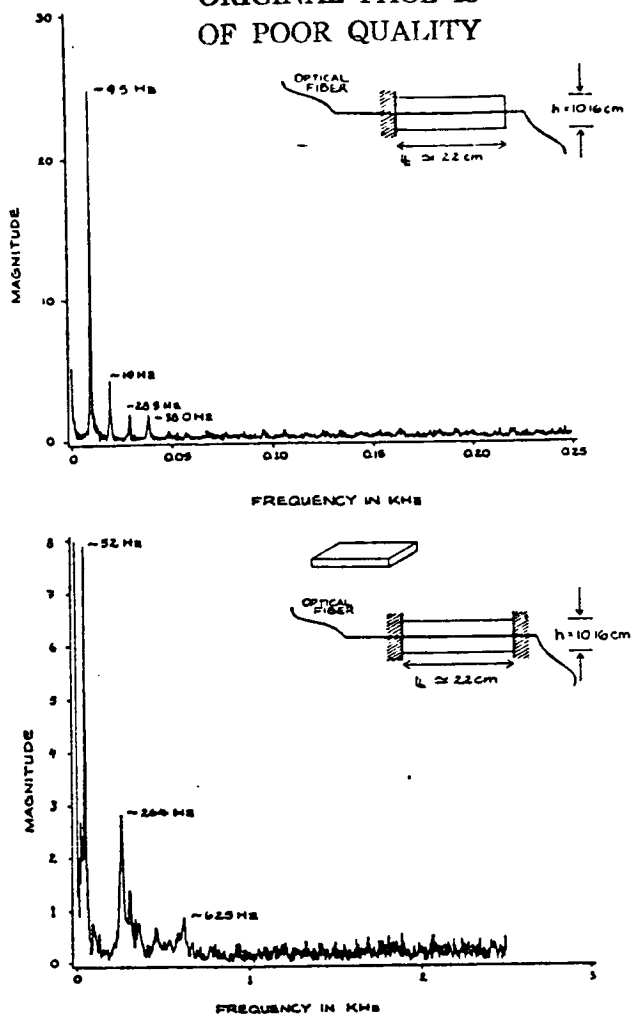


Fig. 4. Optical fiber response to vibration: Frequency spectra of reponses from optical fibers imbedded in the center of clamped-free beams and clamped-clamped beams. Multiple frequency components are due to the inherent phase modulation effects.

phase change is available and fringe counting is not applicable. However, this is not a drawback as the range of applications of this method is intended to be different. These sensors are simple to set up and quite sensitive, but not easily calibrated. They are excellent for non-exacting, simple, rugged, low-cost applications.


## ACKNOWLEDGEMENTS

This work has been sponsored by Simmonds Precision, the NASA Langley Research Center and the Center for Innovative Technology. We wish to acknowledge Bradley Duncan's assistance in the vibration experiments.


## REFERENCES


[1] J.A.Bucaro, H.D.Dardy, and E.F.Carome, Appl. Opt. vol. 16, no. 7, 1761, (1977)

[2] C.D.Butter and G.B.Hocker, Appl. Opt., vol. 17, no. 18, 2867, (1978)

[3] M.R.Layton and J.A.Bucaro, Appl. Opt., vol. 18 no. 5, 666, (1979)

[4] S.A.Kingsley and D.E.N.Davies, Electronics Lett., vol. 14, no. 11, 322, (1978)

[5] K.D.Bennett and R.O.Claus, Proc. IEEE Region 3 Conf. (Richmond, VA), April 1986, pp 95-98

[6] P.A.Ehrenfeuchter, "Modal domain sensing of vibration in beams," M.S. Thesis, Virginia Tech, December 1986

[7] K.D.Bennett, R.O.Claus, and M.J.Pindera, "Internal monitoring of acoustic emission in graphite-epoxy composites using imbeded optical fiber sensors," Proc. Rev. Quant. NDE Conf., (San Diego, CA), August 1986.

[8] B.Culshaw, OPTICAL FIBER SENSING AND SIGNAL PROCESSING, Peter Peregrinus Ltd,, 1984

[9] N.S.Kapany and J.J.Burke, OPTICAL WAVEGUIDES, Academic Press, 1972


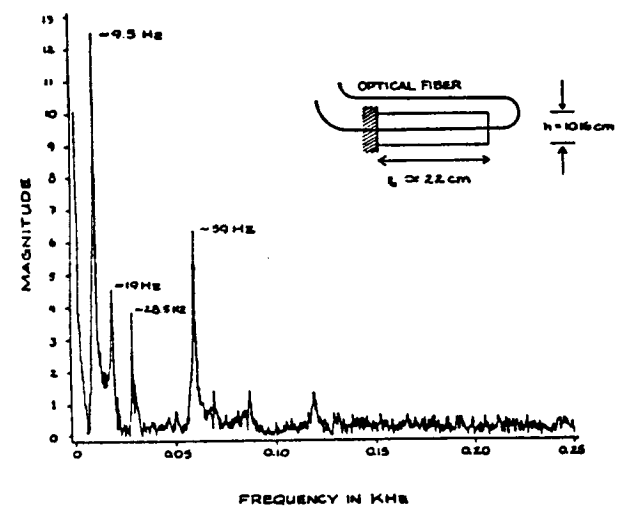


Fig. 5. Optical fiber response to vibration: Frequency spectrum of response from optical fiber imbedded in the center of a cantilever with a return path on the surface.

# Appendix D. Axial Strain Effects on Optical Fiber Mode Patterns

# Axial Strain Effects On Optical Fiber Mode Patterns

by

K.T.Srinivas

Thesis submitted to the Faculty of the

Virginia Polytechnic Institute and State University

in partial fulfillment of the requirements for the degree of

Master of Science

in

Electrical Engineering

APPROVED:

R. O. Claus, Chairman

R. J. Pieper

T. C. Poon

January 1987

Blacksburg, Virginia

# Acknowledgements

I would like to express my sincere appreciation to my advisor, Dr. Richard. O. Claus, for his ideas and guidance, and in particular, his endless enthusiasm. I am particularly grateful to him for having introduced me to the fascinating field of Ftber Optic Sensors. I also wish to thank the other members of my advisory committee, Dr. T.C. Poon and Dr. R.J. Pieper, for their comments, suggestions and encouragement.

I am also grateful to the members of the fiber optic group, Kim D Bennet, N K Shankar, Paul Ehrenfeuchter, Kent Murphy and Mahesh Reddy for their suggestions and help on this project. I would also like to thank Ms. Robin Rogers and Ms. Ann Goette for willing to share their time and helping me with the drawings and figures.

Axial Strain Effects On Optical Fiber Mode Patterns

by

K.T.Srinivas

R. O. Claus, Chairman

Electrical Engineering

(ABSTRACT)

Axial strain effects in multimode fibers are studied. A few-mode fiber is mounted on a tensile testing machine and strained at various speeds. The output of a monochromatic light source passing through it is monitored and recorded. Relations are noted between the light output the magnitude of tension and the rate of the applied axial strain. Flexural behaviour of the optical fiber at various tensions is also studied by monitoring the modal output pattern. Relations are compiled to serve as a beginning to model these and other related modal effects. A theoretical background is also suggested to explain the observed effects.

# Table of Contents


**1.0 Introduction** ..... 1

1.1 Motivations and Overview ..... 5

1.2 Fundamentals of Optical Transmission in Fibers ..... 7

1.3 Polarimetric Sensing ..... 8

1.4 Introduction to 'Modal Domain' Sensing ..... 8

**2.0 Theoretical Background** ..... 10

2.1 Introduction to Stress and Strain in Solids ..... 10

2.1.1 Stress ..... 10

2.1.2 Strain ..... 14

2.1.3 Relation Between Stress and Strain ..... 16

2.2 Optics of Photoelasticity ..... 17

3.0 Mechanisms of Modulation ..... 19

3.1 Phase modulation mechanisms in fibers ..... 19

3.2 Mechanisms of Polarization Modulation ..... 24

**4.0 Experiment and Observations** ..... 29

4.1 Motivation and Reasons ..... 29

4.2 Apparatus ..... 30

4.3 Experiment and Observations ..... 31

**5.0 Conclusions** ..... 37

5.1 Discussion ..... 37

5.2 Conclusion ..... 39

5.3 Suggestions ..... 39

**6.0 References** ..... 41

VITA ..... 43

# List of Illustrations

Figure 1. Basic fiber-optic interferometer ..... 4

Figure 2. Components of force and stress ..... 11

Figure 3. Displacement of line elements ..... 12

Figure 4. Stress components in rectangular co-ordinates ..... 15

Figure 5. Experimental set-up. ..... 33

Figure 6. Output for 0.5 mm/min displacement rate. ..... 34

Figure 7. Output for 1.0 mm/min displacement rate. ..... 34

Figure 8. Output as tension is applied. ..... 35

Figure 9. Output as tension is released. ..... 35

Figure 10. Output due to vibrating beam at the two states of tension. ..... 36

# 1.0 Introduction

The potential of optical fibers as passive non-intrusive sensors of a wide range of physical observables has been well recognized and exploited for more than ten years. The main advantages of optical fibers for sensor applications are their intrinsic dielectric nature, geometric flexibility and small size, providing considerable design versatility particularly suited for certain remote sensing applications.

The development of optical fiber sensors began in 1977 with the development of optical fiber acoustic sensors [1] The following few paragraphs describe some of the past and more recent applications of optical fibers as sensors.

The operation of all-fiber optic sensors is based upon the modulation of the propagation parameters of light which travels through the fibers. These parameters are intensity, phase, polarization, wavelength and mode.

Intensity modulation is the simplest sensing mechanism to implement. The usual measurand is the relative displacement one or two parts attached to the fiber. The sensor is configured as a microbend transducer, either a reflection type or simple butt coupling type [2]. Of these the microbend sensor

is the most sensitive with resolution of fractions of Angstroms. In general this variety of sensors has a dynamic range of 50-70 dB [2].

By comparision, optical phase modulators have a remarkable sensitivity. Dynamic ranges of $10^7$ are quite easily obtained even for quasi static measurements. These are used in the form of interferometers in most cases. It should be noted that other kinds of modulations also manifest themselves as some form of phase modulation. The most useful application of these devices is the monitoring of temperature, pressure and strains.

Polarization is potentially another powerful modulation mechanism. In most polarization-based devices the fiber itself is the sensor. Monomode fibers are used in most cases and depend on the ability of the measurand to alter the polarization state of the light propagating through the fiber. The principal application has been in the sensing of large electric currents.

Wavelength based sensors are usually in the form of color probes. Here the fiber simply serves to feed light from a source to the monitoring region and to return the modulated light for analysis. Usually large core, high NA fiber is used.

The effect of mechanical perturbations on the various modes propagating in a multimode fiber is yet another method of exploiting the usefulness of fibers as sensors. This a relatively new area of research and applications of this method include the monitoring of vibrations, acoustic emission, etc. [3,4].

Given below are some of the specific applications of fibers as sensors which have been available for the past few years. [1]

Acoustic Sensors

Most work in this area was conducted at the Naval Research Laboratories for underwater acoustic detection via hydrophones in the late 1970's. These generally employ the two arm phase modulated

Mach-Zehnder interferometer or the single fiber, polarimetric type. The former consists of a reference arm and a sensing arm (see Figure 1).

In the reference arm some means is provided to either shift the optical frequency or for phase modulation. The two beams are usually recombined on the surface of a photodetector and suitably demodulated. Modulation of light in the fibers is dependent upon the frequency and amplitude of the impressed acoustic signal. Alternatively, such sensors may be configured as a gradient type in which both arms of the interferometer encounter the signal. Here what is sensed is the gradient and the direction of a pressure wave. In the polarimetric version of this sensor, a single mode fiber has the polarization states of its cross polarized components modulated due to differential birefringence effects produced by the ultrasonic signals. In these applications the fiber is generally configured as a coil. Varying the winding density of such coil structures allows us configure arrays of such sensors.

**Magnetic Sensors** The measurement of magnetic fields is based on principally two effects; the Faraday effect and the magnetostrictive effect. The former requires special kinds of fibers to be able to be sufficiently sensitive. Sensitivities of $10^{-4} G/m$ seem possible in rare earth doped optical fibers. Most magnetic sensors generally work on the second principle as it is more sensitve and does not require the use of any specially doped fiber. Here the fiber is placed in close contact with a magnetostrictive material which changes physical dimension in the presence of a magnetic field. This causes a proportional strain in the attached fiber which results in an optical phase change in an interferometric set-up. The key research in this application is in identifying appropriate magnetostrictive materials to be bonded or coated on to the fibers. Magnetic fields from $10^{-5} - 10^{-9}$G/m are predicted to be detectable by this method [1].

**Fiber Optic Gyros** Passive ring interfrometers have shown promise as inertial rotation sensors . Here a single mode fiber is arranged in a ring to form a Sagnac interferometer. Two counterpropagating beams of light are injected into the rotating fiber loop which causes a phase difference between them. When these two beams are recombined on a detetctor we get a rotation dependent intensity modulation of the light. Sensitivities of as small as 1 deg/hr have been announced.

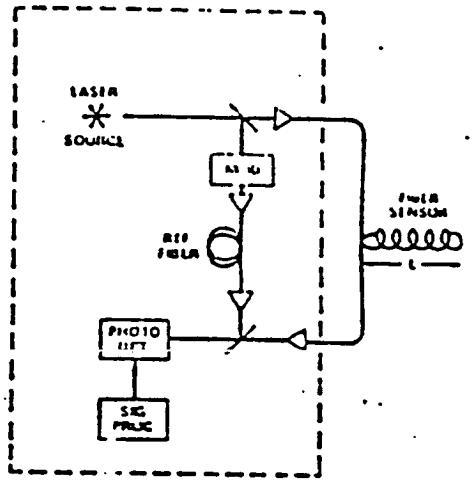


Basic fiber optic interferometer.

Figure 1.

Several other kinds of amplitude sensors are also available[1]. These include microbend type sensors, displacement type sensors and others. The former is based on the principle that a fiber subjected to a spatially periodic bending causes coupling between modes having a propagation constant difference which is proportional to this periodicity. This kind of transducer has been assembled both as a strain and as a dynamic acoustic sensor . Displacement sensors include reflection types that depend upon the movement of a reflecting surface to modulate light being coupled into an adjacent fiber, and the simpler position dependent variety which alters the coupling between two fibers butted together but free to move independently.

## *1.1 Motivations and Overview*

A particularly attractive application of optical fiber sensors is for the monitoring of stress and strain because they have the potential of offering a highly competitive method of nondestructive evaluation in certain hostile or harsh environments. Related applications include the measurement of pressure, temperature, acoustic emission in materials as well as the vibrational modes of strings, beams and similar structures [3]. All these perturbations affect the transmission of light through physically straining the fiber. As a strain sensor, optical fiber is robust. Although the fiber is made of glass its very high elastic modulus makes it remarkably resilient to damage.

There are principally two mechanisms of light modulations that are important in the detection of stress fields, namely polarimetric and interferometric. This is due to the fact that it is the phase and the polarization states of the light transmitted through the fiber that are most sensitive to its variations in refractive index and physical geometry which are modulated by the stress field.

A novel venture in some of these applications is the use of multimode single fiber sensors either imbedded in or firmly attached to the structure being monitored. Here the fiber itself directly

experiences the mechanical perturbations of the structure. Thus, it is certain that there exists a very intimate relation between stresses and strains acting on the fiber and those acting within or on the structures, as the case may be.

From the theory of the mechanics of materials, linear or nearly linear relations should exist for the way the intrinsic material properties and the physical dimensions of the glass fiber are modulated by the mechanical perturbations. Using these relations it should therefore be possible to interpret the variation in the parameters of light output from the fibers using a combination of the electromagnetic theory of propagation in dielectric waveguides and the photoelastic effect, which relates the change in optical properties (refractive index) of a material and an impressed strain. Equations of this nature exist in various publications on specific topics and applications. What has been attempted here is to bring all of these considerations together and to compile those that would specifically serve our purpose of understanding the performance of mechanical perturbation sensors, tailoring those that do not fit our purpose and suggesting some which are not available. This is included in the third chapter of this report. No extensive explanations of the nature and mechanisms of optical transmission through fibers is given. Some of the concepts of stress, strain and the photoelastic effects are however introduced in the second chapter. This forms the first section of this report.

The second section is a report on experiments conducted to establish some basic ideas about the modal domain sensing techniques for strain measurements, being pursued at the Fiber and Elctro-Optics Research Center here at Virginia Tech. These include the work done by Ehrenfeuchter [3] and Shankaranarayanan [4]. In both cases a single multimode fiber was used to monitor stress, specifically vibrations of certain structures [3] and monitoring of acoustic emission in graphite-epoxy coupons [4]. It is evident from these works that the fiber was subjected to a variety of strains. So it was necessary that effects due to specific strains be studied independently so as to be able to model the effects due the combination of strains more thoroughly. So as a prelude to this effort experiments were conducted to subject the fiber to axial strain alone. The

experimental results are presented and the preliminary conclusions are stated. This comprises the fourth and fifth chapters.

## 1.2 Fundamentals of Optical Transmission in Fibers

Optical fibers are structured as two concentric glass cylinders having slightly different refractive indices. Light waves propagating through a fiber may be visualised as being guided along by sucsessive total internal reflection. The resulting incident and reflected waves then set up interfering standing waves along the transverse direction of the waveguide. The field distribution in the transverse direction remains unchanged as the wave propagates along the axis. This kind of stable standing wave field distribution is called a mode. Such a mode may also be defined as an allowable field configuration for a given waveguide geometry, that satisfies Maxwell's equations and all of the boundary conditions. It is the difference in the two indices and the fiber diameter that determine if a particular mode will be guided or not. The quantities of interest here are the V number of the fiber given by,

$$V = k_0 a \sqrt{n_1^2 - n_2^2},$$

and the propagation constant for a mode N

$$\beta_N = f(V,N),$$

where a is the core diameter and $n_1$ and $n_2$ are the core and clad refractive indices, respectively. The V number is a dimensionless quantity which determines how many modes a fiber can support. Note that it is dependent upon the fiber dimension and the refractive index. This is a particularly important parameter in the single fiber multimode sensor applications, to be considered later, as these are precisely the parameters of the fiber that are modulated. $\beta$ is dependent upon the V

number and is modulated in both polarimetric and interferometric sensors, the two main varieties of sensors. The differences in the propagation constants of the modes cause them to interfere with one another which is an important effect as will become clearer later on.

## 1.3 Polarimetric Sensing

All such sensors are single mode types supporting the lowest order mode, the $HE_{11}$ mode. From the theory of dielectric waveguides it is known that in actuality a second orthogonal mode is also guided simultaneously. Ideally these orthogonal modes have the same propagation constants due to the isotropic nature of glass. But any anisotropy induced due to an external (or internal) stress field causes these to vary via a change in the circular symmetry of the fiber and a change in refractive index due to the photoelastic effect. This induces a differential phase change between the two guided modes resulting in a birefringence. Monitoring this variation in phase helps us sense the perturbing mechanical field.

## 1.4 Introduction to 'Modal Domain' Sensing

Modal domain sensing is a method of interferometric sensing. Here the fact that different modes in a fiber have different propagation constants, which are modulated by different amounts by mechanical perturbations, forms the basis of a single multimode fiber acting as an interferometric sensor.

In the conventional Mach-Zender type of interferometer it is the phase difference between the light arriving from two different arms that causes the interference fringe pattern, and the variation in physical length which is mainly responsible for the shift in fringes. By comparison, the far field output pattern of any multimode fiber is observed to be a speckle pattern. It is felt [4] that this speckle pattern is an interference phenomenon between the various modes.

Various experiments involving such multimodal sensors [3,4] have proven that there is a definite rearrangement of this pattern, and a comparison of the experimental observations shows a unique relationship between the mechanical perturbations and the spatial rearrangement of the far field speckle pattern of the output light. This immediately suggests a relationship between the mechanical forces acting on the fiber and the variations in the optical transmission parameters of the fiber undergoing these perturbations. It is therefore necessary that these relations be available to help better quantify the modal domain sensing phenomenon. As a beginning to this end some elementary relations between the mechanical and optical parameters of have been presented.

However a major stumbling block is that the speckle forming mechanism is not too well understood at this moment. Principally due to the complex nature the of mode-mode interaction, it is not possible, in the present work, to also give a proven model for the the speckle rearrangement effect. A practical difficulty is the control of the launching of specific modes in order to know the modes existing in the fiber to be able to model the phenomenon. A more theoretical explanation of this phenomenon may be found in the works of Kapany [5].

But so much is clear that the analysis given in chapter 3 would definitely figure in any further work on this matter, perhaps in some modified form. Therefore, a compilation of this analysis is seen as a helpful supplement in that effort.

# 2.0 Theoretical Background

## *2.1 Introduction to Stress and Strain in Solids*

The following paragraphs briefly introduce some basic definitions and equations concerning stress and strain in solids. Also stated are optical effects due to these and related equations [7,8].

### 2.1.1 Stress

A body subjected to external forces has internal forces induced through the material bulk. The average stress $\sigma_m$ is defined as

$$\sigma_m = F/A, \qquad 2.1$$

where F is the resultant force acting a section of area A. Stress at a point within a body is defined over an area $\delta A$ as the limit

$$\delta F/\delta A. \qquad 2.2$$

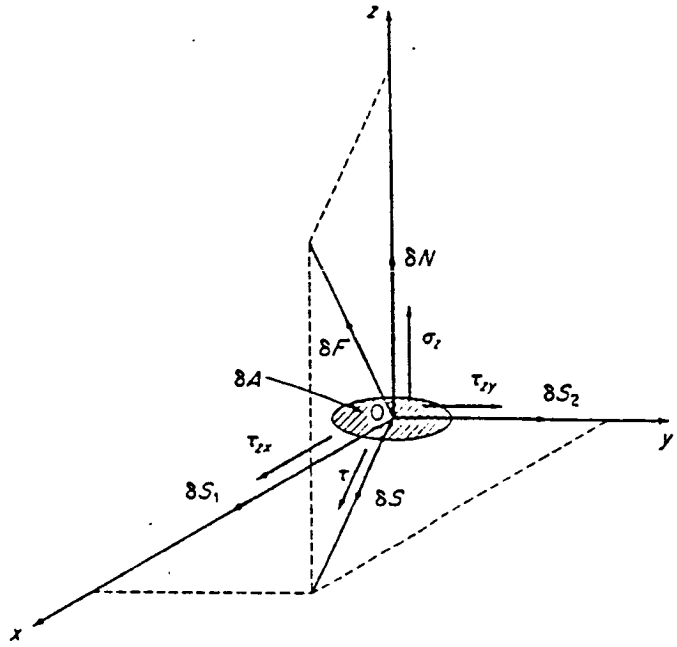


Components of force and stress

Figure 2.

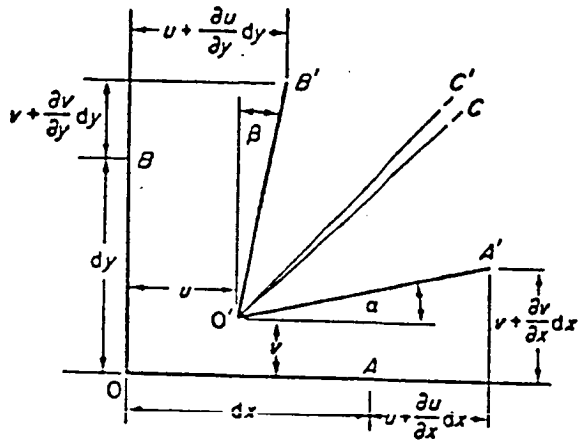


Displacement of line elements in rectangular co-ordinates

Figure 3.

$\delta F$ may be components $\delta N$ acting normal to $\delta A$ and $\delta S$ acting in the plane of the section. In Figure 2 $\delta N/\delta A$ and $\delta S/\delta A$ are, respectively, the normal and shear stress components. Also $\delta S$ may be replaced by $\delta S_1$ and $\delta S_2$ where in the limiting case

$$\delta S_1/\delta A = \tau_{zx}, \qquad 2.3$$

and

$$\delta S_2/\delta A = \tau_{zy} \qquad 2.4$$

The stress components are completely characterized by the forces shown in Figure 2. Here the $\sigma$'s are the normal stresses and $\tau$'s are the shear stresses.

Let us now consider the deformations or strains produced due to the stresses. We start with a spherical element in an unstressed body. If now a uniaxial stress, say tensile, acts on the spere all chords will be changed by amounts proportional to their original lengths. In this way the sphere is transformed into an ellipsoid. The shape of the ellipsoid completely characterizes the state of the stress on the element and can be specified by the independent lengths of the three mutually perpendicular principal axes and their directions.

Displacement of points on the surface of the sphere, in the directions of the axes of the ellipsoid, are purely radial while those of all other points are partly radial and partly tangential. Since radial displacements result from normal stresses and tangential displacements result from shear stresses, it follows that the stresses are purely normal at points in the direction of the principal axes while at all other points both normal and shear stresses are produced. If now the sphere is imagined to be indefinitely reduced and concentrated about a point in a stressed material, there exist three mutually perpendicular directions in which stresses are purely normal. These are referred to as the principal stresses $\sigma_1$, $\sigma_2$ and $\sigma_3$.

### 2.1.2 Strain

To determine the strains at a point O parallel to one of the co-ordinate plane let us consider, as shown in Figure 3, two infinitesimal line elements OA and OB in a rectangular coordinate system. Let these elements be displaced in the strained body to O′, A′ and B′. If O is displaced by u and v to O′, as shown, we write the corrosponding displacements of A′ and B′ as

$$u + \frac{\delta u}{\delta} x dx; v + \frac{\delta v}{\delta} x dx. \qquad 2.5$$

One way of understanding the above expressions is recognizing them as the first two terms of a Taylor series expansion. We define the linear or normal strain as the change in length per unit length. Now the change in the length of element OA in the x direction is given by $(\delta u/\delta x)dx$. Strain therefore is given by $(\delta u/\delta x)dx/dx$, or normal strain in the x direction is given as

$$\varepsilon_x = \frac{\delta u}{\delta x}. \qquad 2.6$$

The shear strain is defined as the sum of the angles $\alpha + \beta$. By considering the two right-angled triangles which include the angles $\alpha$ and $\beta$, assuming these angles to be small, we write the shear stresses as

$$\gamma_{xy} = \alpha + \beta = (\frac{\delta v}{\delta x}) + (\frac{\delta u}{\delta y}). \qquad 2.7$$

In this way we can relate all six components of strain at a point as

$$\varepsilon_x = \frac{\delta u}{\delta x} \quad \varepsilon_y = \frac{\delta v}{\delta y} \quad \varepsilon_z = \delta\frac{w}{\delta z}, \qquad 2.8$$

$$\gamma_{xy} = \delta u/\delta x + \delta v/\delta y \quad \gamma_{yz} = (\delta w/\delta y) + (\delta v/\delta z) \quad \gamma_{zx} = (\delta u/\delta z) + (\delta v/\delta x), \qquad 2.9$$

where u, v, and w are the components of displacements of the point parallel to the x, y and z axes.

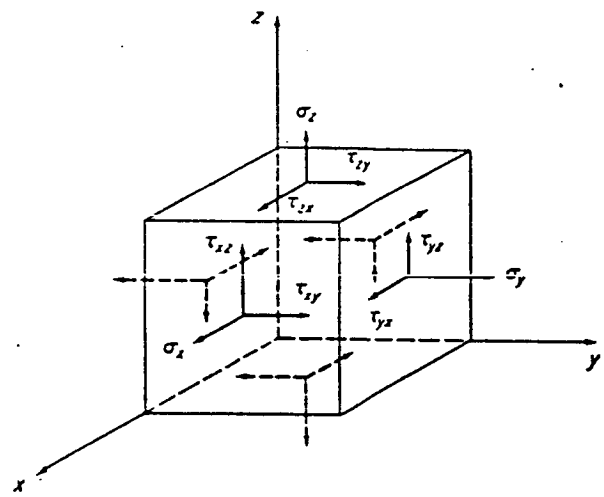


Stress components in rectangular co-ordinates on an infinitesimal element

Figure 4.

### 2.1.3 Relation Between Stress and Strain

All bodies are deformed when loaded. An elastic material is one in which all deformations vanish when load is removed. In the theory of elasticity it is usual to postulate also that in an elastic material the strains are proportional to the applied load and the elastic properties are the same in all directions. Such a material is said to be isotropic. These properties hold over a certain stress range known as the elastic limit.

Consider a long prismatic bar under uniaxial stress $\delta_x$ along the x axis. Within the elastic range the longitudinal strain is

$$\varepsilon_x = \sigma_x/E, \qquad 2.10$$

which is the well known Hooke's law relating stress and strain. Here E is a constant called the modulus of elasticity. The lateral strains $\varepsilon_y + \varepsilon_z$ due to $\sigma_x$ are given by

$$\varepsilon_y = \varepsilon_z = -\nu\varepsilon_x, \qquad 2.11$$

where $\nu$ is Poisson's ratio. The generalized expression for the three dimensional case is given by

$$\varepsilon_x = [\sigma_x - \nu(\sigma_y + \sigma_z)], \qquad 2.12$$

and similarly for the other two directions. Applying these results to shear strains produced by shear stresses we have

$$\gamma_{xy} = \tau_{xy}/G\gamma_{yz} = \tau_{yz}/G\gamma_{zx} = \tau_{zx}/G, \qquad 2.13$$

where G is called the shear modulus or modulus of rigidity.

As a final equation given below are the relations between the polar stresses and their associated strains.

$$\sigma_r^i = \varepsilon_r^i(\lambda^i + 2\mu^i) + \varepsilon_z^i\lambda^i, \qquad \textit{and}$$
$$\sigma_\theta^i = \varepsilon_r^i\lambda^i + \varepsilon_\theta^i(\lambda^i + 2\mu^i) + \varepsilon_z^i\lambda^i, \sigma_z^i = \varepsilon_r^i\lambda^i + \varepsilon_\theta^i\lambda^i + \varepsilon_z^i(\lambda^i + 2\mu^i) \qquad 2.14$$

where i = 1,2 refers to the core and clad region of an optical fiber, respectively, and

$$\lambda^i = \frac{\nu^i E^i}{(1 + \nu^i)(1 - 2\nu^i)}, \qquad \mu^i = \frac{E^i}{2}(1 + \nu^i). \qquad 2.15$$

Thus it is easily seen from the above equations that the stress-strain relations are essentially linear (in the elastic range).

## 2.2 *Optics of Photoelasticity*

Many non-crystalline transparent materials which are ordinarily optically isotropic become anisotropic temporarily when subjected to a stress. This usually vanishes as soon as the stress is removed. The mechanically-induced stress or strain cause intermolecular variations in the structure of the body which alters its optical isotropic character. There exist linear relations between the variations of the refractive index, which is treated here as tensor, and the stresses. These relations are

$$n_1 - n = C_1\sigma_1 + C_2(\sigma_2 + \sigma_3),$$
$$n_2 - n = C_1\sigma_2 + C_2(\sigma_1 + \sigma_3), \qquad 2.16$$
$$n_3 - n = C_1\sigma_3 + C_2(\sigma_1 + \sigma_2).$$

This is known as the stress optical law. Here $C_1$ and $C_2$ are called the stress-optic coefficients and have the inverse units of stress.

Another associated effect is the strain optic effect which gives the relation between change in refractive index and the strain and is given as [9],

$$\Delta\left(\frac{1}{n^2}\right)_i = \sum_{j=1}^{6} p_{ij}\varepsilon_j. \qquad 2.17$$

Here $P_{ij}$ is the strain optic coefficient. With no shear strain $\varepsilon_4 = \varepsilon_5 = \varepsilon_6 = 0$. We need consider only the i,j = 1,2,3 elements and for an isotropic homogeneous material it is given as

$$P_{ij} = \begin{bmatrix} p_{11} & p_{12} & p_{12} \\ p_{12} & p_{11} & p_{12} \\ p_{12} & p_{12} & p_{11} \end{bmatrix}$$

W have therefore seen in this chapter the relations between the stress and strain and also introduced the basic equations relating variation of refractive index of isotropic materials with stress and also the associated strains.

# 3.0 Mechanisms of Modulation

Described below are the two main mechanisms of light modulation that occur in optical fibers under the influence of mechanical perturbations. Relations are given between the stress or strain and the resulting variations in the optical transmission parameters of the fibers.

## *3.1 Phase modulation mechanisms in fibers*

Phase modulation is intrinsically one of the most sensitive measures of environmental changes using optical fibers. There are basically two configurations of fiber sensors that may be used to monitor the phase effects. The first is as the two arms of a Mach-Zehnder interferometer using single mode fibers. The second is the single fiber configuration using multimode fibers which exploits the variation of phase between the different modes in the fiber.

Phase modulation effects are basically due to variations in

physical length of the fiber due to axial strain,

radial dimensions of the fiber due to radial strain, and

refractive index via the photoelsatic effect.

Let us first consider the phase modulation effects in the Mach-Zehnder configuration. Here the basic equation for the phase $\varphi$ of the output of the fiber is given by [9].

$$\varphi = \beta \times L, \tag{3.1}$$

where $\beta$ is the single mode propagation constant of light in the fiber and L the length of the fiber. Also let n be the refractive index of the core, $k_0$ the free space propagation constant and a the core diameter.

Let the fiber be under isotropic stress due to some external condition with no shear components. The change in phase due to strain may be written as [9]

$$\Delta\varphi = \beta\Delta L + L\Delta\beta. \tag{3.2}$$

Here the first term accounts for the physical change in length due to the strain. Here $\Delta L$ may be simply written as

$$\Delta L = \varepsilon_z L. \tag{3.3}$$

The second term involves change in phase due to change in $\beta$ which occurs mainly due to two effects

the variation in refractive index via photoelastic effects

the change in radial dimensions.

It may be represented by

$$L\Delta\beta = L\frac{d\beta}{dn}\Delta n + L\frac{d\beta}{dD}\Delta a. \qquad 3.4$$

The first term in the above expression is due to the variation in the refractive index in the z direction, due to the photoelastic effects. This is given as [9]

$$\Delta n = \frac{1}{2}n^2[\varepsilon_z p_{12} + \varepsilon_x(p_{12} + p_{11})]. \qquad 3.5$$

Here it should be remembered that $\varepsilon_x = \varepsilon_y$.

Now $\beta$ is given by $\beta = k_0 n_{eff}$ where $n_{eff}$ lies between the core and cladding indices. But as these differ only by 1% or so we can write it as $\beta = k_0 n$ and therefore

$$d\beta/dn = k_0.$$

The second term gives the change in $\beta$ due to change in diameter of the core. Here the change in diameter $\Delta a$ is simply

$$\Delta a = \varepsilon_x a.$$

$d\beta/da$ is evaluated as

$$\frac{d\beta}{da} = (V^3/2\beta a^3)\frac{db}{dV}, \qquad 3.6$$

where V is v-number given as $V = k_0 a(n_1 - n_2)^{1/2}$ , $b = \dfrac{\beta^2/k_0^2 - n_2^2}{n_2^2} - n_1^2$ and db/dV is the slope of the b - V curve[9].

Therefore $L\Delta\beta$ may be written as

$$L\Delta\beta = Lk_0\frac{1}{2}n^2\varepsilon_z P_{12} + \varepsilon_x(P_{12} + P_{11}) + L\varepsilon_x V^3/2\beta a^2\frac{db}{dV} \qquad 3.7$$

Therefore change in phase per unit length of fiber due to the various strain components may be written as

$$\Delta\frac{\varphi}{L} = \varepsilon_z(\beta + \frac{1}{2}n^2k_0P_{12}) + \varepsilon_x k_0 n^2(P_{12} + P_{11})\frac{V^3}{2\beta a^2}\frac{db}{dV}. \qquad 3.8$$

We now take up the case of the multimode single fiber configuration. For this the key relation is the one given in Eqn. 3.4. But here as both the 'arms' of the interferometer are the same fiber, change in length effects all the modes in the same manner. So we will consider the effect due to change in β only. This is because each mode has a different propagation constant and the $n_{eff}$ is given as [10].

$$n_{eff}^N = n_1\{1 - \Delta(\frac{N+1}{N_m+1})^2\},$$

where

$$\Delta = \frac{n_1^2 - n_2^2}{2n_1^2} \cong \frac{n_1 - n_2}{n_1.}$$

$$N_m = \frac{V}{\pi/2}$$

where V is the v-number of the fiber.

It has been shown [11] that in such mode-mode interactions effect of change in fiber diameter on change in β for a mode may be neglected for the case of a circularly symmetric plane strain. Using this result we may derive for change in phase for given mode, an expression, as follows.

$$\frac{\Delta\varphi}{L} = \Delta\beta$$

Note that as this expression contains variations due only one term alone compared to the three terms in Eqn. 3.4 it could well be expected that the sensitivity of the single fiber 'interferometer' to be less than the conventiontional Mach-Zehnder type which is indeed verified in practice. In the development of Eqn 3.8 we assumed that $n_{eff}$ was the same as n the core index. But in this case it is the difference in the variation in the of refractive indices that causes phase difference between modes. So to account for this we derive the relation d β/dn using the expression for $n_{eff}$ So

$$\begin{aligned}\beta &= k_0 n_{eff} \\ &= k_0 \left\{ n_1 - \frac{(N-1)\lambda^2(n_1 - n_2)}{(4a\sqrt{n_1^2 - n_2^2} + \lambda)^2} \right\},\end{aligned} \tag{3.9}$$

where N is the mode number. So as β is a function of the core diameter a, the core and cladding indexes $n_1$ and $n_2$, we may derive the total derivative of β

$$\Delta\beta = \frac{\delta\beta}{\delta n_1} dn_1 + \frac{\delta\beta}{\delta n_2} dn_2 + \frac{\delta\beta}{\delta a} da. \tag{3.10}$$

We use the expressions derived by [12] for the dn's, which is $n_z^i = n^i + C_2^i(\sigma_{rr}^i + \sigma_{\theta\theta}^i)$ where i = 1,2 refer to the core and clad regions respectively , $C_2$ the transverse photoelastic constant and $n_z$ the index of refraction along the z axis in the stressed state. Also we write $da$ as $\sigma_{zz}/E$ where E is the Youngs modulus. By partial differentiaion of Eqn. 3.9 we obtain the following expression for change β for a mode N

$$\begin{aligned}\Delta\beta_N = \frac{k_0}{f\sqrt{n_1^2 - n_2^2}} \{ & f\sqrt{n_1^2 - n_2^2} - \{q[4a(n_1^2 - n_2^2) + \lambda\sqrt{n_1^2 - n_2^2}] \times \\ & [C_2^{(1)}(\sigma_{rr}^{(1)} + \sigma_{\theta\theta}^{(1)}) - C_2^{(1)}(\sigma_{rr}^{(2)} + \sigma_{\theta\theta}^{(2)})]\} - \\ & \{8aq(n_1 - n_2)[n_1 C_2^{(1)}(\sigma_{rr}^{(1)} + \sigma_{\theta\theta}^{(1)}) - n_2 C_2^{(2)}(\sigma_{rr}^{(2)} + \sigma_{\theta\theta}^{(2)})]\} + \\ & [4aq(n_1 - n_2)(n_1^2 - n_2^2)\frac{\sigma_{zz}}{E}]\},\end{aligned} \tag{3.11}$$

where $f = (4a\sqrt{n_1^2 - n_2^2} + \lambda)^3$ and $q = (N - 1)\lambda^2$.

Here the expression is in the cylindrical coordinates and unlike the others it has terms for stress an the corrospondding stress-optic coefficients. These may be converted to strain terms using Hookes law and the relation between stress and strain optic coefficients $P_{11} = -2EC_1/n^3$ and $P_{12} = -2EC_2/n^3$ It should however be mentioned that this expression holds only if all the quantities involved are known precisely and the assumed conditions of uniform radial pressure is satisfied.

## 3.2 *Mechanisms of Polarization Modulation*

Polarimetric fiber-optic sensors detect the presence of a physical field via a change in state of polarization of light propagating through a single mode fiber. It must be noted that even in a single mode fiber two 'modes' perpendicularly polarized to each other may propagate. It is the differential change between these that form the mechanism of sensing. The physical field to be sensed causes an asymmetric stress in the fiber cross section thus unequally changing the phase velocities of the orthogonal palarization modes. The mechanism may therefore be analysed similar to the phase modulation.

The following discussion follows that of [13] for a step index fiber under radial pressure which is acting alona diameter.

For this purpose we limit our examination around the center of the fiber as most of the energy in a step index fiber is almost entirely confined to the core. We may therefore write the change in refractive indices as that involving only $n_1$ as

$$n_x = n_1 + (C_1\sigma_x + C_2\sigma_y)$$

$$n_x = n_1 + (C_1\sigma y + C_2\sigma_x).$$

Now writing the β's as

$$\beta^x = n_x k_0, \ \beta^y = n_y k_0,$$

we can write the birefringence as

$$\begin{aligned}\Delta\beta &= \beta^y - \beta^x \\ &= \sigma_y(C_1 - C_2) + \sigma_x(C_2 - C_1)\end{aligned} \qquad 3.12$$

The components of principal stress around the center may be approximated as

$$\sigma_x = \frac{-3f_0}{\pi b}, \qquad \sigma_y = \frac{f_0}{\pi b},$$

where $f_0$ is the external force per unit length. Therefore Eqn 3.12 may be written as

$$\Delta\beta = \frac{8}{\lambda b}(C_1 - C_2)f_0. \qquad 3.13$$

This is also equal to

$$\Delta\beta = \frac{4n_1^2}{\pi}\frac{1+\nu}{E}(P_{12} - P_{11})\frac{f}{2b}, \qquad 3.14$$

where ν is the Poisson's ratio.

The induced linear birefringence may also given by.

$$\Delta\beta = \Delta\beta^y - \Delta\beta^x = -k_0 n_0^3 l\frac{(P_{11} - P_{22})}{2}(\varepsilon_1 - \varepsilon_2) \qquad 3.15$$

where ε's are the principal strains given as

$$\varepsilon_{1(2)} = \left\{ \frac{\varepsilon_{rr} + \varepsilon_{00}}{2} + (-)\frac{1}{2}[(\varepsilon_{rr} - \varepsilon_{00})^2 + 4\varepsilon_{r0}^2] \right\}, \qquad 3.16$$

where $\varepsilon_{rr}, \varepsilon_{\theta\theta}, \varepsilon_{r\theta}$ are the strains in cylindrical coordinates. The P's are the strain optic coefficients. Eqn. 3.14 may easily be got from Eqn. 3.12 by replacing the stress by the strain terms. Eqn 3.14 then becomes

$$\Delta\beta = -k_0 n_0^3 l \frac{(P_{11} - P_{12})}{2}(\varepsilon_{rr} - \varepsilon_{\theta\theta})^2. \qquad 3.17$$

The change in two orthogonal modes is given as

$$\begin{aligned} \Delta\beta^x &= k_0 n_0^3 l(P_{12}\varepsilon_1 + P_{11}\varepsilon_2)/2 \\ \Delta\beta^y &= -k_0 n_0^3 l(P_{11}\varepsilon_1 + P_{12}\varepsilon_2)/2. \end{aligned} \qquad 3.18$$

Twisting a fiber around its axis with a uniform rate $2\pi N$ rad/m where N is the number of turns per meter will induce will induce a circular birefringence unlike in the other cases where the birefringence was linear. The induced birefringence is given by [13].

$$\Delta\beta = \frac{n_1^2}{2}(P_{11} - P_{12})2\pi N \qquad 3.19$$

We have also for a bend induced birefringence a normalized value.

$$\frac{\Delta\beta}{\beta} = \frac{n_1^2}{4}(P_{11} - P_{12})(1 + \nu)(a/R)^2, \qquad 3.20$$

where R is the bend radius and $\beta$ the mean of $\beta_y, \beta_x$ For bending under tension, an additional normalized birefringence is given as

$$\frac{\delta\beta}{\beta} = \frac{n_1^2}{2}(P_{11} - P_{12})\frac{(1 + \nu)(2 - 3\nu)}{1 - \nu}(b/R_0)\varepsilon_{zz}. \qquad 3.21$$

Thus we have-achieved upto a fair degree of completeness the derivation of equations relating the various optical transmission parameters like refractive index, phase, propagation constant and birefringence to the mechanical perturbation parameters stress or strain. Given below is a compilation of the all the important relations that have been derived earlier.

**Refractive Index**

$$n_r = n_0 + (C_1\sigma_{rr} + C_2\sigma_{\theta\theta})$$
$$n_\theta = n_0 + (C_1\sigma_{\theta\theta} + C_2\sigma_{rr})$$
$$n_z = n_0 + C_2(\sigma_{rr} + \sigma_{\theta\theta})$$

**Phase**

$$\frac{\Delta\varphi}{L} = \varepsilon_{zz}(\beta + \frac{1}{2}n^2k_0P_{12}) + \varepsilon_x k_0 n^2(P_{12} + P_{11})\frac{V^3}{2}\beta a^2\frac{db}{dV}$$

**Propagation constant**

$$\Delta\beta_N = \frac{k_0}{f\sqrt{n_1^2 - n_2^2}}\{f\sqrt{n_1^2 - n_2^2} - \{q[4a(n_1^2 - n_2^2) + \lambda\sqrt{n_1^2 - n_2^2}] \times$$

$$[C_2^{(1)}(\sigma_{rr}^{(1)} + \sigma_{\theta\theta}^{(1)}) - C_2^{(1)}(\sigma_{rr}^{(2)} + \sigma_{\theta\theta}^{(2)})]\} -$$

$$\{8aq(n_1 - n_2)[n_1C_2^{(1)}(\sigma_{rr}^{(1)} + \sigma_{\theta\theta}^{(1)}) - n_2C_2^{(2)}(\sigma_{rr}^{(2)} + \sigma_{\theta\theta}^{(2)})]\} +$$

$$[4aq(n_1 - n_2)(n_1^2 - n_2^2)\frac{\sigma_{zz}}{E}]\}$$

**Birefringence**

$$\Delta\beta = \frac{8}{\lambda b}(C_1 - C_2)f_0$$

this is also equal to

$$\Delta\beta = \frac{4n_1^2}{\pi}\frac{1+\nu}{E}(P_{12} - P_{11})\frac{f}{2b}$$

where ν is the Poisson's ratio of Silica. It may also be given as

$$\Delta\beta = -k_0 n_0^3 l \frac{(P_{11} - P_{12})}{2}(\varepsilon_{rr} - \varepsilon_{\theta\theta})^2$$

Twist induced birefringence is given by

$$\Delta\beta = \frac{n_1^2}{2}(P_{11} - P_{12})2\pi N$$

We have also for a bend induced birefringence a normalized value.

$$\frac{\Delta\beta}{\beta} = \frac{n_1^2}{4}(P_{11} - P_{12})(1 + \nu)(a/R)^2$$

where R is the bend radius and β the mean of $\beta_y$ and $\beta_x$ For a bending under tension an additional normalized birefringence is given as

$$\frac{\delta\beta}{\beta} = \frac{n_1^2}{2}(P_{11} - P_{12})\frac{(1+\nu)(2-3\nu)}{1-\nu}(b/R_0)\varepsilon_{zz}$$

It may be mentioned here that following the development of these relations it is realized that these equations may appear in any theory relating to the 'modal domain' sensing techniques perhaps in some modified form without, however, any drastic changes.

# 4.0 Experiment and Observations

## *4.1 Motivation and Reasons*

Modal domain methods involving mode-mode interference effects are being actively investigated at the Fiber and Electro-Optics Research Center at Virginia Tech for applications in the sensing of vibration in structures and acoustic emission in composites [3,4]. In the above applications fibers are firmly bonded to the specimen and experience a combination of strains when the specimens are subjected to perturbations.

A question that arises in these applications is if the observed signals are a function of the well documented bend loss effects. To ascertain this it was necessary to conduct experiments which would not involve any bend loss effects, or at least be limited to only some non-varying kinds. Research on these applications also suggested that the axial strain to be a major factor contributing to observed effects. For example, it has also been noted that ability of the fiber to exhibit the 'modal' sensing effects due to both vibrations of structures and due to acoustic emission was more pronounced when the sensing fiber was bonded in a state of slight tension. For both these reasons

it was felt that it may be pertinent to monitor the 'modal' effects created by subjecting a bare fiber to quasi-static tensile loads.

## 4.2 *Apparatus*

A few-mode optical fiber (core diameter 8 microns; clad diameter 125 microns; NA$\cong$0.10, V$\cong$4) was chosen as the most suitable candidate for this purpose as it was the same kind of fiber used in [3,4] and also the output pattern was such that it was well defined and could be easily reproduced. The pattern was a four lobed configuration as shown in Figure 5.

The tensile loading was provided by a conventional tensile testing machine - the J.J.Lloyd T20000 model. The machine applies a tensile load to a specimen held between two grips. The applied tension and extension from a set position is displayed by a microprocessor unit. The rate at which the tension is applied may be adjusted as required between 0.1 and 50 mm/m in steps of 0.1 mm. The grips may also be driven back to release the applied tension also adjustable between the same range. For our purpose special grips were used to enable the fiber to be axially strained without slipping and without excessive concentration of stress at the grips.

A 5.0 cm section of the fiber was mounted on the tensile testing machine, as shown in Figure 5. Another section of the fiber was bonded to the surface of a steel cantilever beam (t = 0.65 mm, L = 16.0 cm). This was similar to the one used by [3]. The fiber was fixed as a loop as shown in the figure to eliminate a dangling end and increase the length of interaction. This provided a mechanism to subject the fiber to low frequency strain variations of the order of $10^{-4}$. That is to say that the fiber could be subjected to an oscillatory tension around the relatively larger magnitudes of tension provided by the machine.

The tensile testing machine range of 0-50 mm/min displacement (in steps of 0.1 mm/min) corresponds to a lower limit of $10^{-5}$/sec strain for a 20 cm interaction length. A Nicolet digital storage oscilloscope was used to monitor and store the detector output.

## 4.3 Experiment and Observations

The tensile testing machine was operated at speeds of 0.5, 1.0 and 2.0 mm/min to simulate quasi-static loading conditions. A redistribution of the mode pattern was observed. The lobes rotated with speeds proportional to the pulling speeds.

The intensity of the spatially filtered pattern (i.e. the intensity of a small fixed segment of the pattern) was observed to vary in a sinusoidal manner. Because of the known strain rate, the intensity signal could be related directly to the axial strain in the fiber. Output signals for displacement rates of 0.5 and 1.0 mm/min are shown in Figures 6 and 7 respectively. Note that the average time period of the signals is inversely proportional to the displacement rates. This confirms that the change in the intensity mode pattern is due to strain. Note that the time period for the faster strain rate of 1.0 mm/min is almost exactly half the period for the slower case.

To study reversability and repeatability, the strain was applied and removed twice at the same rates. The output signals during tension and release are shown in Figures 8 and 9. Note the excellent reciprocity indicated by the inverted waveforms. The excellent tracking of the strain in both 'directions' reveals the linear relation between the change in the mode pattern and small axial strains.

Note that the intensity is periodic for strains of the order of $10^{-3}$ and the rate of change of intensity with strain is lowest at the 'peaks' and highest in the middle. A low-frequency varying strain of the

order of $10^{-4}$ was generated in the fiber by vibrating the cantilever beam. This was done for two different strain conditions, one slightly above 'peak' and the other in the 'middle' of the sinusoidal variation of the output of the detector monitoring the far field speckle pattern rotation. The output signals are shown in Fig. 10. Note the higher amplitude for the middle case where the rate of change of intensity with strain was highest. The phenomenon reported by [3] was also confirmed as the variation of the signal was at vibrating frequency of the beam.

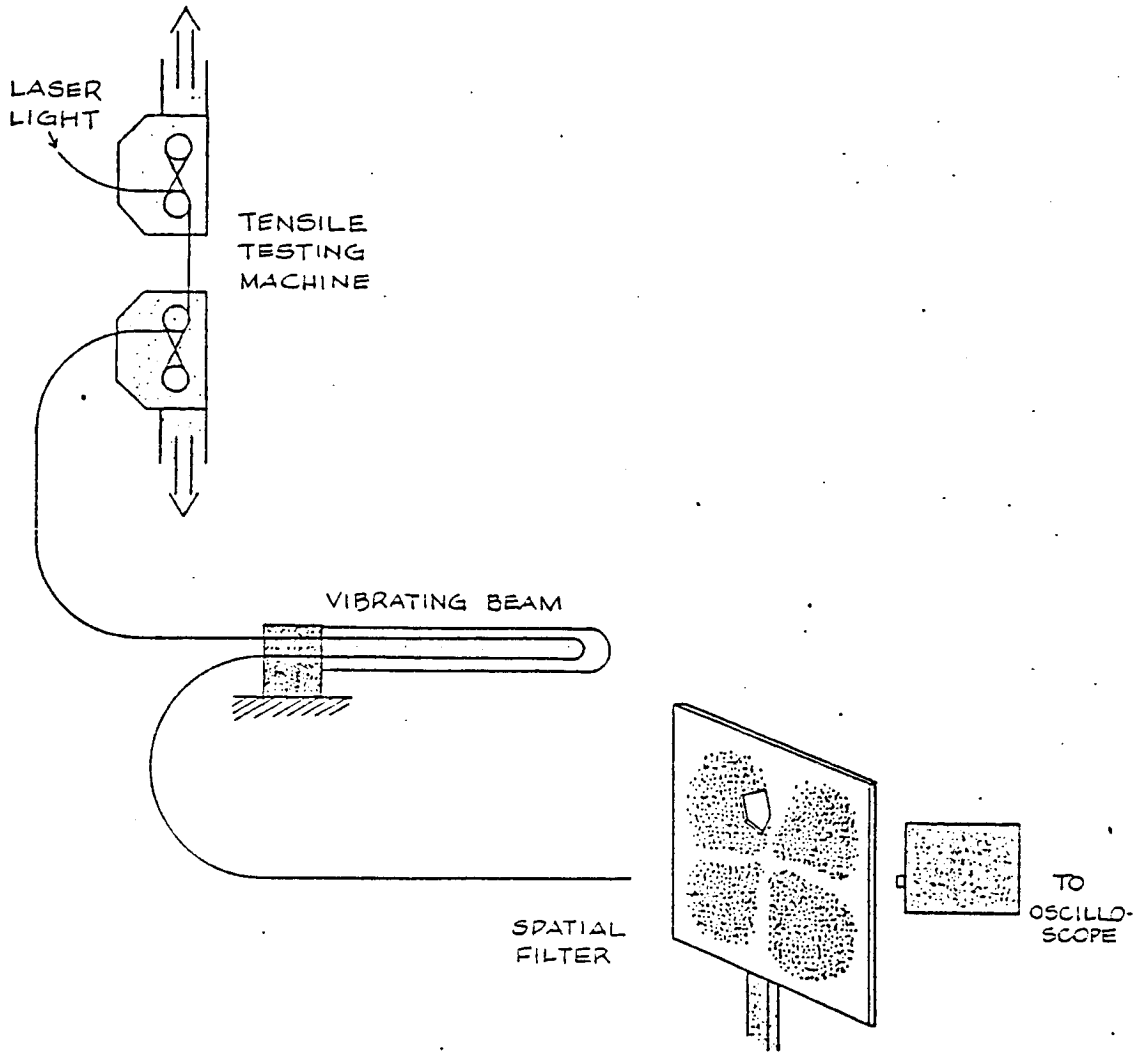


Figure 5. Experimental set-up.

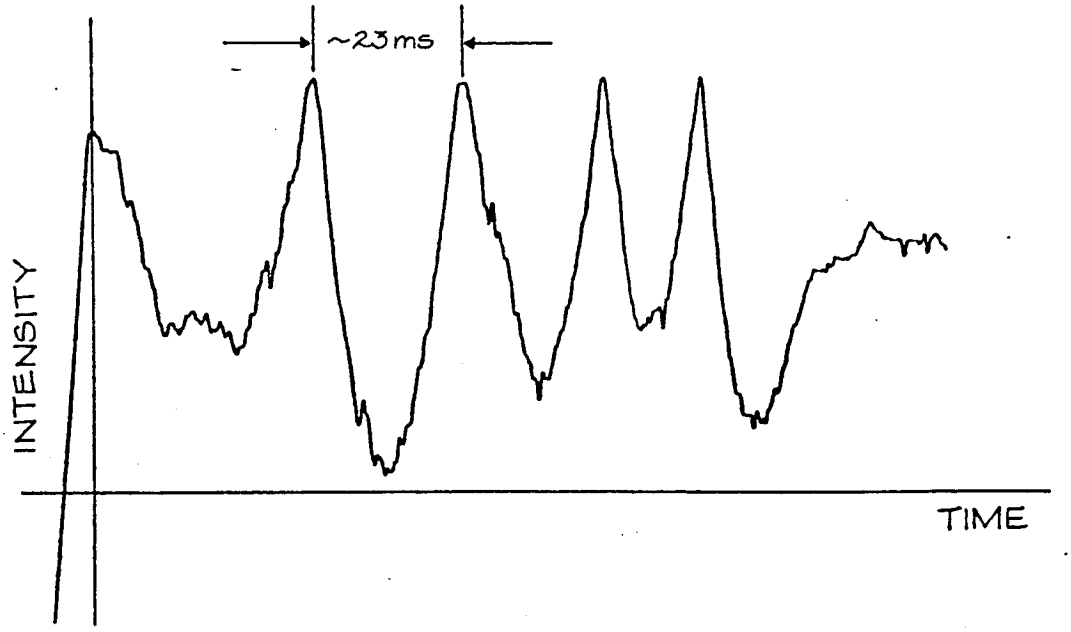


**Figure 6. Output for 0.5 mm/min displacement rate.**

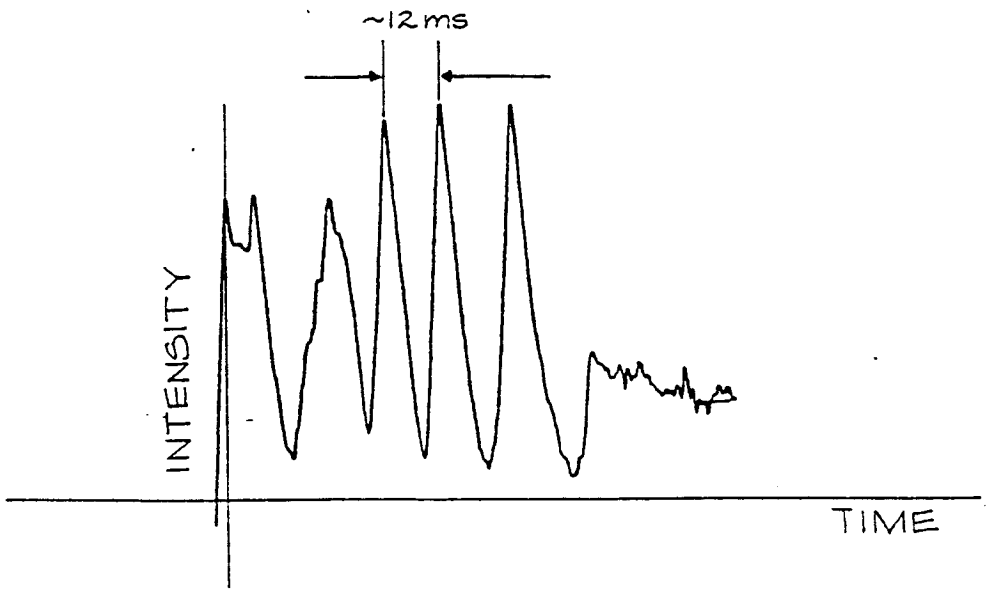


Figure 7. Output for 1.0 mm/min displacement rate.

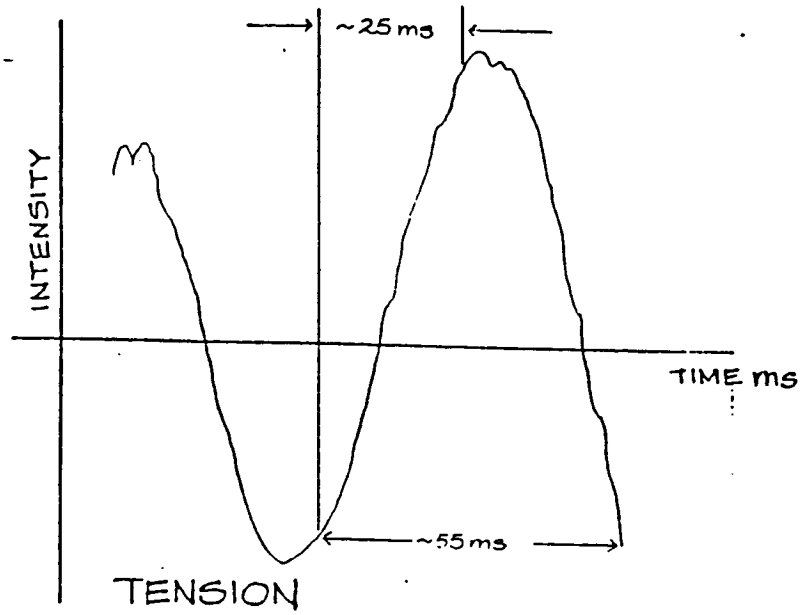


Figure 8. Output as tension is applied.

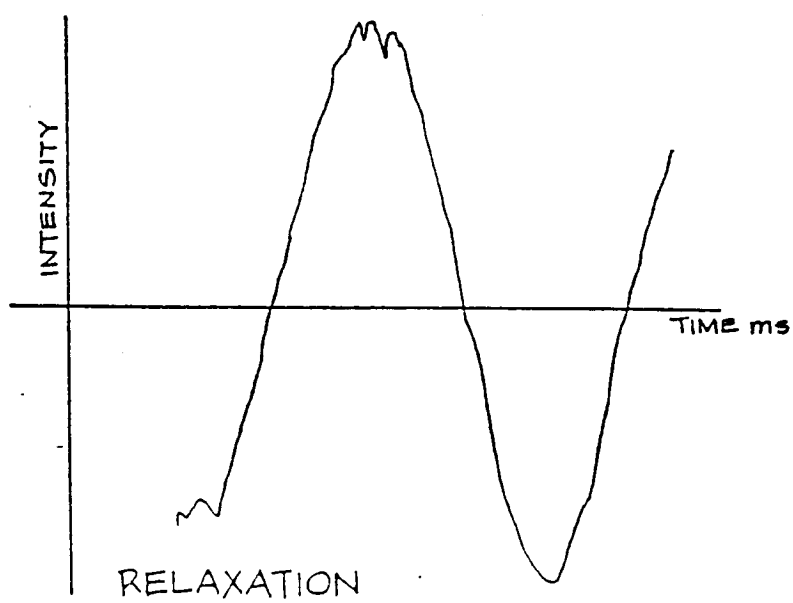


Figure 9. Output as tension is released.

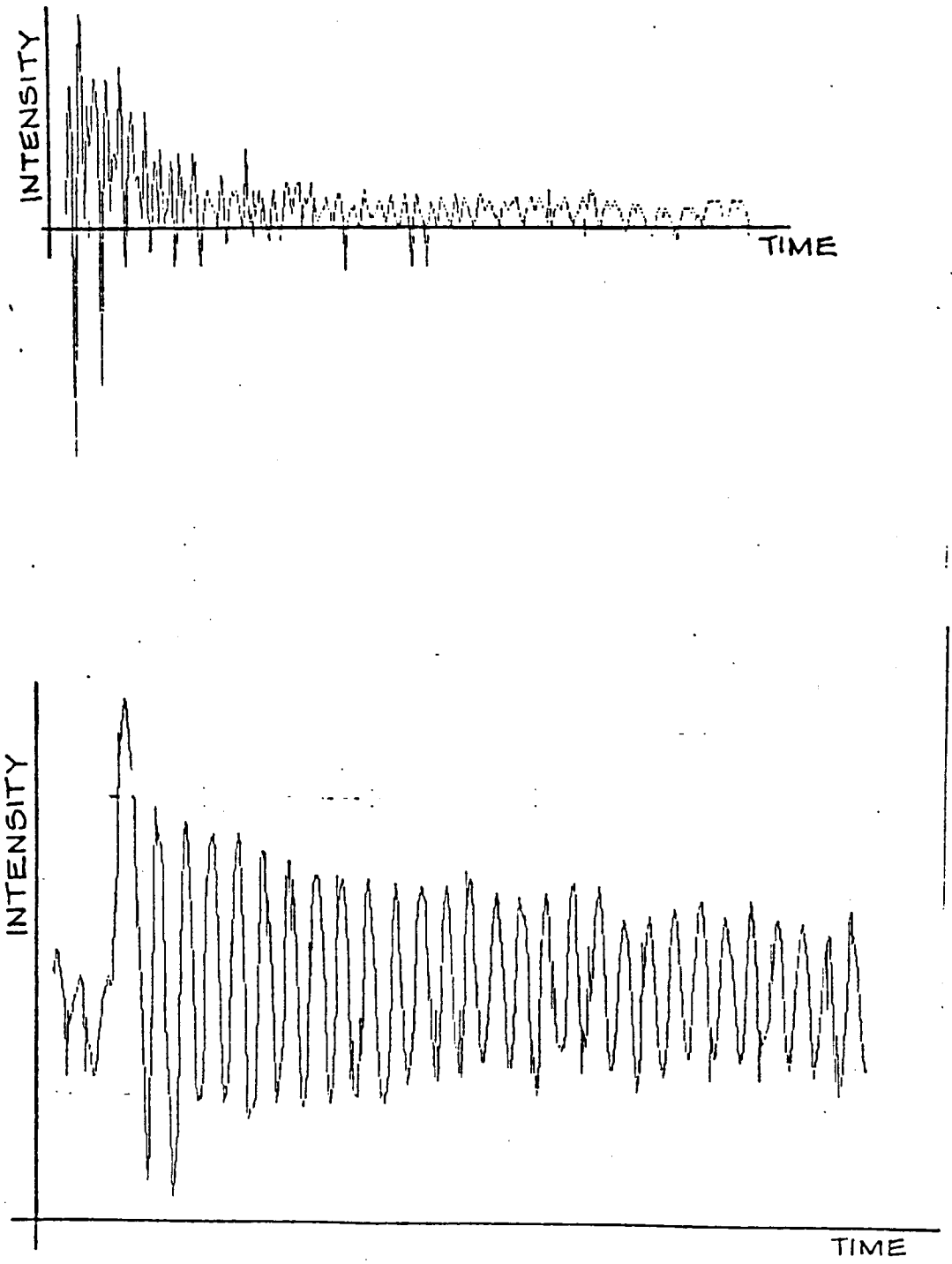


Figure 10. Output due to vibrating beam at the two states of tension.

# 5.0 Conclusions

A modal modulation effect due to axial strain in an optical fiber been observed. The relation between the effect of prestressing the fiber axially and the sensitivity of this 'modal' mechanism to monitor flexural deflections is reported. We are now in a position to offer some preliminary models for the further exploitation of this sensing technique.

## *5.1 Discussion*

For $V \cong 4$, we have seven modes $HE_{11}$, $TE_{01}$, $TM_{01}$, $HE_{21}$, $HE_{12}$, $EH_{11}$, and $HE_{31}$ [10]. The mode pattern used by us with four nodal lines is probably due to the mode combination of $HE_{31}$ and $EH_{11}$ and this mode combination rotates along the fiber [5]. Due to the phase modulation [5] and polarization modulation resulting from strain, there is a change in the mode pattern. A rotation in the mode pattern is observed at the detector if a spatial filter is located on the nodal line. [5] (A nodal line may simply be understood as the dark regions between the 'lobes' of the output pattern.) We could relate the sinusoidal variation of the intensity to the rotation of the nodal line past the spatial filter. A combination of modes should result in a symmetric pattern and the varying

intensities of-the quadrants results from non-circularities of the fiber. It is interesting that the rotation of the nodal line corresponds well to the strain rate as was observed.

The rotation of the mode pattern is also reversible and rotates in the opposite direction when the strain is released. The tensile testing machine does take a finite time to reverse the strain and though we could observe the effect of strain on the fiber, our timing capabilities do not allow a measurement of any hysteresis effects in the reversal.

For small a.c. excitations at an existent 'd.c.' strain, we have observed similarities to typical biasing and load-line situations in a transistor. That is, there seems to be a certain prestressed condition of the the optical fiber which makes it more sensitive to such modal methods of sensing. More importantly the required stress condition seems to be indicated by the rotation of the mode pattern. Just as setting the Q point is important in the operation of a transistor it seems necessary to bias the fiber by prestressing it to be able to monitor such vibrational phenomenon as indicated above. The response to small strains can be tailored by controlling a quasi-static strain elsewhere on the fiber. This could very well be a piezoelectric cylinder in sensor applications.

This principle could be used in a sensor with one region of the fiber exposed to axial strain and another exposed to a controlled strain (e.g. bonded to PVDF cable or wound on a PZT cylinder). If the controlled strain is increased to some value, then by release or enhancement of strain we could nullify the strain changes in the sensing region. This gives us a convenient electrical signal from the control loop as the sensor output. We have an advantage of not having to deal with varying intensities between nodal lines.

## 5.2 *Conclusion*

- We have observed a sinusoidal variation of the detector output from a modal domain detection set-up for small, slowly increasing axial strain. This signal shows reciprocity when the strain is applied and removed.
- This observation indicates that the strain produces a simple rotation in the far field output pattern of te fiber.
- We have subjected the fiber to small a.c. strains under different d.c. strains and have noted the conditions of bias required for such applications.
- We have been able to identify , on the modal pattern, a region of most sensitivity for sensing of flexural vibrations.
- We have indicated a simple model to explain the mode pattern and axial strain effects.

## 5.3 *Suggestions*

As has been mentioned earlier the observed effect of pattern 'rotation' could be combination of phase and polarization effects [5]. To confirm this, further experiments of a similar nature would be useful. The same experiment could be performed, but this time seperating the far field output of the fiber into the two orthogonal eigen modes by passing it through a polarizing element such as a polarizing beamsplitter. A comparative study of the behaviour of these orthogonal componants should indicate the contribution of each of these eigenmodes to the total effect of rotation that has been observed. Indeed even more signifcant it would check out the validity of this effect being dependent on polarization at all.

Another variation to the set up used in this study would be to use coupler at the output so as to seperate out the higher order modes and the lower order ones and the observe varations, if any, in the two outputs. This should give us an indication of the contributions of the lower and higher order modes to the effects described in this report. In fact using the information from the mode patterns in [5] we may also be able to understand how the modes get transferred at the coupler as axial tension is being applied to it.

Indeed it would be worthwhile performing all the experiments of [3,4] to be able to quantify the required pre-stress conditions on the sensing fiber to tailor the sensitivity of this method for these specific applications. A result of significance would be to be able to quantify specific pattern variations and relate them to existing conditions of tension in the optical fiber. A specific experiment suggested is to vibrate the portion of the fiber under tension at a known frequency by using, for example, a tuning fork. This should also simulate the acoustic emission phenomenon of [4].

A related experiment would be to verify if similar phenomenon are observed if the same or similar fiber is attached to a magnetostrictive material and exposed to a magnetic field. As the material expands the optical fiber should also experience the same strain.

# 6.0 References

[1] T. G. Giallorenzi, et al., "Optical Fiber Sensor Technology", IEEE Transactions on Microwave Theory and Techniques, Vol MTT-30, NO. 4 April 1982.

[2] B.Culshaw, "Optical Fiber Sensing and Signal Processing", pp 73-86, Peter Perigrinus, 1982.

[3] Paul Ehrenfeuchter, Masters Thesis, Virginia Tech , December 1986.

[4] N. K. Shankarnarayanan et al., "Optical Fiber Modal Domain Detection of Stress Waves", Proceedings, IEEE Ultrasonics Symposium (Williamsburg, VA), November 1986.

[5] N.S.Kapany and J.J.Burke, "Optical Waveguides", Academic Press 1972.

[6] N.K. Shankarnarayanan, Internal Report, Fiber & Electro-Optics Research Center, Virginia Tech.

[7] A.Kuske and G.Robertson, "Photoelastic Stress Analysis", John Wiley & Sons, 1974.

[8] Theocaris and Gdoutos, "Matrix Theory Of Phtoelasticity", Spriger-Verlag, 1979.

[9] G.B.Hocker,"Fiber Optic Sensing of Pressure and Temperature", Applied Optics, vol. 18, No. 9, !st may 1979.

[10] Yasuharu Suematsu, "Introduction to Optical Fiber Communications", JW&S, 1982.

[11] Namihira, et al., "Effect of Mechanical stress on the Transmission Characteristics of Optical Fiber", Electronics and Communications in Japan, V0l. 60-C, No. 7, 1977.

[12] L.B.Jeunhomme, "Single Mode Fiber Optics", Marcel Dekker Inc., 1983.

# VITA

K. T. Srinivas was born on 4th March, 1961 in Bangalore India. He attended the National High School at Bangalore. He obtained his Bachelor of Engineering degree in Electronics from the Bangalore University in the year 1984. He received his Masters degree in Electrical Engineering in January 1987 from Virginia Polytechnic Institute & State University.

He has co-authored one technical paper. He is a member of the IEEE and the Communications Society. He is an amateur radio enthusiast.

# Appendix E. Single Mode Optical Fiber Vibration Sensor

# SINGLE MODE OPTICAL FIBER VIBRATION SENSOR

A. Flax, C. Pennington, and R. O. Claus

Fiber and Electro-Optics Research Center
Department of Electrical Engineering
Virginia Tech
Blacksburg, VA 24061

## Abstract

A single mode optical fiber is used as a vibration sensor. It is used to detect the vibration of a structure. The vibrating motion of the structure modulates the optical propagation properties of the attached optical fiber. The resulting modulation has been detected to yield mode shape amplitude information about the vibrating structure.

## Introduction

There has been increased interest recently in optical fiber modal domain sensing. A sensing system using this approach has an optical fiber attached to a vibrating structure to detect the frequencies of oscillation, or an embedded fiber in a composite to detect acoustic emission. This type of detection is sometimes preferred to the traditional use of interferometers, because the optical fiber is attached to the structure in question, and the information about the vibrating structure is contained in the modulated output of the optical fiber. The work in the past has been done with multi-mode optical fibers. This work looked at the filtered speckle pattern output of the optical fiber, and analyzed this modulated detected output [1]. This has been done with only a few excited modes in the fiber, and with several excited modes in the fiber.

In this paper we look at the similiar excitation of one mode in the optical fiber, and thus the information contained in the optical fiber's modulated detected output signal.

## Theory

Discrete modes propagate in optical fibers. These modes of propagation are found by applying the boundary conditions to the optical fiber and then by solving Maxwell's equations. The number of modes that can propagate in an optical fiber is determined by the operational wavelength, and by the characteristics of the optical fiber; these can be related to a parameter called the V-number [2].

$$V = (2\pi a/\lambda)^2 \ (n_1^2 - n_2^2) \quad (1)$$

where, $a$ = core radius
$\lambda$ = wavelength
$n_1$ = index of refraction, core
$n_2$ = index of refraction, cladding

For a single mode fiber to be operational, V must be less than 2.405.

Even though only one spatial mode exists in a single mode optical fiber, this spatial mode consists of two linear orthogonal polarized modes [3,4]. When the fiber is introduced to stress, birefringence is introduced, which causes a difference in phase velocities and thus a difference in the group velocities of these two modes [5]. This birefringence also introduces an exchange of power between these two modes [6]. Therefore, this power exchange has introduced a coupling of the two modes, which in itself is a change of polarization. This birefringence can be an internal function of the material characteristics of the waveguide, and an external function of stresses applied to the optical fiber.

Changes of the birefringence due to external stress on the optical fiber results in an amplitude modulated signal [7]. This resulting signal is due to the coupling of the two linear polarized modes. This phenomenon of amplitude modulation in the communications industry is called polarization noise. However, the sensor industry can exploit this phenomenon to analyze external stresses on optical fibers.

Proceedings, IEEE Region 3 Conference (Tampa, FL), April 1987.

ORIGINAL PAGE IS
OF POOR QUALITY

Experiment

To investigate modal domain sensing in a single mode optical fiber, an optical fiber was attached to a cantilever beam. The input to the optical fiber was an He-Ne laser operational at a wavelength of 633 nm. This particular optical fiber supports only one mode at 633 nm and the output is one bright spot.

In the following experiments we are trying to detect the frequencies of oscillation of the cantilever beam. The cantilever beam is described by the following differential equation [8].

$$d^4n/dx^4 = -k(d^2 n/dt^2) \quad (2)$$

The solution to this equation can be represented as a fourier series, and the harmonics of oscillation are described in the following equation.

$$n(t) = 1/2a_0 + \sum_{n=1}^{\infty} (a_n \cos(nw_o t) + b_n \sin(nw_o t)) \quad (3)$$

In the first experimental set-up of Figure 1, we are trying to find information contained in polarization changes of the optical fiber. We placed a polarizing lens at the output of the single mode optical fiber. Then, we found the maximum and minimum points of polarization at the output, while the cantilever beam remained at rest. Then, we connected a detector to the output, which in turn was connected to a optical power meter.

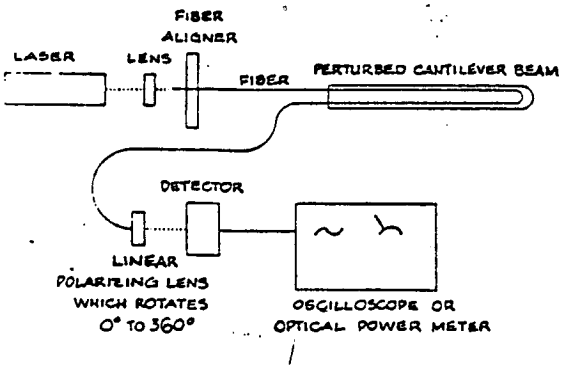


FIGURE 1. EXPERIMENTAL SET-UP FOR MEASURING POLARIZATION CHANGES DUE TO MECHANICAL PERTURBATIONS

As we bent the beam up and down, we saw variations on the optical power meter. Next, we connected the detector to a digital oscilloscope. As we vibrated the cantilever beam, we saw jumps of the voltage on the oscilloscope that corresponded to variations in the position of the cantilever beam. Next, we removed the polarizing lens to see if we could see any variations in the beam; we did not. However, these results were not totally reliable because the detector that we used had a low amplification and a slow response time, and the polarizing lens caused a great loss of power. This system was not conducive to the quick oscillations of the the cantilever beam.

Therefore, in the experimental set-up in Figure 2, we used a faster detector with more amplification. Also, we used a polarizing beam splitter that separates the linearly polarized modes of the single mode fiber. This system also reduces the power loss that was seen with the polarizing lens.

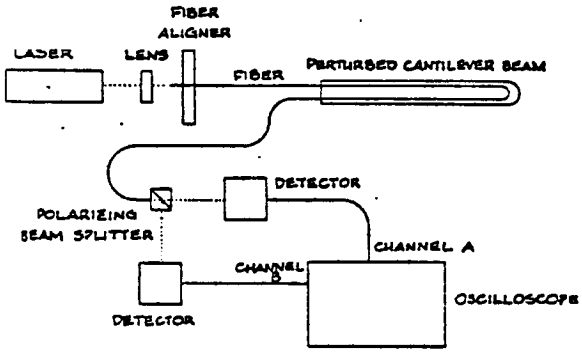


FIGURE 2. EXPERIMENTAL SET-UP TO EXAMINE AMPLITUDE CHANGES IN EACH LINEARLY POLARIZED MODE DUE TO MECHANICAL PERTURBATIONS

At first, we ran the experiment with the polarizing beam splitter in place. As we vibrated the cantilever beam, we saw that one linearly polarized mode increased in amplitude while the other mode decreased in amplitude (Figure 3). More importantly, each of these modes contained information about the mechanical oscillations of the cantilever beam. Specifically, the period of the waveform was the same as the fundametal harmonic of the cantilever beam.

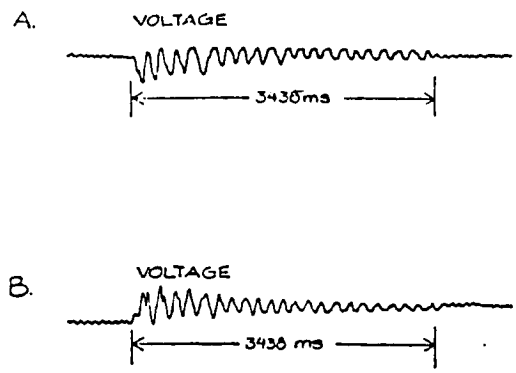


FIGURE 3. OUTPUT OF OPTICAL FIBER DUE TO MECHANICAL PERTURBATIONS OF THE CANTILEVER BEAM. A) CHANNEL A - ONE LINEAR POLARIZED MODE. B) CHANNEL B - THE OTHER LINEAR POLARIZED MODE.

Finally, we removed the polarizing beam splitter to see what results we would obtain. Because of the response of the new detector, we saw that there was a similiar waveform as with the beam splitter in place. Once again, the output waveform waveform contained information about the fundamental frequency of oscillation of the cantilever beam.

## Conclusion

We have demonstrated that we can detect structural vibrations by exploiting the interferance of the two linear polarized modes of a single mode optical fiber. This work could be extended to sense other external induced changes such as temperature, fluid flow, and chemical concentrations.

## Acknowledgements

This work has been supported, in part, by the Simmonds Precision subsidiary of Hercules, Inc.

## References

1. K. D. Bennett and R. O. Claus, "Analysis of Composite Structures Using Fiber Modal Sensing Techniques," Proceedings, IEEE Region 3 Conference (Richmond, VA), April 1986.
2. G. Keiser, 1983, Optical Fiber Communications, New York: McGraw-Hill, p. 34 - 35.
3. R. E. Epworth and M. J. Pettitt, "Polarization Modal Noise and Fibre Birefringence, Standard Telecommunication Laboratories Ltd, England.
4. S. Heckman, "Modal Noise in Single-mode Fibers," Optics Letters, vol. 6, no. 4, p.201, April 1981.
5. S. C. Rashleigh and R. Ulrich, "Polarization Mode Dispersion in Single-Mode Fibers," Optics Letters, vol. 3, no. 2, p. 60, August 1978.
6. S. C. Rashleigh, "Origins and Control of Polarization Effects in Single-Mode Fibers," Journal of Lightwave Technology, vol. LT-1, no. 2, June 1983.
7. Wang Kaibin and Ye Peida, "Polarization Noise in Monomode Fiber Systems," Beijing Institute of Posts and Telecommunications, China.
8. Willim C. Elmore and Mark A. Heald, 1969, Physics of Waves, New York: McGraw-Hill, p. 116.

# Appendix F. Imbedded Optical Fiber Sensor of Differential Strain and Temperature in Composites

# Imbedded Optical Fiber Sensor of Differential Strain and Temperature in Graphite/Epoxy Composites

by

Mahesh Reddy

Thesis submitted to the Faculty of the

Virginia Polytechnic Institute and State University

in partial fulfillment of the requirements for the degree of

Master of Science

in

Electrical Engineering

APPROVED:

R. O. Claus, Chairman

R.J. Pieper

T. C. Poon

November 1986

Blacksburg, Virginia

# Acknowledgements

I would like to express my appreciation to my advisor, Dr. Richard O. Claus, for his ideas, guidance, and in particular, his endless enthusiasm. I also wish to thank the other members of my advisory committee, Dr. T.C. Poon and Dr. R.J. Pieper, for their comments, suggestions, and encouragement.

I am grateful to members of the fiber optic group, Kim D. Bennett, N.K. Shankar, Paul Ehrenfeuchter, K.T. Srinivas, Kent Murphy and Marten de Vries, for their suggestions and help on this project. I would also like to thank Ms. Robin Rogers and Ms. Ann Goette for willing to share their time and helping out with the drawings and figures.

Finally I would like to express my sincere appreciation and thanks to my family, especially my parents, for their unceasing love and moral support.

# Table of Contents

**1.0 Introduction** ..... 1

**2.0 Fiber Optic Sensor Overview** ..... 3

2.1 Intensity Modulated Sensors ..... 3

2.2 Phase (Interferometric) Sensors ..... 8

2.3 Polarization Modulated Sensors ..... 14

2.4 Wavelength Modulated Sensors ..... 16

**3.0 Interferometric Optical Fiber Sensing** ..... 20

3.1 Analytical Model ..... 20

3.2 Optical Signal Detection ..... 23

**4.0 Experiment** ..... 26

4.1 Fiber optic interferometer used for strain and temperature measurement in a graphite-epoxy composite laminate. ..... 33

4.2 Differential Interferometric Measurement of Temperature in 0 ° and 90 ° unidirectional laminates. ..... 41

5.0 Conclusions ..... 55

6.0 References ..... 57

7.0 APPENDIX A ..... 61

7.1 Composite Material Overview ..... 61

7.2 Composite Sample Fabrication ..... 62

7.3 Graphite/Epoxy Curing Cycle ..... 64

7.4 Composite Terminology ..... 65

7.5 Specimen (Laminate) Types ..... 65

8.0 APPENDIX B ..... 67

8.1 Preparation of Single-Mode Fibers for use in an Interferometer ..... 67

9.0 VITA ..... 71

ABSTRACT

# List of Illustrations


Figure 1. Microbend Sensor . . . . . 4

Figure 2. Microbend Sensor for Pressure Measurement. . . . . 6

Figure 3. Proportional Reflection Sensor . . . . . 7

Figure 4. Conventional Interferometric Systems. . . . . 9

Figure 5. Optical Fiber Interferometric Systems. . . . . 10

Figure 6. RF Interferometer System Block Diagram . . . . . 13

Figure 7. Polarization Sensor . . . . . 15

Figure 8. Basic Elements of the Sapphire Blackbody Sensor . . . . . 17

Figure 9. Fiber Optic Temperature Sensor Schematic. . . . . 19

Figure 10. Single-Mode Mach-Zehnder Interferometer . . . . . 27

Figure 11. Fiber Optic Interferometer for Temperature Sensing . . . . . 30

Figure 12. Temperature Measurement Data. . . . . 31

Figure 13. Graphite-Epoxy Prepreg Between Press Plates. . . . . 34

Figure 14. Fiber Optic Interferometer for Strain Measurement. . . . . 35

Figure 15. Strain Measurement Data . . . . . 37

Figure 16. Uncured Graphite-Epoxy Temperature Measurement System. . . . . 38

Figure 17. Uncured Graphite-Epoxy Temperature Measurement Data . . . . . 40

Figure 18. Ninty Degree Gr/Ep. Differential Temperature Sensor. . . . . 42

Figure 19. Zero Degree Gr/Ep. Differential Temperature Sensor. . . . . 43

Figure 20. Temp. Versus Time, Ninty Degree Gr/Ep. Sample . . . . . 47

Figure 21. Diff. Temp. Versus Time, Ninty Degree Gr/Ep. Sample . . . . . 48

Figure 22. Fringe Displ. Versus Time, Ninty Degree Gr/Ep. Sample ..... 49

Figure 23. Fring Displ. Versus Diff. Temp., Ninty Degree Gr/Ep. Sample ..... 50

Figure 24. Temp. Versus Time, Zero Degree Gr/Ep. Sample ..... 51

Figure 25. Diff. Temp. Versus Time, Zero Degree Gr/Ep. Sample ..... 52

Figure 26. Fringe Displ. Versus Time, Zero Degree Gr/Ep. Sample ..... 53

Figure 27. Fringe Displ. Versus Diff. Temp., Zero Degree Gr/Ep. Sample ..... 54

Figure 28. Optical Fiber Placement in Composite Laminate. ..... 63

Figure 29. Fiber V Parameter Versus Number of Modes. ..... 70

# 1.0 Introduction

The nondestructive inspection (NDI) of materials has experienced an explosive growth in the past fifteen years due to the increased need for reliable material structures. Advanced composite materials in particular have progressed from trial applications in secondary structures to primary structural applications during that time. The materials technology has expanded in this area from glass fiber/polymer resin composites, to the current availability of metals, ceramics, and polymers in a variety of forms for both reinforcing fiber and matrix applications [46]. A commonly used preform material is graphite fiber reinforced epoxy tape, which can be stacked and cured to form laminates as shown in Appendix B. The directional mechanical properties of the finished laminate depends upon the fiber orientations in the layup.

Use of fiber reinforced composite structures in military aerospace vehicles is now rapidly expanding to meet performance requirements at minimum structural weight. In order to maintain the structural integrity of a structure, engineers utilize fracture mechanics theory, modelling, stress analysis, and periodic nondestructive inspection.

One promising answer to the near term need for a workable approach to composite structural integrity maintenance is an onboard sensor system which can identify situations requiring mainte-

nance or other corrective action. Sensors are needed which can monitor important parameters, such as strain and temperature in selected critical structural elements.

Fiber optic sensors have specifically been applied to the quantitative nondestructive characterization of materials for several years [1-3]. Due to the inherent similarity of unjacketed glass-on-glass optical fibers to graphite fibers in graphite-epoxy composites in particular, a number of investigators have considered the use of optical fibers as sensors which may be embedded directly within the composite laminae. The effects of temperature and strain integrated along the length of the sensor fiber in a composite specimen can be determined using a variety of simple methods. Spatial resolution of such quantities along the embedded fiber in length may be obtained using several more complicated distibuted fiber sensing techniques. Strain tensor quantites may be determined by both presuming accurate models of the applied stress and knowing the photoelastic and mechanical properties of the embedded fiber.

In this thesis, a novel optical fiber sensor for the measurement of strain, temperature in graphite-epoxy composite materials using differential interferometry is described. Chapter 1 introduces the reader to the development of such a sensor. Chapter 2 presents an overview of the basic sensing concepts, providing a few examples of how each concept has been applied. The third chapter details the theory of interferometric sensing, optical detection and analyzes the specific theory of an optical fiber Mach-Zehnder interferometer, the type used in the experiments discussed in Chapter 4. Experimental details of the optical interferometer are discussed in Chapter 4. In particular, the detection of strain and temperature in graphite-epoxy composites is also reported. Chapter 5 summarizes the experimental results, highlights the important aspects of the system, indicates some problems and limitations, and suggests possible improvements to the system.

Finally, the appendices contain a brief introduction to the basics of optical fibers, preparation of single mode fibers for experiments, and fabrication of graphite-epoxy composite laminates.

# 2.0 Fiber Optic Sensor Overview

There are two generic classes of fiber optic sensors; intrinsic sensors and extrinsic sensors. In the case of the intrinsic sensor, the parameter being measured interacts with a property of the fiber so as to modulate the intensity, the phase, or the polarization of the internally transmitted light. Extrinsic sensors utilize optical fiber as a transmission medium to carry light to and from a region which is external to the fiber and in which the light is modulated. The range of possible interactions include intensity modulation, phase (interferometric) modulation, polarization, and spectral (wavelength) modulation. In the following sections, each of these sensing interactions will be briefly described and a few examples of measurement in each category will be discussed.

## *2.1 Intensity Modulated Sensors*

Sensors based on a wide range of transduction mechanisms can be characterized as intensity modulated sensors or "amplitude" sensors. Any transduction technique which produces a change in optical intensity in response to an applied signal can be classified as such a sensor.

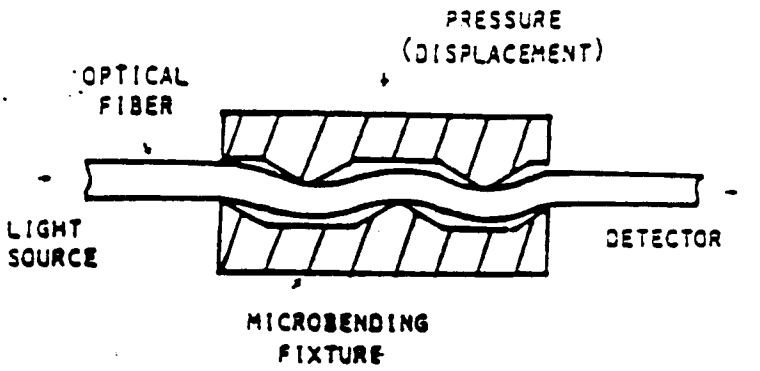


(A) MICROBENDING SENSOR CONFIGURATION

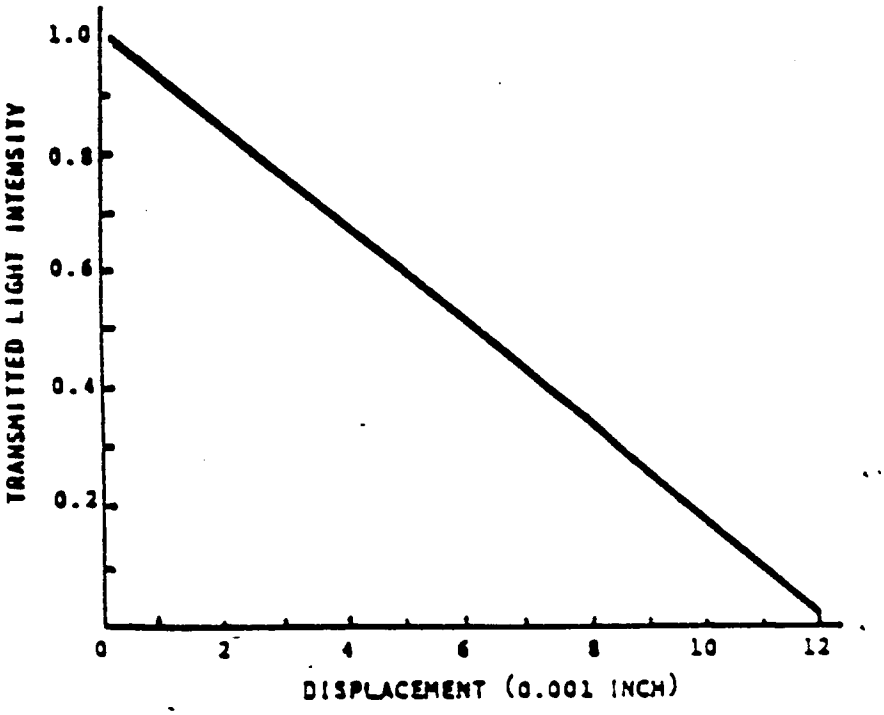


(B) OUTPUT VS DISPLACEMENT CURVE

Figure 1. Microbend Sensor

One class of intensity modulated sensors depends upon the effects of microbending on a multimode fiber. The essence of this sensor is depicted in Figure 1. As the fiber is bent in response to a displacement of the plates, some light is transferred from the core into the cladding, i.e. propagating modes are converted into radiation modes. A linear relationship between displacement and such mode-induced intensity is shown in Figure 1 for small displacements under ideal conditions. Since the range of displacements indicated here is small, this sensor is better configured as a force transducer.

This sensor has the advantages of being immune to the effects of contamination and of having potentially low cost. The major disadvantage of this sensor is that any changes in intensity produced by changes in the source, fiber, or connections result as effective noise and affect the accuracy of measurement.

Figure 2 shows an example of a microbend sensor that has been designed to measure pressure. In this configuration, a more dimensionally stable fused silica diaphragm is used in lieu of a metallic diaphragm to circumvent the problem of creep at elevated temperatures. Repeatable operation at $430^0C$ with better than 1 % measurement accuracy was reported for this device [33].

Another class of intensity modulated but extrinsic sensors depend on the proportional reflection principle. This type of sensor uses a fiber to transmit light to a reflecting surface and to return a fraction of that light to a detector. The intensity of the light coupled into the return fiber is dependent upon the distance of the fiber from the reflecting surface. This is shown in Figure 3.
As is the case with other intensity-based sensors, the accuracy of these devices is affected by changes in source output and fiber attenuation.

This simple type of sensor can be configured, for example as a tachometer. In this case, the input fiber is located at a fixed distance from a rotating shaft and light is returned to a nearby receiving fiber from reflective areas on the shaft. The output of the optical detector connected to the return fiber is a train of pulses, the frequency of which is proportional to the shaft speed. As long as an

ORIGINAL PAGE IS
OF POOR QUALITY

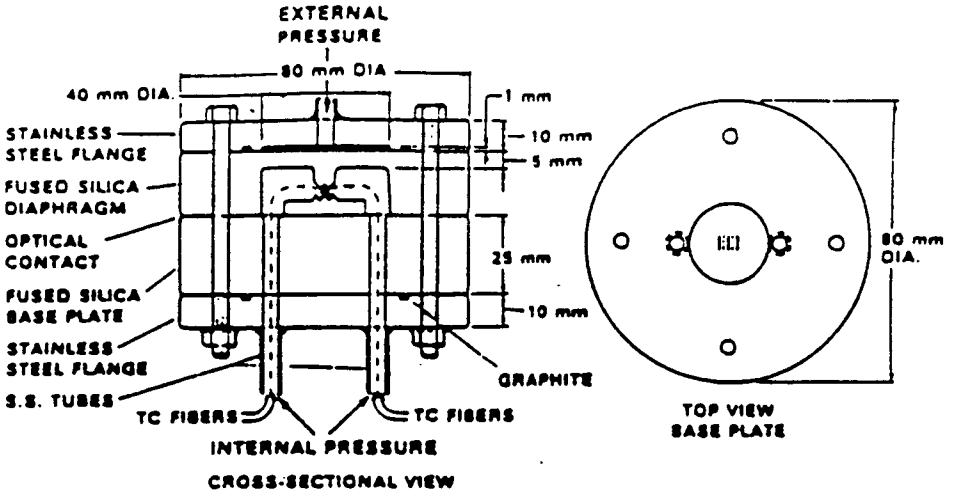


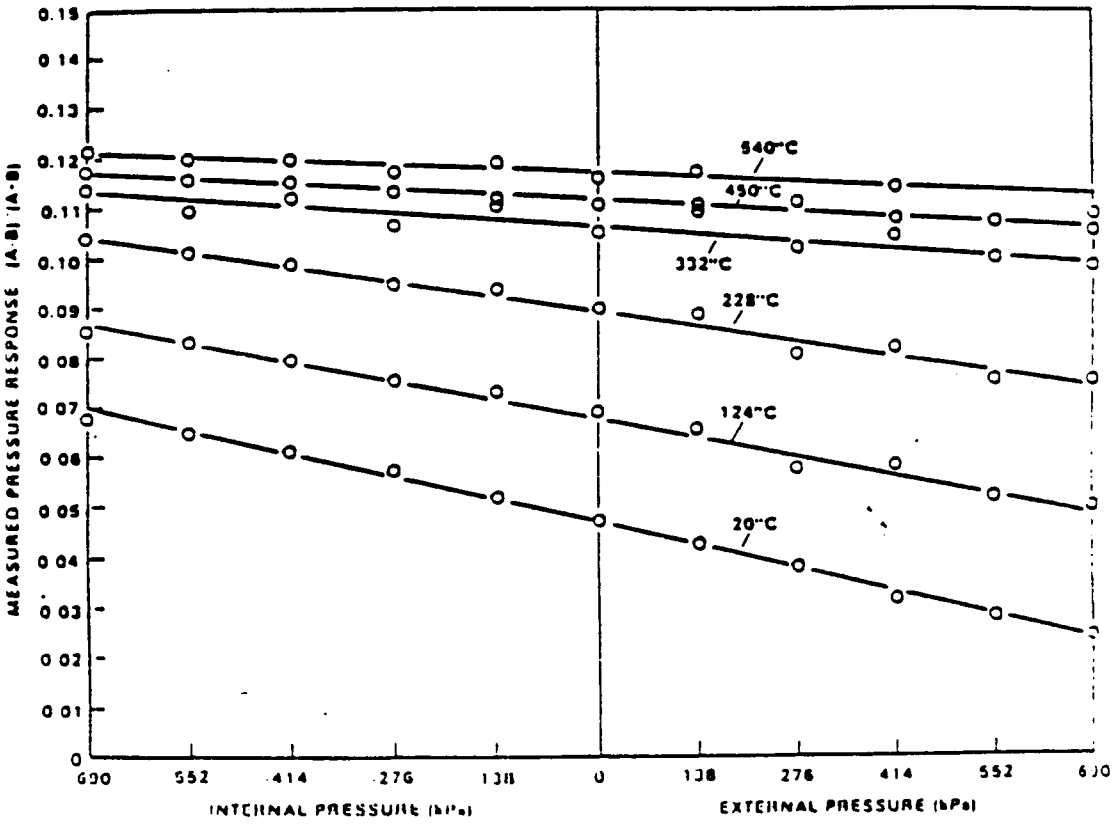


Figure 2. Microbend Sensor for Pressure Measurement.

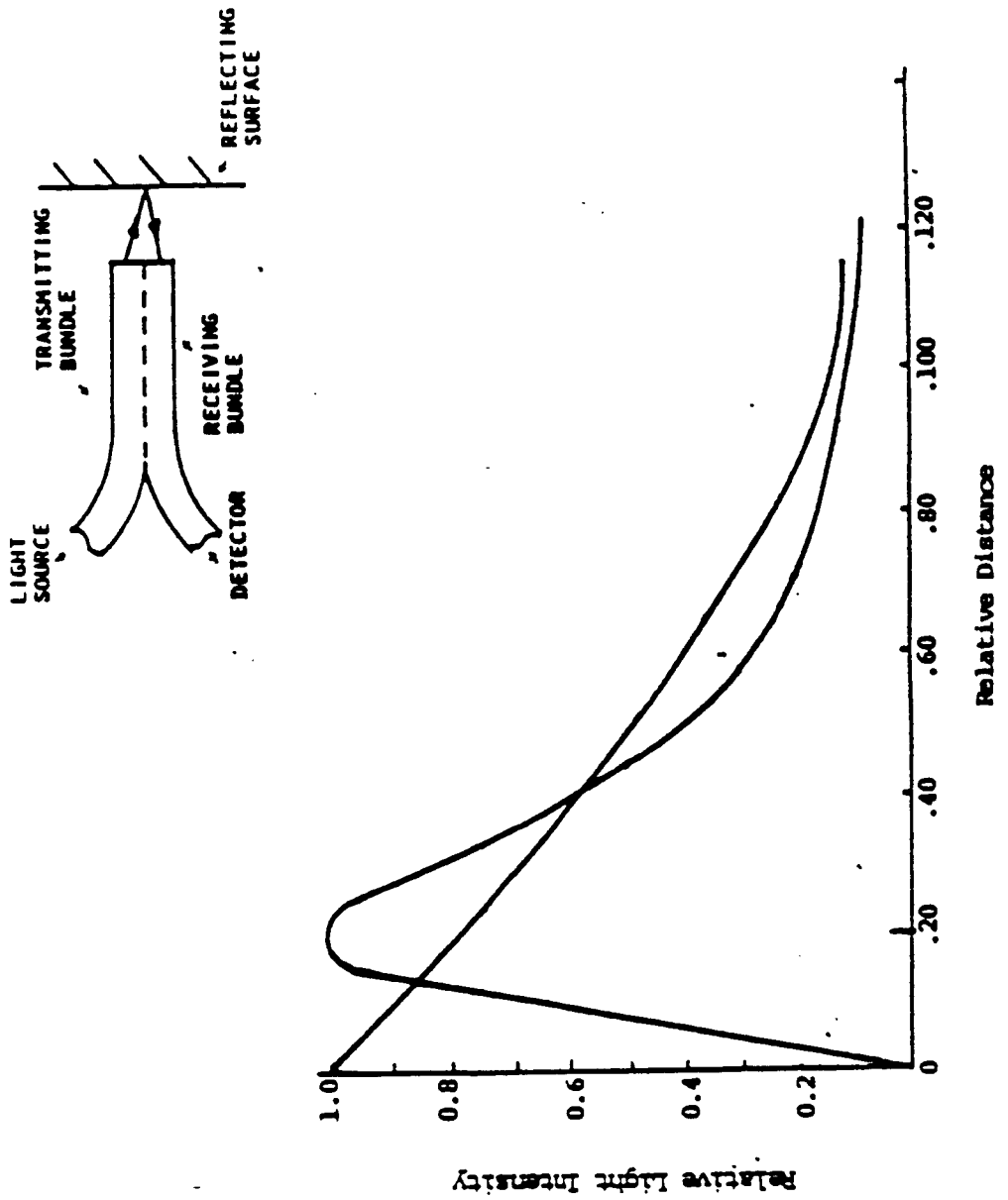


Figure 3. Proportional Reflection Sensor

adequate modulation ratio is maintained, intensity variations resulting from source or fiber degradation does not affect the accuracy of the speed data.

## 2.2 *Phase (Interferometric) Sensors*

Optical interferometry is the basis for all types of phase sensors. Figure 4 shows the four different types of interferometric configuration, namely Michelson, Mach-Zehnder, Sagnac and Fabry-Perot, in terms of a conventional schematic arrangement using airpaths and bulk optical components. Figure 5 shows how the same four systems can be constructed instead with optical fiber elements. Sensors employing the Mach-Zehnder configuration are the most widely used.

During the past several years, the customary configuration of the all-fiber Mach-Zehnder interferometer has undergone a number of modifications in an effort to enhance performance. In early designs, launching light into two optical fibers from a single source required a beamsplitter and two microscope objective lenses. A similar recombining scheme was used to image the output on the detector. The use of these macroscope optics produces two problems. First, the two arms of the interferometer are physically separated by a relatively large distance, making it difficult to control differential perturbations that are not part of the signal to be sensed. Second, dielectric beamsplitters are subject to microphonics, which can prove to be a limiting noise source. To eleminate problems, Sheem and Giallorenzi pioneered an encapsulated etching technique to produce a single-mode fiber optic divider which operates on the following principles [40]. Each mode of a light wave propagating along a fiber has an evanescent field which extends beyond the waveguide core. If two fiber cores can be brought into close contact, the field in one can penetrate into the other and excite a light wave in it. Excessive scattering will occur during this crossover if the change in refractive index in the area between the cores is not kept very small. This can be accomplished by twisting together two fibers that have their polymer coatings removed, and etching

ORIGINAL PAGE IS
OF POOR QUALITY

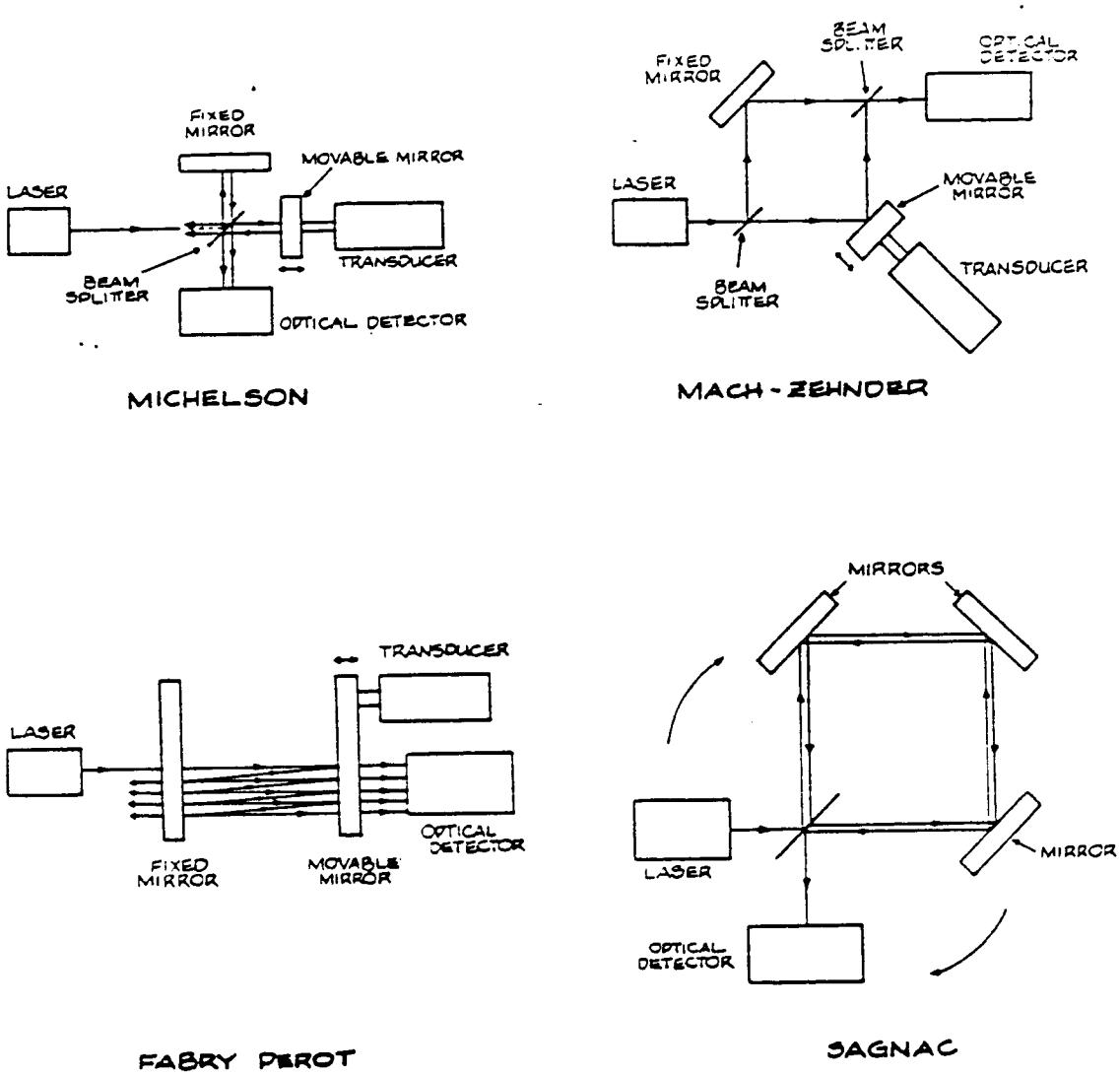


Figure 4. Conventional Interferometric Systems.

ORIGINAL PAGE IS
OF POOR QUALITY

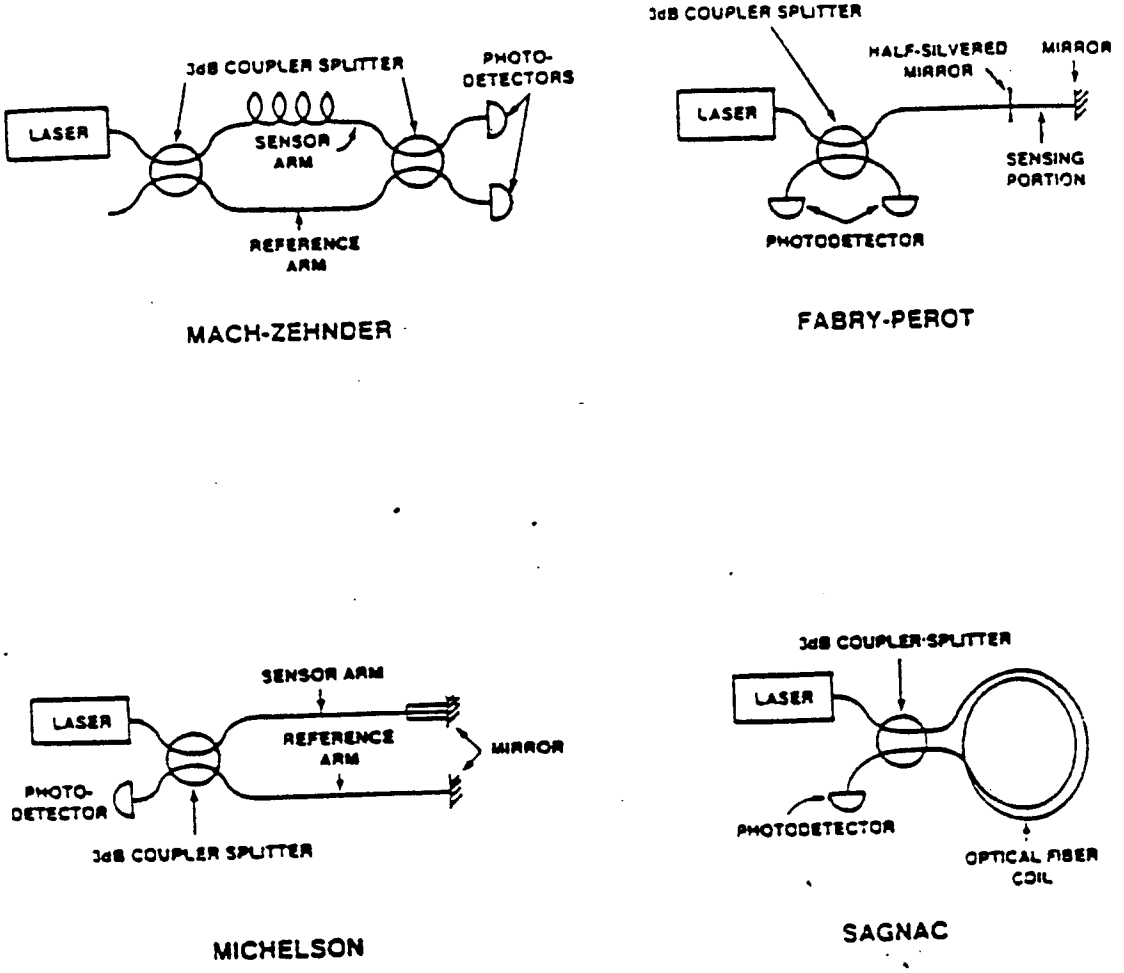


Figure 5. Optical Fiber Interferometric Systems.

away the cladding glass. The fibers are then surrounded by a medium that matches as nearly as possible the index of the core glass. The splitting ratio of such a device can be controlled by adjusting the proximity of the two cores and their interaction length. This 'bottle coupler' can be used to replace the beam splitter and one lens for both launching and recombining the optical beams.

Detection of the phase shift in a fiber interferometer also presents some interesting problems. If the two beams are recombined via a bottle coupler or beamsplitter, the result is an intensity modulated optical field in the coupler output. Alternatively, the output ends of the fibers may simply be brought into close proximity to one another. In this case, the fibers act as a pair of slits or pinhole apertures, as in the classic interference experiment performed by Young in 1802. If the resulting expanding spherical wavefronts from the fiber are allowed to fall on a screen, an interference pattern results. The pattern will have a constant integrated intensity, but will move back and forth across the image plane as the phase relationship between the signals in the two interferometer arms is altered. Regardless of the output orientation, the intensity of the signal falling on the detector will vary sinusoidally either in time or space, or both. This means that the detector will have a variable sensitivity to phase shift, determined by the phase of the two beams at any given time or relative detector position. Because of this, various feedback methods have been developed to hold the output of the interferometer at maximum sensitivity (in quadrature). These methods include incorporating a phase modulator (such as a piezoelectric fiber stretcher in the reference arm), and frequency modulating the light source (laser diode) to maintain the output phase relationship [41,42]. An alternative to these approaches is to incorporate a sophisticated signal processing technique to obtain the requisite phase compensation [43]. One very novel way to eliminate the quadrature drift problem was recently reported by Willsen and Jones in their paper describing a fiber-optic sensor for the detection of static magnetic fields [44]. The output of a Mach-Zehnder interferometer, with the output fibers adjacent to one another, was allowed to fall on a detector that consisted of a linear photodiode array. Since the quadrature position was always somewhere on the array, they were able to determine the phase shift by simply subtracting a zero magnetic field scan

from a non-zero field scan. For small phase shifts the rms value of this difference is directly proportional to the change in phase.

The fiber optic interferometric sensor generally features an extremely high degree of sensitivity because it utilizes interference of light waves (wavelengths on order of 1 um). For the same reason, the use of polarization-maintaining fibers is preferable, since the matching between the polarization planes of the sensing and the reference paths is essential for stable interferometry.

A novel interferometric sensor was recently reported by Rowe, Rausch, and Dean in their paper describing an interferometric approach using the optical signal as a carrier, with radio frequency (RF) modulation [45]. The system was simple, low-cost and not as sensitive as conventional interferometric sensors; see Figure 6. Radio frequency signal modulation was achieved using standard electronic circuitry. Multimode fibers were used as sensors and a coherent optical source (i.e. laser) was not required. This system was used to demonstrate strain measurement with embedded fibers in graphite/epoxy test specimens.

As another example the fiber optic gyro, which has received the most attention in the fiber optic sensor field, uses a Sagnac interferometer. Figure 5 is the basic arrangement. Light from a coherent source is divided and launched into both ends of a coiled single-mode fiber. The rotation of the coil can be determined from the phase difference between the two counter-propagating optical fields, which experience different phase shifts corresponding to their directions of propagation. The stability of polarization states is critical for ultrahigh sensitivity and accuracy (for example, the detection of the rotation rate of the earth). Polarization-maintaining fibers have been employed widely in this field.

ORIGINAL PAGE IS
OF POOR QUALITY

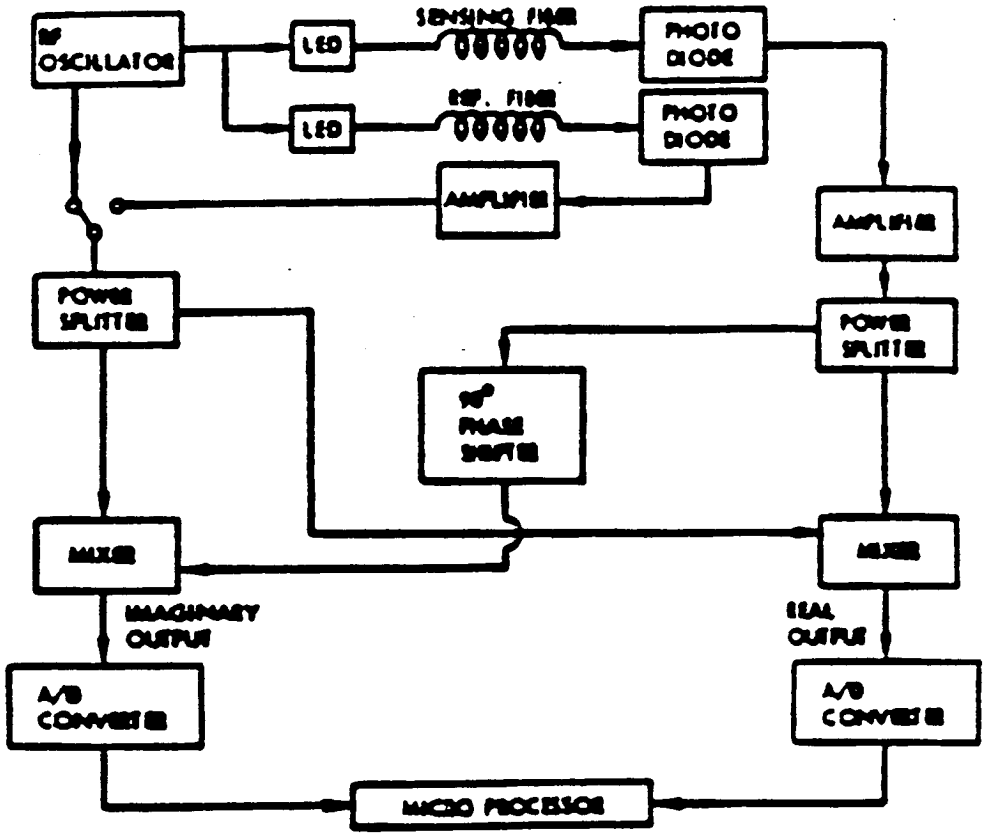


Figure 6. RF Interferometer System Block Diagram

## 2.3 *Polarization Modulated Sensors*

Polarization sensors detect the presence of some physical field via a change in the state of polarization of the light propagating through a fiber. This polarization state change is the result of the phase velocities of the two polarization components of the single-mode fiber field being altered unequally by the action of the applied physical field. Consequently the sensor can be viewed as a differntial interferometer; the two light beams travel within the same fiber but with orthogonal polarizations. This sensor configuration is simpler than that of the conventional Mach-Zehnder interferometric sensors but, because they operate in a differential mode, a 3dB loss in sensitivity usually results. Polarization sensors for detecting various fields, for example, acoustic and magnetic [34,35], temperature [36], and electric current [37], have been demonstrated.

Polarization sensors fall into two categories. In the first, the fiber is attached in some way to a material which is sensitive to the field to be detected and arranged in such a manner that a response of this material asymmetrically stresses the fiber cross-section. This unequally changes the phase velocities of the two orthogonally polarized modes [34]. Alternatively, the physical field directly changes the birefringence in the fiber, for example, via the Faraday effect or the temperature dependence of the internal transverse stress asymmetry, to result in a polarization change.

An example of a polarization based sensor was demonstrated at the Naval Research Laboratory [35]. In this device, light of a known polarization is launched into a single-mode fiber which is attached to a piece of magnetostrictive material. Typically the fiber is wound around, and bonded to, a nickel cylinder. An analysing polarizer is arranged at the other end of the fiber such that in the zero applied field conditions, no light reaches the detector behind it. Application of a magnetic field strains the fiber bonded to the stretcher, and the consequent induced birefringence modifies the state of polarization of light at the output of the fiber and results in a signal at the detector (see Figure 7).

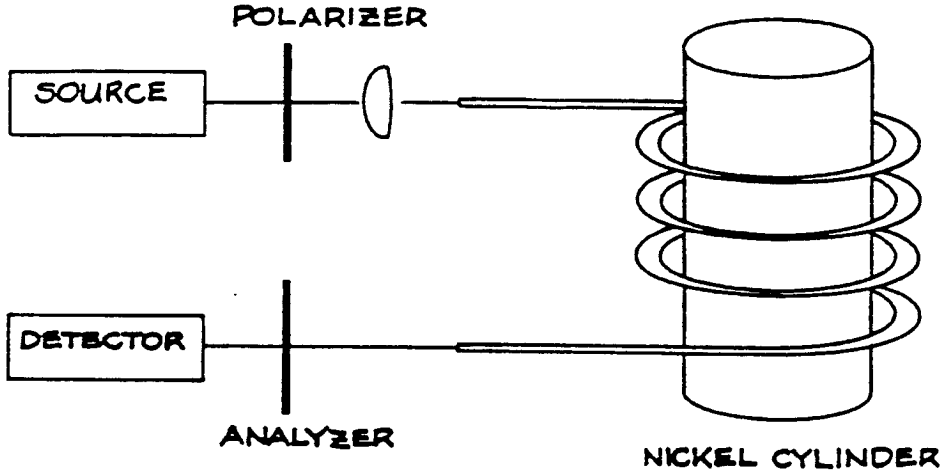


Figure 7. Polarization Sensor

An alternative configuration for polarization sensors has been proposed and demonstrated. It exploits the relationship between the axial stress and the transverse stress asymmetry in high-birefringence fibers. Axially straining the fiber induces a large change in the fiber birefringence.

Polarization sensors are finding applications in distributed sensing due to their large dynamic range. For example they have been used for the monitoring of temperature distributions in large structures, and hot spots in transformers and cables.

## 2.4 *Wavelength Modulated Sensors*

Wavelength modulated sensors are based mainly on the numerous physical phenomena which influence the variation of reflected or transmitted light intensity with wavelength. Four principle areas in which wavelength modulation may be exploited are, in chemical analysis using indicator solutions, in the analysis of phosphorescence and luminescence, in the analysis of blackbody radiation, and in the use of Fabry-Perot, Lyot (polarization based) or similar optical filters. Chemical indicator used for monitoring pH and optical pyrometers used for temperature measurement are a few of the sensors belonging to this category.

Figure 8 for example illustrates an optical pyrometer; this sensor consists of a sapphire fiber connected to miniature blackbody cavity [38]. When the cavity is immersed in the temperature field to be monitored, a continuous distribution of wavelengths is injected into the fiber. The intensity versus wavelength distribution of this radiation is given by Planck's blackbody radiation law. Since the intensity associated with each wavelength is a function of temperature , a ratio of intensity at different wavelengths being radiated by the blackbody can be compared with known curves and the temperature accurately determined. Optical filters can be used to select desired wavelengths to form the ratio, but a multiple channel all-fiber wavelength division multiplexer placed on the end of the

ORIGINAL PAGE IS
OF POOR QUALITY

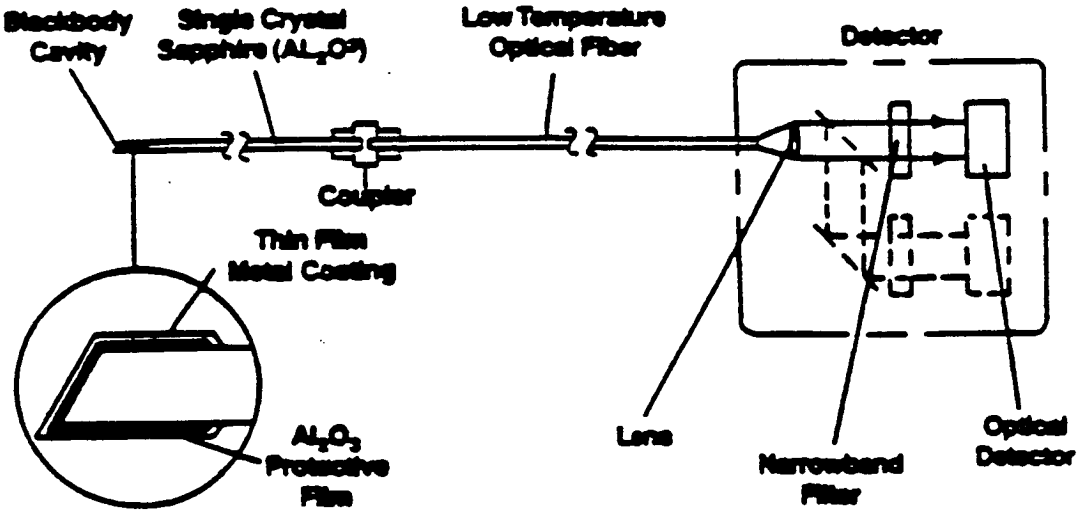


Figure 8. Basic Elements of the Sapphire Blackbody Sensor

fiber eliminates the need for such splitter and filters. Such devices typically have a temperature operation range of 500 to 2000$^0C$ and an accuracy of 0.005 %. Current interest in this device is to replace chromel-alumel thermocouples for measurement of turbine inlet temperatures.

A fiber optic temperature sensor system based on the temperature dependent absorption of a rare earth doped fiber element was demonstrated as shown in Figure 9 by the United Technologies Research Center [39]. The temperature measurement reported here was designed to be independent of the magnitude of the sensing signal and reference wavelengths were taken before and after passage through the rare earth-doped fiber. To avoid drifts in the detector sensitivity, the same detector measured the signal and reference wavelengths after passing through the fiber, but with the two sources alternately pulsed.

ORIGINAL PAGE IS
OF POOR QUALITY

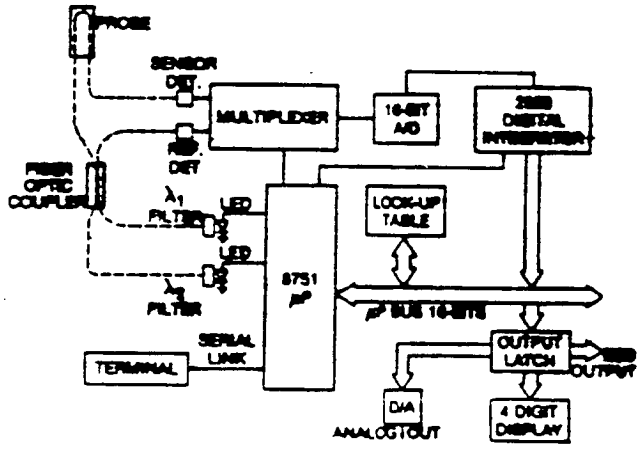


Figure 9. Fiber Optic Temperature Sensor Schematic.

# 3.0 Interferometric Optical Fiber Sensing

Interferometric optical fiber sensor systems measure changes in the phase of an optical field which propagates in a fiber. This phase is a function of the length of the fiber, the index of refraction of the fiber core and the cross-sectional dimensions of the fiber. Each of these factors is in turn dependent upon the mechanical interactions between applied temperature, pressure, or strain perturbations and the fiber. Length variations, for example, are caused either directly by thermal expansion or by the application of longitudinal strain and indirectly by the Poisson effect. Index variations are caused either by changes in temperature or by changes in strain via the photoelastic effect. Fiber dimension variations are caused by changes in radial strain produced by a pressure field, longitudinal strain via Poisson's ratio, or by thermal expansion.

## *3.1 Analytical Model*

The absolute phase of light traveling in a single mode optical fiber of length, L, is :

$$\Phi = \frac{2\pi nL}{\lambda} = \beta L, \tag{3.1}$$

where $\beta$ is the propagation constant for the mode in the fiber core, n is the effective index of refraction of the fiber, and $\lambda$ the optical guide free space wavelength. The effective refractive index must lie somewhere between that of the cladding and the core for a mode at cutoff. In a single mode fiber this is typically less than 1 % difference in these indices, therefore n can be considered to be the core refractive index.

If the fiber is stressed to produce an axial strain $\varepsilon = \frac{\Delta L}{L}$, a phase change

$$\Delta\Phi = \beta\Delta L + L\Delta\beta \tag{3.2}$$

$$= \beta\varepsilon L + L\Delta\beta$$

results.

The first term in equation (3.2) represents the change in fiber length. The second term represents change in the optical waveguide properties due to strain. It has been argued by Butter and Hocker [5] that the most significant of these effects is the change in effective index of refraction along the length.

In the simple case of a pure Silica fiber, the length change can be easily related to the material properties of the guide [6]. If the fiber is subjected to a change in temperature ($\Delta T$) then the optical phase of the light going through it ($\Delta\Phi$) undergoes two effects :

1. The change in fiber length due to thermal expansion or contraction

2. The temperature induced change in the index of refraction.

Thus, since $\Phi = \frac{2\pi nL}{\lambda}$, we can write :

$$\frac{\Delta\Phi}{\Delta T L} = 2\frac{\pi}{\lambda}\left(\frac{n}{L}\frac{dL}{dT} + \frac{dn}{dT}\right) \tag{3.3}$$

Where the effects of the fiber diameter changes are neglected as small.

By assuming the temperature variations to be negligible, the strain measurements can be obtained. The total phase change produced by stress alone may then be written in general as :

$$\Delta\Phi = \frac{2\pi L}{\lambda}[\varepsilon_l - \frac{n^2}{2}(P_{11} + P_{12})\varepsilon_r + P_{12}\varepsilon_l], \tag{3.4}$$

where L is length of the sensing section of the fiber, $\varepsilon_l$ and $\varepsilon_r$ are the longitudinal and radial strain, respectively, n is the core index, and $P_{11}$ and $P_{12}$ are the photoelastic constants of the Silica fiber [4]. This relationship indicates that longitudinal and radial strain contributions cannot be resolved from a single phase measurement. Moreover, if the strain varies along the length of the fiber, the total phase change can be calculated from equation (3.4) by integrating individual contributions along this length.

Phase measurements may be represented in terms of strain components if the geometry of the strain field is known. For example, in the case of pure axial strain the radial strain is

$$\varepsilon_r = -\varepsilon_l v, \tag{3.5}$$

where v is Poisson's ratio, the ratio of strain in the lateral direction to that in the axial direction, and equation (3.4) simplifies to :

$$\frac{\Delta\Phi}{\varepsilon L} = \frac{2\pi}{\lambda}[1 + P_{11}n^2\frac{v}{2} + P_{12}(\frac{n^2 v}{2} + 1)]. \tag{3.6}$$

Poisson's ratio ranges from 0.17 to 0.32.

Substituting values of pure silica (n = 1.458, $P_{11}$ = 0.126, $P_{12}$ = 0.274, and v = 0.17 ) and the Helium-neon laser light freespace wavelength 633 nm, the phase change per meter of standard fiber is $2.2*10^7$ radians, or 0.22 radians per centimeter of fiber per microstrain.

## 3.2 *Optical Signal Detection*

The instantaneous amplitudes of the light propagating in the sample and the reference are $E_1$ and $E_2$ respectively

$$E_1 = E_0 expi[\omega_0 t - k(x \sin\theta + z\cos\theta + \varphi)], \tag{3.7}$$

$$E_2 = E_0 expi[\omega_0 t - k(-x \sin\theta + z\cos\theta - \varphi)], \tag{3.8}$$

where $E_0$ is the maximum amplitude, k the propagation constant, $\omega_0$ the optical radian frequency and $2\varphi$ is the phase difference between the fields in the sample and the reference arms and $\theta$ the angle of incidence of the optical beam measured from a line normal to the surface of the detector.

The beams when superimposed give a total field E,

$$E = E_1 + E_2. \tag{3.9}$$

Simplifying using trigonometric identites yields,

$$E = 2E_0[expi(\omega_0 t - kz\cos\theta)]\cos(kx\sin\theta + \varphi). \tag{3.10}$$

The total optical irradiance is given by the product of the complex conjugates of the total output field,

$$H = EE^* \tag{3.11}$$

$$= 4E_0^2\cos^2(kx\sin\theta + \varphi) \tag{3.12}$$

Since $\theta$ is very small, $\sin\theta = \theta$ and

$$H = 4E_0^2\cos^2(kx\theta + \varphi). \tag{3.13}$$

The above equation represents the straight line interference pattern. From this equation it can be deduced that H is a maximum when $\cos^2(kx\theta + \varphi)$ is a maximum. The cosine term is maximum for $\cos^2(kx\theta + \varphi)$ is a maximum. The cosine term is a maximum when

$$kx\theta + \varphi = m\pi, \qquad m = 0,1,2,3, \textit{and} \tag{3.14}$$

$$x = \frac{(m\pi - \varphi)}{k\theta}. \tag{3.15}$$

The values of x give the positions of intensity maxima, or constructive interference. The changing phase of the beam results in a fringe shift in the x direction, and the amount of light transmitted by a suitably placed Ronchi grid with line spacing

$$d = \Delta x = \frac{\lambda}{2\theta} \tag{3.16}$$

will vary (see Figure 10).

The light flux transmitted by any one slit is

$$\varphi_1 = \int_{x_1}^{x_1} \tfrac{d}{2} H(x)dx \tag{3.17}$$

where $x_1$ is one edge of the slit and $x_1 + \frac{d}{2}$ the other edge. By straight forward integration we obtain

$$\varphi_1 = E_0^2 d - (2E_0^2 \frac{d}{\pi}) \sin[(2\pi \frac{x_1}{d}) + 4\frac{\pi}{\lambda}\Delta L]. \tag{3.18}$$

For m slits the total flux $\Phi = m\varphi_1$.

Using the small signal approximation $\Delta L << \lambda$ and neglecting the terms of the resulting expansion which are independent of optical path length change, equation (3.18) becomes :

$$\Phi = m[E_0^2 d - E_0^2 d(\frac{8\Delta L}{\lambda})]. \tag{3.19}$$

Equation (3.19) shows that the total signal is composed of a dc light flux which depends on the phase shift. The dc term is the major source of shot noise in the detector. If the laser has a total incident power $P_0$ , then the incident power transmitted to the detector is given by :

$$P = (\frac{P_0}{2}) - P_0(\frac{4\Delta L}{\lambda}). \tag{3.20}$$

Since the Ronchi ruling transmits only half the power, the detector receives $\frac{P_0}{2} \propto mE_0^2 d$. The signal current at the detector is proportional to the incident power and is given by :

$$i_s = 4\alpha P_0 \frac{\Delta\Phi}{2\lambda}, \tag{3.21}$$

where $\alpha$ is the sensitivity of the optical detector [7,8].

# 4.0 Experiment

A form of Mach-Zehnder interferometer was constructed using single-mode fibers for the two arms as shown in Figure 10. If the optical pathlengths of the two arms are nearly equal ( to within the coherence length of the source ), the light from the two fibers interferes to form a series of bright and dark fringes. A change in the relative phase of the light of one fiber with respect to the other is observed as a displacement of the fringe pattern, a phase change of $2\pi$ radians causing a displacement the width of one fringe.

The phase of light leaving a fiber can be changed, as detailed in section 3.1, by dimensional and/or index of refraction changes in the fiber. Thus, if one fiber is subjected to a different strain, pressure or temperature, than the other, this difference results in as a displacement of the fringes at the output. These effects can thus be measured by this displacement.

The fiber-optic interferometer implemented used a He-Ne laser light source ( $\lambda = 0.633um$) and two lengths of Newport Corporation F-SV step-index optical fiber, single-mode at the laser wavelength. The laser output was expanded, divided by a beamsplitter, and the resulting two beams coupled into two fibers by a pair of 5X microscope objectives with NA = 0.1. The output ends of the fibers were placed side by side, so that their axes were parallel, separated by one fiber diameter, and their expanding output beams overlapped. Fiber pairs of two to three meter lengths each

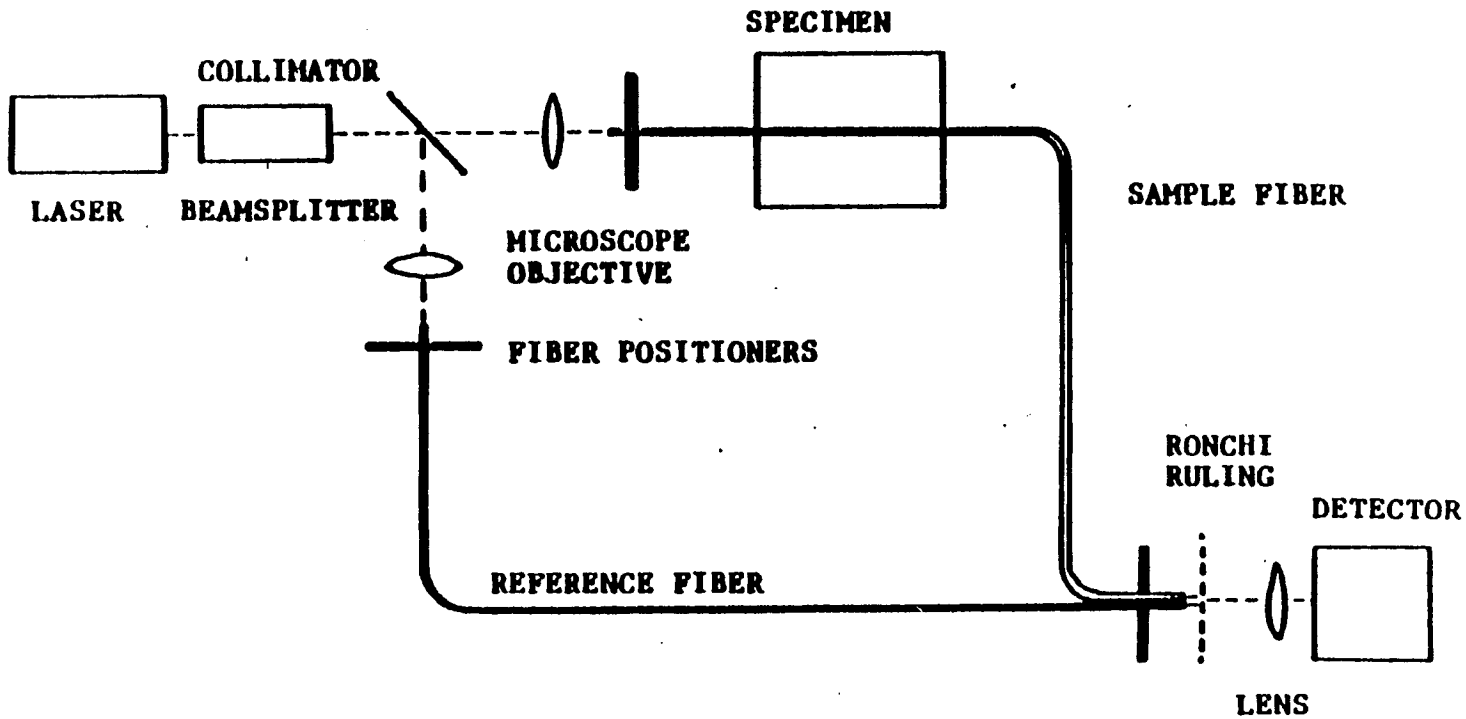


Figure 10. Single-Mode Mach-Zehnder Interferometer

were used with lengths matched to within a few centimeters. The overlapping output beams were observed on a screen, where they formed parallel bright and dark interference fringes.

The experiments which were performed using the generic Mach-Zehnder interferometer system are as follows :

1. Fiber optic interferometer used for temperature sensitivity measurement.

2. Fiber optic interferometer used for strain and temperature measurement in a graphite-epoxy composite laminate.

3. Differential interferometric measurement of temperature in a $0^0$ and $90^0$ unidirectional graphite-epoxy laminates.

A temperature sensitivity measurement was made by placing a 0.09 m section of one of the fibers on an aluminum plate. The plate was heated using heating elements which were connected to a digital temperature controller, as shown in Figure 11 The reference fiber was taped to the optical bench to remain at room temperature ( 20 − 25$^0$ c ). The slight variation was due to the air flow in the laboratory. The temperature was varied and the fringe displacements were recorded on video tape for repeated playback and measurement. The average of the readings were recorded as shown in Table 1.

Taking the case of He-Ne laser source and fused silica fiber, we use the values [46-48]

$$\frac{dL}{dT} = 5*10^7/^0c,$$

$$\frac{dn}{dT} = 10*10^{-6}/^0c,$$

L = 0.09,

n = 1.456,

$\lambda = 0.6328*10^{-6}m$

so that equation (3.3) yields $\frac{\Delta\Phi}{\Delta TL}$ = 180.6 radians per degree centigrade per meter. Stated differently, this implies a fringe displacement of 29 fringes per degree centigrade per meter.

The value for the thermal expansion coefficient and the temperature dependent refractive index can vary greatly for multi-component glasses. $\frac{dn}{dT}$ can actually be positive or negative around room temperature. Morover, $\frac{dn}{dT}$ is itself a function of temperature and wavelength, and most tabulated values are averaged over a rather large temperature range and given for only a few wavelengths. Therefore, the value of $\frac{\Delta\Phi}{\Delta TL}$ could be different from that given in equation (3.3) for other glass compositions.

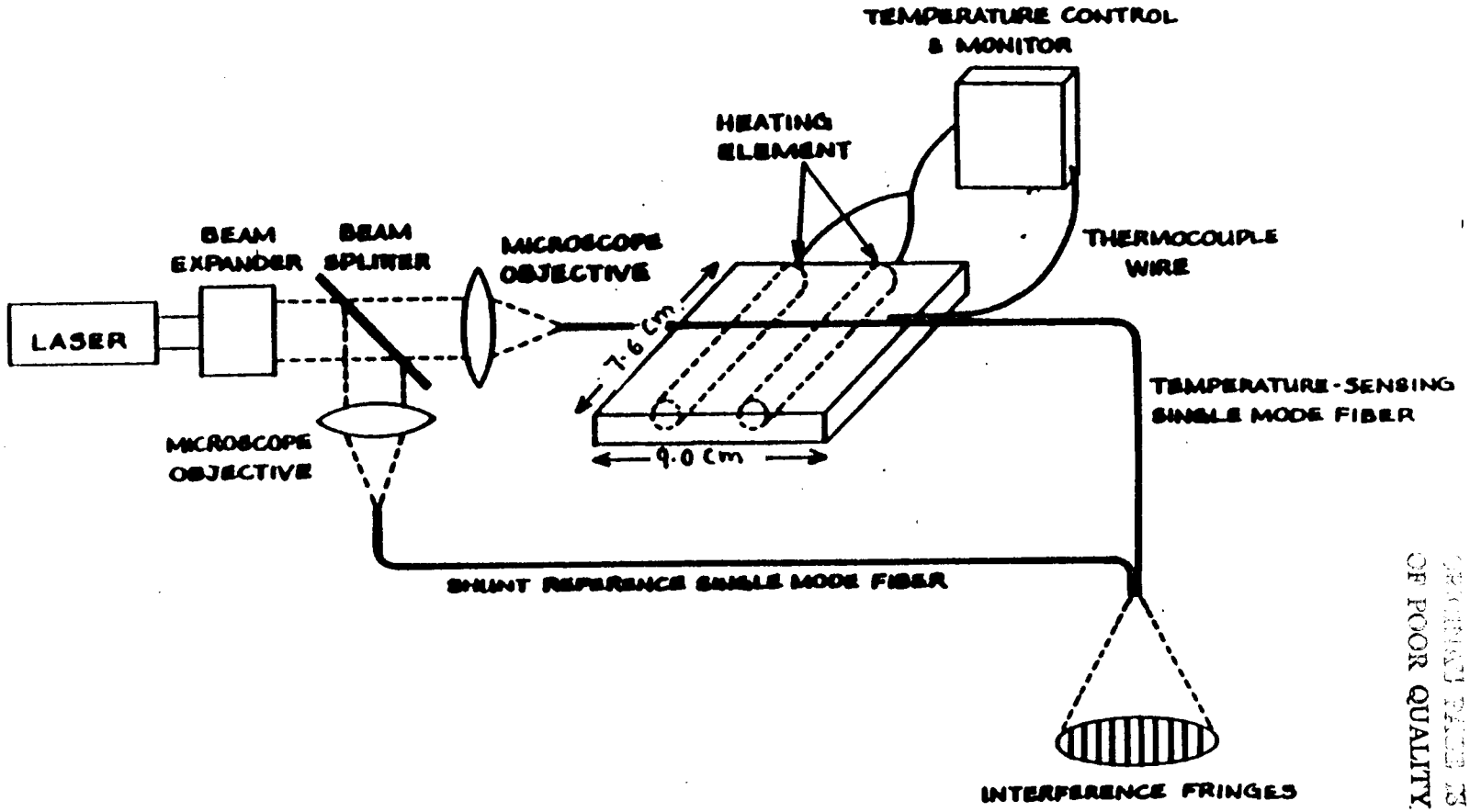


ORIGINAL PAGE IS
OF POOR QUALITY

Figure 11. Fiber Optic Interferometer for Temperature Sensing Measurement.

ORIGINAL PAGE IS
OF POOR QUALITY

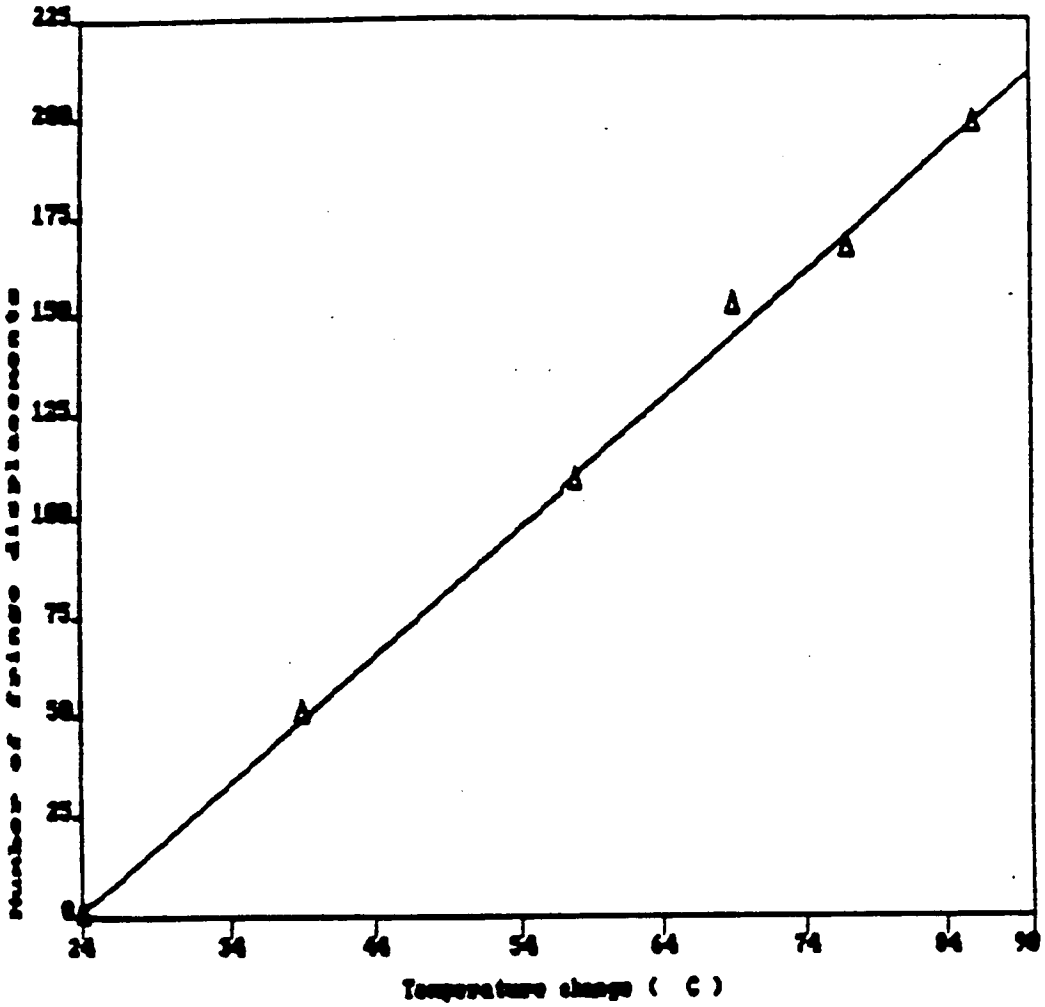


Figure 12. Temperature Measurement Data.

The average fringe displacement measured was 36 fringes $/^0C - m$. Taking into account the drift in room temperature and the region in which the thermocouples were placed to monitor the temperature, we consider the experimental results obtained to be good.

## *4.1 Fiber optic interferometer used for strain and temperature measurement in a graphite-epoxy composite laminate.*

Optical fibers which were single-mode at 633 nm were imbedded between adjacent plies of graphite-epoxy prepreg as shown in Figure 13 (see Figure 28 also). Once the symmetric cross-ply (see appendix B) laminate of dimensions, 17.78 by 5.08 cm was fabricated and cured, the specimen was subjected compressive force in a 15 cm by 15 cm plate press and the resulting strain at the location of the fiber measured by monitoring optical phase modulation as shown in Figure 14. The fringe displacement was again recorded on video tape for repeated measurement. The results are shown in Table 2 and plotted in Figure 15. The theoretical results were calculated from equation (3.6). The experimental results obtained correlate well with those of the theoretical analysis. Hence, we consider the experimental results obtained to be good.

An uncured composite sample of dimensions 17.78 by 5.08 cm was fabricated (see Appendix B) with a single mode fiber imbedded between adjacent plies of the graphite-epoxy prepreg. The sample was used in the sensing arm of the interferometer as shown in Figure 16. The specimen was then placed between the press plates and heated. The resulting temperature at the location of the fiber measured by monitoring the temperature using thermocouples placed close to the imbedded optical fiber. The fringe displacement was again recorded on video tape for repeated measurement. The results are shown in Table 3 and plotted in Figure 17. The results indicate a nonlinear relationship. The optical fiber seems to be very sensitive at higher temperatures, particularly above $65^0C$. The above results can be used as a preliminary cure cycle monitoring of graphite-epoxy laminates.

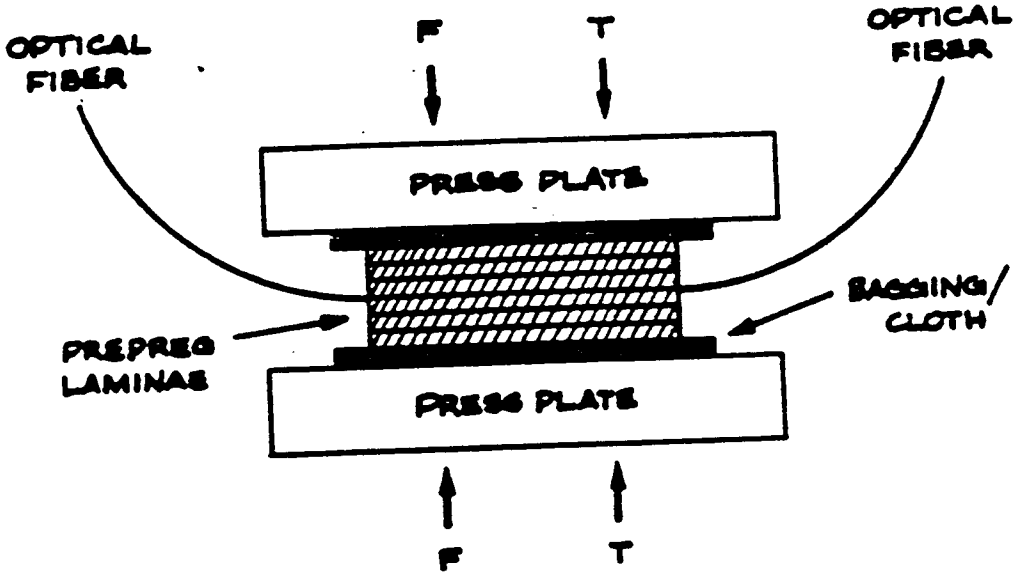


Figure 13. Graphite-Epoxy Prepreg Between Press Plates.

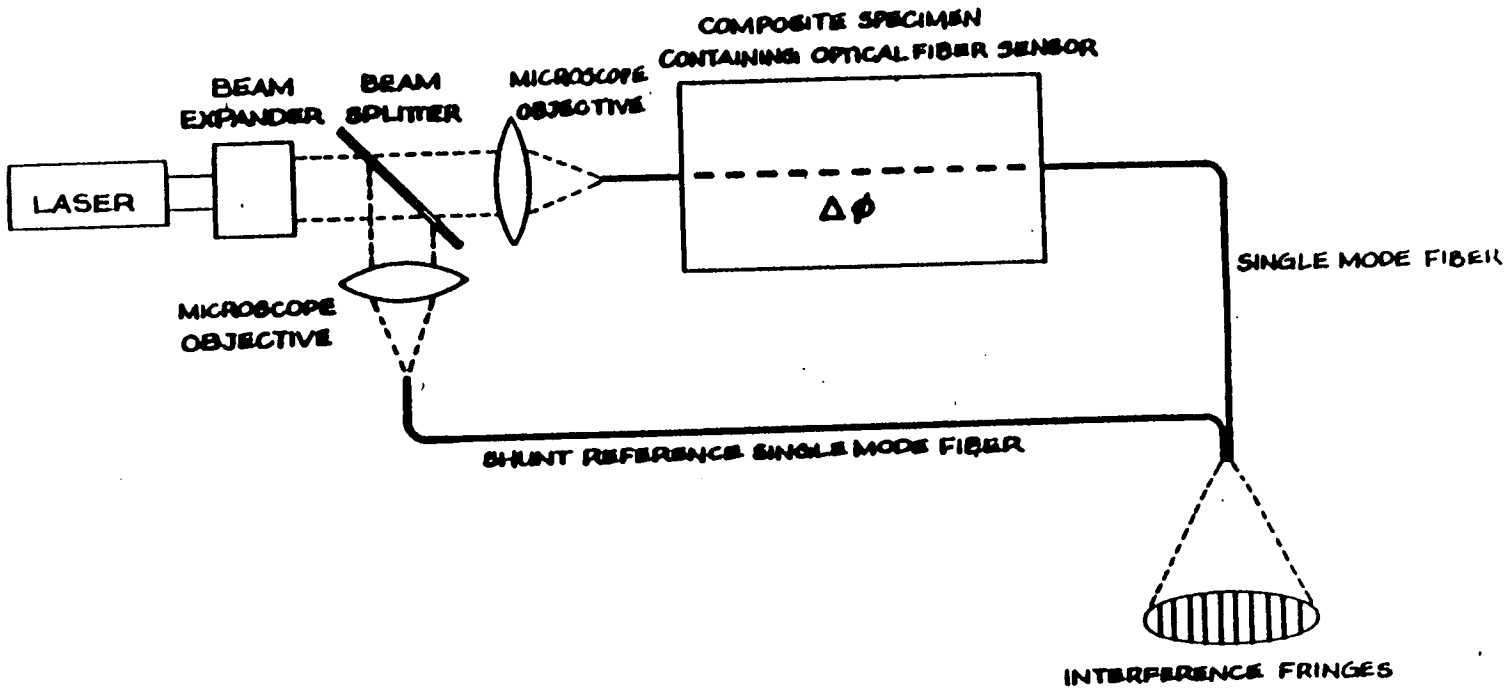


Figure 14. Fiber Optic Interferometer for Strain Measurement.

| Strain | Phase Theoretical (rads) | Phase Experimental (rads) |
|---|---|---|
| 0.0 | 0.0 | 0.0 |
| 0.88 | 16.5 | 19.0 |
| 1.65 | 34.0 | 43.5 |
| 2.48 | 50.0 | 56.5 |
| 3.30 | 67.5 | 76.0 |
| 4.11 | 85.0 | 94.0 |

**Table 1. Strain Measurement Data.**

ORIGINAL PAGE IS
OF POOR QUALITY

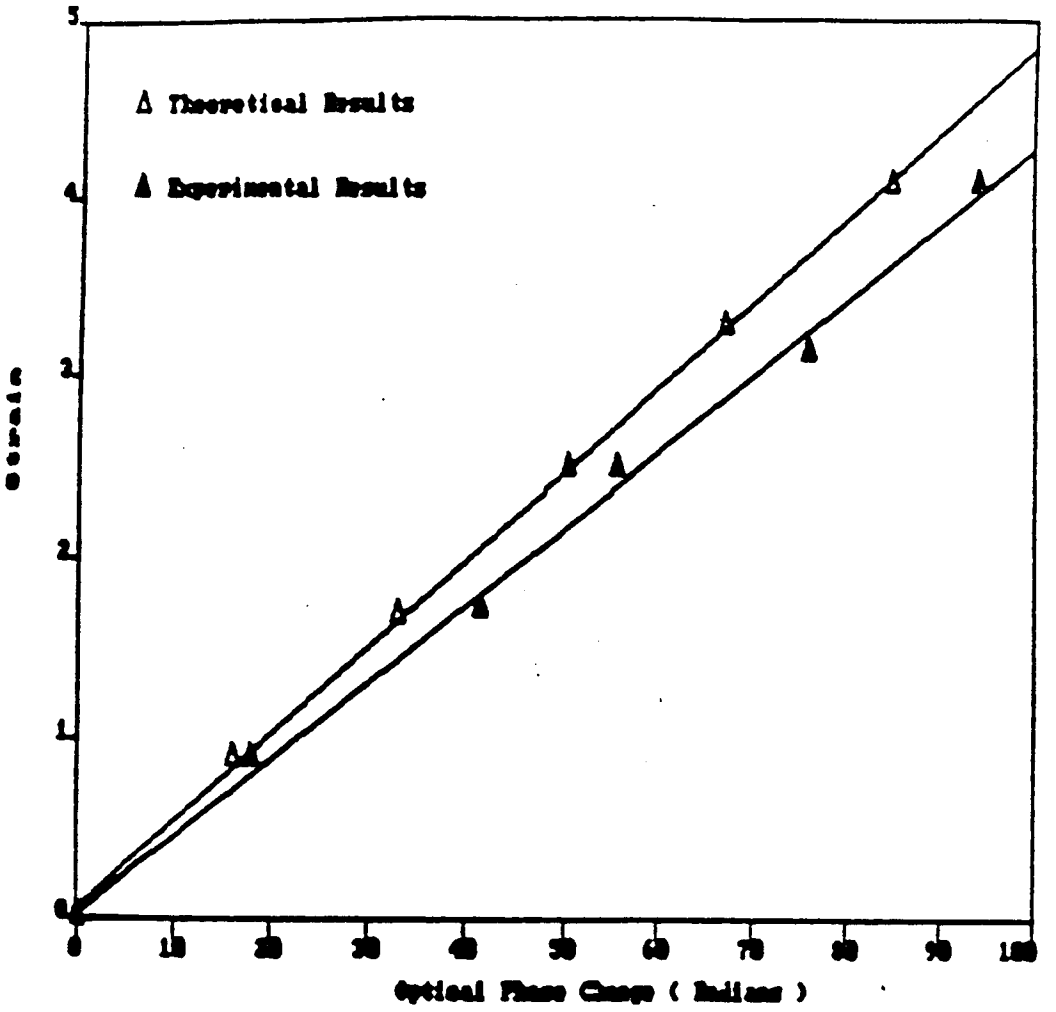


Figure 15. Strain Measurement Data

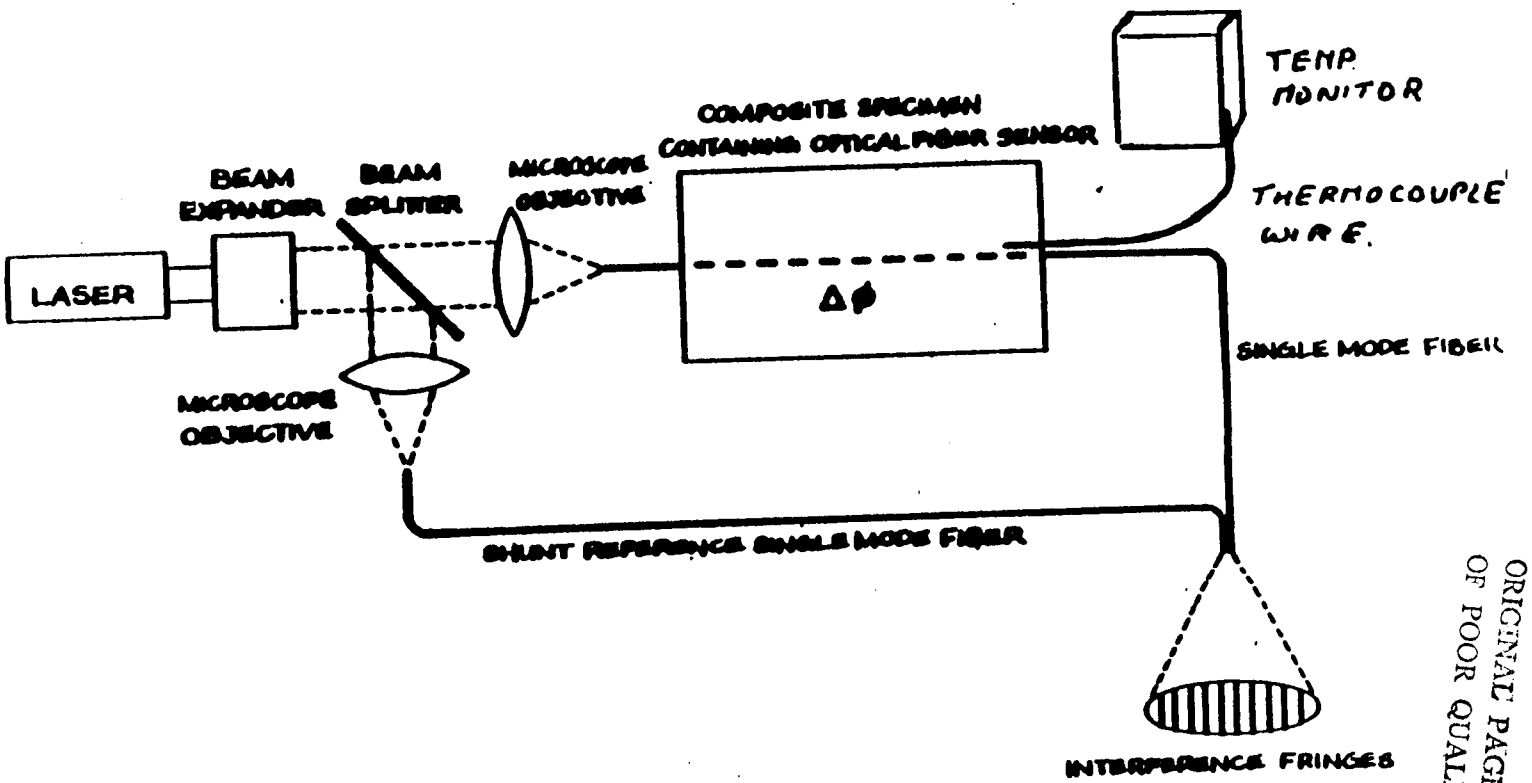


ORIGINAL PAGE IS OF POOR QUALITY

Figure 16. Uncured Graphite-Epoxy Temperature Measurement System.

ORIGINAL PAGE IS
OF POOR QUALITY

| Temperature change (deg C) | Number of fringe displacements |
|---|---|
| 22 | 0 |
| 30 | 64 |
| 40 | 114 |
| 50 | 152 |
| 60 | 210 |
| 70 | 326 |
| 75 | 380 |
| 80 | 434 |
| 85 | 544 |
| 90 | 632 |

Table 1. Unstressed Graphite-Epoxy Temperature Data.

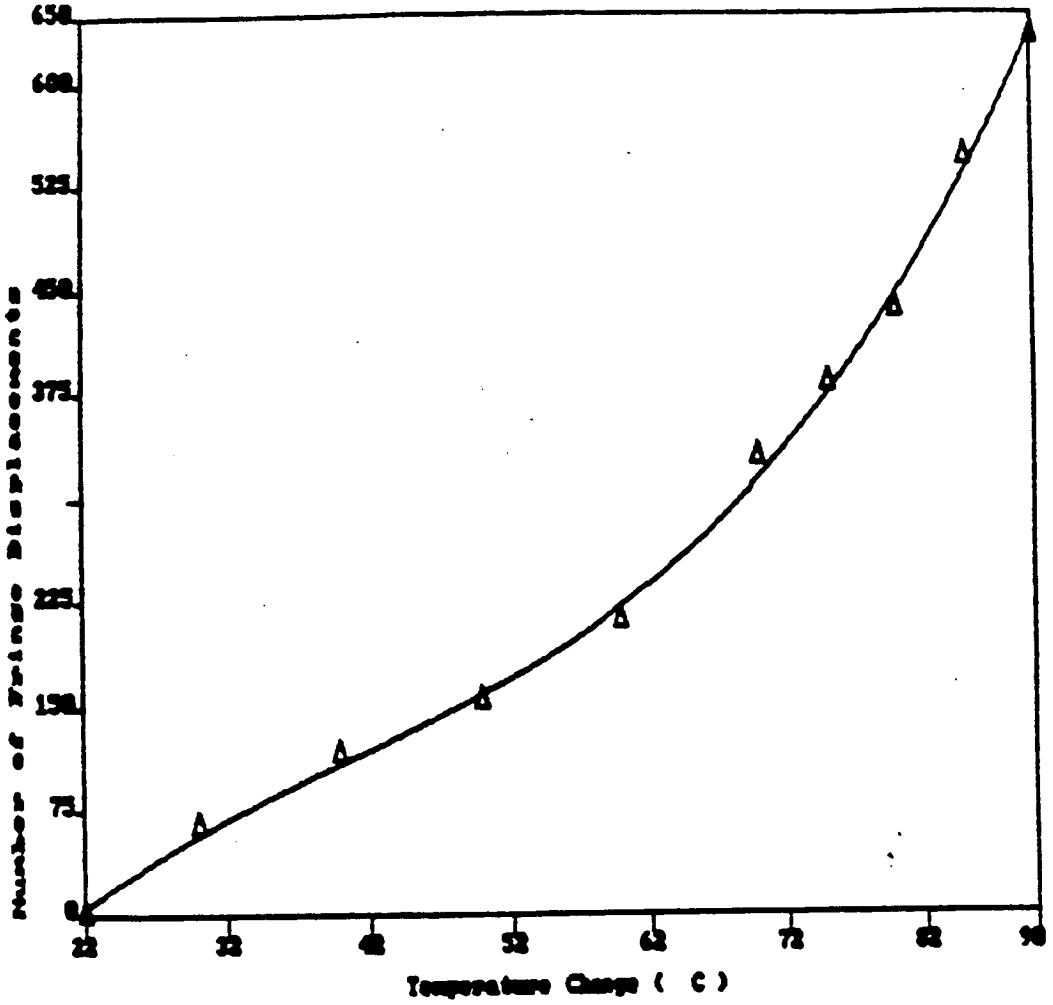


Figure 17. Uncured Graphite-Epoxy Temperature Measurement Data

## 4.2 *Differential Interferometric Measurement of Temperature in $0^0$ and $90^0$ unidirectional laminates.*

The experiments thus far, considered a fiber sensing system similar to that shown in the latter experiments. Here, the sensor fiber is imbedded inside the specimen to be studied and a second reference fiber shunts the specimen. By interferometrically observing the difference between the stationary phase of the signal in the reference fiber and the varying phase of the signal in the sensing fiber, temperature and strain were determined. As in most interferometric systems, the sensitivity of such an arrangement is very high and thus subject to the random effects of environmental conditions which independently perturb the fibers. If, instead, the two fibers are both imbedded in the specimen, the difference in the phase between the fields in the two may be measured and such common mode noise reduced. Two such systems were considered for the measurement of differential temperature in composites.

1. Single-mode fibers placed perpendicular to the direction of the graphite-epoxy fibers, as shown in Figure 18.

2. Single-mode fibers placed parallel to the direction of the graphite-epoxy fibers, as shown in Figure 19.

Experiments consisted of heating and cooling the individual graphite-epoxy composite laminates, the differential temperature change at the location of the fibers was then measured via thermocouples which were imbedded while curing the prepreg composite laminate. The fringe displacement was again recorded on video tape for repeated measurement. The results for the $90^0$ and $0^0$ unidirectional differential temperature measurements were recorded in Tables 4 and 5, respectively. Data was recorded every 60 seconds. Various combination of the results are plotted in Fig-

ORIGINAL PAGE IS
OF POOR QUALITY

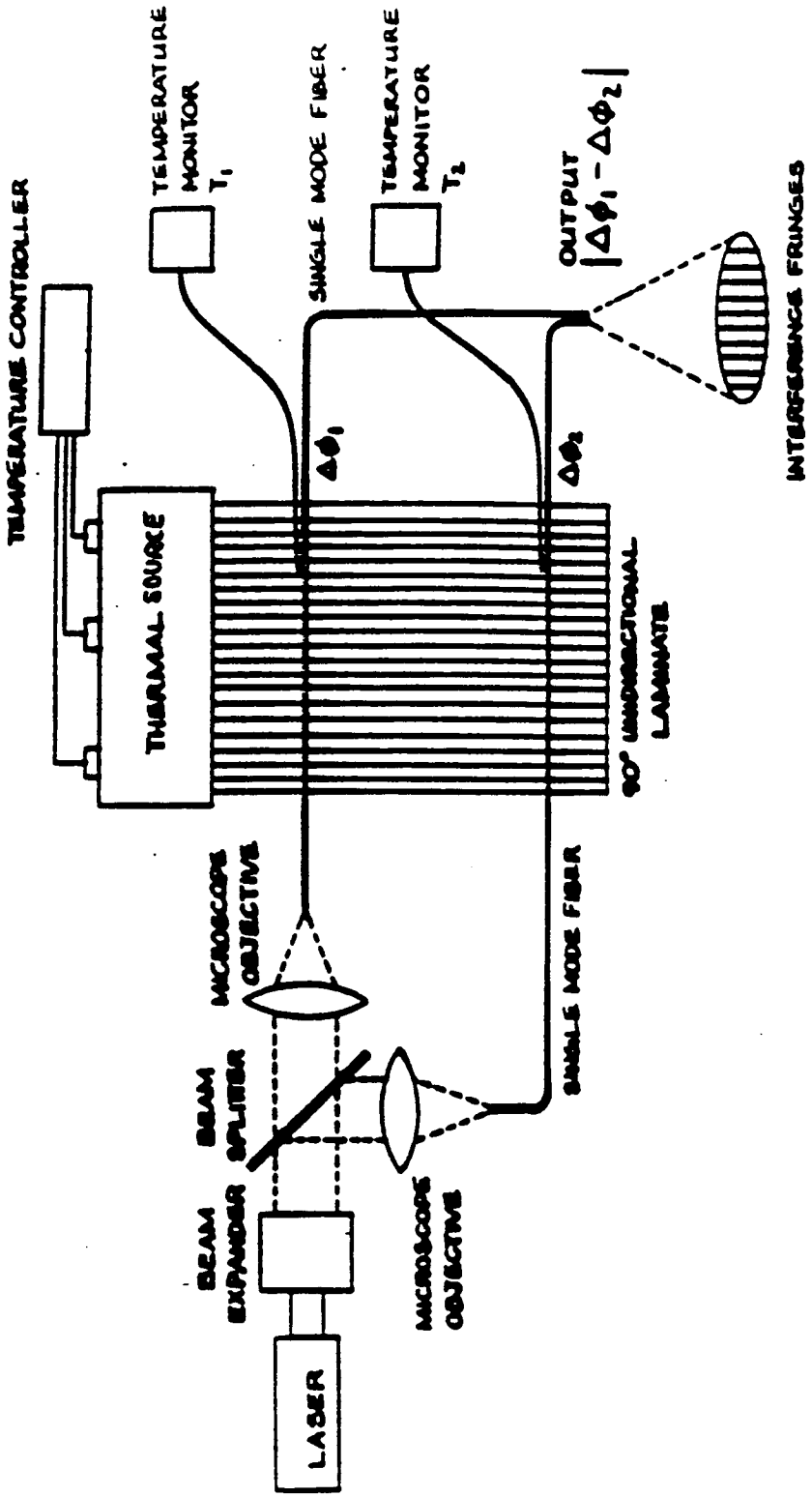


Figure 18. Ninty Degree Gr/Ep. Differential Temperature Sensor.

ORIGINAL PAGE IS
OF POOR QUALITY

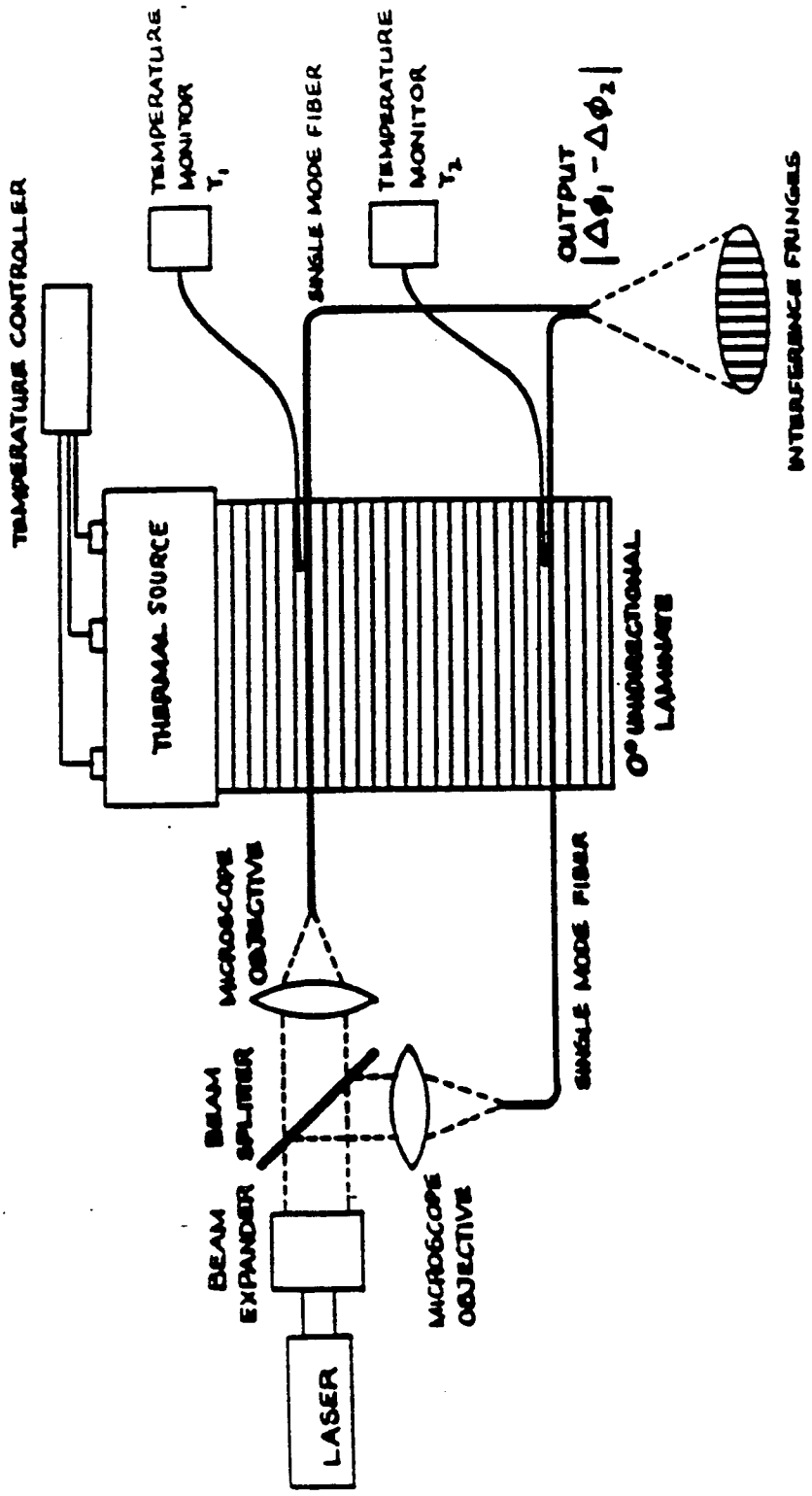


Figure 19. Zero Degree Gr/Ep. Differential Temperature Sensor.

ures 20-23 and Figures 24-27 respectively. Theory predicts that heat is transferrd much faster when it flows along the graphite fiber orientation. This is confirmed by the experimental results as shown in Figures 19-22 compared with Figures 23-26. But note, when the heat flow comes in contact with the optical fiber, the temperature flow rate for the $90^0$ unidirectional specimen apparently reduced from that of the $0^0$ unidirectional specimen. This indicates that the optical fiber is slowing the heat transfer through the $90^0$ unidirectional sample. From Figure 22 and Figure 26 we conclude that the $90^0$ unidirectional graphite-epoxy composite specimen can be used for larger differential temperature measurement than the $0^0$ specimen. The $90^0$ unidirectional system can monitor a maximum differential temperature of $35^0C$ while the $0^0$ unidirectional system can monitor a maximum differential temperature of $27^0C$. Both the systems depart from a linear trend during the cooling cycle.

ORIGINAL PAGE IS
OF POOR QUALITY

| Time in mins. | Temp. T1 in (deg C) | Temp. T2 in (deg C) | Temp. T1-T2 in (deg C) | Number of fringe displacement |
|---|---|---|---|---|
| 1 | 30 | 29 | 1 | 30 |
| 2 | 30 | 29 | 1 | 150 |
| 3 | 32 | 29 | 3 | 322 |
| 4 | 35 | 29 | 6 | 514 |
| 5 | 40 | 30 | 10 | 706 |
| 6 | 46 | 31 | 15 | 896 |
| 7 | 50 | 33 | 17 | 1110 |
| 8 | 55 | 34 | 21 | 1296 |
| 9 | 59 | 36 | 23 | 1434 |
| 10 | 63 | 36 | 27 | 1548 |
| 11 | 66 | 37 | 29 | 1658 |
| 12 | 69 | 37 | 32 | 1828 |
| 13 | 71 | 39 | 32 | 1966 |
| 14 | 75 | 40 | 35 | 1998 |
| 15 | 79 | 41 | 38 | 1996 |
| 16 | 81 | 42 | 39 | 1912 |
| 17 | 82 | 42 | 40 | 1850 |
| 18 | 81 | 41 | 40 | 1794 |
| 19 | 81 | 42 | 39 | 1736 |
| 20 | 80 | 42 | 38 | 1684 |
| 21 | 79 | 42 | 37 | 1632 |
| 22 | 78 | 40 | 38 | 1580 |
| 23 | 77 | 41 | 36 | 1522 |
| 24 | 77 | 42 | 35 | 1478 |
| 25 | 76 | 41 | 35 | 1438 |
| 26 | 75 | 40 | 35 | 1402 |
| 27 | 74 | 39 | 35 | 1374 |
| 28 | 74 | 39 | 35 | 1346 |
| 29 | 73 | 40 | 33 | 1320 |
| 30 | 72 | 40 | 32 | 1296 |
| 31 | 71 | 39 | 32 | 1272 |
| 32 | 71 | 39 | 32 | 1252 |
| 33 | 69 | 39 | 30 | 1228 |
| 34 | 69 | 38 | 31 | 1204 |
| 35 | 69 | 38 | 31 | 1180 |
| 36 | 68 | 39 | 29 | 1160 |
| 37 | 66 | 39 | 27 | 1138 |
| 38 | 66 | 38 | 27 | 1112 |
| 39 | 65 | 37 | 28 | 1098 |
| 40 | 64 | 37 | 27 | 1026 |
| 41 | 64 | 37 | 27 | 988 |
| 42 | 64 | 37 | 27 | 956 |
| 43 | 63 | 36 | 27 | 928 |
| 44 | 63 | 36 | 27 | 906 |
| 45 | 62 | 36 | 26 | 886 |
| 46 | 62 | 36 | 25 | 872 |
| 47 | 61 | 35 | 25 | 866 |
| 48 | 60 | 35 | 25 | 856 |
| 49 | 60 | 35 | 25 | 844 |
| 50 | 59 | 35 | 24 | 832 |
| 51 | 59 | 35 | 24 | 824 |
| 52 | 58 | 36 | 22 | 818 |

Table 1. Ninty Degree Unidirectional Temperature Sensor Data

ORIGINAL PAGE IS
OF POOR QUALITY

| Time in mins. | Temp. T1 in (deg C) | Temp. 12 in (deg C) | Temp. 11-12 in (deg C) | Number of fringe displacement |
|---|---|---|---|---|
| 1 | 30 | 29 | 1 | 18 |
| 2 | 30 | 29 | 1 | 40 |
| 3 | 32 | 29 | 3 | 80 |
| 4 | 35 | 30 | 5 | 120 |
| 6 | 42 | 32 | 10 | 198 |
| 7 | 46 | 34 | 12 | 236 |
| 8 | 50 | 35 | 15 | 268 |
| 9 | 54 | 37 | 17 | 304 |
| 10 | 59 | 39 | 20 | 330 |
| 11 | 62 | 40 | 22 | 362 |
| 12 | 65 | 41 | 24 | 392 |
| 13 | 69 | 42 | 27 | 414 |
| 14 | 72 | 44 | 28 | 414 |
| 15 | 73 | 44 | 29 | 414 |
| 16 | 75 | 45 | 30 | 414 |
| 17 | 75 | 46 | 29 | 414 |
| 18 | 74 | 44 | 30 | 420 |
| 19 | 74 | 44 | 30 | 420 |
| 20 | 74 | 43 | 31 | 420 |
| 21 | 75 | 44 | 31 | 420 |
| 22 | 75 | 44 | 31 | 420 |
| 23 | 74 | 44 | 31 | 408 |
| 24 | 73 | 43 | 30 | 412 |
| 25 | 73 | 43 | 30 | 400 |
| 26 | 72 | 42 | 30 | 384 |
| 27 | 71 | 41 | 30 | 379 |
| 28 | 71 | 40 | 31 | 373 |
| 29 | 70 | 41 | 29 | 369 |
| 30 | 69 | 40 | 29 | 369 |
| 31 | 69 | 41 | 28 | 369 |
| 32 | 69 | 41 | 28 | 369 |
| 33 | 68 | 40 | 28 | 369 |
| 34 | 68 | 40 | 28 | 369 |
| 35 | 68 | 40 | 28 | 369 |
| 36 | 67 | 42 | 25 | 351 |
| 37 | 66 | 40 | 26 | 343 |
| 38 | 65 | 39 | 26 | 337 |
| 39 | 65 | 38 | 27 | 327 |
| 40 | 64 | 39 | 25 | 313 |
| 41 | 64 | 40 | 24 | 305 |
| 42 | 63 | 39 | 24 | 291 |
| 43 | 63 | 39 | 24 | 285 |
| 44 | 62 | 38 | 24 | 273 |
| 45 | 61 | 38 | 23 | 272 |
| 46 | 61 | 38 | 23 | 271 |
| 47 | 61 | 37 | 24 | 270 |
| 48 | 60 | 38 | 22 | 270 |
| 49 | 60 | 38 | 22 | 270 |
| 50 | 60 | 39 | 21 | 270 |
| 51 | 58 | 38 | 20 | 270 |
| 52 | 59 | 38 | 21 | 260 |

Table 1. Zero Degree Unidirectional Temperature Sensor Data

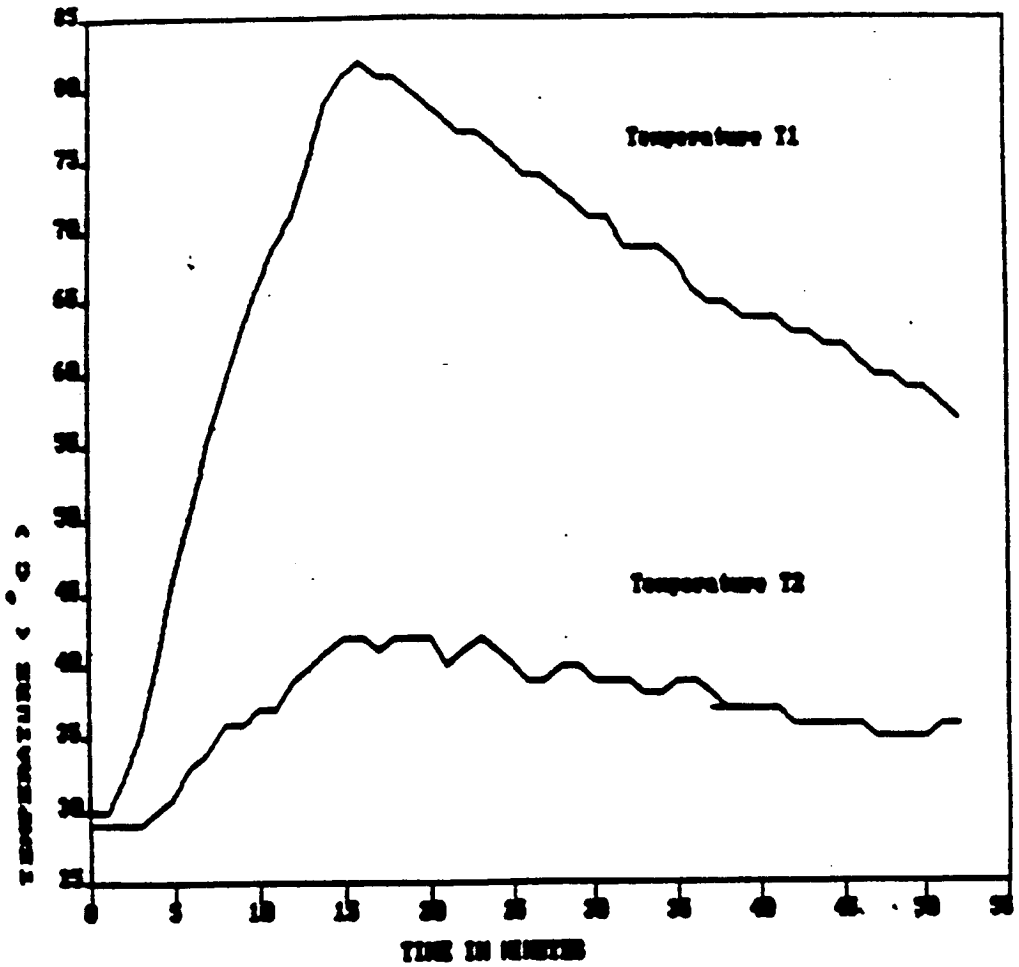


Figure 20. Temp. Versus Time, Ninty Degree Gr/Ep. Sample

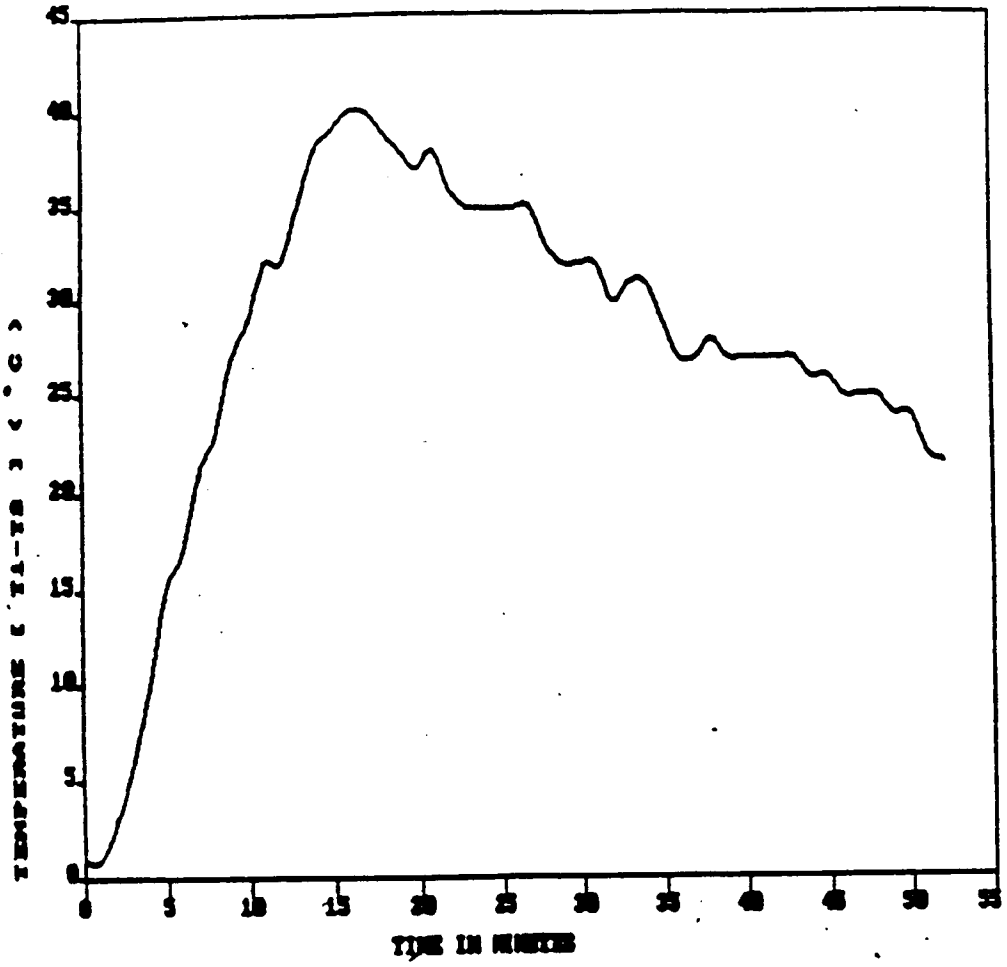


Figure 21. Diff. Temp. Versus Time, Ninty Degree Gr/Ep. Sample

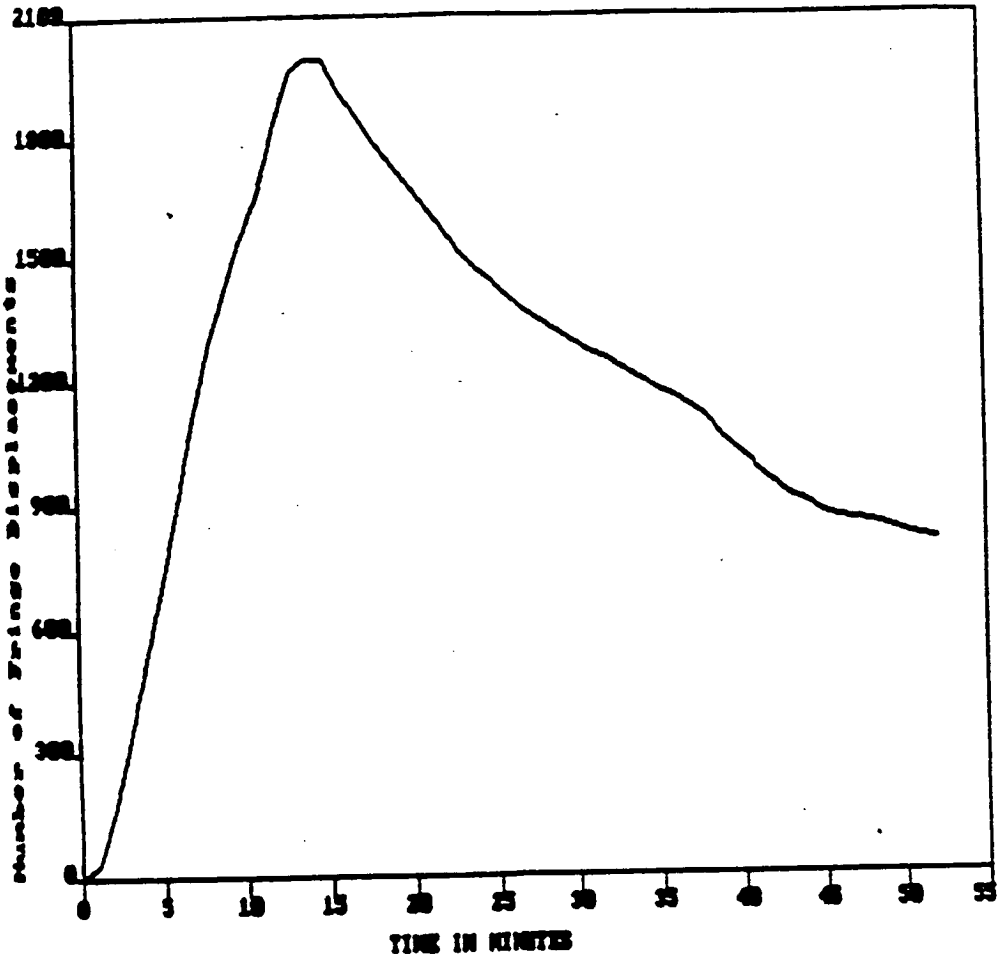


Figure 22. Fringe Displ. Versus Time, Ninty Degree Gr/Ep. Sample

ORIGINAL PAGE IS
OF POOR QUALITY

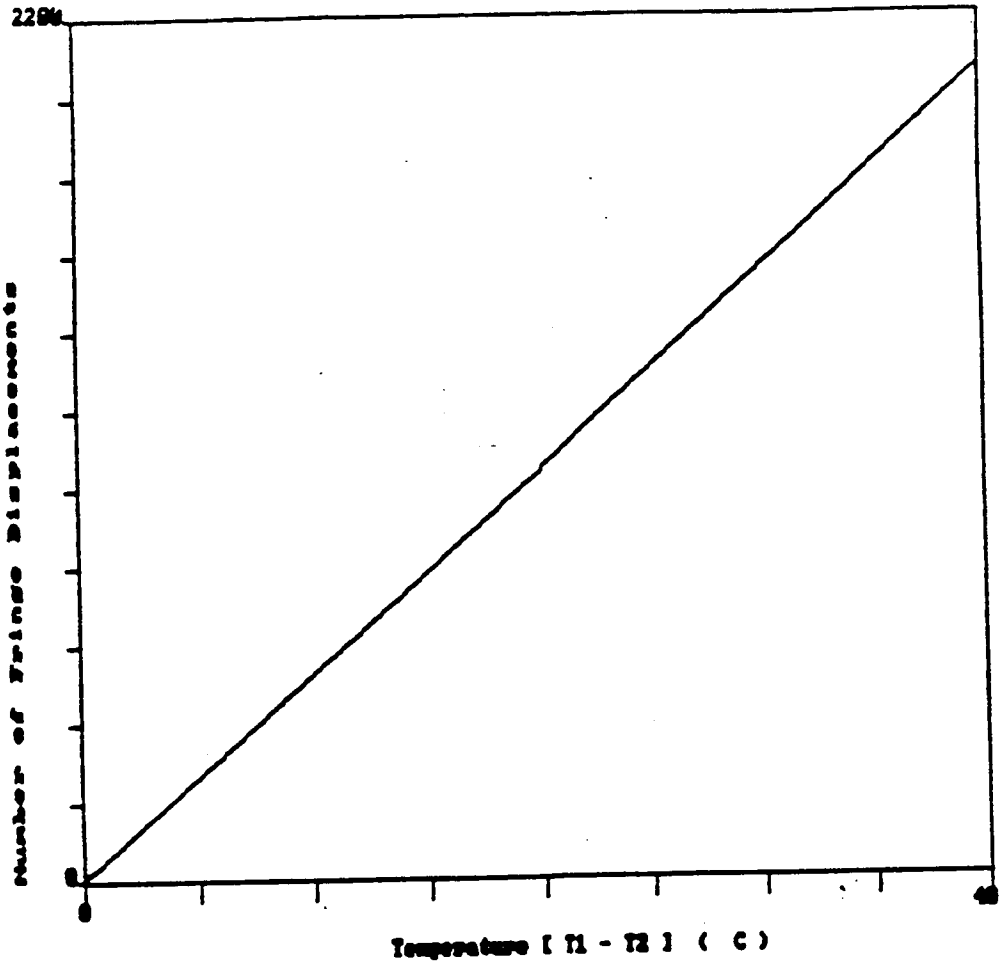


Figure 23. Fring Displ. Versus Diff. Temp., Ninty Degree Gr/Ep. Sample

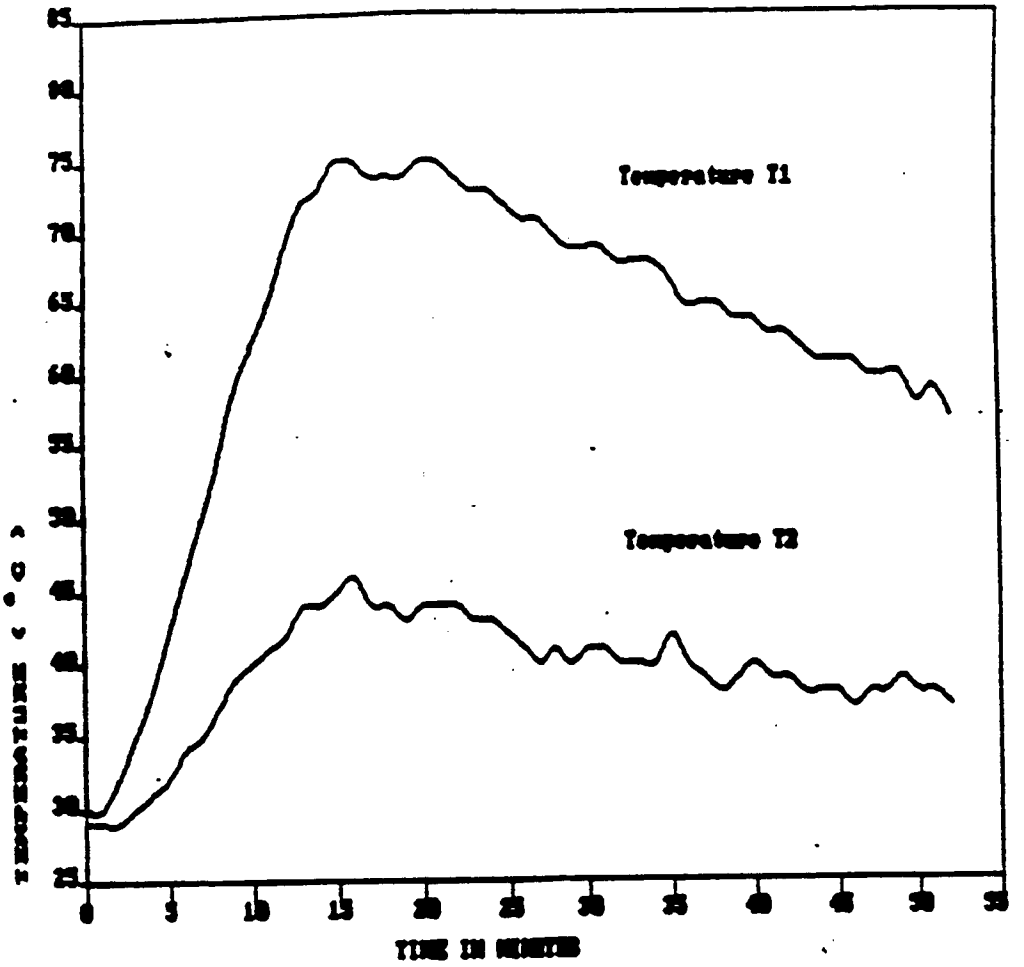


Figure 24. Temp. Versus Time, Zero Degree Gr/Ep. Sample

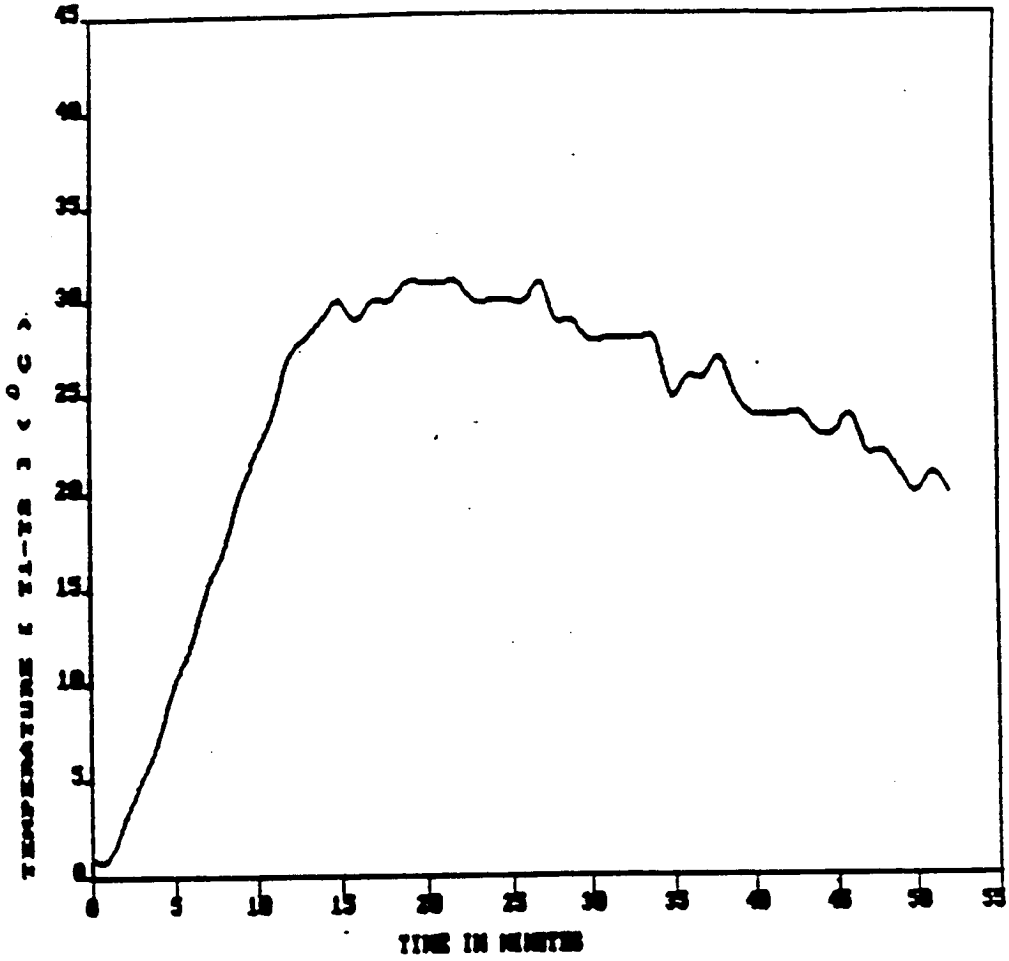


Figure 25. Diff. Temp. Versus Time, Zero Degree Gr/Ep. Sample

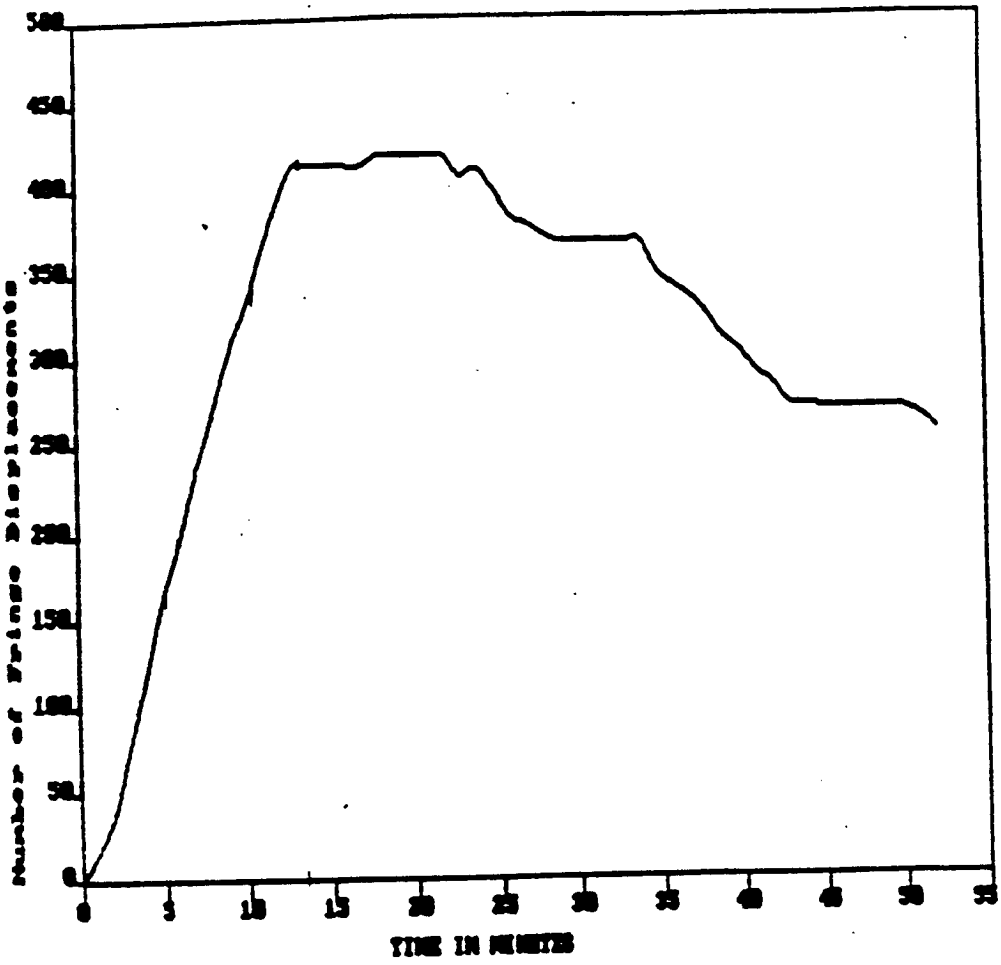


Figure 26. Fringe Displ. Versus Time, Zero Degree Gr/Ep. Sample

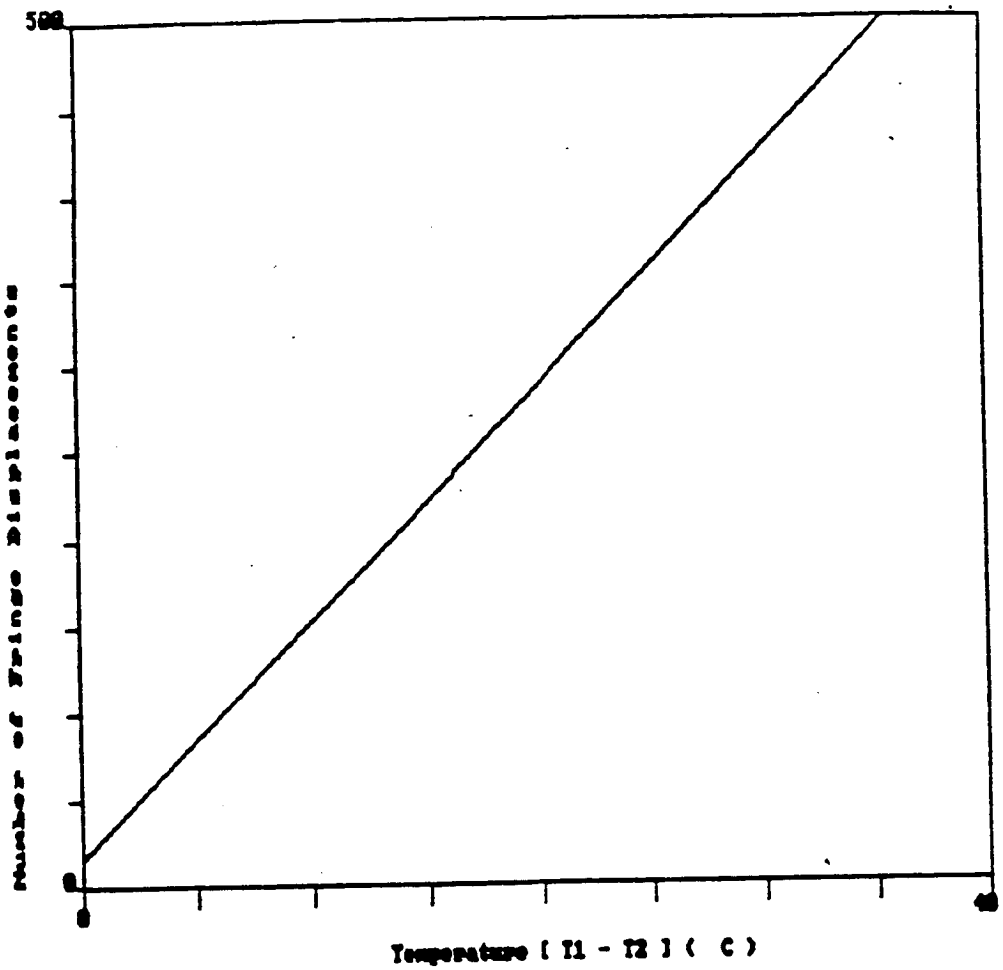


Figure 27. Fringe Displ. Versus Diff. Temp., Zero Degree Gr/Ep. Sample

# 5.0 Conclusions

It has been shown that a single mode interferometer can be used to detect and measure temperature changes. The sensitivity of such an interferometer measurement is high, experimentally 36 fringes/$^0$ C.. Optical phase changes produced by strain have been recorded using imbedded optical fibers in graphite-epoxy composite specimen. Analyses of this data correlates well with those calculated from theory. Optical phase changes produced by temperature have also been recorded using imbedded fibers in graphite-epoxy composite specimens, the results indicate a nonlinear relationship. This data can be utilized for preliminary cure cycle monitoring of graphite-epoxy laminates.

Differential temperature measurements have also been obtained. This was achieved by imbedding both the fibers in the specimen of the different graphite-fiber orientations. The results predict that the 90$^0$ unidirectional specimen can monitor a larger differential temperature range than the 0$^0$ unidirectional composite laminate.

The problems encountered during the research emphasize several points to be considered in any research. Simple physical problems are not always simple mathematical problems. Therefore, detailed theoretical analysis should be outlined prior to experimentation so that the initial experimental conditions may be chosen to obtain a solution that is mathematically and physically meaningful.

The disadvantages of the single-mode Mach-Zehnder system used in this research include the alignment requirements for the interferometer, and the need to observe the motion of optical fringes. Before this system can be implemented in an industrial environment, simple repeatable methods for cutting the fibers to achieve a flat surface perpendicular to the fiber axis must be developed.

The results demonstrate the potential use of imbedded optical fibers as process control sensors in graphite-epoxy composite manufacturing systems, and will serve as the basis for further investigation and refinement of integral/instrumentation systems for aerospace structures in test and service environments.

# 6.0 References


1. R.O. Claus and J.C. Wade, J. Nondestructive Evaluation 4, 23 (1984).
2. G. Meltz and J.R. Dunphy, Proc. SPIE 566, 159 (1985).
3. B.W. Brennan, W.B. Spillman and J.R. Lord, Proc. 3rd Ann. SEM Conf. on Hostile Env. and High Temp. Measurements, (Cincinnatti, OH), March 1986.
4. B. Culshaw, Optical Fiber Sensing and Signal Processing, (Peter rinus, Ltd., 1984).
5. C.D. Butter, and G.B. Hocker, "Fiber Optics Strain Gage," Applied Optics, vol, 17, pp. 2867-286, September, 1978.
6. G.B. Hocker, "Fiber-Optic Sensing of pressure and temperature," Applied Optics, 18 (9), 1445 (1979).
7. R.O.Claus and J.H. Cantrell, "Detection of ultrasonic waves in solids by an optical fiber interferometer," Proc. IEEE Ultrasonics Symp. 2, 719 (1980).
8. C.H. Palmer and R.O. Claus, "Ultrasonic wave measurement by differential interferometry," Applied Optics 16, 1849 (1977).
9. K. Spenner, M.D. Singh, H. Schultz, H.J. Boehnel, "Experimental investigations of fiber optic liquid level sensor and refractometer," First International Conference on Optical Fiber Sensors, 26-28 April 1983.

10. W.H Quick, K.A. Jones and J.E. Coker, "Fiber optic sensing techniques First International Conference on Optical Fiber Sensors, pp. 6, 26-28 April 1983.

11. W.J. Rowe, E.O. Raush, and P.D. Dean, "Embedded optical fiber sensor for composie structure applications," SPIE Conference on Fiber Optics Sensors, Cambridge, Mass., 21-26 Sept. 1986.

12. T.G. Giallorenzi, "Fiber-optic sensing of pressure and tmperature," Optics and Laser Technology 13, 73, (1982).

13. V. Vali and R. Shorthill, "Fiber ring interferometer," Applied Optics , 15, 1099 (1976).

14. J.A. Bucaro, H.D. Dardy, and E.F. Carome, "Fiber-optic detection of sound," Applied Optics 16, 1761 (1977).

15. J.A. Bucaro and E.F. Carome, "Single fiber interferometric acoustic sensor," Applied Optics 17, 330 (1978).

16. J.H. Cole, R.L. Johnson, and P.G. Bhuta, "Fiber-opptic detection of sound," J. Acoust. Soc. Am. 62, 1136 (1977).

17. D. Marcuse, "Light transmission optics," New York : Van Norstrand and Rheinhold Co., 1972.

18. J.C. Wade, P.S. Zerwekh, and R.O. Claus, "Detection of acoustic emission in composites by optical fiber interferometry," Proc. IEEE Ultrasonics Symp. 2, 849 (1981).

19. D.P. Jablonowski, "Simple interferometer for monitoring Rayleigh waves," Applied Optics 17, 2064 (1978).

20. R.O. Claus and J.C. Wade, "Distributed strain measurement in a rectangular plate using an array of optical fibers," J. Nondestructive Evaluation 41, 106 (1983).

21. C.H. Palmer and R.O. Claus, "Ultrasonic wave measurement by differential interferometry," Applied Optics 16, 1849 (1977).

22. W.J. Rowe, "Prospects for intelligent aerospace structures," AIAA-86-1139, presented at AIAA/SOLE 2nd Aerospace Maintenance Conference , San Antonio, Texas, 21-23 May, 1986.

23. J.R. Dunphy, G. Meltz, and R.M. Elkow, "Composite integral response sensing," AFATL-TR-85-37, United Technologies Research Center, Air Force Armament Laboratory, Contract No. F08635-83-C-0287, Sept. 1985.

24. D. Uttam, B. Culshaw, J.D. Ward and D. Carter, " Interferometric optical strain measurement, " J. Phys. E :Sci. Instum., Vol. 18, pp. 290-293, 1985.

25. L.G. Cohen, and J.W. Fleming, "Effects of temperature an transmission in lightguides," Bell Systems Technical Journal, Vol. 58, No. 4, pp. 945-951, April, 1979.

26. M. Martinelli, "The dynamical behavior of single mode optical fiber strain-gage," IEEE Journal of Quantum Electronics Vol. QE-18, No. 4, April 1982.

27. D.A. Jackson, A. Dandridge, and S.K. Sheem, "Measurement of small phase shifts using a single-mode optical fiber interferometer," Optics Letters, Vol. 5, No. 4, April 1980.

28. R.O. Claus, K.D. Bennett, and B.S. Jackson, "Nondestructive evaluation of composite materials by pulsed time domain methods in imbedded optical fibers,"

29. R.L. Crane, "Fiber optics for a damage assessment system for fiber reinforced plastic composite naval structures," ARO/DARPA work-shop on NDE of Polymers and Polymer-Based Composites (Wrightsville Beach, NC), April 1982.

30. R.L. Crane, A.B. Macander, and J. Gagorik, "Fiber optics for a damage assessment system for fiber reinforced plastic composite structures," Review of Progress in Quantitative NDE (San Diego, CA), August 1982.

31. S.C. Lee, K.D. Bennett, and R.O. Claus, "Integrity of composites containing imbedded opptical fiber sensors," submitted to eighth Symposium on C0mposite Materials Testing and Design (Charlston, SC), April 1986.

32. K.D. Bennett and R.O. Claus, "Microbending losses of optical fibers imbedded in composite materials, " paper 104, Opt. Soc. of Am. meeting (Washington, DC), October 1985.

33. J.W. Berhold, "Industrial applications of fiber optic sensors," Proc. of SPIE's 29th Annual Technical Symposium, 18-23 August 1985, San Diego, Ca..

34. S.C. Rashleigh, Optics Letters, 5, 392-394, 1980.

35. S.C. Rashleigh, "Magnetic field sensing with a single-mode fiber," Optics Letters 6, 19-21, 1981.

36. W. Eickhoff, Optics Letters 6, 204-206, 1981.

37. S.C. Rashleigh, and R. Ulrich, Applied Phys. Letts., 34, 768-770, 1979.

38. J.R. Cooper, "Optical fiber thermometry : quest for precision," Photonics Spectra, pp. 71-76, Nov. 1985.

39. E. Snitzer, W.W. Morey, and W.H. Glenn, "Fiber optic rare earth temperature sensors," First International Conference on Optical Fiber Sensors, pp. 79-82, 26-28 April 1983.

40. S. Sheem, T. Giallorenzi, Optics Letters, 4(1), 29 (1979).

41. D. Jackson, R. Priest, A. Dandridge, A. Tretan, Applied Optics, 19 (17), 2926 (1980).

42. A. Dandridge, A. Tretan, Optics Letters, 7 (6), 279 (1982).

43. A. Kersey, M. Cooke, D. Jackson, Electronics Letters, 18, 392 (1982).

44. S. Willson, R. Jones, Optics Letters, 8 (6), 333 (1983).

45. M. Reddy, K.D. Bennett, and R.O. Claus, "Imbedded optical fiber sensor of differential strain in composites," Proc., Review of Progress in Quantitative NDE Conference, San Diego, August, 1986.

46. C. Zweben, "Advanced composites-a revolution for the designer," AIAA-81-0894, presented at AIAA annual meeting, Long Beach, California, May 1981.

47. D.A. Pinnow, "Elastooptical Materials," in Handbook of lasers, R.J. Pressley, Ed. (CRC, Cleveland, Ohio, 1971)

48. "Optical Fused Qurtz and Fused Silica," Amersil Inc. Publication EM-9227 (1975).

49. D.E. Gray, Ed., AIP Handbook (McGraw-Hill, New York, 1972), p. 6-29.

50. R.M. Jones, "Mechanics of composite materials," McGraw-Hill Book Company, 1975.

# 7.0 APPENDIX A

## *7.1 Composite Material Overview*

The use of composites in aerospace structural applications has been growing for more than thirty years. Their high specific strength and specific modulus, excellent corrosion and fatigue resistance, and design flexibility make composites ideally suited to numerous aerospace primary and secondary structures.

Graphite fibers, together with epoxy and other organic matrix resins, allow the designer to tailor structures to meet applied loads more effectively through deliberate fiber orientation, and more efficiently by reducing fiber content where loads are moderate. Thus weight may be decreased in certain structures an average of 20 to 30 % relative to metals, with some reductions running as high as 50 %.

This is vitally important in aerospace applications, where weight reduction is often more important than price. For example, aircraft designers estimate that based on fuel and cargo-capacity considerations, they can afford between $80 and $300 to reduce weight by one pound in a transport plane.

Weight is even more important in military aircraft, where reduced structural weights translates directly into increased armament, armor, ammunication, and fuel.

## 7.2 *Composite Sample Fabrication*

The fabrication of the composite sample consists of several stages.

1. Formation of fiber tows (bundles).

2. Formation of tow sheet.

3. Compression of pre-preg sheet (single ply material).

4. Lay-up of laminae.

5. Compression of pre-preg sheets (plys), i.e. forming an uncured composite laminate (specimen).

6. Curing of the laminate.

The first step, the development of tows, consists of bundling a few thousand graphite filaments (threads) together and adding resin (glue) to fill in the matrix as the tows are compressed. The second step, forming tow sheets, is done on non-stick siliconized sheets. Next, this sheet is compressed together until the squashed tows are barely touching, forming a pre-preg sheet (single ply material). Pre-preg sheets are then stacked in different orientations (see Figure 28) as desired, with the 633 nm optical fiber imbedded inbetween these pre-preg sheets (plys), and the sample is then finally pressed and cured.

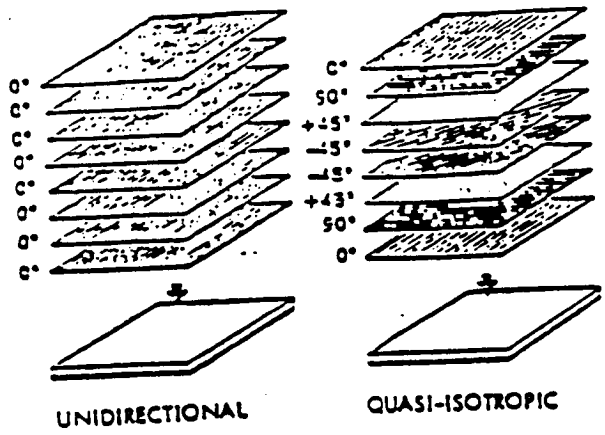


Composite Laminate from Tape Preform

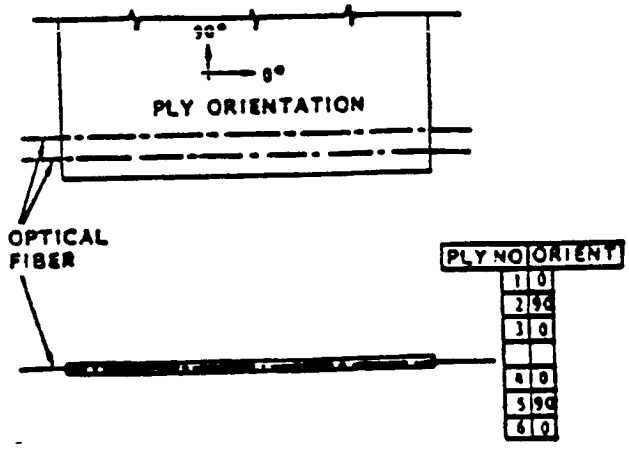


Figure 28. Optical Fiber Placement in Composite Laminate.

Different types of composite specimens (laminates) exist depending on ply orientations; they include uniaxial, cross-ply, symmetric, balanced, angle-ply and quasi-isotropic [50].

## 7.3 Graphite/Epoxy Curing Cycle

The heat and pressure cure cycle.....

1. $275^0F$ .....15 minutes at 0 psi

2. $275^0F$ .....45 minutes at 85 psi

3. $350^0F$ .....120 minutes at 85 psi

4. Cool at 85 psi to $150^0F$ in not less than 120 minutes

5. Remove pressure

## 7.4 Composite Terminology

**Lamina** A single reinforced composite ply or layer ( plural, laminae).

**Laminate** A series of laminae stacked to form a single composite specimen.

**Tow** An untwisted bundle of continuous fibers or filaments. Filaments measure 5-15 um in cross-section. Individual tows lose their identity during the pressurized cure of a laminate.

**Pre-preg** Short for "Pre-impregnated" referring to the fact that single-ply material comes with fiber tows already set in uncured epoxy.

## 7.5 Specimen (Laminate) Types

**Uniaxial** Fibers in all plies are aligned in a single direction, for test specimens, the $0^0$, long, tensile-loaded direction.

**Cross-Ply** One in which ply orientations are perpendicular to each other, usually $0^0$ and $90^0$.

**Symmetric** One whose stacking sequency above its midplane is the mirror image of that below the midplane.

**Balanced** Any laminate which contains a ply with a $-\theta$ orientation ( with respect to the principal axis ) for every ply with a $+\theta$ orientation.

**Angle-Ply** Any balanced laminate containing only ? $\theta$ oriented plies, where $\theta \neq 0^0$ or $90^0$.

**Quasi-Iso.** Quasi-Isotropic: Any symmetric laminate containing equal numbers of identical plies with n orientations ( $n \geq 3$ ) such that the angles between plies are $\frac{360i}{n}$ degrees, where i = 0,1,.....,n-1.

Examples : n = 3 : [ 0, -60, + 60 ]s, where s means symmetric

n = 8 : [ 0, 45, 90, -45 ]2s

# 8.0 APPENDIX B

## *8.1 Preparation of Single-Mode Fibers for use in an Interferometer*

Optical fibers are dielectric waveguides which may be used to transmit electromagnetic energy at optical wavelengths. In optical fibers, the basic optical parameter is the index of refraction which classically is defined as :

$$n = \frac{c}{v} \tag{b.1}$$

where c is the speed of light in vacuum and v its speed within the material. There are three basic types of optical fibers : step-index multimode, graded-index multimode, and step-index single-mode fibers.

The step-index fibers consists of two circularly symmetrical coaxial elements of homogeneous but differing refractive indices where the outer element (cladding) is of lower refractive index than the inner element (core). Within the step-index fiber, optical energy propagation occurs through total

internal reflection at the core-cladding interface. In this type of fiber the mode rays may be thought to propagate along a zig-zag path at greatly varying grazing angles, so that some reach the end of the fiber by longer and others by shorter routes. This leads to a difference in transit times which limits the bandwidth of such fibers. In a single-mode fiber only one mode will propagate so this bandwidth limitation does not occur.

In graded-index fibers there is a variation of refractive index across the fiber core. The purpose of this variation is to equalize the group velocities of the various propagating modes, improving communication bandwidth.

One important parameter for evaluating fiber optics is the numerical aperture (NA), which is a measure of the light power which can be coupled into a fiber. When light enters a fiber from air, NA is computed as :

$$NA = \sqrt{n_1^2 - n_2^2} = \sin\theta, \qquad (b.2)$$

where $n_1$ is the core refractive index, $n_2$ is the cladding refractive index, and $\theta$ is half the planar angle of acceptance.

The propagation of light in an optical fiber is governed by Maxwell's electromagnetic field equations, which may be used to predict the number of modes that will propagate through a given fiber. The parameter which determines how many modes a fiber can support is the normalized frequency V, given by

$$V = \left(\frac{2\pi a}{\lambda}\right)\sqrt{n_1^2 - n_2^2}, \qquad (b.3)$$

where $\lambda$ is the wavelength of the light being transmitted and a is the radius of the core of the fiber.

It can be shown that the number of propagating modes is approximately equal to M where,

$$M = \frac{V^2}{2} \tag{b.4}$$

This is valid for step index fibers only. Thus, it can be seen from Figure 29 and above equations that single-mode propagation in a step-index fiber takes place when the value of V is below 2.405. Below this value all other modes are forced into cutoff, i.e. only the $HE_{11}$ (fundamental) mode propagates in the fiber.

In any optical interferometer experiment, the most critical part of experimental preparation is the preparation of the optical fibers. Incident light will not propagate down the fiber if the end faces are not perpendicular to the fiber axis and free of debris such as dust or dirt. There are several techniques used to strip and cleave the fibers, but the conventional razor blade and the diamond scribe was used in this work. Stripping and cleaving of the single-mode fiber was done in stages as follows :

1. Tape approximately 2 inches of the fiber to a hard surface.

2. Hold the fiber near the taped end so that it is under tension.

3. Remove the jacket using a sharp razor blade.

4. Nick the fiber with a diamond scribe while maintaining tension on the fiber.

5. Holding the fiber at the end, gently pull.

6. Examine the end under a microscope to be sure that no splinters are left on the sides and that the cut is perpendicular to the fiber axis

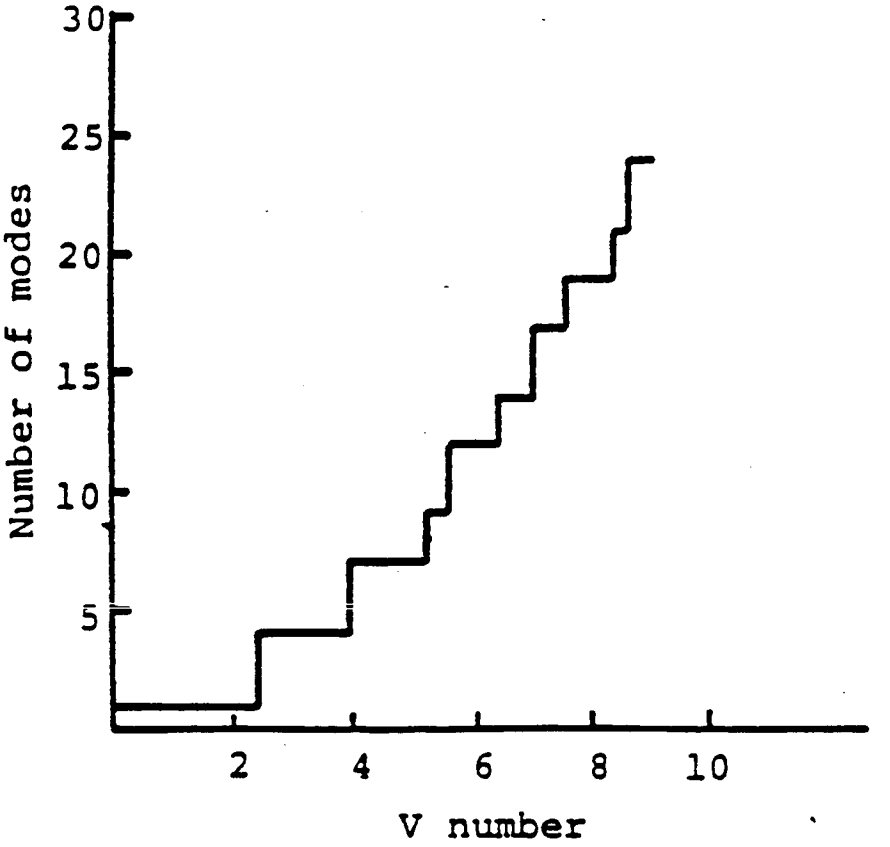


Figure 29. Fiber V Parameter Versus Number of Modes.

# 9.0 VITA

Mahesh Reddy was born on July 17, 1962 in Bangalore, India. He received his secondary education at Faraday High School in London, England. He completed his Bachelor of Science Degree in Electronics and Communications Engineering at Polytechnic of North London, England in June 1984. He entered Virginia Polytechnic Institute and State University in January 1985 and received his Master's Degree in Electrical Engineering in December 1986. He was a cooperative education student with General Electric Company in Charlottesville, Virginia. He held positions as a graduate research and teaching assistant and worked as a Fiber Optic Consultant for Polyscientific, Litton Systems Inc., Blacksburg, Virginia. He is a member of the Institute of Electrical and Electronic Engineers and Society of Photo Optical Engineers. He has coauthored one technical paper.

Mr. Reddy is an avid sportsman, enjoying squash, tennis, and soccer.

# IMBEDDED OPTICAL FIBER SENSOR OF DIFFERENTIAL STRAIN AND TEMPERATURE IN GRAPHITE/EPOXY COMPOSITES

by

Mahesh Reddy

Dr. Richard O. Claus, Chairman

Electrical Engineering

(ABSTRACT)

A novel optical fiber sensor for the measurement of strain and temperature in graphite-epoxy composite materials using differential interferometry is described. The sensor ues two single-mode optical fiber waveguides imbedded within the composite during prepreg ply lay-up. Strain and temperature changes are obtained as a motion of an optical interference pattern. Values are calculated for the strain and temperature dependence of the fringe motion. The results of measurement which attempt to duplicate modelled loading conditions are reported and compared with analytical results. Analytical and experimental extensions of the technique to the measurement of the differential temperature in graphite-epoxy composite specimens during cure cycle processing are also considered.

# Appendix G. Damage Monitor System Using Imbedded Fibers

OF POOR QUALITY

# FIBER OPTIC COMPOSITE IMPACT MONITOR

R. Kuhlman, B. Duncan, and R.O. Claus

Department of Electrical Engineering
Virginia Polytechnic Institute and State
University Blacksburg, VA 24061

## ABSTRACT

An optical fiber sensing system is used to monitor impact and resulting damage in graphite-epoxy composite materials. The monitor system consists of an array of multimode optical fiber waveguides imbedded within the composite. The internal damage location and severity is determined by either observing the changes in optical fiber output power after the material is subjected to mechanical impact loads, or performing fiber modal domain measurements during impact.

## INTRODUCTION

Advanced composite materials have become attractive alternative materials for critical high strength aerospace structural applications due to their high strength-to-weight ratio. Perhaps the largest drawback to the straightforward application of such materials is lack of knowledge and experience concerning how such materials behave upon dynamic mechanical loading conditions in a wide range of environmental conditions, and how the materials fail. One particulary troublesome property of graphite epoxy composites is significant decrease in strength which can be caused by mechanical impact loading. The most popoular model of composite mechanics states that damage associated with the impact event results in localized material weakness that may lead to failure. In the future, replacing rather than repairing large composite parts will be more economical; therefore, a damage monitor which provides damage location and severity could prove very helpful in determining the usefulness of the damaged composite. However, few if any, methods exist to analyze impact-damaged composite materials in which the damage level is not catostrophic.

This paper describes a simple inexpensive optical fiber method which yields information concerning impact damage location and severity. The damage assessment system consists of an array of multimode optical fiber waveguides which are imbedded between successive layers of the composite during prepeg ply lay-up. Light is coupled into all of the fibers using a novel one-to-nineteen fused biconical tapered coupler. The output fiber ends are arranged in a two dimensional array of nineteen rows and nineteen columns. By observing either the changes in individual fiber output powers immediately after the material is subjected to mechanical impact loads or dynamically measuring differential modal modulation spectral reflections using modal domain tests, the location of the impact and its approximate amplitude may be determined.

The imbedding and curing processes used in this experiment are explained. The mechanical boundary conditions between the optical fibers and the composite matrix material are considered. The experimental procedure is described and the results using output power readings and modal domain testing are presented.

## OPTICAL FIBERS IMBEDDED IN COMPOSITE MATERIALS

The objective of this experiment is to imbed optical fibers between the layers of a graphite epoxy cross-ply laminate to measure the damage location and severity produced by mechanical loading. First, the properties of the composite and optical fibers need consideration.

Our composite contains six adjacent 12.5 cm X 12.5 cm prepeg layers, each containing parallel graphite fiber rows across the full length of the layer. Between each graphite fiber and each layer lies epoxy resin that, when cured, bonds everything together. Each layer is oriented such that its graphite fibers are perpendicular to the graphite fibers in the adjacent layers to provide greater strength to the composite.

ORIGINAL PAGE IS
OF POOR QUALITY

Composite materials are intrinsically complicated inhomogeneous and anisotropic media. Imbedding optical fibers inside composites may further complicate the structure by introducing local perturbations in the region near the fiber. Ideally the epoxy resin matrix will cure completely around the fiber as shown in Figure 1a. Examination of sections of composites containing fibers; however, indicates a structure more like that of Figure 1b in which a void region is shown directly adjacent to the fiber. Such a void precludes the continuity of both particle displacement and stress at the local fiber-composite interface, thus reducing the effectiveness of the sensor at determining impact event characteristics.

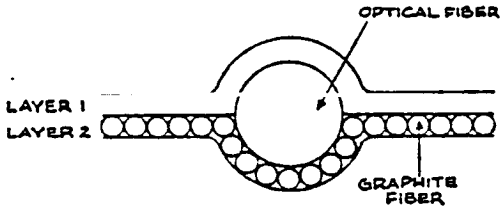


FIGURE 1a.

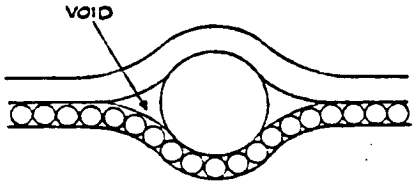


FIGURE 1b.

In our experiment two different layers of optical fibers were imbedded between the layers of graphite epoxy prepeg prior to curing. The first layer consists of nineteen multimode fibers oriented in the zero degree direction between the second and third laminae. The second fiber layer consists of nineteen multimode fibers laid in the 90 degree direction between the fourth and fifth laminae. Each set of fibers is coupled using a fused bioconical tapered coupler (See Figure 2).

FIGURE 2.

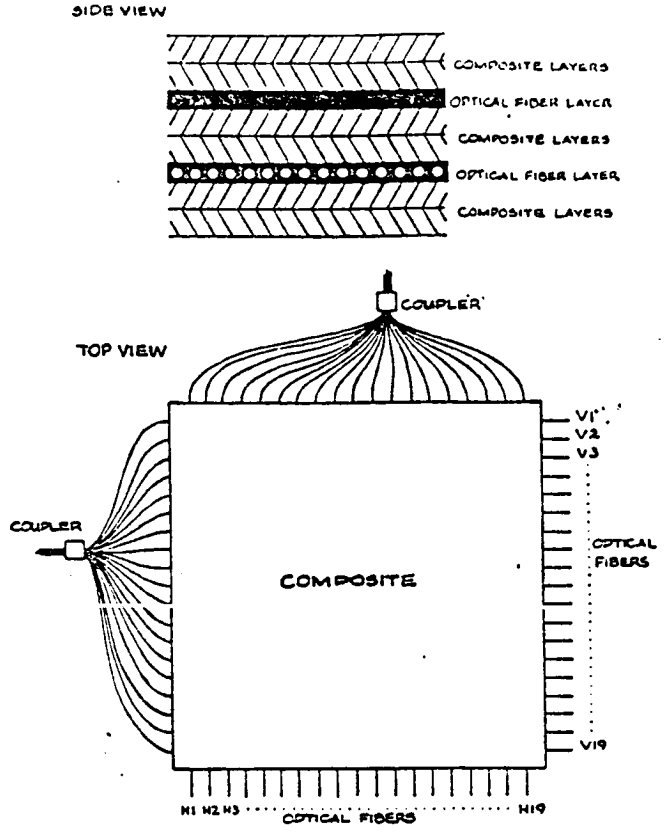


The above prepeg configuration was cured for five hours in a heated platen press. In preliminary experiments we found that the optical fibers at the points of entering the composite became brittle and tended to break. To prevent such fiber breakage, we extended the curing cloth over the edge of the composite to trap the melted epoxy thus protecting the fibers from breakage.

## EXPERIMENT

The damage monitor system (imbedded fiber composite) was mounted on a 1.9 cm thick aluminum block (See Figure 3). Laser light was coupled into each fiber in the imbedded array and output power was measured using an optical detector and power meter. The composite was then impacted with a steel ball as shown, and the output power was measured again after impact.

ORIGINAL PAGE IS
OF POOR QUALITY

Ideally the monitoring system would produce a three-dimensional view of impact. Using the optical fiber array as a grid pattern, we could see, as in Figure 4, that fibers X and Y were perturbed most, with the fibers farther away suffering less power loss. A two-dimensional system could also be used.

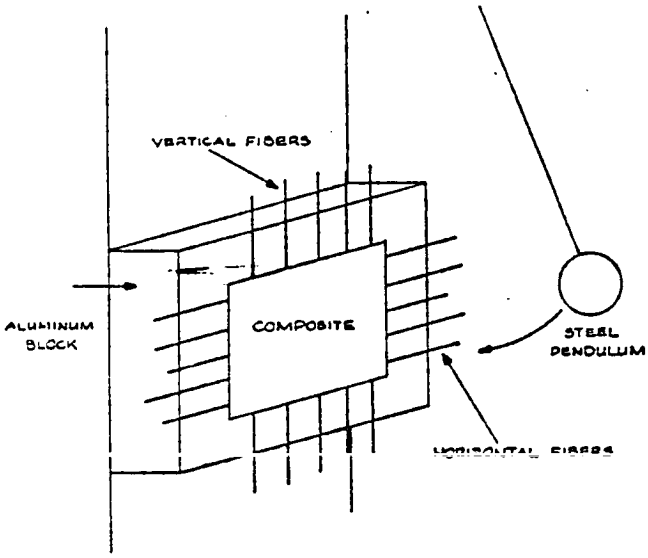


FIGURE 3.

The composite specimen was impacted with forces ranging from 1.2 to 7.8 ft lbs and only negligible power loss was found. This could be due to the inaccuracies found in our power meter or optical detector. Puncturing the composite; however, broke the optical fibers which produced total power loss.

FIGURE 4.

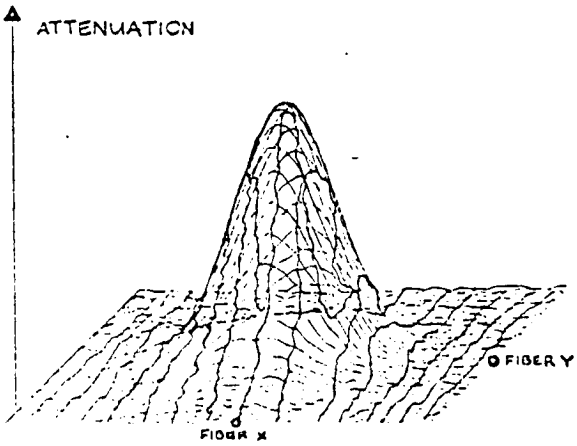


Modal domain tests also were performed on the composite. The composite was impacted at the same spot many times; each time a different fiber's signal was monitored on the oscilloscope. Output waveforms were produced by all fibers measured, indicating fiber continuity. The fibers closer to the impact spot displayed higher attenuation than those located farther away. The grid of these attenuation results is shown in Figure 5 and the actual waveforms of two of the fibers are shown in Figure 6. Due to limited equipment, the modal domain modulation signal from only one fiber could be measured at a time; therefore, only two-dimensional grids can be displayed here.

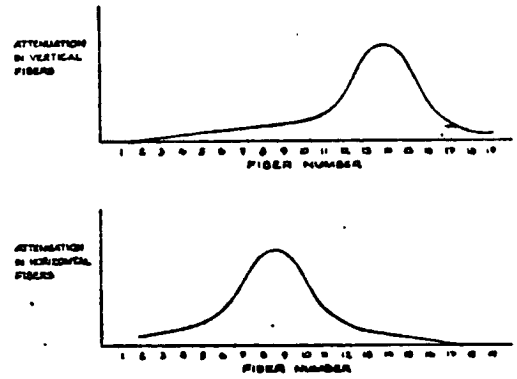


FIGURE 5

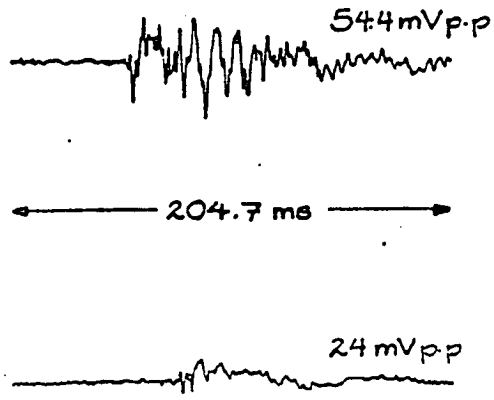


FIGURE 6

ORIGINAL PAGE IS
OF POOR QUALITY

## RESULTS AND OBSERVATIONS

We have observed impact events using an array of optical fiber waveguides imbedded within a graphite-epoxy cross-ply laminate. Determination of impact location and severity was tried by measuring residual fiber attenuation, but was unsuccessful in our experiment. Real time impact event signatures have been obtained by modal fiber measurements.

If each fiber in the array were connected to a detector, real time damage could be monitored by noting the amount of attenuation in each fiber during and after impact. Ideally, the detectors could be connected to a computer which could present a three-dimensional image of the area impacted. This image would show both grid location and amount of damage.

Several extensions of this work are suggested.

## ACKNOWLEDGEMENTS

The authors thank K. Murphy for designing and making the fused biconical tapered couplers and the Fiber Optics Research group at Virginia Tech for their assistance.

## REFERENCES

1. R.O. Claus, B.S. Jackson, K.D.Bennet, "Nondestructive Testing of Composite Materials by OTDR in Imbedded Optical Fibers", PROC SPIE, vol. 263, 1984.

2. Designers Guide to Fiber Optics, Amp Incorporated, Harrisburg, PA, 17105, 1982.

# Appendix H. Acoustic Fiber Waveguide Devices

ORIGINAL PAGE IS
OF POOR QUALITY

# ACOUSTIC FIBER WAVEGUIDE DEVICES

A. L. Matthews, K. Murphy, A. Safaai-Jazi and R. O. Claus

Fiber and Electro-Optics Research Center
Department of Electrical Engineering
Virginia Tech
Blacksburg, VA 24061

## ABSTRACT

Acoustic fiber waveguides are described, and methods of determining appropriate materials for core and cladding are discussed. Propagation characteristics of guided modes, especially weakly guided modes, is reviewed. Laboratory preform fabrication and draw methods are discussed in detail. Possible uses of the fabricated fiber will be mentioned, as well as potential applications of acoustic fiber in general.

## INTRODUCTION

Acoustic fiber waveguides were first described in 1977 by Thurston, Boyd, and Coldren [1]. When first invented, they were intended for long-delay serial information storage purposes. (Due to the performance of semiconductor devices, however, this is no longer of interest.) Since then, Jen, Safaai-Jazi, and Farnell have done extensive theoretical work on fiber acoustics. Harrold and Sanjana have done experimental work on thin acoustic waveguides, procedures which may be able to be duplicated with acoustic fibers. Recent applications of acoustic fibers include sensing and nondestructive testing.

Acoustic waveguides (of 1.5 mm. diameter polyester-fiberglass rods) have been imbedded in composites to sense stress, strain, and external impact, to locate sites of impact, and to monitor cure processes [2]. These rods are sensitive to viscosity changes in the composite in which it is imbedded. They can also be used in the "listening mode" as an "internal microphone." In this manner, acoustic emissions from both external and internal events can be detected.

## BACKGROUND

Acoustic fiber waveguides are similar to optical fiber waveguides in that they consist of a long cylindrical core of one material, coated by a long cylindrical cladding of another material. These two materials differ only slightly. The outer diameter of the acoustic fiber, however, is much larger than that of the optical fiber. This is, in part, so that it is possible to couple acoustic energy into the fiber from a relatively large transducer.

The two waveguides differ in that optical fibers transmit electromagnetic waves and acoustic fibers transmit mechanical waves. For optical fibers, we need be concerned with the index of refraction, n. In acoustics, we are concerned with the shear velocity, $V_S$, the longitudinal velocity, $V_L$, and the density $\rho$; or the Lamé constants $\lambda$ and $\mu$, and the density $\rho$ [3]. V is the phase velocity of a guided mode (one which stays in the core), where

$$V_S = [(\lambda + 2\mu)/\rho]^{1/2}$$

$$V_L = (\mu/\rho)^{1/2}, \text{ and}$$

$$V = \omega/\beta. \qquad [4]$$

"Weakly guiding" acoustic fibers have small differences between $V_{Li}$, $V_{Si}$, and $\rho_i$, where i = 1,2 refers to the core and cladding [5]. The conditions for weak guidance are as follows:

$$\epsilon_S = |V_{S_2} - V_{S_1}|/V_{S_1} << 1$$

$$\epsilon_L = |V_{L_2} - V_{L_1}|/V_{L_1} << 1, \text{ and}$$

$$\epsilon_\rho = |\rho_2 - \rho_1|/\rho_1 << 1. \qquad [3]$$

When these conditions hold, the fibers require a larger core diameter for single mode operation, a thicker cladding, but have more bend loss and less dispersion [6].

ORIGINAL PAGE IS
OF POOR QUALITY

The exact analysis of acoustic fibers is complex. The conditions of weak guidance allow for an approximate analysis of waveguide properties. Therefore, the weak guidance conditions will be assumed here. Also assumed is that the cladding has an infinite thickness and that the acoustic fields have the form exp $j(\omega t - \beta z)$, where $\omega$ is the radian frequency and $\beta$ is the axial propagation constant [7].

In weakly guiding acoustic fibers, there are two sets of modes. In shear-type modes, the axial component of the particle displacement vector has a negligible contribution to the power flow. These modes may be radial, flexural, or torsional. They propagate with shear velocities less than $V_{S_2}$, and are basically independent of longitudinal velocities. In longitudinal-type modes, the power is carried by the axial component of the particle displacement vector. These modes are leaky ($\beta$ is complex, and they lose power as they propagate) and travel with phase velocities such that $V_{L_1} < V < V_{L_2}$. They attenuate as they propagate unless $V_{S_1} = V_{S_2}$ and $\rho_1 = \rho_2$ [5].

The cutoff frequency of a guided mode in an acoustic fiber is the frequency below which the mode becomes detached from the core [7].

In acoustic fiber with infinitely thick cladding, cutoff occurs when $V = V_{S_2}$. Cutoff in fiber with finite cladding thickness is called core-mode cutoff, below which most of the power is in the cladding. This is found from the general form of the dispersion equation, $f(\omega,\beta) = 0$, with $V \rightarrow V_{S_2}$ [8].

The first flexural mode, the $F_{11}$ mode, has a zero cutoff frequency. This is the first mode that can be excited, and is the dominant one [4]. This is the prevalent mode when the fiber is in single mode operation.

Group velocities of modes are obtained from the definition

$$V_g = \frac{\partial \omega}{\partial \beta}, \qquad [4]$$

with the dispersion equation again generalized to $f(\omega,\beta) = 0$.

## WAVEGUIDE FABRICATION AND MEASUREMENTS

Before attempting to fabricate a true acoustic fiber, we practiced "pulling fiber" from glass rods. The main idea is to heat the rod until it is soft enough to pull, using a pair of pliars, into a fiber. Originally we had problems: (1) The movement of the flame of the oxy-propane torch we used was unpredictable. The torch needed to be held steady until the rod was soft enough to pull. Once the rod became soft, the torch had to be moved upward very slowly so that the rod would not melt through and so that the rest of the rod would stay at a constant softness. (2) The draw rate was not constant. This was because the draw speed depended upon the movement of the flame, which was previously stated as unpredictable. If the torch was not moved upward at a constant rate, the rod could not be pulled down at a constant rate since then the glass would not be continuously soft enough to pull.

To overcome these problems, we used the apparatus shown in Figure 1. We added a metal bar, in which to place the glass rod, across the bottom of a micrometer and added a clamp to the turning mechanism of the micrometer. By manually spinning the clamp at a constant rate, the slab of the micrometer (and thus the glass rod) is lowered at a constant rate. Since the rod is now being lowered, there is no need to move the flame upward. Therefore, we mounted the torch as shown. As a result, the draw rate could be controlled to a certain degree.

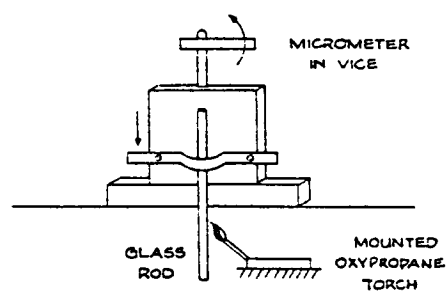


FIGURE 1.

We were successful at pulling several 2.2 m. sections of fiber with this method. Note that the diameter of the fiber was not constant throughout its entire length, but there were sections where several feet were of uniform diameter.

Using the criteria previously described, Corning glass 7070 ($V_S$ = 3128 m/s, $V_L$ = 5221 m/s) was chosen for the core, and Corning glass 7740 ($V_S$ = 3420 m/s, $V_L$ = 5585 m/s) was chosen for the cladding of our fiber.

We had to make a preform out of these glasses before we could pull any fiber. To do this, we needed to collapse a 7740 tube onto a 7070 rod. The apparatus we used is shown in Figure 2.

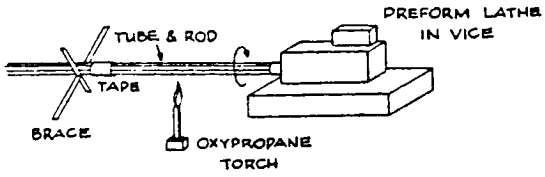


FIGURE 2.

We placed the rod inside the tube and placed this assembly into the preform lathe. As the lathe (in this case, a drill) spun, we moved the torch up and down the length of the rod and tube. When they were warm, we moved the torch very slowly down the length of the rod and tube, trying to collapse the tube onto the rod. This attempt was not totally successful. There was an air pocket noticeable in the end product.

The next step was to try to transmit a signal through the fiber. Light propagated through the fiber very nicely, but sound did not. In fact, there was minimal transmission. This, we believe, is due to the following problems:

(1) The transducer we used to excite the fiber was very large compared to the size (cross-sectional area) of the fiber. Thus, it is likely that not much of the acoustic energy from the transmitting transducer was coupled into the fiber. Also, it seems that even a smaller amount of this energy (due to attenuation and loss as it travels the length of the fiber) will be detected by the receiving transducer. The receiving transducer also has a larger area than the fiber. If any signal did propagate through the fiber, it would probably be so small that this transducer could not detect it anyway.

(2) The air pocket and inconsistensies in the diameter of the fiber are sources of loss or attenuation.

Since we were unable to make a "good" preform, we took some of the 7070 rod and 7740 tube to ITT Electro-Optical Products Division in Roanoke, VA. People there used an acetylene torch to collapse the tube onto the rod. We now have a "good" preform about 20 cm. long. The only foreseeable problem with this preform is that the thickness of the core is much greater than that of the cladding; thus, any fiber we pull from this preform will have the same characteristics.

We were able to construct an acoustic coupler from some of the fiber we drew. We hope to be able to input acoustic energy into one fiber and have an output in two fibers. See Figure 3.

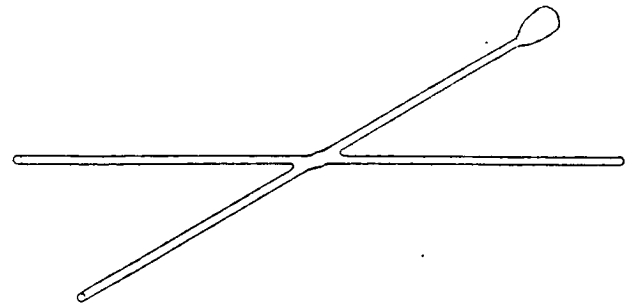

FIGURE 3.

## CONCLUSION

We were able to fabricate some acoustic fiber in the laboratory. Minimal transmission of acoustic signals was observed, but we believe this was due to transduction problems. We constructed a coupler with a fused biconical taper, similar to the manner in which optical fiber couplers are made. Hopefully, we will be able to use this coupler to divide a signal propagating through the fiber. Scientists at ITT made us a preform, which will allow us to pull fiber with uniform dimensions.

Once the fabrication and transmission processes are perfected, we hope to be able to construct acoustic sensors. For example, and interferometer-type sensor (in which we would use the coupler) to detect temperature and strain and stress. Or perhaps imbed the fiber in a composite and sense changes in material properties. Since acoustic waves are sensitive to changes in the viscosity of the medium in which they are travelling, it should be feasible to detect changes in material properties during a cure process. An imbedded acoustic fiber should also be able to sense an applied bending stress.

Acoustic fiber will allow materials to be examined internally, which could provide more accurate information about defects and locations of defects than could external examinations. Another application is in signal processing, due to the relatively slow speed of acoustic waves. This slow speed may allow a wave in an acoustic fiber many meters long to be sampled and interacted with at a number of locations, thus permitting high precision convolution, correlation, and other processing functions to be realized.

ORIGINAL PAGE IS
OF POOR QUALITY

ORIGINAL PAGE IS
OF POOR QUALITY

ACKNOWLEDGEMENTS

The authors would like to thank the Virginia Center for Innovative Technology for supporting this research, ITT for making the preform, and Corning Glass Works for donating the 7070 rod.

REFERENCES

[1] G. D. Boyd, L. A. Coldren, and R. N. Thurston, "Acoustic Clad Fiber Delay Lines," IEEE Transactions on Sonics and Ultransonics," vol. SU-24, No. 4, July, 1977.

[2] R. T. Harrold and Z. N. Sanjana, "Material Cure and Internal Stresses Monitored via Embedded Acoustic Waveguides," Westinghouse Research and Development Center, Pittsburgh, PA, Feb., 1986.

[3] A. Safaai-Jazi, C. K. Jen, and G. W. Farnell, "Fiber Acoustic Waveguides," Final Report, Chapter 1, Summary of Analysis, Feb., 1986.

[4] A. Safaai-Jazi, C. K. Jen, and G. W. Farnell, "Analysis of Weakly Guiding Fiber Acoustic Waveguide," IEEE Transactions on Ultrasonics, Ferroelectrics, and Frequency Control, vol. UFCC-33, No. 1, pp.59-68, Jan., 1986.

[5] A. Safaai-Jazi, C. K. Jen, G. W. Farnell, and J. F. Bussiere, "Longitudinal Modes in Weakly Guiding Fiber Acoustic Waveguides," IEEE 1985 Ultrasonics Symposium, San Francisco, CA, Oct. 16-18, 1985.

[6] C. K. Jen, "Similarities and Differences Between Fiber Acoustics and Fiber Optics," IEEE 1985 Ultrasonics Symposium, San Francisco, CA, Oct. 16-18, 1985.

[7] C. K. Jen, A. Safaai-Jazi, G. W. Farnell, and E. L. Adler, "Review of Progress in Quantitative NDE," Williamsburg, VA, June 23-28, 1985.

[8] A. Safaai-Jazi, C. K. Jen, and G. W. Farnell, "Cutoff Conditions in an Acoustic Fiber with Infinitely Thick Cladding," IEEE Transactions on Ultrasonics, Ferroelectrics, and Frequency Control, vol. UFCC-33, No. 1, pp. 69-73, Jan., 1986.

ORIGINAL PAGE IS
OF POOR QUALITY

# Appendix I. BASIC Program for Processing of Digitized Waveforms

```
REM WAVEFORM PROCESSING PROGRAM
' THIS PROGRAM IS DESIGNED TO TRANSFER DATA ON THE IEEE488
' BUS.  METROBYTE CARD IE-488 MUST BE INSTALLED IN THE PC.
' THE PROGRAM READS AND WRITES DATA TO A PERIPHERAL AND PLOTS
' WAVEFORM DATA ON THE SCREEN.  IT CAN ALSO BE USED TO STORE
' DIGITIZED WAVEFORM POINTS ON DISK.
DIM DAT.ARY(2048),D%(2048),VAR%(2)
KEY OFF
GOSUB 230
KEY (1) ON : KEY (2) ON : KEY (3) ON: KEY (4) ON: KEY (5) ON
KEY (6) ON
ON KEY (1) GOSUB 230
ON KEY (2) GOSUB 1950 ' SAVE WAVEFORM
ON KEY (3) GOSUB 440 ' READ WAVEFORM FRM DISK
ON KEY (4) GOSUB 2380 ' READ WAVEFORM FROM SCOPE
ON KEY (5) GOSUB 3300 ' FIND PEAK TO PEAK AMPLITUDE
ON KEY (6) GOSUB 3490 ' PLOT WFM IN PC MEMORY
KEY (1) ON: KEY (2) ON: KEY (3) ON
KEY (4) ON: KEY (5) ON: KEY (6) ON
GOTO 200
'
' ****************************************************
'            ***** SUBROUTINE MENU *****
' THIS ROUTINE SETS UP THE WAVEFORM PROCESSING MENU
' ****************************************************
SCREEN 0,1
COLOR 15,1
WIDTH 80
SCREEN 0,1 : CLS
PRINT: PRINT: PRINT
PRINT TAB(20); "WAVEFORM PROCESSING PROGRAM"
PRINT: PRINT
PRINT TAB(15); "PRESS FUNCTION KEY FOR DESIRED ROUTINE"
PRINT
PRINT TAB(20); "F1-PRINT MENU"
PRINT TAB(20); "F2-SAVE WAVEFORM ON DISK"
PRINT TAB(20); "F3-READ WAVEFORM FROM DISK"
PRINT TAB(20); "F4-READ WAVEFORM FROM SCOPE"
PRINT TAB(20); "F5-CALCULATE PEAK TO PEAK AMPLITUDE"
PRINT TAB(20); "F6-PLOT WFM IN PC MEMORY"
RETURN
'
' ****************************************************
'          ***** SUBROUTINE RDWFM.DSK *****
'  THIS ROUTINE READS WAVEFORMS FROM DISK
' ****************************************************
CLS
PRINT:PRINT: PRINT
PRINT TAB(22): PRINT "ENTER THE DATA FILE NAME TO BE READ"
PRINT TAB(22): PRINT "NAME MUST END WITH  .  ": PRINT
PRINT TAB(30): INPUT FILE$: PRINT
PRINT TAB(22): INPUT "IS DATA FILE NAME CORRECT? (Y OR N)";ANS$
IF ANS$="N" THEN 470
' ** CALL READ DATA FILE
GOSUB 690
'  RETURN FROM SUBROUTIN RDDATFIL W/ WFM DATA IN DAT.ARY
'  NORMALIZE DATA FOR PLOTTING AND SCALE SCREEN
'** CALL SCALE
GOSUB 1070
```

```
'  PLOT DATA
'** CALL PLOT
GOSUB 1790
KEY OFF
LOCATE 25,2
PRINT "ENTER F1 FOR MENU, F2 TO SAVE WAVEFORM";
RETURN
'
' ************************************************
'     ***** SUBROUTINE READ DATA FILE  *****
' THIS ROUTINE READS THE WAVEFORM DATA FROM DISK
' ************************************************
FILEX$="A:"+FILE$+"DOC"
OPEN "I",#1,FILEX$
'** CALL READ DOC
GOSUB 930
FILEX$="A:"+FILE$+"DAT"
OPEN "I",#1,FILEX$
' ** CALL READ DATA
GOSUB 830
RETURN
'
' ************************************************
'       ***** SUBROUTINE READ DATA *****
' THIS ROUTINE READS WAVEFORM POINTS FROM DISK
' ************************************************
FOR I= 1 TO NPTS
INPUT #1,DAT.ARY(I)
NEXT I
CLOSE #1
RETURN
'
' ************************************************
'        ***** SUBROUTINE READ DOC *****
' THIS ROUTINE READS WAVEFORM DOCUMENTATION FROM DISK
' ************************************************
IF LOF(1) > 25 THEN 1010 ELSE 970
' UNDOCUMENTED DATA FO
INPUT #1,NPTS,VNORM,HNORM
CLOSE #1
0 RETURN
0 ' DOCUMENTED DATA FILE
0 INPUT #1,NPTS,VNORM,HNORM,TIT$,STIT$,TIM$,DA$,XLBL$,YLBL$
0 CLOSE #1
0 RETURN
0 '
0 ' ************************************************
0 '         ***** SUBROUTINE SCALE *****
0 ' NORMALIZES DATA & SETS UP SCREEN FOR PLOT
0 ' ************************************************
0 'FIND MIN AND MAX OF DATA
0 MIN=DAT.ARY(1)
0 MAX=DAT.ARY(1)
0 FOR I=2 TO NPTS
0 IF DAT.ARY(I)> MAX THEN MAX=DAT.ARY(I)
0 IF DAT.ARY(I)< MIN THEN MIN=DAT.ARY(I)
0 NEXT I
0 ' SETUP SCREEN SCALE
0 IF MAX=MIN OR MIN > 0 THEN MIN=0
0 YSCAL=ABS(150/(MAX-MIN))
```

ORIGINAL PAGE IS
OF POOR QUALITY

```
IF MIN < 0 THEN OFFST=ABS(MIN*YSCAL) ELSE OFFST=0
XSCAL=536/NPTS
' PLOT COORDINATE AXES
SCREEN 2:CLS
LINE (79,34)-(79,184)
IF OFFST=0 THEN ZRAX=184 ELSE ZRAX=184-ABS(MIN*YSCAL)
LINE (79,ZRAX)-(615,ZRAX)
' CALCULATE AND PLOT AXES TICS
IF ZRAX > (184-75) THEN 1290 ELSE 1450
FOR I= 5 TO 11
IF I*15/YSCAL => MAX THEN J=I-1 ELSE 1320
I=20
NEXT I
PROW=0
FOR I=0 TO 9
TIC=ZRAX-15*(J-I)
LINE (75,TIC)-(83,TIC)
' PRINT TIC LABELS
LBL=((184-OFFST-TIC)/YSCAL)*VNORM
ROW=CINT((TIC+1)/8)
IF ROW-PROW <= 1 THEN ROW=ROW+1
PROW=ROW
LOCATE ROW,1
PRINT USING "##.##^^^^";LBL;
NEXT I: GOTO 1600  '30
FOR I= 5 TO 11 '20
IF I*15/YSCAL > ABS(MIN) THEN J=I-1 ELSE 1480
I=20
NEXT I
PROW=0
FOR I=0 TO 9
TIC=ZRAX+15*(J-I)
LINE (75,TIC)-(83,TIC)
LBL=((184-OFFST-TIC)/YSCAL)*VNORM
ROW=CINT((TIC+1)/8)
IF ROW-PROW <= 1 THEN ROW=ROW+1
PROW =ROW
LOCATE ROW,1
PRINT USING "##.##^^^^";LBL;
NEXT I
FOR I=0 TO 5  '30
TIC=79+I*107
YLOC1=ZRAX-2 : YLOC2=ZRAX+2
LINE (TIC,YLOC1)-(TIC,YLOC2)
LBL=((TIC-79)/XSCAL)*HNORM
COL=INT((TIC+1)/8)-5
LOCATE 24,COL
PRINT USING "##.##^^^^";LBL;
NEXT I
IF TIT$="" THEN RETURN
LOCATE 1,1: PRINT TIT$;
LOCATE 1,65 : PRINT DA$;
LOCATE 2,1 : PRINT STIT$;
LOCATE 2,65 : PRINT TIM$;
LOCATE 4,10 : PRINT YLBL$;
LOCATE 25,65 : PRINT XLBL$;
RETURN
'
' ************************************************
'        ***** SUBROUTINE PLOT *****
```

ORIGINAL PAGE IS
OF POOR QUALITY

```
0 ' THIS ROUTINE PLOTS DATA FROM ARRAY DAT.ARY
0 ' ***********************************************
0 YPNT1=184-(OFFST+YSCAL*DAT.ARY(1))
0 XPNT1=79+CINT(XSCAL)
0 IF NPTS=>512 THEN STP=4 ELSE STP=1
0 FOR I=2 TO NPTS STEP STP
0 YPNT2=184-(OFFST+YSCAL*DAT.ARY(I))
0 XPNT2=79+CINT(XSCAL*I)
0 LINE (XPNT1,YPNT1)-(XPNT2,YPNT2)
0 YPNT1=YPNT2
0 XPNT1=XPNT2
0 NEXT I
0 RETURN
0 '
0 '
0 ' ******************************************************
0 '      ***** SUBROUTINE SAVE WFM ON DISK *****
0 ' THIS ROUTINE WRITES WAVEFORM DATA AND DOCUMENTATION TO DISK
0 ' ******************************************************
0 SCREEN 0,1: CLS
0 COLOR 0,4
0 SCREEN 0,1: CLS
0 PRINT: PRINT
0 PRINT TAB(28): PRINT "WAVEFORM DOCUMENTATION" : PRINT
0 COLOR 15,4: PRINT
0 PRINT TAB(5);
0 INPUT "ENTER A FILENAME FOR THE WAVEFORM DATA (MUST END WITH . )";FILE$
0 PRINT
0 PRINT TAB(5) :PRINT "ENTER A TITLE FOR THE WAVEFORM."
0 PRINT TAB(5): INPUT TIT$
0 PRINT
0 PRINT TAB(5) :PRINT "ENTER A SUBTITLE, IF DESIRED."
0 PRINT TAB(5): INPUT STIT$
0 PRINT
0 PRINT TAB(5) :PRINT "ENTER A Y AXIS LABEL."
0 PRINT TAB(5): INPUT YLBL$
0 PRINT
0 PRINT TAB(5) :PRINT "ENTER A X AXIS LABEL."
0 PRINT TAB(5): INPUT XLBL$
0 PRINT
0 PRINT TAB(5): INPUT "IS ENTERED DOCUMENTATION SATISFACTORY? (Y OR N)";ANS$
0 IF ANS$="N" THEN GOTO 1950: CLS
0 DA$=DATE$
0 TIM$=TIME$
0 FILEX$="A:"+FILE$+"DOC"
0 OPEN "O",#1,FILEX$
0 PRINT #1, NPTS,VNORM,HNORM
0 WRITE #1, TIT$,STIT$,TIM$,DA$,XLBL$,YLBL$
0 CLOSE #1
0 ' OUTPUT DATA
0 FILEX$="A:"+FILE$+"DAT"
0 OPEN "O",#1,FILEX$
0 FOR I=1 TO NPTS
0 PRINT #1,DAT.ARY(I)
0 NEXT I
0 CLOSE #1
0 GOSUB 230
0 RETURN
0 ' ****************************************
0 '  ***** SUBROUTINE READ FROM SCOPE *****
```

ORIGINAL PAGE IS
OF POOR QUALITY

```
0 ' THIS ROUTINE READS WAVEFORM DATA FROM THE DIGITAL SCOPE
0 ' ****************************************
0 ' ** CALL INITIALIZE
0 GOSUB 2810
0 ' ** CALL READ NORMALIZATION
0 GOSUB 2930
0 ' ** CALL INITIALIZE
0 GOSUB 2810
0 OPEN "O",#1,"C:DUMDAT."
0 DAT$="D3D2"
0 DAT1$=" "
0 CMDCL$="CLEAR 14,15"
0 CMDOP$="OUTPUT 15[$]"
0 CMDIP$="ENTER 14[WD,1,2048]"
0 I=1
0 CALL IE488 (CMDOP$,DAT$,FLG%,BRD%)
0 IF FLG%<>0 THEN PRINT HEX$(FLG%)
0 VAR%(1)=&HFFFF
0 VAR%(2)=(VARPTR(D%(1))+1)
0 CALL IE488(CMDIP$,VAR%(1),FLG%,BRD%)
0 FOR I=1 TO 500
0 NEXT I
0 FOR I=1 TO NPTS
0 PRINT #1, D%(I)
0 NEXT I
0 CLOSE #1
0 CALL IE488 (CMDCL$,DAT1$,FLG%,BRD%)
0 'IF FLG%<>0 THEN PRINT HEX$(FLG%)
0 OPEN "I",#1,"C:DUMDAT."
0 ' ** CALL READ DATA
0 GOSUB 830
0 ' ** CALL SCALE
0 TIT$=""
0 GOSUB 1070
0 ' **CALL PLOT
0 GOSUB 1790
0 LOCATE 25,2
0 PRINT "ENTER F1 FOR MENU, F2 TO SAVE WAVEFORM";
0 RETURN
0 '
0 ' ************************************************
0 '       ***** SUBROUTINE INITIALIZE *****
0 ' THIS ROUTINE SENDS INITIALIZATION COMMANDS TO IE-488
0 ' ************************************************
0 DEF SEG = &HC000
0 CMDIN$ = "SYSCON MAD=3, CIC=1, NOB=1, BA0=&H300"
0 IE488 = 0
0 A% = 0 : FLG% = 0 : BRD% = 0
0 CALL IE488 (CMDIN$, A%, FLG%, BRD%)
0 IF FLG%<>0 THEN PRINT "INSTALLATION ERROR"
0 RETURN
0 '
0 ' ************************************************
0 '     ***** SUBROUTINE READ NORMALIZATION *****
0 ' THIS ROUTINE READS NORMALIZATION DATA FROM THE SCOPE
0 ' ************************************************
0 DOC$=SPACE$(27)
0 FLG%=0 :BRD%=0
0 DAT$="N0"
0 DAT1$=" "
```

ORIGINAL PAGE IS
OF POOR QUALITY

ORIGINAL PAGE IS
OF POOR QUALITY

```
0 CMDCL$="CLEAR 14,15"
0 CMDOP$="OUTPUT 15[$]"
0 CMDIP$="ENTER 14[$#]"
0 CALL IEEE (CMDOP$,DAT$,FLG%,BRD%)
0 IF FLG%<>0 THEN PRINT FLG%
0 CALL IE488(CMDIP$,DOC$,FLG%,BRD%)
0 IF FLG%<>0 THEN PRINT HEX$(FLG%)
0 CALL IE488 (CMDCL$,DAT1$,FLG%,BRD%)
0 IF FLG%<>0 THEN PRINT FLG%
0 DUM$=MID$(DOC$,3,1)
0 MEM=VAL(DUM$)
0 'IF MEM<>1 THEN 2840
0 PRINT " "
0 PRINT " "
0 PRINT "NUMBER OF POINTS MUST CORRESPOND TO MEMORY SETTING ON SCOPE"
0 PRINT "ENTER 2 FOR 2048 POINTS"
0 PRINT "ENTER 4 FOR 1024 POINTS"
0 INPUT NUM
0 IF NUM=MEM THEN 3230
0 PRINT "IF YOU ARE SELECTING ONLY SOME POINTS FROM THE ORIGINAL"
0 PRINT "ENTER 2 FOR A REDUCTION BY HALF"
0 PRINT "ENTER 4 FOR A REDUCTION BY QUARTER"
0 INPUT REDN
0 DUM$=MID$(DOC$,14,7)
0 VNORM=VAL(DUM$)
0 NPTS=4096/NUM
0 DUM$=MID$(DOC$,21,7)
0 HNORM=VAL(DUM$)*REDN
0 RETURN
0 '
0 '*********************************************
0 '   ****SUBROUTINE  PEAK TO PEAK AMP****
0 'DETERMINES PK TO PK AMPLITUDE OF WFM WINDOW
0 '*********************************************
0 '
0 CLS
0 PRINT: PRINT : PRINT
0 PRINT TAB(20): INPUT "ENTER STARTING POINT OF PEAK SEARCH";PKSTRT
0 IF (PKSTRT+512)>2048 THEN PKEND=2048 ELSE PKEND=PKSTRT+512
0 PKMAX=DAT.ARY(PKSTRT)
0 PKMIN=PKMAX
0 FOR I=PKSTRT+1 TO PKEND
0 IF DAT.ARY(I)>PKMAX THEN PKMAX=DAT.ARY(I)
0 IF DAT.ARY(I)<PKMIN THEN PKMIN=DAT.ARY(I)
0 NEXT I
0 VPK=HNORM*(PKMAX-PKMIN)
0 PRINT: PRINT TAB(20): PRINT "PEAK TO PEAK VOLTAGE=";VPK
0 PRINT: PRINT: PRINT TAB(20); "ENTER F1 FOR MENU, F6 FOR WAVEFORM"
0 RETURN
0 GOSUB 1170
0 GOSUB 1790
0 RETURN


:LIST 3000_-
0 CMDCL$="CLEAR 14,15"
0 CMDOP$="OUTPUT 15[$]"
0 CMDIP$="ENTER 14[$#]"
0 CALL IEEE (CMDOP$,DAT$,FLG%,BRD%)
```